The University of Sheffield

Understanding the structure and radiation behaviour of complex ceramic oxides Ln_2TiO_5 (Ln = lanthanide) for actinide immobilisation

Daniel Anthony Austin

A thesis is submitted in partial fulfilment of the requirement for the degree of Doctor of Philosophy

Primary supervisors: Neil C. Hyatt & Russell J. Hand

Associate supervisors: Martin C. Stennett & Luke T. Townsend

Abstract

The generation of electricity from nuclear power sources, whilst proving a low carbon emission alternative to fossil fuel based sources, produces large amounts of actinide containing radioactive wastes as a by-product. As these radioactive wastes pose a significant potential risk to both the environment and public health, a means of safely disposing of them is required. The UK government, and indeed many others across the globe, consider disposal of these wastes in geological repository, using a multi-barrier approach, as the safest method. A principal component of the multi-barrier approach is to either vitrify waste products in glass mediums, such as borosilicate, or immobilise them in ceramic systems. Ceramics are of particular interest due to their high aqueous durability, favourable physical qualities, tolerance of radiation damage and high potential waste loading.

The ability of a ceramic wasteform to resist and have predictable responses to radiation damage is key to their implementation. The development of novel Ln_2TiO_5 ceramics as nuclear wasteforms has recently been undertaken due, in large part, to their reportedly high radiation tolerance. This study aims to characterise the local atomic arrangements of structures associated with Ln_2TiO_5 series of ceramics and their response to radiation damage by utilising multiple X-ray absorption techniques. The Ln_2TiO_5 series of ceramics form the end member of the $Ln_2(Ti_{2-x}Ln_x)O_{7-x/2}$ (x = 0.667) pyrochlore solid solution and as such are often referred to as stuffed pyrochlores due to the additional lanthanide cations 'stuffed' onto the Ti-site. Dependent on ionic radius of the lanthanide used, pressure and temperature, different structure types can be obtained. The structures that Ln_2TiO_5 stuffed pyrochlores have been commonly observed to form include orthorhombic *Pnma*, hexagonal *P6$_3$/mmc* and cubic *Fd-3m* and *Fm-3m* symmetries. The radiation tolerance of these materials is highly dependent upon the crystal structure used.

Whilst the long-range order of these materials is relatively well described there is a significant lack in understanding of the short-range order. Various studies have reported conflicting conclusions about the short-range structure of cubic Ln_2TiO_5. The long-range structures have been observed to be defect-fluorite *Fm-3m* and the short-range order to be possibly consist of a series of *Fd-3m* pyrochlore nanodomains or to have orthorhombic *Pnma* symmetry. Through a combination of X-ray absorption near edge spectroscopy (XANES) and extended X-ray absorption fine structure (EXAFS) analyses, the local structure is shown to be well represented by a model based off of a *Fd-3m* structure where the Ti-O coordination is 5-fold (reduced from an initial 6-fold coordination of the pyrochlore structure).

Examination of Ln_2TiO_5 stuffed pyrochlores, that adopt either an orthorhombic or hexagonal symmetries through X-ray diffraction (XRD), using XAS techniques concludes that they are well represented by models based upon the same structure assigned to their long-range ordering. Furthermore, it is shown that the TiO_5 polyhedra associated with both orthorhombic and hexagonal structures are found to have different degrees of centro-symmetry.

Understanding the local structure of these materials is vital to predicting how they will behave under extreme environmental conditions, such as in high intensity radiation fields. The successful design of XAS models allowed for further study of the local structural environments of Ln_2TiO_5 stuffed

pyrochlores through the application of glancing angle X-ray absorption spectroscopy (GAXAS). This technique was used to probe the damaged surface region of ion beam irradiated (Au^{2+} and Kr^{+}) bulk monoliths of orthorhombic Gd_2TiO_5, hexagonal Dy_2TiO_5 and cubic Yb_2TiO_5. The results of this study gave key insights into the structural responses of these materials to radiation damage and allowed for the development of an understanding of mechanisms that drive their responses.

The comprehensive study of the structures and radiation response of Ln_2TiO_5 stuffed pyrochlores provided in this PhD study will facilitate future tailoring of their applications for roles within the nuclear industry and beyond.

'There is no route out of the maze. The maze shifts as you move through it, because it is alive'

– Philip K. Dick, VALIS

Acknowledgments

First and foremost, I would like to offer my sincerest gratitude to my supervisors Prof. Neil Hyatt and Dr. Martin Stennett. This thesis is testament to the endless care, support, and encouragement you have shown me. Thank you for believing in me. I am also grateful to Prof. Russell Hand who, when needed, helped get this thesis over the line. Thank you to Dr. Luke Townsend, who gave much of his time, expertise and enthusiasm helping me write and edit this thesis. As far as a supervisory team goes, I could not ask for more. You all inspire me to do better and reach further. Your friendships will be carried with me, always.

As we all know, it takes a village to complete a PhD. As such this work was not completed in absence of support from many talented individuals. I would like to thank the beamline staff at DCF, Dr. Carl Andrews and Dr. Andrew Smith, who gave great advice and tuition towards completing my radiation damage experiments. A huge thanks goes to my international collaborator Dr. Bruce Ravel, who contributed much of his invaluable expertise and experience, and the staff at NSLS-II for their welcoming and accommodating nature. I am also grateful to Prof. Shi-Kuan Sun and Dr. Daniel Bailey, who supported my experimental and written work, and were huge inspirations to me throughout my tenure. Whilst I have named but a few, my work would not be what it is today without the effort and attention of countless others, both within and without the university. Thank you to you all.

I would also like to thank the EPSRC and University of Sheffield for the opportunity to do, and funding of, this work.

Throughout the duration of my PhD I have experienced some of my biggest highs and biggest lows. It takes a special group of people to pick you up after those lows, and make you feel confident and happy to continue onwards. I would, therefore, like to show my appreciation to the many friends I have made over the last few years. Thank you to Chris and Lewis, who I started my PhD with and have remained two of the people I consider amongst my closest friends. I would like to thank Lucas, Mark and Robin who I have spent long evenings playing DnD with and have been steadfast friends. I would also like to recognise the friendship of Luke, Liam and Dan P, which I treasure dearly. I extend my heartfelt gratitude to all the many other friends I have made at the ISL, you have all touched my life in ways that I will never forget. I also want to thank my brother, Ryan, who has always believed in me and has been an ever-present friend.

I cannot express just how much the unconditional love, support and belief of my mom and dad has meant to me. Without the morals and work ethic you instilled in me, I would be where I am today. You are my role models and my inspirations. I hope that I can live up to example you have set me, you make me so very proud. I love you.

Whilst I have met many amazing people during my PhD, none compared to the person I met during our first ISL Christmas meal. Since that day, you have been my constant supporter, my best friend, my confident and my reason to be. I love you, Hannah. I would also like to thank Poppy for her sage advice and critique of my EXAFS models in addition to all the loves and walks you has provided.

Thank you, everyone.

Common abbreviations

Act- Actinide

BCA – binary collision approximation

BNL – Brookhaven national laboratory

BSE – Back-scattered electron

BWR – Boiling water reactor

CFS – Crystal field splitting

CN – Coordination number

CPS – Cold press and sinter

DAFNE – Dalton accelerator for nuclear experiments

DCF – Dalton Cumbria facility

dpa – Displacements per atom

ED – Electron diffraction

EDX – energy dispersive X-ray spectrometry

EXAFS – Extended X-ray absorption fine structure

FEG – Field emission gun

FT – Fourier transform

GAXAS – Glancing-angle X-ray absorption spectroscopy

GAXRD – Glancing-angle X-ray diffraction

GDF – Geological disposal facility

HIP – Hot isostatic pressing

HLW – High-level waste

ILW – Intermediate-level waste

IPG – Iron phosphate glasses

LCF – Linear combination fitting

LINAC – Linear accelerator

LLW – Low level Waste

Ln – Lanthandie

MAS – Magnesium aluminosilicate

MBS – Magnesium borosilicate

MC-SNIC – multi-cathode source of negative ions by caesium sputtering

MSS – Molten salt synthesis

NDA – Nuclear decommissioning authority

NSLS-II – National synchrotron light source II

PDF – Pair distribution function

PWR – Pressurised water reactor

RPM – Rotations per minute

SE – Secondary electron

SEM – Scanning electron microscopy

SNF – Spent nuclear fuel

SRIM – Stopping range of ions in matter

SSS – Solid-state synthesis

SXAS – soft X-ray absorption spectroscopy

T_C – Critical temperature

TEM – Transmission electron microscopy

TEY – Total electron yield

XAFS – X-ray absorption fluorescence spectroscopy

XANES – X-ray absorption near edge spectroscopy

XAS – X-ray absorption spectroscopy

XRD – X-ray diffraction

Contents

1. Introduction

Radioactive waste is primarily generated by civil nuclear fuel cycle activities supporting the generation of nuclear energy, although historic nuclear defence activities have contributed significantly to radioactive waste and decommissioning challenges in the nuclear weapons states. Radioactive wastes that cannot be consigned to normal landfill disposal, require treatment and disposal in a near surface or deep engineered facility, to protect the biosphere until such time as the radiological inventory has sufficiently decayed.

Nuclear activities will generate radioactive waste at every point in the nuclear fuel cycle, from the tailings produced by uranium mining to spent nuclear fuel. The volume and radioactivity of these wastes vary widely, and each requires specifically tailored disposal methodologies. The ionising radiation (α, β or γ) produced by these wastes can pose a significant risk to human health, particularly that arising from spent fuel. These wastes are classified in the UK as [1]:

- High-Level Waste (HLW) – Waste in which the temperature may rise significantly due to its radioactivity, sufficiently so that this has to be taken into account in the design of disposal methods. HLW constitutes, primarily, fission products and transuranics arising from nuclear fission inside a reactor and as a by-product of reprocessing spent fuel. The 1,390 m^3 of HLW accounts for less than 1% of the UK's waste inventory volume.
- Intermediate-Level Waste (ILW) – Waste that exceeds the threshold of radioactivity generated to be classified as low-level wastes but does not need to account for heat generation when designing storage or disposal facilities. ILW consists of wastes from stripped fuel cladding, reactor components and materials contaminated with plutonium (e.g. filters or graphite from the reactor core) and sludges from the radioactive liquid effluents. ILW accounts for 6% of the UK's radioactive waste inventory volume (247,000 m^3).
- Low-Level Waste (LLW) – Wastes containing radioactive materials other than those acceptable for disposal with ordinary refuse, but not exceeding 4 GBq/t alpha or 12 GBq/t beta/gamma. LLW consists mainly of discarded equipment and personal protective equipment, scrap metal, building materials and office supplies suspected of contamination. This waste mostly arises in the UK from the operation and decommissioning of nuclear sites. LLW accounts for 93% of the UK's radioactive waste inventory volume (1,480,000 m^3).
- Very Low-Level Waste – Waste containing less than 400 kBq beta/gamma in a volume of 0.1 m^3 or individual items not exceeding 40 kBq of activity. This waste can be safely disposed alongside in municipal, commercial or industrial waste at specified landfills.

The estimated quantities of radioactive wastes arising in the UK and worldwide are compared in Table 1.1 and Table 1.2, respectively, to illustrate the scale of the challenge. Of particular note, in the UK is

that more than 65% of the overall volume of ILW and 98% of the overall volume of LLW remain to be generated by the UK nuclear decommissioning program. It should be noted, that the estimated future arisings indicates a negative value. This is due to the combination of HLW being conditioned (which will reduce the overall volume) and vitrified waste being exported to overseas customers. The projected discounted cost of UK nuclear decommissioning was estimated as £349 billion in 2020, with a time frame of 100 years for completion [2]. However, in the UK, no higher activity waste (i.e. ILW or HLW) has yet been disposed of, due to the absence of a suitable deep Geological Disposal Facility (GDF). Recently, the UK government launched a siting process to find a location for such a facility, with community engagement [3]. Internationally, it is evident that no high-level waste has been disposed of and only ILW from the US nuclear weapons programme has been disposed at the WIPP repository in New Mexico. WIPP is currently the only licensed and operating facility for disposal of higher activity wastes in world, although a construction license was granted for the Onkalo GDF in Finland in 2015, with construction expected to begin in 2023 [4].

Table 1.1: Volume arising in the UK Radioactive Waste Inventory, according to UK classification [1]

Classification	**Volume (m^3)**		
	Reported at 1 April 2019	**Estimated future arisings**	**Lifetime Total**
HLW	2,150	-760	1,390
ILW	102,000	145,000	247,000
LLW	27,400	1,450,000	1,480,000
VLLW	1,040	2,830,000	2,830,000
Total	**133,000**	**4,420,000**	**4,560,000**

Table 1.2: Volume arising of radioactive waste internationally, according to UK classification [5]

Classification	**Solid radioactive waste in storage (m^3)**	**Solid radioactive waste in disposal (m^3)**	**Proportion of waste type in disposal (vol.%)**
HLW	29,000	0	0%
ILW	2,740,000	133,000	4.6%
LLW	1,471,000	18,499,000	92.6%
VLLW	2,918,000	11,842,000	80.2%

In addition to the national and global radioactive waste inventories summarised in Tables 1 and 2, there exists a substantial quantity of separated fissile material which is of international concern, as reported in Table 3 (data submitted under INFCIRC/549). As can be seen, the UK holds the world's largest stockpile of separated civil plutonium, which is projected to reach 140 tons at the end of reprocessing operations at Sellafield [6]. At present, UK plutonium is held in safe and secure interim

storage at the Sellafield site, however, the Nuclear Decommissioning Authority have acknowledged that this approach is not sustainable indefinitely due to the need for periodic repacking of the material [6]. Several international authorities and learned societies have highlighted the need for urgent action to either re-use UK plutonium in mixed-oxide $(U,Pu)O_2$ or immobilise and dispose of plutonium into a GDF when available. At the time of writing, current Government policy is to reuse suitable plutonium in mixed oxide fuel for use in light water reactors. However, this is challenged by the lack of appetite by operators: neither the existing Sizewell B or planned Hinkley Point C reactors are licensed for MOX use, and the operator, EDF, has no plans to seek such a licence [6]. Consequently, there is growing interest in immobilisation and disposal of the UK plutonium stockpile if the policy for reuse cannot be realised. At least 5% of the UK stockpile will, in any case, require immobilisation and disposal since it is not suitable for MOX fuel manufacture [6]. Therefore, the NDA is currently sponsoring research aimed to develop the material, process and safety case to enable immobilisation of the UK plutonium stockpile if required. Internationally, interest in the immobilisation of surplus civil and defence plutonium is also growing in the USA and Japan.

Table 1.3: World stocks of fissile materials, as of February 2018; source: International Panel on Fissile Materials. Reported by International Atomic Energy Agency (IAEA) under INFCIRC/549 obligations by member state signatories.

Nation	**High Enriched Uranium (tons)**	**Defence Pu (tons)**	**Civilian Pu (tons)**
Russia	678	128	63
USA	562	79.7	8
UK	22.6	3.2	115.8
France	30	6	74.7
Others	39.1	4.9	54.4
TOTAL	1,331.7	221.5	315.9

This project is therefore concerned with the design, processing, characterisation and performance of advanced titanate ceramics for the immobilisation of actinide waste products, e.g. Pu, from nuclear activities. Of particular interest is the Ln_2TiO_5 family of ceramics, which is related to the parent pyrochlore group $Ln_2Ti_2O_7$ through the introduction of additional lanthanide cations ($Ln_2(Ti_{1.33}Ln_{0.67})O_{6.67}$) and, as such, is commonly referred to as a 'stuffed' pyrochlore. Ln_2TiO_5 ceramics have shown great versatility in crystalline phase formation, dependant on the size of ionic radii of cations and thermal history [7], [8]. Room temperature phases obtainable through typical solid-state synthesis routes are orthorhombic *Pnma*, hexagonal *$P6_3/mmc$* and cubic defect fluorite *Fm-3m.* In addition to the inherent larger retention of lanthanide elements, these pyrochlores have demonstrated greater radiation tolerance than the related $Ln_2Ti_2O_7$ pyrochlore [9] but the response

to radiation damage is highly dependent on the crystal structure, with cubic Ln_2TiO_5 compounds demonstrating the greatest tolerance [9]–[11].

The contributions in this thesis aim to give detailed accounts of the complex local-ordering exhibited by Ln_2TiO_5 crystal structures measured using X-ray absorption spectroscopy (XAS). The Ln_2TiO_5 samples and their physical properties that are of interest to this thesis are summerised in Table 1.4. It should be noted that, whilst there is consensus on the long-range ordering of the different Ln_2TiO_5, there is a lack of understanding and agreement on their complex short-range ordering. One of the primary aims of this thesis is to make use of XAS techniques to resolve the complex local coordination exhibited by these materials. A detailed understanding of a materials local structure is a key facet for understanding, and predicting, its response to adverse conditions found in geological disposal environments (radiation damage, corrosion etc.). Ion beam irradiation was used to simulate α-recoil damage of Ln_2TiO_5 ceramics, and the local structures of irradiated materials were characterised through the application of glancing angle X-ray absorption (GAXAS). GAXAS has been little explored previously but as demonstrated the current work shows major potential for the interpretation of damage arising from irradiation.

Figure 1.4: Summary of samples used in this thesis. + indicates that this space group is presumed but no evidence has been currently published. * indicates that the current literature indicates that this structure is likely/possibly but is not certain [7-11]. O – Orthorhombic, H – Hexagonal and C – Cubic. Coordination Numbers (written as LnO_x and TiO_x) are given for the different crystal structures of the possible polymorphs that a specific Ln2TiO5 can be stabilised in.

Ln_2TiO_5	Crystal Structure [7-11]	Space Group	Short-range Ordering	Coordination Number	
				LnO_x	**TiO_x**
La_2TiO_5	O	Pnma	*Pnma*	LaO_7	TiO_5
Pr_2TiO_5	O	Pnma	*Pnma*	PrO_7	TiO_5
Nd_2TiO_5	O	Pnma	*Pnma*	NdO_7	TiO_5
Sm_2TiO_5	O	Pnma	*Pnma*	SmO_7	TiO_5
$Eu2TiO_5$	O	Pnma	*Pnma*	EuO_7	TiO_5
Gd_2TiO_5	O/ H	Pnma $P6_3/mmc$	*Pnma* *P63/mmc+*	GdO_7 **GdO_6^+**	TiO_5 TiO_5
Tb_2TiO_5	O/ H	Pnma $P6_3/mmc$	*Pnma* *P6₃/mmc*	TbO_7 TbO_6	TiO_5 TiO_5
Dy_2TiO_5	O/ H/ C	Pnma $P6_3/mmc$ Fm-3m	*Pnma* *P6₃/mmc* *Fd-3m**	DyO_7 DyO_6 *DyO_8**	TiO_5 TiO_5 TiO_6
Ho_2TiO_5	C	Fm-3m	*Fd-3m**	HoO_7	TiO_7

				*HoO_8**	TiO_6
Er_2TiO_5	C	Fm-3m	*Fd-3m**	ErO_7 *ErO_8**	TiO_7 TiO_6
Tm_2TiO_5	C	Fm-3m	*Fd-3m**	TmO_7 *TmO_8**	TiO_7 TiO_6
Yb_2TiO_5	C	Fm-3m	*Fd-3m**	YbO_7 *YbO_8**	TiO_7 TiO_6
Lu_2TiO_5	C	Fm-3m	*Fd-3m**	LuO_7 *LuO_8**	TiO_7 TiO_6
Y_2TiO_5	C	Fm-3m	*Fd-3m**	YO_7 *YO_8**	TiO_7 TiO_6

The structure of this thesis will contain a broad literature review, in chapter 2, considering topics ranging from nuclear power generation and subsequent waste arisings, review of pertinent literature regarding the radiation response of ceramic wasteforms, with a particular emphasis on Ln_2TiO_5 ceramics, and applications of XAS in the development of nuclear waste immobilisation materials. The experimental review will feature in-depth discussions of the experimental methodologies throughout this thesis. Chapter 3 features an in-depth discussion and review of the experimental methods used throughout this research. The result chapter 4, contains a manuscript that has been submitted for publication and chapters 5 and 6, contain draft manuscripts ready for submission for publication.

The results of chapter 4 are focused on the characterisation of cubic Yb_2TiO_5 and Y_2TiO_5 compounds, synthesised through different cooling regimes *via* X-ray diffraction (XRD) and XAS, to study the long- and short-range ordering of the crystal structures, respectively. Literature highlights the complexity observed in the local structural ordering of cubic Ln_2TiO_5 compounds and there is a lack of an apparent consensus on its exact nature.

Chapter 5 was designed to study a broad range of Ln_2TiO_5 (Ln = La – Lu) compounds across a variety of different crystal structures, characterised *via* a variety of experimental techniques, including XAS. This study is the first full XAS description of the entire Ln_2TiO_5 series and further elucidates the nature of the local coordination of orthorhombic and hexagonal compounds. In addition to the previous chapter, both contributions not only aim to address specific questions regarding the local structure of these materials but also form a basis for further XAS studies of these materials once they have been degraded through radiation damage.

In the third results chapter 6, surfaces of orthorhombic, hexagonal, and cubic Ln_2TiO_5 (Ln = Gd, Dy, Yb) ceramic monoliths were irradiated using two different heavy ions (Kr^+ and Au^{2+}) at different fluences to obtain a variation in damage profile. GAXAS and glancing angle X-ray diffraction (GAXRD) was used to probe the structure of the damaged surface layers of these materials, comparing them to pristine Ln_2TiO_5 monoliths.

Chapter 7 is supplementary to the main thesis and contains a published manuscript that compares molten salt synthesis and solid-state synthesis of orthorhombic Gd_2TiO_5. an additional section in chapter 7 compares initial trials using the same synthesis methods for Dy_2TiO_5 and Yb_2TiO_5.

Finally, chapter 8 collates the conclusions where the key findings and implications of the results will be discussed. Chapter 8 also includes recommendations of future work that will further the development of Ln_2TiO_5 ceramic wasteforms and applications of XAS in the study of nuclear materials.

1.1 References

[1] Nuclear Decomissioning Auhtority (NDA), "2019 UK Radioactive Waste Inventory," 2019. [Online]. Available: https://ukinventory.nda.gov.uk/the-2019-inventory/2019-inventory-reports/. [Accessed: 25-Mar-2022].

[2] Nuclear Decommissioning Authority (NDA), "NDA Business Plan 2021 to 2024," 2021. [Online]. Available: https://www.gov.uk/government/publications/nda-business-plan-2021-to-2024. [Accessed: 20-Mar-2022].

[3] E. & I. S. (BEIS) Department for Business, "Implementing Geological Disposal - Working with Communities," 2018. [Online]. Available: https://www.gov.uk/government/publications/implementing-geological-disposal-working-with-communities-long-term-management-of-higher-activity-radioactive-waste. [Accessed: 20-Mar-2022].

[4] NDA, "Geological Disposal: Overview of international siting process 2017," 2017. [Online]. Available: https://webarchive.nationalarchives.gov.uk/ukgwa/20211004151355/https://rwm.nda.gov.uk/publication/geological-disposal-overview-of-international-siting-processes-2017/. [Accessed: 24-Mar-2022].

[5] I. A. E. A. (IAEA), "Status and Trends in Spent Fuel and Radioactive Waste Management, Nuclear Energy Series," 2022. [Online]. Available: https://www.iaea.org/publications/11173/status-and-trends-in-spent-fuel-and-radioactive- waste-management. [Accessed: 21-Mar-2022].

[6] Nuclear Decommissioning Authority (NDA), "Progress on Plutonium Consolidation, Storage and Disposition," 2019. [Online]. Available :https://www.gov.uk/government/publications/progress-on-plutonium-consolidation-storage-and-disposition. [Accessed: 21-Mar-2022].

[7] R. . G. M.A Petrova, A.S. Novikova, "Polymorphism of Ln_2TiO_5 Rare-Earth Titanates," *zv. Akad. Nauk SSSR, Neorg. Mater.*, vol. 18, no. 2, pp. 287–291, 1982.

[8] S. Park *et al.*, "A_2TiO_5 (A = Dy, Gd, Er, Yb) at High Pressure," *Inorg. Chem.*, vol. 57, no. 4, pp. 2269–2277, Feb. 2018.

[9] K. R. Whittle, M. G. Blackford, R. D. Aughterson, G. R. Lumpkin, and N. J. Zaluzec, "Ion irradiation of novel yttrium/ytterbium-based pyrochlores: The effect of disorder," *Acta Mater.*, vol. 59, no. 20, pp. 7530–7537, Dec. 2011.

[10] R. D. Aughterson *et al.*, "The ion-irradiation tolerance of the pyrochlore to fluorite $Ho_{(x)}Yb_{(2-x)}TiO_5$ and Er_2TiO_5 compounds: A TEM comparative study using both in-situ and bulk ex-situ irradiation approaches," *J. Nucl. Mater.*, vol. 507, pp. 316–326, Aug. 2018.

[11] R. D. Aughterson, N. J. Zaluzec, and G. R. Lumpkin, “Synthesis and ion-irradiation tolerance of the Dy_2TiO_5 polymorphs,” *Acta Mater.*, vol. 204, p. 116518, Feb. 2021.

2. Literature Review

2.1 Introduction

With the move towards low-carbon or carbon-neutral electricity production, nuclear power is essential in providing baseload electricity generation. Since the first commercially operated nuclear power station, Calder Hall-1 at Windscale, around 440 nuclear power reactors have been constructed in 32 countries, accounting for 10% of global electricity production and 28% of low-carbon based electricity production [1]. Nuclear power utilises the nuclear fissioning of atomic nuclei to generate large amounts of energy with comparatively little generation of greenhouse gases. However, this process does create extensive inventories of highly radioactive waste, a serious issue that nations are now considering how to handle. Immobilisation and disposal strategies for this waste are areas of ongoing research, wherein ceramic systems have been proposed to play a significant role in the eventual disposal of radioactive wastes. This review will consider topics ranging from nuclear fission and the nuclear fuel cycle to potential ceramic wasteforms options.

2.2 Nuclear fission

2.2.1 Ionising radiation

Nuclei, consisting of positively charged protons and neutral neutrons, are stable when the Coulomb repulsion of protons acting on one another is balanced by an appropriate number of neutrons, overcoming the electrostatic repulsion through the strong nuclear force. When a nucleus has too many or too few protons or neutrons, it becomes unstable. When a nucleus becomes unstable, it will undergo random and spontaneous radioactive decay. Radioactive decay is the emission of energy in the form of ionising radiation and, for alpha and beta decay, results in transmutation of chemical elements. The three types of radioactive decay are [2]:

- Alpha decay – the emission of two protons and two neutrons bound together, identical to the He nucleus (He nuclei are tightly bound and stable). This type of radiation, shown in Equation 2.1, occurs in nuclei that are large enough that the nuclear force holding them together is not sufficient to overcome the electrostatic repulsion of the protons. The reduction in the size of the nuclei increases its stability. Alpha particles are highly ionising but will often interact with other elements due to their large mass and low velocity, giving them very little penetrating power.

$$^{92}_{235}U \rightarrow {}^{90}_{231}Th + {}^{2}_{4}He \qquad \textbf{Equation 2.1}$$

- Beta-decay – the process in which a beta particle is emitted from a nucleus. When there are too many neutrons in a nucleus, a neutron may be converted into a proton and emit an electron and antineutrino. This is known as β^- decay shown in Equation 2.2.

$$^{27}_{60}Co \rightarrow {}^{28}_{60}Ni^* + e^- + \overline{\nu_e}$$ **Equation 2.2**

Where $*$ denotes that a decay product is left in an excited state.

A second type of beta-decay is positron emission wherein a positron (e^+) and neutrino are emitted when a proton in the nucleus of an atom is converted into a neutron. This is known as β^+ decay shown in Equation 2.3. Positron decay results in the transmutation of the atom into another chemical element where the atomic number is one less and the ejection of an orbital electron to maintain the charge balance of the atom. As such positron decay occurs when the parent nuclei has mass greater than the daughter nuclei by the mass of two electrons (1.822 x 10^{-30} kg).

$$^{90}_{39}Y \rightarrow {}^{90}_{38}Zr + e^+ + \nu_e$$ **Equation 2.3**

- Gamma decay – when a nucleus undergoes a previous radioactive decay type, the daughter nuclei may be left in an excited state. The nuclei can decay into a more stable, lower energy state through the emission of high energy gamma rays as shown in Equation 2.4. Gamma decay can also occur following other nuclear reactions such as neutron capture.

$$^{28}_{60}Ni^* \rightarrow {}^{28}_{60}Ni + \gamma$$ **Equation 2.4**

The stability of atoms related the number of protons and neutrons is illustrated in Figure 2.1. Heavier nuclei are more prone to undergo alpha decay, whereas lighter nuclei are more like to undergo beta decay.

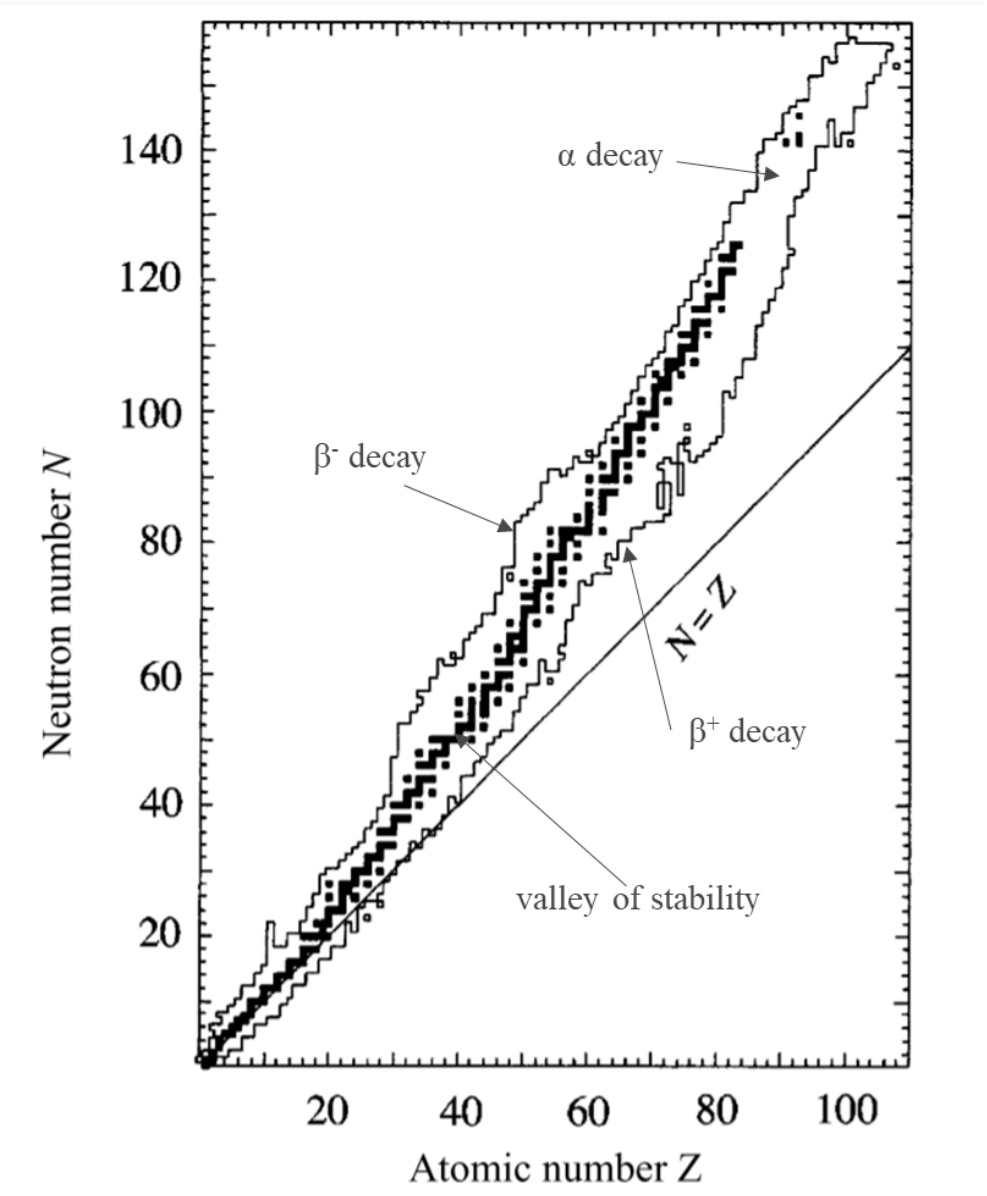

Figure 2.1: The distribution of stable nuclei. Squares represent stable nuclei. Unstable nuclei are found within the jagged lines. Decay modes for unstable nuclei are indicated. Taken from *Martin (2019)* [3].

2.2.2 Nuclear Fission

Nuclear fission is the process by which unstable heavy elements are split into two constituent, lighter elements (fission products). Whilst this can occur spontaneously, the timescale for this to happen is too long to be of practical use. Instead, heavy fissile elements such as uranium-235 are bombarded with neutrons to artificially initiate nuclear fission in a reactor. Neutrons absorbed by uranium-235 form unstable uranium-236. Uranium-236 will undergo nuclear fission, splitting into two daughter nuclei and emitting two or three neutrons. The mass defect, the difference in mass of the fission

products and the parent nuclei, is converted into energy according to Einstein's mass-energy equivalence, $E = mc^2$ [2]. Equation 2.5 illustrates this process:

$$^{92}_{235}U + n \rightarrow {}^{92}_{236}U^{*} \rightarrow {}^{36}_{92}Kr + {}^{56}_{141}Ba + 3n + 200\ MeV \qquad \textbf{Equation 2.5}$$

The neutrons released in the reaction can then cause a chain reaction, initiating nuclear fission in additional fissile uranium-235 nuclei. However, the neutrons emitted from the fission process are too fast to be absorbed by the fissile material. Fast neutrons have smaller thermal de Broglie wavelengths than the radius of uranium-235 and are unlikely to be absorbed (Equation 2.6) [4].

$$\lambda(E) = \frac{h}{\sqrt{2mE}} \qquad \textbf{Equation 2.6}$$

where λ is the thermal de Broglie wavelength, h is Planck's constant, m is the mass of a neutron and E is the kinetic energy of the neutron.

The fast neutrons are moderated or slowed down by a moderator through collisions with light elements, such as hydrogen, losing energy in the process. The slower thermal neutrons can be absorbed by the remaining fissile material. To prevent the chain reaction from exponentially growing, control rods made of a neutron absorbing material such as boron are used to keep the reaction at criticality. Criticality is reached when the effective neutron multiplication factor, $k_{eff} = 1$. If $k_{eff} > 1$ the reaction will grow exponentially and lead to serious safety issues. If this occurs and cannot be rectified through standard reactor operations, the control rods are entirely inserted to end the reaction before it can grow too large. If $k_{eff} >> 1$ the fissile atoms will release all their energy over a short period of less than 0.01 microseconds; this is the general basis for a nuclear bomb. If $k_{eff} < 1$ the reaction cannot be sustained and will terminate quickly [2]. The energy released from this process at criticality forms the basis of nuclear power generation.

2.2.3 Nuclear Fuel Cycle

The nuclear fuel cycle describes the various processes involved in producing electricity from nuclear power (Figure 2.2). Safety informs every step of the nuclear fuel cycle and is the paramount consideration when designing the systems used in the nuclear industry. This approach informs the development of new technologies and practices across the industry, leading to improved reactor and fuel designs that are not only safer but more efficient.

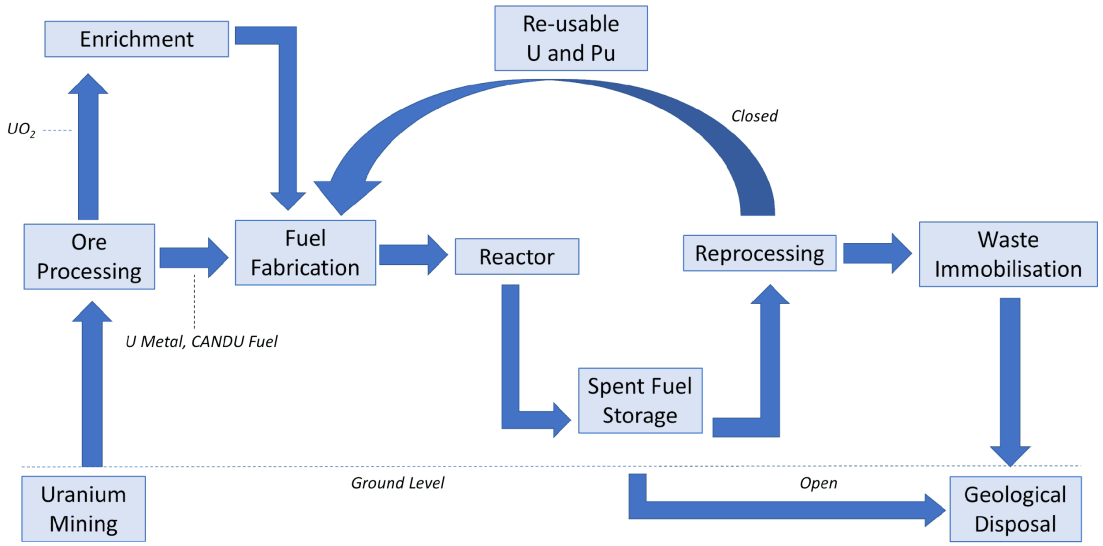

Figure 2.2: The nuclear fuel cycle [2].

The initial step is the mining and milling of uranium-238 and uranium-235, the latter of which is found only in trace amounts (0.7%). The extracted U_3O_8 concentrate, or 'yellowcake', from the milling process is converted into UO_2. The refined UO_2 is a suitable fuel for some rectors, such as the CANDU series, that do not require enriched fuel due to the use of heavy water as a moderator allowing for a better neutron economy [2]. Due to the low levels of uranium-235, which is the fissile isotope of uranium, enrichment is often needed, typically to around 3-5% uranium-235 via such methods as diffusion or centrifuge techniques. For reactors that require enriched uranium, the majority of which do, the UO_2 is converted into uranium hexafluoride, UF_6. Enrichment processes utilise the differences in physical properties of the two uranium isotopes, specifically the 1% mass difference. UF_6, which is gaseous at temperatures above 56 °C, is fed into a centrifuge where rapidly spinning rotors separate the uranium-238 from uranium-235 until the desired enrichment level is achieved. The resulting enriched UF_6 is converted back into UO_2 and sintered into dense ceramic fuel pellets. The ceramic fuel pellets are packed into rods and encased in some form of metallic cladding (e.g. zirconium alloy) to protect the fuel from its environment and contain the radionuclides inside [5]. The design and production of nuclear fuel pellets and the fuel rods are carefully controlled to ensure safety, consistency, and compatibility with a particular reactor type. Bundles of fuel rods are inserted into a reactor core surrounded by an appropriate moderator. The choice of moderator heavily depends upon the design of the reactor and the type of fuel. Common moderators include water (which has been purified but is otherwise typical water) and is used as both coolant and moderator in pressurised water reactors (PWR) and boiling water reactors (BWR), heavy water containing heavier deuterium atoms (D_2O) and graphite. Deuterium and carbon have smaller thermal neutron absorption cross-sections than hydrogen, which prevents desirable neutrons from being absorbed rather than being thermalised. However, due to the mass difference of deuterium and carbon compared to hydrogen (twice and twelve times, respectively), the energy transfer of colliding neutrons is less efficient. A

coolant, typically water or CO_2, transfers heat from the fuel in the core to create steam to operate a turbine to generate electricity [6].

Spent nuclear fuel (SNF) is fuel from a reactor that is no longer useful for maintaining nuclear reactions due to the build-up of reactor poisons. Reactor poisons are fission products or species with large thermal neutron absorption cross-sections, such as samarium-149. The spent fuel from a reactor will contain many highly radioactive elements, which produce significant amounts of heat associated with the radioactive decay of short-lived fission products. On removal from the reactor, it is stored in a cooling pond.

The nuclear fuel cycle can either be a closed or open one. In a closed cycle, the fuel, after it has been removed from the reactor, is stored until it can be permanently disposed of. Some countries opt to store spent fuel for 10 – 20 years in a cooling pond prior to being moved to dry-cask storage to await permanent disposal. In a closed cycle, after a required amount of time in a cooling pond, SNF is then reprocessed, separating the re-usable uranium and plutonium for future use. This has seen the UK coming into possession of largest stockpile of civil plutonium in the world, reported to be approximately 112 tHM (tonnes of heavy metal) in addition to 99,000 tHM of uranium stock and 6,100 tHM of spent fuel (in reactors and storage) [7].

Large amounts of radioactive waste are generated throughout in both open and closed cycles, requiring tailored disposal solutions. The Nuclear Decommissioning Authority (NDA), the public body responsible for the disposal of the UK's legacy waste, is now looking at the immobilisation of actinide rich nuclear wastes in a ceramic systems prior to disposal in a dedicated Geological Disposal Facility (GDF) [8]. Glass matrices and cement have already seen use for the immobilisation and encapsulation of HLW and ILW, respectively. A GDF is an engineered, multi-barrier approach to nuclear waste disposal. Waste will be buried deep underground, which allow the overlaying rock to provide an extra barrier to prevent radionuclides from being released into the biosphere, with the wasteform (glass, ceramic or SNF) providing the initial barrier [9].

2.2.4 Fission products

Fission products, the fragments left behind after a nucleus has undergone nuclear fission, are a source of significant radioactivity in irradiated fuel. Unstable fission products can decay into a vast array of elements, covering elements from copper to gadolinium; however, the most common fission products of uranium-235 have mass numbers around 95 and 135 (Figure 2.3). Whilst some fission products will reach stability rapidly; others will have longer half-lives and pose a significant health risk. Radioactive strontium-90 and caesium-137, which have half-lives of 28.8 years and 30 years, respectively, are also biologically active in addition to being highly radioactive. Fission products account for around 3% of the waste in spent nuclear fuel but account for the majority of overall radioactivity and heat generated. The amount of radiation and heat generated by fission products relatively quickly reduces as shorter-

lived isotopes decay, leaving behind longer lived isotopes. Whilst the majority of fission products will need to be disposed of, valuable isotopes for nuclear medicine can be separated for future applications in both the diagnosis and treatment of medical conditions [10].

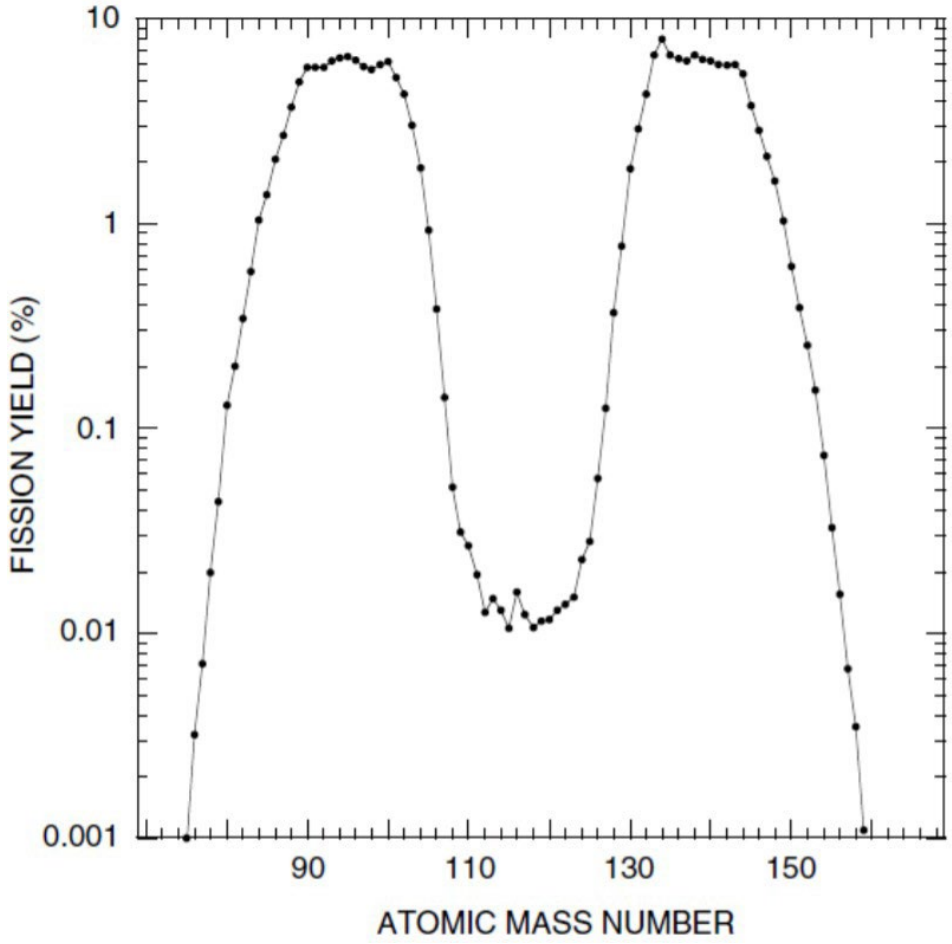

Figure 2.3: Thermal fission yield of ^{235}U as a function of A. Taken from *Bodansky (2004)* [11].

2.2.5 Transmutation and transuranic isotopes

Whilst the none fissile nuclei do not directly contribute to the energy production of a nuclear reactor, they can absorb neutrons to form unstable isotopes, which may be fissionable, through a process of transmutation. These unstable isotopes, through a series of decay events, will form isotopes of the minor actinides (actinides beyond plutonium). For example, uranium-238, after absorbing a neutron to form uranium-239, will beta decay into neptunium-239 and can eventually form americium-244 through a series of decay events and absorption of thermal neutrons. The production of radioactive minor actinides, whilst only a small proportion of the waste generated from fuel burn up, still

contributes to radioactive inventory that needs to be disposed of and which impacts disposal strategies.

2.3 Wasteforms for Actinide Wastes

Glass and ceramic wasteforms are considered as the credible options for immobilisation and disposal of the UK plutonium stockpile, minor actinides and fission products arising from nuclear fission [12]–[16]. Cement wasteforms are not considered a credible option for these materials because the waste incorporation rate would be prohibitively low, so as to prevent problematic heat generation and radiolysis effects [12]. Glass wasteforms have the advantage, compared to ceramics, of already being accepted for radioactive waste immobilisation and there exists considerable experience of high-level waste glass vitrification in the UK. However, ceramic materials have the major advantage that they can be designed to be thermodynamically stable in disposal environments, whereas glasses are thermodynamically metastable by definition.Although the thermodynamic stability of some natural glasses, such as obsidian, are known out to 10^8 years. The selection of a material to act as a host for radioactive waste immobilisation is made on the assessment of several, often competing factors, including, but not limited to:

- High waste loading, so as to reduce the volume of waste required to be stored and then disposed within a waste repository
- A simple processing method, maximising the economics of production; ideally batchwise for fissile materials to safeguard against process criticality.
- Chemically flexible so that contaminant or additive species (such as neutron poisons) can be accommodated within the phase assemblage.
- Resistance to both radiation damage and aqueous alteration which control the source term or rate of radionuclide release in the disposal environment.
- Ideally having natural analogues, allowing for assessment on the behaviour of a wasteform over geological timescales. [8]

2.3.1 Borosilicate glass

The immobilisation of HLW via vitrification is a well-established process, being the current practice used in a number of countries, including the UK. Many different glass systems have been, and currently are, the subject of research on vitrification. However, borosilicate glasses are usually seen as the most appropriate choice as they satisfy a broad criteria of desirable properties. Borosilicate glasses can have a high waste loading of HLW of between 25 – 30%, good thermal and mechanical stability, ease of processing, low leachability, and a high resistance to radiation damage. Additionally, borosilicate glass as a vitrification technology has already been demonstrated and the material was already well characterised. However, some waste products, notably plutonium and americium chlorides, have low solubility in borosilicate glasses and as such they are not well-suited material to host these wastes.

Other vitreous systems are currently being researched to address this problem. Ceramic systems can potentially make direct use of contaminated chlorine salts arising from pyro-reprocessing (e.g. PuCl) as part of a molten salt mediated reaction.

2.3.2 Perovskite

Perovskite has a prototypical formula $CaTiO_3$, with space group *Pbnm* (Figure 2.4). The ideal cubic structure (Pm-3m) of ABO_3 perovskite is made up of corner sharing TiO_6 octahedra, this framework effectively encapsulates the A site cation in a regular AO_{12} dodecahedron. In $CaTiO_3$, due to the small size of Ca ions, the TiO_6 octahedra are distorted, causing them to become tilted. This tilting alters the coordination environment of Ca, lowering the coordination number from 12 to 8 [17], giving rise to an orthorhombic structure. Such octahedral tilting arises as a result of bond length mismatch when the ratio r_A / r_B < 1 (where r_A is the ionic radius of cation A, and r_B is the ionic radius of cation B); consequently, as a result of thermal expansion, perovskites commonly exhibit a sequence of reversible phase transitions, for example $CaTiO_3$ will undergo a reversible phase transformation to I4/mcm at 1512 K [18].

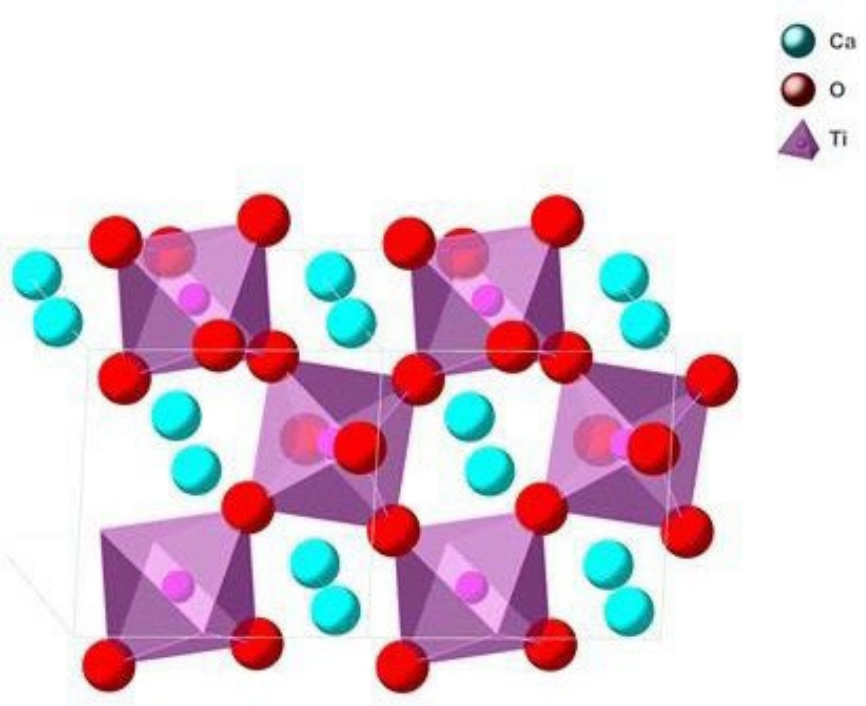

Figure 2.4: Schematic crystal structure $CaTiO_3$ *Pbnm* (based on the structure refined by *Liu 1993 [19])*

Actinides and lanthanides may be incorporated on the Ca site by having elements such as Fe^{3+} or Al^{3+} substituted for Ti, to provide a charge compensation mechanism. U^{4+} and Pu^{4+} can be partly incorporated on the Ca site up to the limit of at least 0.1 formula units (f.u.) [20]. The response to radiation damage for perovskites has been extensively researched. They have been determined to have a possibly more resistant response to radiation than other ceramic phases such as zirconolite and pyrochlore by a factor of 2 or more [21], although there is difficulty in comparing natural samples due to significant variations in structure, thermal history and chemical composition. In situ ion beam irradiation and transmission electron microscopy electron diffraction (TEM/ED) experiments (800 keV Kr^{+} radiation) have determined that $CaTiO_3$ will amorphise above 0.75 dpa (displacements per atom), compared to $SrTiO_3$ at 0.93 dpa, $LiTaO_3$ at 0.42 dpa, and $LiNbO_3$ at 0.32 dpa [22]. Natural analogues of perovskite have been found in various parts of the world. It has been found that samples of perovskite dating from 1.33 to 5.00 x 10^8 years ago, which had received a dose of 0.3 x 10^{16} α-decays mg^{-1} had shown little evidence of radiation damage and remained crystalline [23], though the data set was limited. Natural perovskites, that had received an equivalent dosage that the proposed SYNROC wasteform would receive after 0.5 x 10^6 years of storage, had remained crystalline [23]. Further, in the same study, it was found that comparative samples of zirconolite were less resistant to the effects of radiation damage. That said, significant damage was exhibited by naturally occurring perovskite containing 6 wt. % of ThO_2 after receiving 1 x 10^{17} α-decays mg^{-1}, equivalent to 0.93 dpa [24]. A review of literature data from natural occurring perovskite samples found that critical doses reported for natural perovskite were significantly less constrained than those of other natural analogues (e.g., zirconolite), where the reported critical dose for natural perovskite being within the range of 0.3 – 2.6 x 10^{16} α-decays mg^{-1} [21].

2.3.3 Brannerite

Brannerite has the prototypical formula ATi_2O_6 and crystallises in the space group *C2/m* (Figure 2.5), with A = Ce, U, Th; brannerite is the specific mineral species with A = U dominant. The species with A = Th dominant is known as thorutite. [25], [26]. Natural brannerites show considerable substitution of Fe, Zr on the Ti-site, and Ca, Ln on the U/Th site [17]. The brannerite crystal structure consists of layers formed by corner and edge sharing TiO_6 octahedra, which are linked by A-site cations also in octahedral co-ordination.

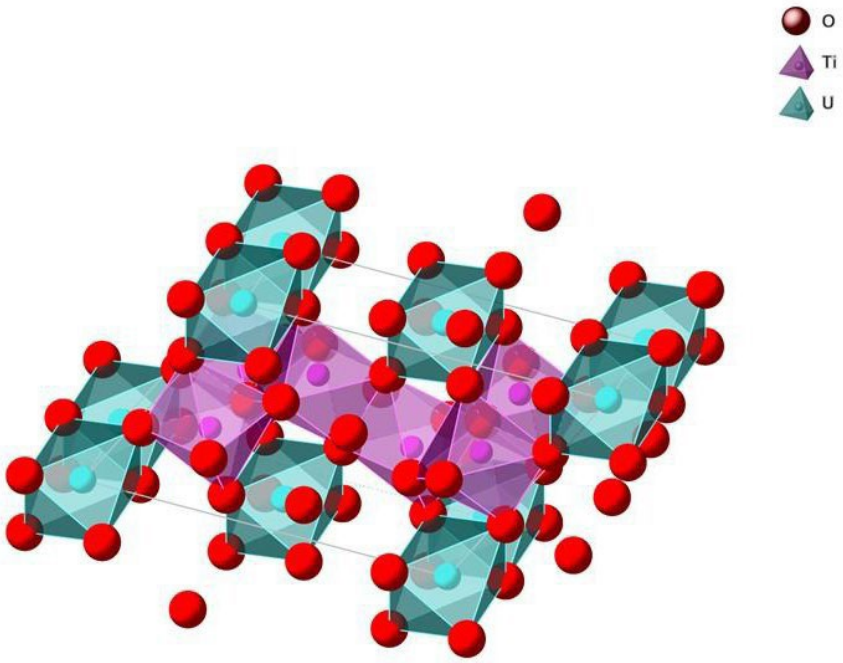

Figure 2.5: Schematic crystal structure of UTi_2O_6 brannerite *C2/m* (structure based on refinement by *Szymanski (1982)* [26])

The solid-state synthesis of $PuTi_2O_6$ with the brannerite structure in air at 1400 °C was reported by *Vance et al* [18]. Brannerites with a significant U^{5+} content were reported by substitution of e.g. Ca, Ln or Fe on the A site of UTi_2O_6 [27], [28]. Natural brannerites, of sufficient age (>10^6 years), are generally metamict, *Lumpkin et al* estimate a critical dose for amorphisation of 0.7 – 0.9 dpa based on data from specimens of a Swiss locality dated to 11 x 10^6 years age [29]. In situ and ex situ ion beam irradiation experiments have determined a critical dose of similar magnitude for synthetic $CeTi_2O_6$ and UTi_2O_6, in the range 0.09 – 0.15 dpa [30].

2.3.4 Zirconolite

Zirconolite has the prototypical formula $CaZrTi_2O_7$, space group C2/m (Figure 2.6). This material is currently the leading candidate for immobilisation of the UK plutonium stockpile [31]. The crystal structure is related to that of pyrochlore, but with Ca and Zr in 8- and 7-fold co-ordination by oxygen, respectively, and three Ti sites, two of which are 6-fold co-ordinated and one of which is 5-fold co-ordinated by oxygen (the latter is 50% occupied) [32]. The TiO_6 and TiO_5 polyhedra share corners to form layers, separated by the CaO_8 and ZrO_7 polyhedra. Actinide elements, An^{3+} or An^{4+} are targeted

for substitution on the Ca^{2+} and/or Zr^{4+} sites, with charge compensation provided, if required, by substitution of e.g. Al^{3+} or Fe^{3+} on the Ti^{4+} site [33].

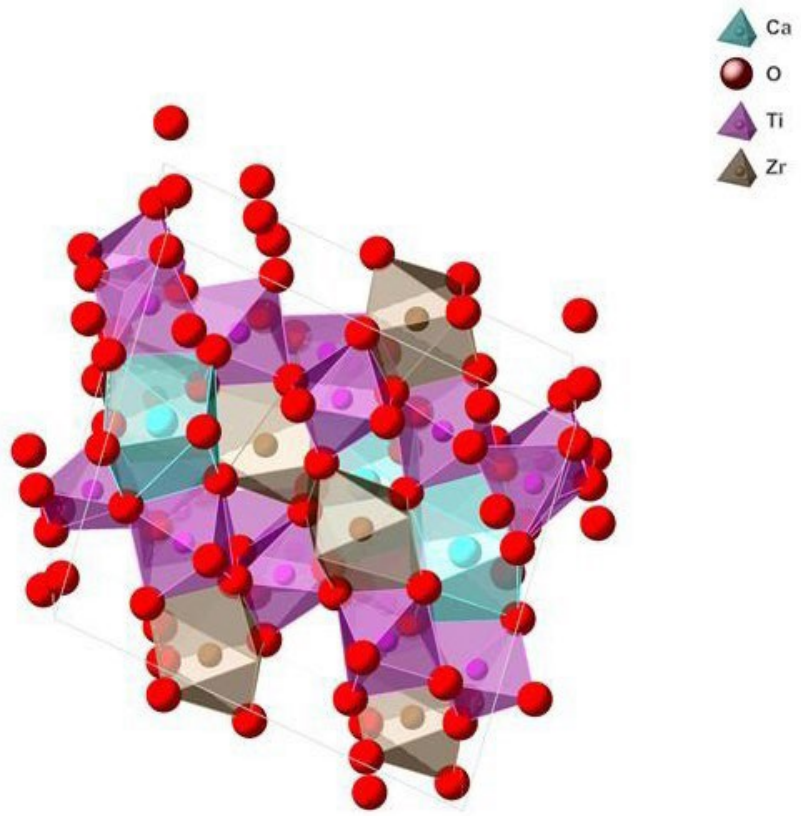

Figure 2.6: Schematic crystal structure of $CaZrTi_2O_7$, zirconlite-2m *C2/m* structure (based on the structure refined by *Whittle et al. (2012)* [34])

Although many studies have examined the incorporation of actinides and their surrogates within the zirconolite structure, with and without charge compensation, a systematic understanding is yet to be developed, due to the complexity of the crystal structure. The zirconolite structure is retained with substitution of up to 0.4 f.u. of U on the Zr site and up to at least 0.4 f.u. of Np or Pu on the Ca site [30], [35]–[38]. The relative ionic size and co-ordination preference of the Ca, Zr and actinide (Act) ions, determine the effective stacking sequence of the layers formed by TiO_n polyhedra. This gives rise

to polytype structures, designated nS, where n- is the periodicity of the stacking sequence and S the arising space group symmetry. The prototype structure adopts the 2M polytype, which is retained for low Act substitution, but gives way to the 4M polytype at higher doping (M, monoclinic). 3O (orthorhombic) and 3T (tetragonal) polytypes are also known; it is hypothesised that these polytypes may show different radiation damage tolerance and dissolution rates [30], [35]–[38]. As reviewed by *Lumpkin et al*., natural zirconolites have been dated to 10^6-10^9 years, with U and Th bearing compositions being fully amorphous (metamict) as a result of self-radiation damage [30], [39]. However, the U and Th inventory is reported to be immobile in geochemically altered examples [30], [39]. Natural zirconolites are reported to amorphise at a damage level of 2 dpa, whereas accelerated damage from ion beam, neutron irradiation and ^{244}Cm or ^{238}Pu doping, leads to amorphisation in the range 0.2 – 1.0 dpa [30]. This difference is believed to be associated with dose rate effects; with slow defect recombination processes assisting the recovery of damage in mineral analogues. The comparison of relative radiation resistance of zirconolite and perovskite has been frequently visited by literature. The reported critical dose for natural perovskite were within the range of 0.3 – 2.6 x 10^{16} α-decays mg^{-1}. Whilst perovskite is often noted to be more radiation damage resistant than zirconolite this prevents certainty on this conclusion.

As such, irradiation of synthetic zirconolites samples reported that the damage cross-section of zirconolites exposed to 3 MeV Ar^+ ions was 0.014 nm^2, compared to perovskite samples irradiated under the same condition where the damage cross-section (where the damage cross-section is the sum of the cross-section by elastic scattering of irradiating particles and the cross-section by nonelastic interactions of particles with nuclei) was 0.32 nm^2, implying that perovskite should more readily amorphise under irradiation conditions [41], [42]. 1 MeV Kr^+ irradiations of Gd-doped perovskite ($Ca_{0.8}Gd_{0.2}TiO_3$) and zirconolite ($Ca_{0.75}Gd_{0.5}Zr_{0.75}Ti_2O_7$) samples measured at 20 K to limit effects of thermal recovery, on the other hand, indicated that the zirconolite will become amorphous at a rate 3 times faster [43]. In another comparative study of zirconolite and perovskite, Pu-doped zirconolite and perovskite samples after a dose of 8 x 10^{15} α-decays mg^{-1} found that the dose dependent macroscopic swelling of perovskite continued to increase however for zirconolite it had reached saturation. This result was supposed to demonstrate the superior radiation resistance of perovskite however, macroscopic swelling used as metric for determining whether a compound has been rendered amorphous has been shown to be flawed as $CmAlO_3$ (perovskite) was shown to continue swelling after it had already amorphised. Moreover, techniques that probe the long-range atomic structure of compounds, such as X-ray diffraction (XRD) have shown that perovskite of the formulation $CmAlO_3$ became amorphous after a dose of 0.3 x 10^{16} α-decays mg^{-1}, equivalently zirconolite doped with ^{238}Pu became X-ray amorphous at the same dose [21]. This further demonstrates that macroscopic swelling is not an ideal metric to measure radiation tolerance. These results indicate the difficulty in measuring radiation damage response, particularly that of natural minerals, due to variations in thermal history, geological conditions, structures, and chemical compositions.

2.3.5 Pyrochlore

Lanthanide pyrochlores have the general chemical formula $A_2B_2O_7$, for B = Ti and A = Ln = Sm… Lu adopt the space group *Fd-3m* (a schematic of crystal structure can be found in Figure 2.7d). The $Ln_2Ti_2O_7$ compounds with larger lanthanides, Ln = La… Nd, crystallise in a layered perovskite structure, space group $P2_1$. The stability of the pyrochlore structure can be considered in terms of the ratio of A and B cation radii r_a/r_b. The *Fd-3m* pyrochlores have a fluorite *Fm-3m* derived superstructure with one eighth of the anions removed in an ordered fashion. The A site cation is in a disordered 8-fold co-ordinate scalenohedron (with 6 + 2 unique Ln-O bond lengths). B-site cations are in a 6-fold coordination, within distorted octahedral sites (trigonal antiprisms, with 6 equal B-O bond lengths) [44]. If the cation ionic radii ratio is $r_a/r_b = 1.78$, then the $P2_1$ monoclinic structure is formed [45]. This structure consists of double layers of corner sharing TiO_6, which are separated by Ln cations in four distinct sites comprising 2 x 12, 1 x 10, and 1 x 9 co-ordinate sites [46], [47].

Pyrochlores have received considerable interest as a host for the immobilisation of actinides. It is reported that titanate pyrochlores can accommodate a waste loading of up to 35 wt.% of plutonium or other actinides on the A site [48]. The effect of radiation damage has been examined for all $Ln_2Ti_2O_7$ pyrochlores, using in situ ion beam irradiation coupled with TEM/ED observation, the most comprehensive data (discussed in the following) are for 1 MeV Kr^+ irradiation [49]. At room temperature, $Ln_2Ti_2O_7$ pyrochlores are amorphised after a dose of 0.2 – 0.5 dpa. As the ratio r_A/r_B increases from Lu (1.61) to Gd (1.74), the critical temperature for amorphisation, T_c, where crystalline recovery due to thermal annealing effects is greater than the rate of amorphisation, is reported to increase from 480 K to 1120K. For Sm, $r_A / r_B = 1.80$, T_c is reported to decrease slightly to 1045 K, however, the small number of data points reported for the associated dose curve means that there is likely considerable uncertainty in this value [50]. It has been found that by the substitution of Ti by Zr, the radiation tolerance of a pyrochlore can be increased. In the system $Gd_2Ti_{2-x}Zr_xO_7$, T_c shows an approximately linear dependence as values of x increase, within the range $0.2 < x < 0.8$ ($1.50 < r_A / r_B < 1.68$); and for x = 1.8 the ceramic could not be amorphised at a dose of 5 dpa (1 MeV Kr^+ at 25 K) [50], [51].

This shows that both A- and B- site doping can be used to tune the radiation tolerance of the perovskite structure. The r_A / r_B ratio of the pyrochlore structure has been used as a prediction of radiation tolerance: below a critical ratio of $r_A / r_B = 1.46$ A, compounds of the $Ln_2Ti_2O_7$ stoichiometry adopt a defect fluorite structure, in which the A site, B site, and oxygen vacancy sites are disordered. The defect fluorite structure thus has an inherently higher capacity for accommodating anti-defects, compared to the ordered pyrochlore structure, and thus a lower defect energy for formation of anti-site defects. This enables the structure to recover from atomic displacements induced by radiation damage, conferring a degree of radiation tolerance. Thus, for $Ln_2Ti_2O_7$ pyrochlores, the T_c decreases as r_A / r_B tends to 1.46; for the $Gd_2Ti_{1.2}Zr_{0.8}O_7$ composition, with $r_A / r_B = 1.50$, at the edge of the defect

fluorite stability field, the compound does not undergo a crystalline to amorphous phase transition [49].

As an additional means for separately evaluating radiation damage, naturally occurring pyrochlores can be used as an analogue. They are commonly found in evolved rock types and contain up to 30 and 9 wt. % of UO_2 and ThO_2, respectively [30]. Geological samples of U and Th bearing pyrochlores, dating from 1.6 x 10^7 to 1.4 x 10^9 years, have shown to have become completely metamict, i.e. amorphous, after 1.2 to 10 dpa [52]. Comparisons of pyrochlore doped with short lived ^{238}Pu and ^{244}Cm and geological samples showed that the critical dose of amorphisation was between 2 – 4 times greater in natural samples, likely due to the relatively high temperatures (100 – 200 ^oC) host rocks containing these geological samples are found at, allowing some amount of crystalline recovery [30]. In a broad comparative study of the ion irradiation response of pyrochlore, perovskite and zirconolite samples (undoped, Nd-doped, U-doped and Th-doped) irradiated under 1.5 MeV Kr^+ ions at a flux of 3.4 x 10^{14} ions m^{-2} s^{-1} studied by *in-situ* TEM/ED. The fluence was increased in steps of 1.7,0.85 or 4.3 x 10^{18} ions m^{-2} until diffuse rings were observed in the electron diffraction patters (indicating an amorphous structure). The critical dose of amorphisation at room temperature of the synthetic uranium-doped pyrochlore was 4.1 x 10^{18} ions m^{-2}, this was found to fall within the range of the zirconolite samples, between 3.5 – 6.1 x 10^{18} ions m^{-2}, depending on the polytype and chemical composition of the zirconolite sample (thorium-doped zirconolite of the 3T polytype having the highest critical dose and neodymium-doped zirconolite of the 4M polytype the lowest). Perovskite was found to have a value 3 – 5 times greater than the zirconolite at 18 x 10^{18} ions m^{-2} [21].

2.3.6 Ln_2TiO_5 ''stuffed pyrochlores'' for actinide immobilisation

This project is concerned with the synthesis and properties of Ln_2TiO_5 compounds, colloquially known as "stuffed pyrochlores", which have recently received interest as ceramic wasteforms for actinide immobilisation [53]–[64]. These compounds can be considered as end members of a solid solution $Ln_{2+x}Ti_{2-x}O_{7-x/2}$ with x = 0.67, i.e. $Ln_2(Ti_{1.33}Ln_{0.67})O_{6.67}$. Effectively this stoichiometry is achieved by "stuffing" extra lanthanides onto the B site of the $A_2B_2O_7$ pyrochlore [65], with charge compensation through formation of ordered oxygen vacancies. The primary motivation for this application is the structural similarity with $Ln_2Ti_2O_7$ pyrochlore compounds, which have been proposed for this purpose, targeting $Act^{3+/4+}$ substitution on the Ln site, with appropriate charge compensation. The crystal structures and radiation damage behaviour of Ln_2TiO_5 compounds has been the focus of renewed study over the last decade, as reviewed in the next section.

In addition to application as actinide ceramic wasteforms, of interest to this work, the physical, magnetic and electronic properties of Ln_2TiO_5 compounds have also received attention for other nuclear applications. Dy_2TiO_5 was investigated for potential application as a control rod material in light water reactors, due to its high melting point (~1870°C), compatibility with cladding materials, and low swelling under neutron radiation damage, in addition to its high neutron absorption cross

section [66]. Dy_2TiO_5 control rods are reported to have been successfully operated in several Soviet designed reactors, including 17 years in MIR (a Be moderated, water cooled test reactor), 4 years in a VVER-1000 (pressurised water reactor), and 2 years in an RBMK 1000 (water cooled, graphite moderated reactor) [66]. Gd_2TiO_5 has been proposed as a burnable neutron poison in UO_2 fuels, to smooth reactivity loss due to depletion of fissile material over burnup [67]. The Korea Atomic Energy Research Institute has successfully proven Gd_2TiO_5 for this application in a heterogeneous configuration (i.e. as separate pellets within a fuel rod), in the HANRO test reactor [67]. Beyond nuclear applications, Sm_2TiO_5 has been utilised in thin film bio-sensors for urea detection and dielectric applications [68], [69], whereas Gd_2TiO_5 has been investigated as a potential cathode material for Li and Na battery applications [70]. Ln_2TiO_5 phases have also been the focus of investigation with respect to ordering Ln^{3+} magnetic moments as model systems for complex magnetically frustrated lattices [71]–[73].

2.3.7 Crystal structures of Ln_2TiO_5 compounds at room temperature and pressure

In 1966, *Guillen and Bertaut* reported La_2TiO_5 as the first member of the Ln_2TiO_5 family of compounds, with an orthorhombic crystal structure *Pnma* [74]. To date, Ln_2TiO_5 crystal structures have been reported for all lanthanides, except Ln = Ce; the synthesis of Ce_2TiO_5 is expected to be challenging since stabilisation of Ce^{3+} would require strongly reducing conditions. Ln_2TiO_5 phases adopt one of three crystal structures, Figure 2.7, as shown in the pseudo-phase diagram reproduced in Figure 2.8, according to Shepelev and Petrova [56].

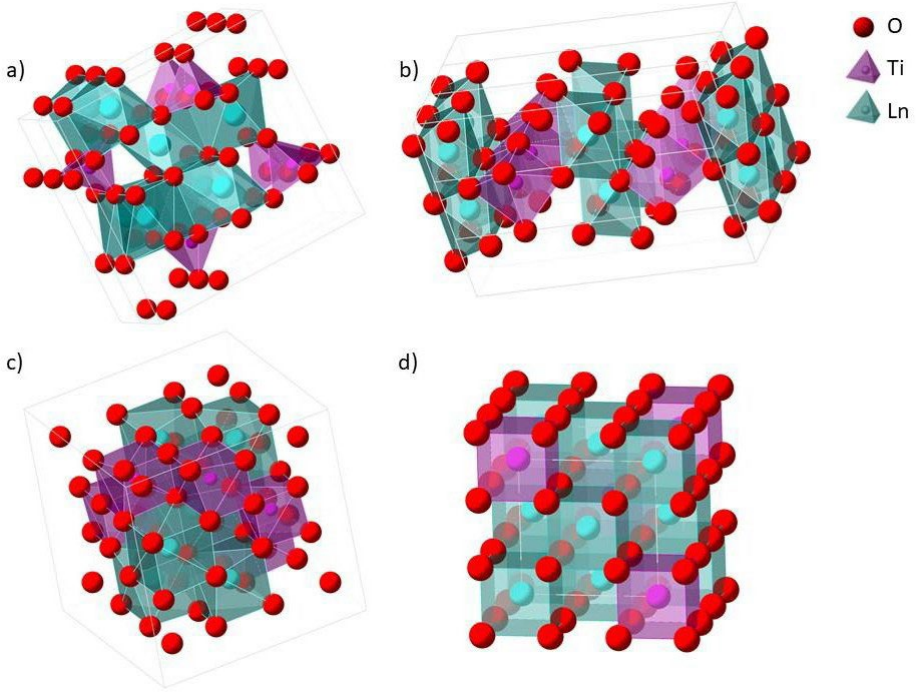

Figure 2.7: Schematic crystal structures of Ln_2TiO_5 and $Ln_2Ti_2O_7$ pyrochlore phases; a) Ln_2TiO_5 orthorhombic, *Pnma* (based on the structure of La_2TiO_5 refined by Aughterson *et al.* [75]); b) Ln_2TiO_5 hexagonal, *$P6_3/mmc$* (based on the structure of Dy_2TiO_5 refined by Aughterson *et al.*,[64]); c); d) $Ln_2Ti_2O_7$ cubic, *Fd-3m* (based on the structure refined by [76]), Ln_2TiO_5 cubic, *Fm-3m* (based on the structure of Yb_2TiO_5 refined by Aughterson *et al.* [59], A- and B-site cations are randomly distributed).

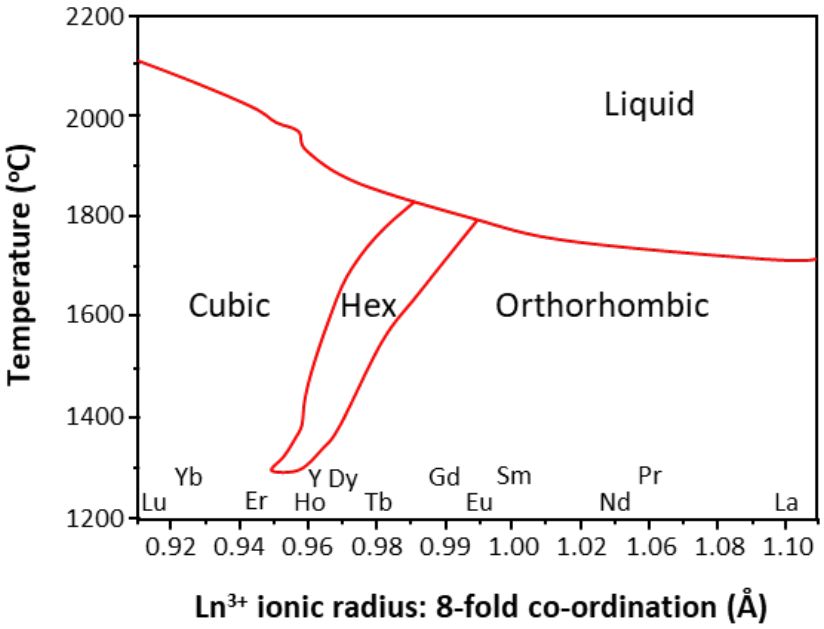

Figure 2.8: Pseudo phase diagram of Ln_2TiO_5 phases, reproduction based on work by *Shepelev and Petrova* [56].

2.3.7.1 Orthorhombic structure: Pnma

The larger lanthanides Ln = La – Dy adopt an orthorhombic Ln_2TiO_5 structure at room temperature, Figure 2.8, in space group *Pnma*, a = 11.0 Å, b = 3.9 Å, c = 11.4 Å. This assignment was made by *Aughterson et al.,* based on systematic Rietveld analysis of synchrotron XRD data [75]. These conclusions are generally consistent with previous and more recent reports, which applied laboratory XRD or electron diffraction. The orthorhombic Ln_2TiO_5 crystal structure is best described as a framework formed by intersecting columns of edge sharing LnO_7 polyhedra, with the Ti cations occupying interstices within the tunnels forming TiO_5 square pyramids, Figure 2.7a.

2.3.7.2 Hexagonal structure: $P6_3/mmc$

The Ln_2TiO_5 phases of the intermediate size lanthanides, Ln = Gd, Tb and Dy were reported to transform to a high temperature hexagonal phase, *$P6_3/mmc$* a = 3.6 Å and c = 11.8 Å, by *Shepelev and Petrova*, as shown in Figure 2.8. Such a phase transition was also induced by "chemical pressure" in the $Sm_{2-x}Yb_xTiO_5$ solid solution, with the hexagonal phase stabilised for x = 0.6, 1.0 [59]. Rietveld analysis of synchrotron XRD data have provided the most accurate determination of the hexagonal structure for $Sm_{1.4}Yb_{0.6}TiO_5$ and $SmYbTiO_5$ compositions [59]. This structure, Figure 7b, may be considered as layers of edge sharing LnO_6 or mixed $(Ln,TiO)_6$ octahedra, separated by TiO_5 trigonal bi-

pyramids. The layers of LnO_6 and mixed $(Ln,TiO)_6$ octahedra alternate along the c-axis; the mixed site contains ca. 20% cation vacancies. The TiO_5 polyhedra have a 30% Yb occupancy $(Ti,Yb)O_5$. As Yb cations have a smaller ionic radius than Sm, closer to that of Ti, they are able to partially occupy Ti sites. Additional supercell reflections were apparent in electron diffraction data of $Sm_{2-x}Yb_xTiO_5$ compositions with x = 0.6 and 1.0, which were interpreted as a commensurate modulation relating to cation / vacancy ordering; a detailed model of the ordering pattern could not be ascertained due to the complexity of the supercell and diffuse scattering [59]. It has also been recently shown that polycrystalline, hexagonal Dy_2TiO_5 can be produced through typical solid state synthesis routes through the rapid cooling of the ceramic compound. TEM/ED analysis of hexagonal Dy_2TiO_5 appeared to exhibit different reflection intensities and diffuse scattering features than the $SmYbTiO_5$ compound previously studied [64].

2.3.7.3 Defect fluorite structure: Fm-3m

The Ln_2TiO_5 phases of the small lanthanides, Ln = Ho… Lu, Y (Figure 2.8) are reported to crystallise in an average defect fluorite-like structure, Fm-3m a = 5.1 Å, as indicated in Figure 2.7c (note 16.5% of the oxygen sites shown will be vacant) [59], [65], [72], [73]. In the parent pyrochlore structure, the Ln and Ti cations are 8- and 6-fold co-ordinated by oxygen, respectively, as shown in Figure 2.7d. The disorder of cation and anion vacancy sites in a defect fluorite structure, derived from a parent pyrochlore structure, would yield, 7-fold co-ordinate cation sites; the average co-ordination number would be slightly lower in Ln_2TiO_5 defect fluorites on average due to the additional oxygen vacancies. Some defect fluorite Ln_2TiO_5 phases, such as Ho_2TiO_5, show very complex commensurate structural modulations in electron diffraction data, which are not fully understood [73]. $Sm_{0.6}Yb_{1.4}TiO_5$, was shown to adopt an average defect fluorite structure but with weak supercell reflections that could be indexed on a pyrochlore supercell [59]. Neutron, synchrotron X-ray and electron diffractions studies of Yb_2TiO_5 have variously reported evidence for and absence of diffuse or weak reflections implicit of an additional structural modulation [54], [59], [72]. Taken together, these data demonstrate that defect fluorite Ln_2TiO_5 compounds may exhibit complex structural modulations, presumably associated with cation and / or vacancy ordering. It has also been argued that some defect fluorite Ln_2TiO_5 compounds are in fact comprised of highly strained nanodomains (ca. 50 Å) of a local pyrochlore structure, which collectively average to give a defect fluorite structure [73]. The orthorhombic *Pnma* structure has been shown to also satisfactorily model the short-range order of Yb_2TiO_5 when studied using neutron pair distribution function (PDF) analysis, where it was found that the R_{wp} of the fit was 0.111, where R_{wp} is the weighted profile R-factor, a statistical measure of the goodness-of-fit. Compared to a model using the cubic pyrochlore structure, which had a R_{wp} = 0.306, the orthorhombic modelled managed to accurately models Ti-O and O-O bonds, where Ti had a coordination number of 5. Crystal Field Splitting (CFS) energy analysis of the Ti L_3-edge of compounds $Yb_2(Ti_2\text{-}xYb_x)O_{7-(x/2)}$ (x = 0.00 – 0.67) showed a gradual shift from 6- to 7-fold coordinated geometry [77].

2.3.7.4 Influence of cooling rate on crystal structure

The structural studies of Ln_2TiO_5 compounds reviewed above highlight the potential for subtle structural modulations associated with cation and anion vacancy order / disorder, particularly in the cubic defect fluorite structure [54], [59], [72], [73]. Consequently, the structure adopted, and presence or absence of structural modulations, may be expected to depend on both precise composition and thermal history of the material. A complete systematic study of the relationship between Ln_2TiO_5 structure and thermal history has not been undertaken, although *Shiyakhtina et al* have undertaken a preliminary study of Ln_2TiO_5 structures as a function of cooling rate for Ln = Dy… Lu [78]. This work used laboratory XRD characterisation, which is not always sufficiently sensitive to probe diffuse scattering and additional supercell reflections. However, the presence of weak additional pyrochlore supercell reflections were identified in Ln = Er – Lu compositions, when cooled from 1650 ^oC at 5 ^oC/min [78]. This was observed to be correlated with reduced oxygen ion conductivity, compared to rapidly cooled defect fluorite phases. However, additional reflections were observed in the XRD patterns of slow cooled samples, which were assigned to an unidentified impurity phase (although it is possible that they could relate to an additional structural modulation). Since compositional variation will also impact cation / oxygen vacancy ordering, it is difficult to be confident that the observed pyrochlore ordering is a consequence of cooling rate only. Further investigation on the effects of cooling rate would be desirable.

2.3.7.5 Pressure induced phase transitions

La_2TiO_5 and Nd_2TiO_5 were shown to undergo a pressure induced phase transition from an orthorhombic to hexagonal structure, at room temperature and 6 and 10 GPa, respectively [53]. However, this phase transition was accompanied by partial decomposition, involving ex-solution of Ln_2O_3, and the high-pressure phase was reported to be isostructural with the high temperature Na_2SO_4 compound (*$P6_3/mmc$*), rather than the high temperature hexagonal phase of Ln_2TiO_5. A subsequent room temperature high pressure diffraction study of Ln_2TiO_5 with Ln = Gd, Dy, Er and Yb, identified a sequence of structural phase transitions [55]. In general, these compounds transform from cubic pyrochlore / defect fluorite, to hexagonal, to orthorhombic structures with increasing pressure [55], however, the high pressure phases are not isostructural with those reported at room pressure (Figure 2.7). The phase transitions are reported to be “sluggish” with co-existence of structures at high pressure [53] [55], some of which may be quenched to room pressure. No high temperature – high pressure studies have yet been undertaken on Ln_2TiO_5 compounds; it is possible that such an approach might yield metastable Ln_2TiO_5 phases in the high temperature hexagonal or room temperature orthorhombic structure, through temperature assisted ionic diffusion.

2.3.7.6 Ln_2TiO_5 stability and Pauling's Rule

The stability of any coordination polyhedra of a given cation-anion pair can be dependent upon the ratio of their ionic radii, r_C/r_A. This rule, often referred to as Pauling's First Rule, can be useful in making initial assessments on what coordinating polyhedra are likely to be stable for a given structure [79]. For example, the r_{Eu}/r_O of Eu and O in an orthorhombic sample of Eu_2TiO_5 (where Eu is found to be in 7-fold coordination with O) is 0.98/1.42 = 0.71. This falls within the geometrically derived stability range for a 7-fold coordination determined by Pauling (see Table 2.1 for a list of stability ranges for polyhedra of differing coordination numbers). However, it should be noted that Pauling's First Rule, which is based upon a hard-sphere model of atoms, does not apply to all atomic local environments. *George et al.* conducted a survey of over 5000 oxide compounds and found that only 66% of tested local environments agreed with Pauling's First Rule [80]. However, Pauling has argued that a polyhedra can be stretched by the incorporation of larger cations and remain stable but the polyhedra with smaller than ideal cations are fundamentally unstable and rarely will violate Pauling's First Rule [79]. This can be observed in Table 2.2 where, for instance, Nd_2TiO_5 has an r_{Nd}/r_O of 0.74 but the stability range for 7-fold coordinated environments is 0.59 – 0.73. This is reasonable as Pauling's First Rule largely considers only ionic bonding of atoms and does not make allowances for any potential covalent bonding or Van der Walls attractions that may occur (such as in the Ti environment of Na_2TiSiO_5) [81].

Table 2.1: Table of stability ranges of radius ratios for different cation-anion coordinating polyhedra. Stability ranges were obtained from Pauling [79].

Radius Ratio (r_C/r_a)	Coordination Number
0.16 - 0.23	3
0.23 - 0.32	4
0.32 - 0.41	5
0.41 - 0.59	6
0.59 - 0.73	7
0.73 - 1.00	8

Table 2.2: The lanthanide and oxygen ionic radii ratios, rLn/rO, for different cation-anion pairs in Ln2TiO5 (Ln = La – Lu, Y) series used in throughout these studies. A – denotes no value, all rLn/rO values are determined by taking the ratio of ionic radii of a lanthanide and oxygen atom in a given coordination combination.

Element	**Coordination Number**	**Ionic Radius (Å)**	**r_{Ln}/r_O**

O^{-2}	4	1.38	-
O^{-2}	5	1.39	-
O^{-2}	6	1.4	-
O^{-2}	7	1.41	-
O^{-2}	8	1.42	-
La^{+3}	7	1.1	0.77
Pr^{+3}	7	1.06	0.75
Nd^{+3}	7	1.05	0.74
Sm^{+3}	7	1.02	0.72
Eu^{+3}	7	1.01	0.71
Gd^{+3}	7	1	0.70
Tb^{+3}	7	0.98	0.69
Dy^{+3}	6	0.912	0.65
Y^{+3}	8	1.1019	0.78
Ho^{+3}	8	1.015	0.71
Er^{+3}	8	1.004	0.71
Tm^{+3}	8	0.994	0.70
Yb^{+3}	8	0.985	0.69
Lu^{+3}	8	0.977	0.69
Ti^{+4}	5	0.51	0.37
Ti^{+4}	6	0.605	0.43

2.4 Radiation damage in ceramics

A key performance criterion for wasteform selection is the response of the material to radiation damage. With regard to ceramic wasteforms for actinide immobilisation, the most significant impact arises from atomic displacements induced by recoil of the heavy daughter nucleus following α decay. The recoil nucleus typically has kinetic energy the range of 70 keV - 100 keV, whereas the α particle typically has kinetic energy in the range 4.5 - 5.5 MeV [14], [82], [83]. Recoil nuclei interact with a crystalline material on an atomic level through a ballistic process, wherein they create displacements through elastic scattering events – this is typically referred to as the nuclear stopping regime. Due to their large mass, recoil nuclei are able to displace an atom and transfer energy much more efficiently than α particles which transfer most of their energy through ionisation – typically referred to as the electronic stopping regime. However, α particles still have sufficient energy to overcome the threshold displacement energy of atoms causing a few 100 atomic displacements over their range of ca. 20 microns in a ceramic material [14], [82], [83]. In contrast, the recoil nucleus typically induces ca. 1,000 – 2,000 atomic displacements over a range of 30 – 40 nm in a ceramic material [14], [82], [83]. The large number of displacements is a product of the recoil nucleus being very effective at transferring kinetic energy through collisions with neighbouring atoms, causing a knock-on effect, and the resultant cascade of displaced atoms interacting with and displacing other atoms. The energy of the displaced atoms dissipates through these interactions and will eventually be less than the threshold

displacement energy. At this point, the displaced atoms will come to the stop and form Frenkel pairs (Frenkel pairs form when an atom, or ion, occupies a vacant position within the crystal lattice or becomes an intgerstial, leaving behind a vacancy) [84]. Interstitials and vacancies may recombine at the end of the damage cascade, enabling partial recovery of the damaged crystal lattice [84]. Since the energy released by α decay is fully recovered within the ceramic material, it may result in self-heating for significant Pu incorporation, which must be managed during storage and initial disposal.

There are several consequential effects of damage induced by α decay in a ceramic material which may challenge wasteform performance. Over time the overall impact of α decay results in the formation of voids from accumulated point defects, gas bubbles from diffused He nuclei, and swelling of the wasteform arising from atomic displacements which may induce a crystalline to amorphous phase transition. The change in volume and density of the ceramic results in the formation of micro-cracks within the material [14], [82], [83]. Collectively, these effects may negatively impact the solubility of the material and increase the surface area available for groundwater dissolution in the disposal environment.

2.4.1 Radiation Damage in Ln_2TiO_5 ceramics

The radiation tolerance of Ln_2TiO_5 has been extensively studied using ion beam irradiation methods. *Whittle et al., Zhang et al.,* and *Aughterson et al*. investigated the radiation tolerance of orthorhombic Ln_2TiO_5 with Ln = La… Dy, and cubic defect fluorite Ln = Y, Yb, in response to 1 MeV Kr^{2+} ion irradiation, using in situ TEM / ED observation [54], [58], [60]. In this approach, both electronic and nuclear stopping power contribute to radiation damage. The results of these studies are in broad agreement and show that all compounds undergo a crystalline to amorphous phase transition after irradiation to a fluence of ca. 2 x 10^{14} ions cm^{-2}. The critical temperature for amorphisation increases with increasing r_A / r_B ratio, from ca. T_c = 600 K for Ln = Y, to T_c = 1200 K for Ln = Sm – La.

Aughterson et al., report a modest decrease in T_c for Ln = Sm – La, whereas *Zhang et al*., report saturation at ca. 1200 K [54], [85]. Dy_2TiO_5 had the highest critical fluence of all orthorhombic compounds studied, this appears to correspond to a trend in the increasing Ln(site-2)-Ti defect formation energies as the lanthanide ionic radius decreases. The variance was suggested by Aughterson *et al.* to be due to error in temperature measurement [85], though the uncertainties in both dose and temperature are large, and analysis depends on relatively few data points. The orthorhombic Ln_2TiO_5 phases typically showed radiation damage induced transformation to a cubic defect fluorite structure, prior to amorphisation [54], [58], [60]. *Aughterson et al*, also investigated the radiation tolerance of Er_2TiO_5, $Yb_{2-x}Ho_xTiO_5$, and $Yb_{2-x}Tb_xTiO_5$ using the *in situ* ion beam irradiation approach with 1 MeV Kr^{2+} ions. These compounds variously adopt orthorhombic, hexagonal or cubic Ln_2TiO_5 structures at room temperature, as would be expected according to the average size of the Ln cation [63], [86]. The critical temperature for amorphisation scales with r_A / r_B ratio as also observed

elsewhere [54], [58], [60]. The radiation damage behaviour of Ln_2TiO_5, with Ln = La… Gd, Y, has also been studied by *Park et al*., in response to swift heavy ion irradiation with 1.47 GeV Xe^+ and 2.2 GeV Au^+ ions [84]. In this approach damage is induced within ion tracks primarily by electronic excitation, leading to melting of the material within the core of a track, which may quench to yield an amorphous structure. All Ln_2TiO_5 phases were rendered partly amorphous in these experiments at a fluence of 10^{12} ions cm^{-2}, as determined from XRD and Raman spectroscopy, with Ln = Nd, Gd and Yb becoming almost completely amorphous at a fluence of ca. $10^{13} – 10^{14}$ ions cm^{-2} [87]. The fluence required to induce amorphisation increased with decreasing r_A / r_B ratio, as observed in the *in situ* amorphisation experiments discussed above. Overall, increased radiation tolerance (lower T_c) associated with lower r_A / r_B ratio is similar to that observed in the structurally related $Ln_2Ti_2O_7$ pyrochlores and is suggested to be a consequence of the lower defect energy for formation of anti-site defects as the structure tends toward a defect fluorite arrangement [54], [58], [63], [86].

A comparative study of orthorhombic *Pnma*, hexagonal *P6₃-mmc* and cubic *Fd-3m* Dy_2TiO_5 investigated the radiation response of chemically identical but structurally different compounds when subjected to 1 MeV Kr^{2+} ions. The critical fluence $F_{c(300\ K)}$ at room temperature remained consistent between the samples but the critical temperatures, T_c, deviated significantly (orthorhombic T_c = 711 K, hexagonal T_c = 1130 K and cubic = 761 K, comparatively cubic *Fd-3m* $Dy_2Ti_2O_7$ had a T_c = 910 K under the same conditions [50]). Hexagonal Dy_2TiO_5 did have a considerably higher $F_{c(300\ K)}$ value than other hexagonal Ln_2TiO_5 compounds studied [61], [86], [88]. This is speculated to be due to the broader stability range of hexagonal Dy_2TiO_5. Though cubic and orthorhombic Dy_2TiO_5 had the lowest T_c, they also issues related to the synthesis of bulk ceramic products. Cubic Dy_2TiO_5 required the highest sintering temperature (1630 ^oC) and a more complex synthesis route whereas the bulk orthorhombic Dy_2TiO_5 product was porous, likely requiring iterative sintering steps to achieve a dense single-phase ceramic.

2.4.2 Radiation damage induced crystalline to amorphous phase transition

There are two principal mechanisms by which ceramic materials may undergo a radiation damage effected crystalline to amorphous phase transition: homogenous or heterogeneous amorphisation. Homogeneous amorphisation is considered to be a more progressive process, driven by the growth and accumulation of defects with increasing dose, which results in amorphisation after a threshold dose is reached. This mechanism can be modelled by using a Rate Theory model, such as that developed by *Mottat and Olander* [89]. Few ceramic materials that are of interest as actinide hosts exhibit this behaviour as amorphization due to α-decay or heavy-ion implantation is known to occur heterogeneously [83], except when exposed to electron irradiation, and, as such, this mechanism will not be considered in further detail. In heterogeneous amorphisation, a crystalline to amorphous phase transition is affected locally, in a small region of the material, by each radiation damage event when the defect density is sufficiently high. In the direct impact cascade model, with increasing dose, these amorphous regions form a continuous percolating network, eventually yielding a completely

amorphous material; this behaviour is exhibited by $Ca_2(La,Nd)_8(SiO_4)_6$ in response to ion beam irradiation [90]. Alternatively, in the cascade overlap model, the amorphous region is formed in the volume of material affected by two overlapping cascades, this mechanism is exhibited by $ZrSiO_4$, zircon [91]. It has also been argued that a crystalline to amorphous phase transition may be affected by multiple processes, occurring in parallel, or sequentially [92]. Figure 2.9 summarises the progression of the crystalline to amorphous phase transition as a function of normalised dose for different mechanisms. Understanding the relevant mechanism and rate of amorphisation for ceramic materials is important, since this ultimately provides the required predictive model of future behaviour, such as swelling and micro-crack formation, required to assure safe disposal.

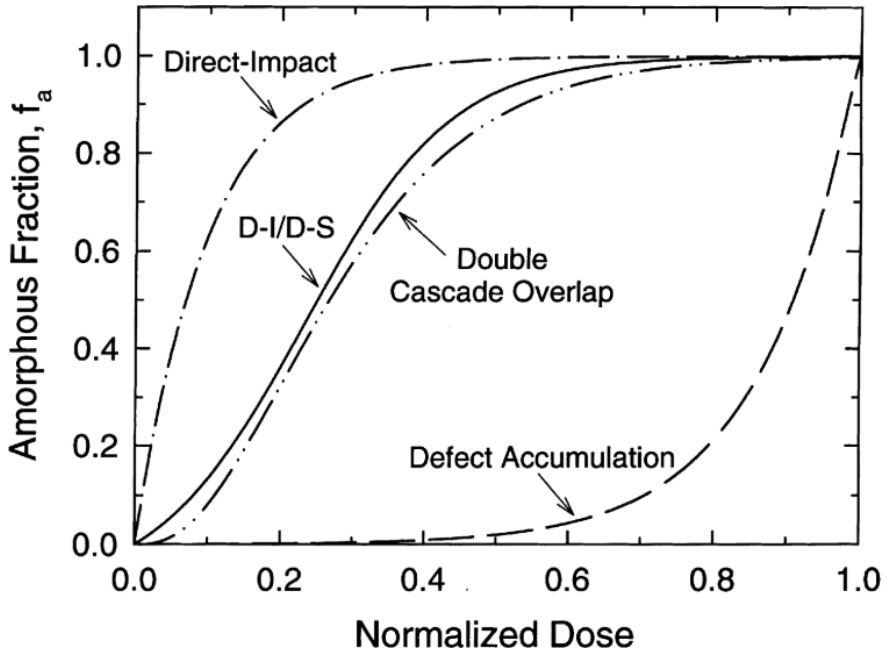

Figure 2.9: Showing how dose received effects the amorphous fraction generated in a ceramic and the rate of damage types being accumulated. DI-DS refers to the direct-impact/defect-simulated processes. Taken from [93].

Models describing heterogeneous amorphisation are described by differential equations. The rate at which amorphisation occurs for simple models, which do not consider effects from temperature and are valid in the limit of low temperatures, can be expressed in Equation 2.7:

$$\frac{df_a}{dt} = \sum_i P_{ai} g_i(f_a) \qquad \textbf{Equation 2.7}$$

where P_{ai} is the amorphous production term for some *i*th process, f_a is the amorphous fraction and $g_i(f_a)$ is the probability for that process to take place for a given value of f_a. As the temperature of the sample increases so does the rate of recrystallisation [94]. These simultaneous recovery processes can act as to mitigate the damage caused through irradiation. This recovery can be driven by damage and temperature effects, and is described by Equation 2.8:

$$\frac{df_a}{dt} = \sum_i P_{ai} g_i(f_a) - \sum_j K_j(T) h_j(f_a)$$ **Equation 2.8**

where $K_j(T)$ describes the rate of recovery at some temperature T for some jth process, $h_j(f_a)$ is the probability that a recovery process takes place for some value of f_a. The latter term is dependent on where the recovery process is taking place, for instance, if the recovery is happening within the bulk of the material, then it will be equal to $(1 - f_a)$, if the recovery process is active at the crystalline/amorphous interface then it will be proportional to $f_a(1 - f_a)$. At some temperature, it is reasonable to assume that the crystalline structure can no longer be made amorphous due to the recrystallisation rate being equal to or greater than the rate of amorphisation, specifically, if $\frac{df_a}{dt}$ is equal to 0 then, $P_{ai} g_i(f_a) = K_j(T) h_j(f_a)$. As thermal recovery processes become more dominant, the critical temperature for amorphisation, T_c, is reached where no more amorphisation can take place. As $f_a \to 1$ then $P_{ai} = K_j(T)$ at the critical temperature [94]. Thus, T_c, can be expressed by Equation 2.9:

$$T_c = \frac{E_{th}}{k \, ln(\frac{v_{th}}{\sigma_a \phi})}$$ **Equation 2.9**

where σ_a is the dominant cross-section for the process that causes amorphisation near the critical temperature, E_{th} is the activation energy of thermal recovery, v_{th} is the effective attempt frequency for thermal recovery, ϕ is the ion flux and k is the Boltzmann constant (1.38 x 10^{-23} J K^{-1}). v_{th} is often taken as the Debye frequency, $\sim 10^{13} s^{-1}$, but as it must also account for local coordination and average jumps to recovery it can be within the range of $10^9 s^{-1}$ to $10^{14} s^{-1}$ [95].

The quantities D_c and T_c are useful metrics of the radiation tolerance of ceramic wasteforms and can be quantified by in situ ion beam irradiation and TEM. D_c is the dose needed from an ion beam to fully amorphous the sample (observed by a lack of Bragg diffraction intensities) and T_c the temperature at which the rate of thermal recrystallisation is the same as the damage rate.

D_c and T_c are related to each other through Equation 2.10 [85] and is achieved by a least-squares numerical analysis of the critical dosage against temperature. The equation can also be used to determine the critical dosage at 0 K, D_{c0}.

$$D_c = \frac{D_{c0}}{1 - exp[E_a / k_b (\frac{1}{T_c} - \frac{1}{T})]}$$ **Equation 2.10**

where E_a is the activation energy for crystalline recovery, k_b is the Boltzmann constant (8.617 x 10^{-5} eV K^{-1}) and T is temperature.

where E_a is the activation energy for crystalline recovery, k_b is the Boltzmann constant (8.617 x 10^{-5} eV K^{-1}) and T is temperature.

Using Equation 2.10, the E_a value is usually undervalued, due to there being two components to the kinetics of recovery (irradiation effects, such as interstitial-vacancy recombination, and thermal annealing) and it is recommended to use an approaches that considers non-kinetic properties [85]. A better value for E_a can be obtained through the use of Equation 2.11:

$$E_a = T_c k_b ln\left(\frac{D_{c0} v}{\phi}\right) \qquad \textbf{Equation 2.11}$$

Values for T_c and D_{c0} can be estimated from values generated from equation 2.10. ϕ is the incident ion flux and v the effective frequency jump ($\sim 10^{12}$).

2.4.3 Simulating Radiation Damage

The isotope of primary importance for actinide immobilisation is Pu-239, with half-life $t_{1/2}$ = 24,000 years. However, laboratory experiments require accelerated radiation damage techniques to deliver the cumulative lifetime dose experienced by the ceramic material in a reasonable time frame. One approach is to dope candidate ceramic materials with a short-lived α-nuclide, such as Pu-238 ($t_{1/2}$= 88 y) or Cm-244 ($t_{1/2}$= 18.1 y), such that the effect of α -recoil damage can be investigated over a few years. For example, *Weber et al.* [96] observed volume swelling of ^{244}Cm-doped $Gd_2Ti_2O_7$ and $CaZrTi_2O_7$ samples increased by 5 to 6 %, decreases in sample hardness, a crystalline to amorphous transition amorphisation at approximately 2.0 x10 ^{25} α decays/m^3, and dissolution of key elements into water (Pu leached from amorphous material), and then tested the sample's thermal recovery (crystal structure recovered was observed to between 600 °C to 750 °C). However, handling of such short-lived nuclides, requires specialist infrastructure, and is resource intensive, which limits the extent of the research that can be undertaken.

An alternate approach is to utilise ion beam irradiation, either in situ with TEM or applied to bulk ceramic materials, using keV to MeV ions produced by an ion accelerator, spanning the nuclear to mixed nuclear and electronic stopping regimes. Ion beam irradiation coupled with TEM observation has been widely exploited to investigate radiation damage behaviour of ceramic materials and estimate D_c and T_c as reviewed by *Lian et al* [97]. However, a limitation of this approach is that TEM foils are typically <100 nm thick, resulting in a high surface-area to irradiated-volume ratio. The critical dose for amorphisation may then be overestimated as a result of electron beam induced annealing effects due to the intense and localized heat generated by the beam, which results in the migration and annihilation of defects at the surface [97]. In addition, no insight is provided with regard to the atomic scale structure or properties of the amorphised material. Consequently, in recent years, there has been more attention devoted to ion beam irradiation studies of bulk ceramic substrates, in which keV to MeV ions will yield a surface amorphous layer some 100 – 1000 nm thick [98].

This approach allows techniques such as XRD (XRD) and X-ray absorption spectroscopy (XAS) to be applied to characterise the atomic scale structure of the ion beam amorphised material, in a surface sensitive mode such as grazing angle geometry[98], [99]. For example, *Reid et al.,* applied glancing angle XRD and Ti K-edge glancing angle XAS to characterise the structure of the 1000 nm surface amorphised layer produced by 2 MeV Kr^+ irradiation of zirconolite to 5 x 10^{15} ions cm^{-2} [98]. The ion beam amorphised layer was shown to be indistinguishable from that of naturally metamict zirconolite, comprising TiO_5 polyhedra; the formation of such small co-ordination species is hypothesised to introduce the additional degrees of structural freedom required to stabilise an amorphous structure [98]. Further studies by *Lawson et al.* have used both 1 MeV Kr^+ and 5 MeV^+ ion irradiation to investigate the resistance to amorphisation of $Ca_{1-x}La_{2x/3}TiO_3$ (x = 0, 0.2, 0.4, 0.5, 0.6, 0.7, 0.9) perovskites *via* GAXRD [99]. The tow conditions were used to investigate the effect varying electronic-nuclear stopping (ENSP) ratios and different irradiating ions have on radiation response. *Lawson et*

al. calculated the amorphous fraction of the GAXRD pattern of irradiated samples using a pseudo-Voigt peak analysis. Under both Kr^+ and Au^+ ion irradiation conditions, the samples where $0.1 \leq x \leq 0.4$ were found to have the smallest amorphous fraction (and as such were resistant to radiation damage). The proposed mechanism for this apparent enhanced tolerance to radiation, compared to $Ca_{1-x}La_{2x/3}TiO_3$ with higher levels of La doping, is due to an increase in the mobility of A-site cation vacancies due to intrinsic vacancy induction through La doping [99].

Some self-healing or non-representative effects can be caused by ion beam irradiation, such as point defect recombination or larger amounts of defect diffusion, this is particularly notable for ion beams with energies larger than 1 MeV [101]. A further approach is the use of so called swift heavy ion beams, of GeV energy, to induce amorphisation of macroscopic quantities of polycrystalline powder material, which requires powerful particle accelerators, such as the GANIL facility in France [102]. However, damage is induced primarily by electronic excitations and hence swift heavy GeV ions are a much less effective proxy for α recoil damage compared to MeV implantation.

2.5 X-ray absorption spectroscopy applications in nuclear wasteform science

XAS measurements require high energy X-rays of a definitive energy, this often requires synchrotron light sources however there have been great strides in laboratory based XAS equipment facilitating more routine measurements [103]–[105]. In an XAS experiment, samples are bombarded with X-rays and absorbed by atoms exciting or ejecting a core electron. The intensity of the incident X-ray beam, once compared to the transmitted beam (or the fluorescent X-rays given off by an atom as a core orbital hole is filled), can be used to quantify the interaction. XAS measurements are conducted over a range of energies (e.g., 7150 eV to 7500 eV) in discrete steps. The measurement of the transmitted X-ray intensity at each energy step generates a characteristic XAS spectrum. Analysis of the X-ray absorption near edge structure (XANES) and extended X-ray absorption fine structure (EXAFS) regions of the spectra yield information about the local atomic ordering which can be used to determine the oxidation states, coordination environment of absorbing atoms and bond distances of neighbouring atoms, amongst other structural features [106]. A more detailed explanation of the theory and implementation of XAS is given in section 3.5.

Due to its powerful and wide-ranging analytical capabilities, x-ray absorption spectroscopy (XAS) has been used to study a wide range of problems posed in the design and characterisation of nuclear wasteforms and their behaviours under a variety of conditions, such as irradiation and corrosion. Additionally, XAS has also been frequently employed in other research areas related to nuclear waste such environmental sciences [107]–[109] and cement encapsulation [110]–[112]. However, in the context of this thesis, the focus of the discussion here will aim to provide highlights of the application of XAS in the development of glass and ceramic wasteforms and the pivotal role it can occupy to further such development.

2.5.1 X-ray absorption near edge spectroscopy

A common application of XAS is to provide information about the oxidation state of constituent elements which is an important consideration as oxidation state can affect a wide-range of properties of a wasteform such as the leachability and chemical stability [113], [114]. This information can be obtained through analysis of the XANES region of the XAS spectra, with one such example being provided by *Blackburn et al.* who showed that the redox environment of a hot isostatic pressing (HIP) canister (made from grade 316 stainless steel) was sufficient to maintain a U^{4+} oxidation state in $CaZr_{0.8}U_{0.2}Ti_2O_7$ zirconolite as determined by linear regression of the absorption edge positions (E_0) in the XANES of standard compounds ($CrUO_4$, UTi_2O_6, $MgUO_4$) and the zirconolite sample in addition to qualitative comparisons of their XANES spectra [113]. XANES collected in microfocus XAS mode were used to study the effective oxidisation of U species (using the U L_3-edge found at 17166 eV) in magnesium aluminosilicate (MAS) and magnesium borosilicate (MBS) glasses synthesised using corroded and metallic uranium and magnesium waste simulants. This approach utilised a focused X-ray beam (spot size of 1 μm^2) to study individual facets of a sample's heterogenous surface. It was determined that both metallic and corroded waste streams were oxidised, with MBS and MAS metallic waste formulations having U oxidation states of 4.9 ±0.1 and 5.2 ± 0.1, respectively, whereas MBS and MAS glasses synthesised from corroded waste streams had oxidation states of 5.5 ± 0.1 and 5.7 ± 0.1, respectively [115]. XAS was also used in the study of the average oxidation state of Ce cations in $Ca_{0.9}Zr_{0.9}Ce_{0.2}Ti_2O_7$ zirconolite synthesised via a molten salt mediated reaction for the purpose of the immobilising pyroprocessing molten salt wastes in a zirconolite wasteform. Here, samples were reacted between 1100 °C – 1400 °C, in 100 °C steps, for two hours in air. XANES spectra were collected at the Ce L_3-edge from a number of samples over the temperature range and the spectra were analysed using a linear combination fitting (LCF) of spectra (which is a routine that uses a least-squares minimisation, to fit linear combinations of various reference compounds, to a narrow region around the pre-edge) from both the samples and a suite of standards (CeO_2, $CeAlO_3$, $CePO_4$). LCF results showed that as reaction temperature increased the relative proportion of Ce^{3+} also increased (54% Ce^{3+} at 1100 °C and 71% Ce^{3+} at 1400 °C, with the remainder being Ce^{4+}), correlating with the increased presence of zirconolite-2M and -3T polytypes and a decrease in perovskite secondary phases as the reaction kinetics become faster at higher temperatures providing a better environment for the formation of zirconolite and conversion of the 3T polytype to 2M, and hence the retention of Ce species due to the higher durability of the 2M polytype. This work demonstrates clearly how XANES may be used to influence decisions on wasteform manufacturing as the control of unwanted secondary phases, such as perovskites, is key for wasteform design [116].

Another area of XANES analysis that is commonly used to determine chemical speciation and coordination is that of the pre-edge features. Pre-edge features, found ~ 10 eV below the main absorption line, result from dipole-forbidden *1s* → *3d* excitations, which are allowed in non-

centrosymmetric coordination's where *d-p* orbital mixing is able to occur. The relative position and intensity of this feature relate to an absorbing cations oxidation state and coordination environment [117], [118]. Quantitative analysis of pre-edge features can allow comparisons of oxidation state and coordination environment as the relative position and intensity of this feature relate to these. This analytical technique has been broadly applied and has found significant use in the analysis of nuclear materials. Analysis of the Ti K-edge pre-edge features collected on explosive melt glasses derived from the Trinity nuclear bomb test (these materials are commonly referred to as trinitite) showed that, whilst Ti remained in a 4+ oxidation state for all samples, the Ti-O coordination environment changes significantly, ranging between 4- to 6-fold coordination [119]. This is reflective of the varied thermal histories and local chemistries found in the heterogenous microstructure of trinitite samples. Another study compared spectra collected at both a synchrotron beamline and from a laboratory based XAS spectrometer and used the Fe K-edge pre-edge features of iron phosphate glasses to understand the Fe speciation for samples prepared by both conventional and microwave melting methods. This study successfully demonstrated the applicability of laboratory XAS spectrometers and confirmed the majority presence of Fe^{2+} in octahedral coordination's [120]. In the context of nuclear wasteform design, higher fractions of Fe^{2+} have been shown to adversely affect glass formation in addition to its radiation tolerance and so understanding how processing conditions may affect the abundance of Fe^{2+} in these systems is of key importance [121], [122].

2.5.2 Extended X-ray absorption fine structure

Analysis of the EXAFS region (~> 250 eV past the absorption line) of an XAS spectra has been frequently employed to study the coordination environment of absorbing atoms in addition to determining bond distances and disorder parameters of nearest neighbour and next-nearest neighbour atoms. XANES analysis of the Pu L_3-edge of $Nd_{1.9}Pu_{0.1}Zr_2O_7$ and $Nd_{1.8}Pu_{0.2}Zr_2O_7$ pyrochlores showed, through comparison of the E_0 positions of Pu^{3+} and Pu^{4+} standards, that the average Pu valence state was 3.98 and 3.92, respectively. Quantitative analysis of the EXAFS region was used to validate the incorporation of Pu^{4+} on A-site positions, in the expected 8-fold coordination and determine the bond lengths of the coordinating oxygens [123]. The bond distances of coordinating O anions were reported to consist of six short Pu-O bonds (2.29 Å) and two longer Pu-O bonds (2.52 Å) [123]. Contrarily, molecular modelling results from the same study indicate that the Pu^{4+}-O bonds should consist of two short and six long bonds. This can be satisfied if Pu has a partial occupancy across both A- and B-sites (charge balanced through the introduction of oxygens into vacancy positions), which would result statistically in 69% shorter Pu-O bond lengths (*ca.* 2.3 Å). An EXAFS model including 50% Pu^{4+} on both cation sites successfully demonstrated this, however, its validity is questionable due to limitations in the number of variables that could be supported by the information available in the data [123]. EXAFS was used to model the local structural environment of Nd^{3+} cations in vitusite ($Na_3RE(PO_4)_2$ RE = rare earth) glass-ceramic composites designed for the immobilisation of rare-earth cations generated from pyroprocessing wastes. It was shown that Nd cations were found in an average 6.9 O coordination in vitusite and that next-nearest neighbours consisted of Na^+ and P^{5+} pairs, which preferentially

accumulated in the vitusite crystalline phase. This result was used to infer that chemical durability was enhanced as a greater amount of Na^+ ions were present in the more durable crystalline phase [124]. Mo K-edge EXAFS were used by *Calas et al.* to study the local environment of molybdenum and its role in the broader structure of nuclear waste glasses. The low Mo solubility, separation of Mo-rich phases in melts and nucleation of molybdates in nuclear glasses was explained to be due to the formation of MoO_4 tetrahedra located in alkaline or alkaline-earth rich domains and not directly connected the glass network, facilitating favourable charge compensation over boron in borosilicate glasses giving rise to the observed chemical difference in molybdates formed by phase separation during melts or by the recrystallisation process of glasses that have been heated [125].

2.5.3 Use of XAS to evaluate radiation damaged nuclear wasteforms

XAS techniques have also been applied to study the response of nuclear material to radiation damage and evaluate the effects on local coordination and structural environments [83]. The coordination environment of metamict zirconolite minerals was investigated through fitting of pre-edge features of Ti K-edge data collected on the zirconolite mineral along with a suite of standards [126]. Crystalline zirconolite contains two octahedral Ti sites (6-fold coordination) and one trigonal bipyramidal Ti site (5-fold coordination) with Ti split evenly across these two coordination geometries. However, upon examination of the pre-edge features of Ti K-edge XAS spectra of metamict zirconolite it was shown that the majority of Ti was coordinated in a trigonal bipyramidal geometry (~80-90 ± 0.5 %). The change in Ti local coordination environment was determined through the use of mechanical mixtures of 5- and 6-fold Ti standards, which produced a trend in the position and height of the pre-edge position which was related to different ratios of Ti coordination numbers (CN) [127].

Utilising XAS to study radiation effects in nuclear wasteforms is typically conducted on samples of naturally occurring metamict minerals or through substitution of radioactive nuclides. This is achievable due to fact that the radiation damage of these samples occurs throughout the entire specimen and is an average measurement finely ground powder samples that are dispersed into a binder (e.g. polyethylene glycol) or onto an adhesive tape (e.g. Kapton). Bulk samples irradiated with heavy ions only generate localised damage profiles on the surface of the monolith (up to 1000 nm), therefore glancing-angle XAS (GAXAS) geometries must be used to probe the surface layers of irradiated samples (see section 3.5 for a more detailed discussion of the technique). Although the literature is limited on studies that utilise this geometry to study radiation effects, the method does provide safe and convenient means to probe radiation effects and the results are encouraging. For instance, GA-XANES of Ti K-edge data collected on zirconolite ceramics irradiated by 2 MeV Kr^+ ions at a fluence of 5 x 10^{15} ions cm^{-2} confirmed the results by *Farges et al.* showing Ti to be in a majority 5-fold coordination with O, providing validity of the GAXAS methodology [98]. Coordination number of Ti-O in a $Gd_2Ti_2O_7$ pyrochlore irradiated by 2 MeV Kr^+ ions at a fluence of 5 x 10^{15} ions cm^{-2} was reduced to 5 ± 0.3 and the Ti-O bond length was reduced 1.981 Å to 1.913 Å [128]. In another study Gd_2Ti_{2-}

$_xSn_xO_7$ (x = 0, 1, 2) were irradiated by 2 MeV Au^+ ions to a fluence of 1×10^{15} and 5×10^{15} ions cm^{-2} and probed by GAXAS. Observations of both the XANES and EXAFS spectra showed that Sn inclusions prevented an order-disorder a phase transition to a defect-fluorite structure due to the strength covalent bonding of Sn-O B-site cations and the more disparate average ionic radius ration of A-site to B-site cations (r_{Gd} / r_{Sn} = 1.53 Å), this conclusion was also consistent with literature [129]–[131]. As such, the higher concentration of Sn the more susceptible to radiation damage as they became amorphous whereas at an equivalent dose $Gd_2Zr_2O_7$ compounds undergo the aforementioned phase transition to a defect-fluorite crystal structure because of the low ionic radius ratio (r_{Gd} / r_{Zr} = 1.46 Å) [130].

The coordination environment of Pu-substituted (^{238}Pu and ^{239}Pu) zirconolite samples ($CaPuTi_2O_7$) was investigated by *Greegor and Lytle* [133]. $CaPuTi_2O_7$ undergoes a transition from monoclinic to a cubic fluorite structure after 6 x 10^{25} α/m^3; a process that can be rapidly simulated by the inclusion of greater concentrations of ^{238}Pu as it has a half-life of 87.4 years, compared to more common ^{239}Pu which has a half-life of 24390 years. XANES/EXAFS results on Pu-substituted zirconolite show that the Pu is located on a Ca-like site (8-fold coordinated with O) and that there were contractions of Pu-O bond lengths (from 2.30 Å to 2.27 Å) and expansions of more distant Pu-cation bond lengths (4.26 Å to 4.36 Å and 4.81 Å to 4.90 Å), corresponding to 6-7 % macroscopic volume swelling [133]. In another study investigating radiation damage induced structural changes in metamict zirconolite, alongside an annealed and a crystalline zirconolite, XANES and EXAFS analysis were used to conclude that the most likely structure for a full damaged zirconolite is a random network, showing no crystallinity beyond the first coordination sphere [134]. Comparisons of the coordination number of Ca and Ti cations between metamict and annealed zirconolite samples showed that there was a 25 – 40% and 25% reduction of CN, respectively. The Ti-O bond length, were also shown to decrease from 1.90 Å to 1.77 Å and the Ca-O bond length decreased from 2.46 Å to 2.41 Å, corresponding well to the reduction in CN and further to the disordering of the Ti-O coordination shell [134].

Another method for measuring XAS spectra on samples damage by heavy ion irradiation is the use of soft X-ray absorption spectroscopy (SXAS), as the lower energy X-rays are less penetrating and can be used to evaluate surface layers which is beneficial to the study of heavy ion irradiated materials due to the shallow damage profile at the surface. *Dube et al.* used this technique to probe the Fe $L_{2,3}$-edge in Ce doped iron phosphate glasses (IPG) irradiated by 750 keV Au^+ at a fluence of 2x10 10^{15} ions cm^{-2}. Fe L_3-edges are characterised by two maxima (707 eV and 712 eV), the intensities of which relate to the proportion of Fe^{2+} and Fe^{3+} present in a system. The intensity of the edge feature corresponding to Fe^{2+} of irradiated Ce-doped IPG spectra increased significantly compared to both the pristine sample as well as an undoped irradiated IPG [135], showing there that the ratio of Fe^{2+}:Fe^{3+} in the system had increased. Fe^{3+} reduction to Fe^{2+} can lead to the formation of crystalline $Fe_2(P_2O_7)$ phases, detrimental to the chemical durability of Ce-doped IPG samples [136].

When samples are bombarded with X-rays, they will also yield electrons (both Auger and photelectric), the energy of which is equal to the difference between the incident X-ray and an

electron's binding energy, this measurement mode is known as total electron yield (TEY). Electrons emitted from a sample in this manner are generally measuring up to 100 nm, though a larger depth can be obtained depending on the density of the sample (e.g. ~150 nm) [137]. Though the measurable depth is comparatively shallow compared to what a GAXAS geometry can achieve can still be used to evaluate radiation damage. Fe K-edge data collected on IPG glasses (60 mol% P_2O_5 – 40 mol% Fe_2O_5) irradiated by 2 MeV Kr^+ and 2 MeV Au^+ implantation to a fluence of 2 X 10^{16} ions cm^{-2} and 5 x10^{15} ions cm^{-2} were collected in TEY mode. The resultant spectra were analysed with a combination of XANES and EXAFS [138]. In this study 23 ± 0.4 – 24 ± 0.4 % of Fe^{3+} was shown to reduce to Fe^{2+}, when irradiated by Au^+ or Kr^+ ions, respectively, compared to structural models of pristine IPG glass. The concurrent average presence of octahedrally coordinated Fe^{3+} increased by 15 – 16 ± 0.6 % (average CN increased from 5.4 to 5.7 ± 0.1 and the Fe-O bond length by 0.3 ± 0.01 Å.

2.6 Summary

Nuclear power is, and will continue to be, an integral part of securing the UK's plans for reducing carbon emissions generated as a product of electricity generation as well as being a strategic means of energy independence. Therefore, the UK's inventory of ILW and HLW is set to only expand and a clear and robust strategy for disposal of hazardous materials is needed. This will necessitate further developments and implementation of advanced wasteform technologies. Currently only immobilization *via* vitrification in borosilicate glass is the only commercial method currently in operation for the immobilisation of HLW inventories. Second generation nuclear wasteforms are currently being explored and candidates often include ceramic systems due to their high levels of chemical and physical durability. Of note the Ln_2TiO_5 ceramic system is of current interest thanks to its reported high levels of radiation resistance compared to other ceramic systems. The use of this material as a nuclear wasteform will require scrupulous research to ensure that its characteristics are well understood and documented. XAS can be a vital tool that can be applied to further elucidate the nature of the complex local ordering of these materials as well as probe the material's response to radiation sources, adding to the already discussed catalogue of studies probing the systems viability.

2.7 References

[1] "Nuclear Power Today | Nuclear Energy - World Nuclear Association." [Online]. Available: https://world-nuclear.org/information-library/current-and-future-generation/nuclear-power-in-the-world-today.aspx. [Accessed: 15-Feb-2022].

[2] P. D. Wilson, *The nuclear fuel cycle: from ore to wastes*. Oxford University Press, pp. 1-162, 1996.

[3] B. R. Martin and S. Graham, *Nuclear and Particle Physics: An Introduction, 3rd Edition*, 3rd ed. Chinchester: Wiley & Sons Ltd, p. 52, 2019.

[4] R. W. Bauer, J. D. Anderson, S. M. Grimes, D. A. Knapp, and V. A. Madsen, "Application of a Simple Ramsauer Model for Neutron Total Cross Sections," *Nucl. Sci. Eng.*, vol. 130, no. 3, pp. 348–360, 1998.

[5] I. W Donald, B. Metcalfe, and R. N. J Taylor, "Review: The Immobilization of High Level Radioactive Wastes Using Ceramics and Glasses," *J. Mater. Sci.*, vol. 32, pp. 5851–5887, Nov. 1997.

[6] G. F. Hewitt and J. G. Collier, *Introduction to Nuclear Power*, 2nd ed. CRC Press, pp. 28-34, 2018.

[7] Nuclear Decommissioning Authority (NDA), "2019 UK Radioactive Material Inventory," 2019. [Online]. Available: https://ukinventory.nda.gov.uk/wp-content/uploads/2020/01/2019-Materials-Report-Final.pdf. [Accessed: 17-Feb-2022].

[8] W. E. Lee, M. I. Ojovan, M. C. Stennett, and N. C. Hyatt, "Immobilisation of radioactive waste in glasses, glass composite materials and ceramics," *Adv. Appl. Ceram.*, vol. 105, no. 1, pp. 3–12, Feb. 2006.

[9] Nuclear Decommissioning Authority (NDA), "Integrated waste management: Radioactive waste stratergy," 2019. [Online]. Available:https://assets.publishing.service.gov.uk/government/uploads/system/uploads/attachment_d ata/file/838828/Radioactive_Waste_Strategy_September_2019.pdf. [Accessed: 17-Feb- 2022].

[10] P. Goodhand, R. Drouin, T. Masin, and E. Turcotte, “Report of the Expert Review Panel on Medical Isotope Production,” 2009. [Online]. Available: http://cins.ca/docs/panrep-rapexp-eng.pdf. [Accessed: 17-Apr-2022].

[11] D. Bodansky, *Nuclear energy : principles, practices, and prospects*. New York: Springer, p. 145, 2004.

[12] Nuclear Decommissioning authority (NDA), “Plutonium: Credible Options Technical Analysis,” 2009. [Online]. Available: https://webarchive.nationalarchives.gov.uk/ukgwa/20211004154523/https://rwm.nda.gov.uk/publication/nda-plutonium-topic-strategy-credible-options-technical-analysis-january-2009/. [Accessed: 17-Apr-2022].

[13] R. C. Ewing, “Plutonium and ‘minor’ actinides: safe sequestration,” *Earth Planet. Sci. Lett.*, vol. 229, no. 3–4, pp. 165–181, Jan. 2005.

[14] R. C. Ewing, “Nuclear waste forms for actinides,” *Proc. Natl. Acad. Sci.*, vol. 96, no. 7, pp. 3432–3439, Mar. 1999.

[15] R. C. Ewing, “Actinides and radiation effects: impact on the back-end of the nuclear fuel cycle,” *Mineral. Mag.*, vol. 75, no. 4, pp. 2359–2377, Aug. 2011.

[16] R. Ewing, “The Design and Evaluation of Nuclear-Waste Forms: Clues from Mineralogy,” *Can. Mineral. - CAN Mineral.*, vol. 39, pp. 697–715, Jun. 2001.

[17] M. W. Lufaso and P. M. Woodward, “Structural Science Prediction of the crystal structures of perovskites using the software program SPuDS,” *Acta Cryst*, vol. 57, pp. 725–738, 2001.

[18] M. Yashima and R. Ali, “Structural phase transition and octahedral tilting in the calcium titanate perovskite $CaTiO_3$,” *Solid State Ionics*, vol. 180, no. 2–3, pp. 120–126, Mar. 2009.

[19] X. Liu and R. C. Liebermann, “X-ray powder diffraction study of $CaTiO_3$ perovskite at high temperatures,” *Phys. Chem. Miner. 1993 203*, vol. 20, no. 3, pp. 171–175, Aug. 1993.

[20] E. R. Vance, M. L. Carter, B. D. Begg, R. A. Day, and S. H. F. Leung, “Solid solubilities of Pu, U, Hf and Gd in candidate ceramic phases for actinide waste immobilisation,” *Mater. Res. Soc. Symp. - Proc.*, vol. 608, pp. 431–436, 2000.

[21] K. L. Smith, N. J. Zaluzec, and G. R. Lumpkin, “In situ studies of ion irradiated zirconolite, pyrochlore and perovskite,” *J. Nucl. Mater.*, vol. 250, no. 1, pp. 36–52, Nov. 1997.

[22] A. Meldrum, L. Boatner, W. Weber, and R. Ewing, “Amorphization and recrystallization of the ABO_3 oxides,” *J. Nucl. Mater.*, vol. 300, no. 2–3, pp. 242–254, Feb. 2002.

[23] W. Sinclair and A. E. Ringwood, “Alpha-recoil damage in natural zirconolite and perovskite,” *Geochem. J.*, vol. 15, no. 5, pp. 229–243, 1981.

[24] G. R. Lumpkin, M. Colella, K. L. Smith, R. H. Mitchell, and A. O. Larsen, “Chemical Composition, Geochemical Alteration, and Radiation Damage Effects in Natural Perovskite,” *MRS Proc.*, vol. 506, p. 207, 1997.

[25] M. C. Stennett, C. L. Freeman, A. S. Gandy, and N. C. Hyatt, “Crystal structure and non-stoichiometry of cerium brannerite: $Ce_{0.975}Ti_2O_{5.95}$,” *J. Solid State Chem.*, vol. 192, pp. 172–178, Aug. 2012.

[26] J. T. Szymanski and J. D. Scott, “A crystal-structure refinement of synthetic brannerite, UTi_2O_6, and its bearing on rate of alkaline-carbonate leaching of brannerite in ore,” *Can. Mineral.*, vol. 20, no. 2, pp. 271–279, 1982.

[27] E. R. Vance, J. N. Watson, M. Carter, R. A. Day, and B. D. Begg, “Crystal Chemistry and Stabilization in Air of Brannerite, UTi_2O_6,” *J. Am. Ceram. Soc.*, vol. 84, pp. 141–144, Dec. 2004.

[28] D. J. Bailey, M. C. Stennett, B. Ravel, D. Grolimund, and N. C. Hyatt, “Synthesis and characterisation of brannerite compositions $(U_{0.9}Ce_{0.1})_{1-x}M_xTi_2O_6$ (M = Gd^{3+}, Ca2+) for the immobilisation of MOX residues,” *RSC Adv.*, vol. 8, no. 4, pp. 2092–2099, 2018.

[29] G. R. Lumpkin, S. H. F. Leung, and J. Ferenczy, “Chemistry, microstructure, and alpha decay damage of natural brannerite,” *Chem. Geol.*, vol. 291, pp. 55–68, Jan. 2012.

[30] G. R. Lumpkin, “Alpha-decay damage and aqueous durability of actinide host phases in natural systems,” *J. Nucl. Mater.*, vol. 289, no. 1–2, pp. 136–166, Feb. 2001.

[31] S. M. Thornber *et al.*, “A preliminary validation study of PuO_2 incorporation into zirconolite glass-ceramics,” *MRS Adv.*, vol. 3, no. 20, pp. 1065–1071, 2018.

[32] M. R. Gilbert, “Molten salt synthesis of titanate pyrochlore waste-forms,” *Ceram. Int.*, vol. 42, no. 4, pp. 5263–5270, Mar. 2016.

[33] B. M. Gatehouse, I. E. Grey, R. J. Hill, and H. J. Rossell, “Zirconolite, $CaZr_xTi_{3-x}O_7$; structure refinements for near-end-member compositions with x = 0.85 and 1.30,” *Acta Crystallogr. Sect. B*, vol. 37, no. 2, pp. 306–312, Feb. 1981.

[34] K. R. Whittle *et al.*, “Combined neutron and X-ray diffraction determination of disorder in doped zirconolite-2M,” *Am. Mineral.*, vol. 97, no. 2–3, pp. 291–298, Feb. 2012.

[35] J. Squire, E. R. Maddrell, N. C. Hyatt, and M. C. Stennett, “Influence of lubricants and attrition milling parameters on the quality of zirconolite ceramics, consolidated by hot isostatic pressing, for immobilization of plutonium,” *Int. J. Appl. Ceram. Technol.*, vol. 12, no. S2, pp. E92–E104, May 2014.

[36] E. R. Vance *et al.*, “Incorporation of Uranium in Zirconolite (CaZrTi2O7),” *J. Am. Ceram. Soc.*, vol. 85, no. 7, pp. 1853–1859, Jul. 2002.

[37] P. Pöml *et al.*, “The mechanism of the hydrothermal alteration of cerium- and plutonium-doped zirconolite,” *J. Nucl. Mater.*, vol. 410, no. 1–3, pp. 10–23, Mar. 2011.

[38] G. R. Lumpkin, K. P. Hart, P. J. McGlinn, T. E. Payne, R. Giere, and C. T. Williams, “Retention of actinides in natural pyrochlores and zirconolites,” *Radiochim. Acta*, pp. 469–474, 1994.

[39] R. C. Ewing and L. M. Wang, “Amorphization of zirconolite: alpha-decay event damage versus krypton ion irradiation,” *Nucl. Instruments Methods Phys. Res. Sect. B Beam Interact. with Mater. Atoms*, vol. 65, no. 1–4, pp. 319–323, Mar. 1992.

[40] K. L. Smith, N. J. Zaluzec, and G. R. Lumpkin, “The relative radiation resistance of zirconolite, pyrochlore and perovskite to 1.5 MeV Kr^{+1} ions,” *21. Symp. Sci. basis Nucl. waste Manag. Davos (Switzerland), 28 Sep - 3 Oct 1997*, Mar. 1997.

[41] F. G. Karioris, K. Appaji Gowda, L. Cartz, and J. C. Labbe, “Damage cross-sections of heavy ions in crystal structures,” *J. Nucl. Mater.*, vol. 108–109, no. C, pp. 748–750, Jul. 1982.

[42] W. J. Weber and N. J. Hess, “Ion beam modification of $Gd_2Ti_2O_7$,” *Nucl. Instruments Methods Phys. Res. Sect. B Beam Interact. with Mater. Atoms*, vol. 80–81, no. PART 2, pp. 1245–1248, Jan. 1993.

[43] T. J. White, R. C. Ewing, L. M. Wang, J. S. Forrester, and C. Montross, “Temperature dependence of amorphization for zirconolite and perovskite irradiated with 1 MeV krypton ions,” *Mater. Res. Soc. Symp. - Proc.*, vol. 353, no. 2, pp. 1413–1420, 1995.

[44] M. A. A. Subramanian, G. Aravamudan, and G. V. V. Subba Rao, “Oxide pyrochlores — A review,” *Prog. Solid State Chem.*, vol. 15, no. 2, pp. 55–143, Jan. 1983.

[45] S. Park *et al.*, “Response of $Gd_2Ti_2O_7$ and $La_2Ti_2O_7$ to swift-heavy ion irradiation and annealing,” *Acta Mater.*, vol. 93, pp. 1–11, Jul. 2015.

[46] U. Balachandran and N. G. Eror, “X-ray diffraction and vibrational-spectroscopy study of the structure of $La_2Ti_2O_7$,” *Mater. Res.*, vol. 4, no. 6, pp. 1525–1528, 1989.

[47] F. X. Zhang *et al.*, “Structural change of layered perovskite $La_2Ti_2O_7$ at high pressures,” *J. Solid State Chem.*, vol. 180, no. 2, pp. 571–576, Feb. 2007.

[48] S. C. Finkeldei, “Pyrochlore as nuclear waste form Actinide uptake and chemical stability,” 2015.

[49] R. C. Ewing, W. J. Weber, and J. Lian, “Nuclear waste disposal—pyrochlore ($A_2B_2O_7$): Nuclear waste form for the immobilization of plutonium and ‘minor’ actinides,” *J. Appl. Phys.*, vol. 95, no. 11, pp. 5949–5971, Jun. 2004.

[50] J. Lian *et al.*, “Radiation-induced amorphization of rare-earth titanate pyrochlores,” *Phys. Rev. B*, vol. 68, no. 13, p. 134107, Oct. 2003.

[51] J. Lian, L. Wang, J. Chen, R. Ewing, and K. V. G. Kutty, *Heavy Ion Irradiation of Zirconate Pyrochlores*, vol. 713. 2002.

[52] G. R. Lumpkin and R. C. Ewing, “Alpha-Decay Damage in Minerals of the Pyrochlore Group,” *Phys Chem Miner.*, vol. 6, pp. 2–20, 1988.

[53] F. X. Zhang, J. W. Wang, M. Lang, J. M. Zhang, and R. C. Ewing, “Pressure-induced structural transformations in lanthanide titanates: La_2TiO_5 and Nd_2TiO_5,” *J. Solid State Chem.*, vol. 183, no. 11, pp. 2636–2643, Nov. 2010.

[54] K. R. Whittle, M. G. Blackford, R. D. Aughterson, G. R. Lumpkin, and N. J. Zaluzec, “Ion irradiation of novel yttrium/ytterbium-based pyrochlores: The effect of disorder,” *Acta Mater.*, vol. 59, no. 20, pp. 7530–7537, Dec. 2011.

[55] S. Park *et al.*, “A_2TiO_5 (A = Dy, Gd, Er, Yb) at High Pressure,” *Inorg. Chem.*, vol. 57, no. 4, pp. 2269–2277, Feb. 2018.

[56] Yu. F. Shepelev and M. A. Petrova, “Crystal Structures of Ln_2TiO_5 (Ln = Gd, Dy) Polymorphs,” *Inorg. Mater.*, vol. 44, no. 12, pp. 1354–1361, 2008.

[57] S. Hayun and A. Navrotsky, “Formation enthalpies and heat capacities of rear earth titanates: RE_2TiO_5 (RE=La, Nd and Gd),” *J. Solid State Chem.*, vol. 187, pp. 70–74, Mar. 2012.

[58] J. Zhang, F. Zhang, M. Lang, F. Lu, J. Lian, and R. C. Ewing, “Ion-irradiation-induced structural transitions in orthorhombic Ln2TiO5,” *Acta Mater.*, vol. 61, no. 11, pp. 4191–4199, Jun. 2013.

[59] R. D. Aughterson *et al.*, “Crystal structures of orthorhombic, hexagonal, and cubic compounds of the $Sm_{(x)}Yb_{(2-x)}TiO5$ series,” *J. Solid State Chem.*, vol. 213, pp. 182–192, May 2014.

[60] R. D. Aughterson *et al.*, “Ion-irradiation resistance of the orthorhombic Ln_2TiO_5 (Ln = La, Pr, Nd, Sm, Eu, Gd, Tb and Dy) series,” *J. Nucl. Mater.*, vol. 467, pp. 683–691, 2015.

[61] R. D. Aughterson, G. R. Lumpkin, K. L. Smith, and J. M. Cairney, “Novel complex ceramic oxides, Ln_2TiO_5 (Ln = La, Sm, Gd, Tb, Dy, Ho, Er, and Yb), for polyphase nuclear waste-forms,” *J. Am. Ceram. Soc.*, vol. 103, pp. 5536–5545, Jun. 2020.

[62] R. D. Aughterson, G. R. Lumpkin, K. L. Smith, G. J. Thorogood, and K. R. Whittle, “Synthesis and Characterisation of Ln_2TiO_5 Compounds,” *MRS Proc.*, vol. 1107, p. 365, Jan. 2008.

[63] R. D. Aughterson *et al.*, “The ion-irradiation tolerance of the pyrochlore to fluorite $Ho_{(x)}Yb_{(2-x)}TiO_5$ and Er_2TiO_5 compounds: A TEM comparative study using both in-situ and bulk ex-situ irradiation approaches,” *J. Nucl. Mater.*, vol. 507, pp. 316–326, Aug. 2018.

[64] R. D. Aughterson, N. J. Zaluzec, and G. R. Lumpkin, “Synthesis and ion-irradiation tolerance of the Dy_2TiO_5 polymorphs,” *Acta Mater.*, vol. 204, p. 116518, Feb. 2021.

[65] G. C. Lau, T. M. McQueen, Q. Huang, H. W. Zandbergen, and R. J. Cava, “Long- and short-range order in stuffed titanate pyrochlores,” *J. Solid State Chem.*, vol. 181, no. 1, pp. 45–50, Jan. 2008.

[66] V. D. Risovany, A. V. Zakharov, E. M. Muraleva, V. M. Kosenkov, and R. N. Latypov, “Dysprosium hafnate as absorbing material for control rods,” *J. Nucl. Mater.*, vol. 355, no. 1–3, pp. 163–170, Sep. 2006.

[67] H. S. Kim, C. Y. Joung, B. H. Lee, S. H. Kim, and D. S. Sohn, “Characteristics of $Gd_xM_yO_z$ (M=Ti, Zr or Al) as a burnable absorber,” *J. Nucl. Mater.*, vol. 372, no. 2–3, pp. 340–349, Jan. 2008.

[68] T.-M. Pan, M.-D. Huang, and C.-W. Lin, “Thin Sm_2TiO_5 Film Electrolyte–Insulator–Semiconductor for pH Detection and Urea Biosensing,” *J. Electrochem. Soc.*, vol. 157, no. 8, p. J275, Aug. 2010.

[69] C.-H. Kao, H. Chen, and S. P. Lin, “The Comparison of the High-k Sm_2O_3 and Sm_2TiO_5 Dielectrics Deposited on the Polycrystalline Silicon,” *Electrochem. Solid-State Lett.*, vol. 14, no. 2, p. G9, 2011.

[70] J. C. Pramudita, R. Aughterson, W. M. Dose, S. W. Donne, H. E. A. Brand, and N. Sharma, “Using in situ synchrotron x-ray diffraction to study lithium- and sodium-ion batteries: A case study with an unconventional battery electrode (Gd_2TiO_5),” *J. Mater. Res.*, vol. 30, no. 3, pp. 381–389, 2015.

[71] J. Shamblin *et al.*, “Crystal structure and partial Ising-like magnetic ordering of orthorhombic Dy 2 TiO 5,” *Phys. Rev. B*, vol. 94, p. 24413, 2016.

[72] J. Shamblin *et al.*, “Structural and magnetic short-range order in fluorite Yb_2TiO_5,” *Phys. Rev. B*, vol. 96, p. 174418, 2017.

[73] G. C. Lau *et al.*, “Structural disorder and properties of the stuffed pyrochlore Ho_2 TiO_5,” *Phys. Rev. B*, vol. 76, no. 5, p. 054430, 2007.

[74] M. Guillen and E. F. Bertaut, “Determination de la structure de La_2TiO_5 aux rayus x et aux neutrons,” *C. R. Hebd. Seances Acad. Sci. B*, vol. 262, pp. 962–965, Jan. 1966.

[75] R. D. Aughterson, G. R. Lumpkin, G. J. Thorogood, Z. Zhang, B. Gault, and J. M. Cairney, “Crystal chemistry of the orthorhombic Ln_2TiO_5 compounds with Ln =La, Pr, Nd, Sm, Gd, Tb and Dy,” *J. Solid State Chem.*, vol. 227, pp. 60–67, Jul. 2015.

[76] A. V. Shlyakhtina *et al.*, “Neutron diffraction investigation of the evolution of the crystal structure of oxygen-conducting solid solutions $(Yb_{1-x}Ca_x)_2Ti_2O_7$ (x = 0, 0.05, 0.10),” *Crystallogr. Reports 2009 541*, vol. 54, no. 1, pp. 25–30, Feb. 2009.

[77] B. G. Mullens *et al.*, “Average and local ordering of $Yb_2(Ti_{2-x}Yb_x)O_{7-(x/2)}$ ‘stuffed’ pyrochlores: The development of a robust structural model,” *J. Solid State Chem.*, vol. 302, p. 122412, Oct. 2021.

[78] A. V. Shlyakhtina, D. A. Belov, O. K. Karyagina, and L. G. Shcherbakova, “Ordering processes in Ln_2TiO_5 (Ln = Dy-Lu): The role of thermal history,” *J. Alloys Compd.*, vol. 479, no. 1–2, pp. 6–10, 2009.

[79] P. Linus, “The nature of the chemical bond and the structure of molecules and crystals; an introduction to modern structural chemistry", Cornel University Press, pp. 543 – 562, 1960

[80] J. George *et al.*, "The Limited Predictive Power of Pauling's Rules", *Angew. Chem. Int*., vol. 59, pp. 7569, 2020

[81] A. A. Sharma *et al.*, "RDF analysis, positron annihilation and Raman spectroscopy of $xTiO_2$–(60−x)SiO_2–40Na_2O non-linear optical glasses: III. Non-bridging oxygen bonds tracing and structure analysis", *J. Non. Cryst. Sol*., vol. 353, pp. 28, 2007

[82] R. C. Ewing, W. J. Webert, and F. W. Clinard, "Radiation Effects in Nuclear Waste Forms for High-Level Radioactive Waste," *Prog. Nucl. Energy*, vol. 29, no. 2, pp. 63–121, 1995.

[83] W. Weber *et al.*, "Radiation Effects in Crystalline Ceramics for the Immobilization of High-Level Nuclear Waste Plutonium," *J. Mater. Res.*, vol. 13, no. 6, pp. 1434–1484, Jun. 1998.

[84] V. Dubinko, "New principles of radiation damage and recovery based on the radiation induced emission of Schottky defects," *arXiv Prepr. cond-mat/0212154*, Dec. 2002.

[85] R. D. Aughterson *et al.*, "Ion-irradiation resistance of the orthorhombic Ln_2TiO_5 (Ln = La, Pr, Nd, Sm, Eu, Gd, Tb and Dy) series," *J. Nucl. Mater.*, vol. 467, pp. 683–691, Dec. 2015.

[86] R. D. Aughterson, G. R. Lumpkin, K. L. Smith, Z. Zhang, N. Sharma, and J. M. Cairney, "The crystal structures and corresponding ion-irradiation response for the $Tb_{(x)}Yb_{(2-x)}TiO_5$ series," *Ceram. Int.*, vol. 44, no. 1, pp. 511–519, Jan. 2018.

[87] S. Park *et al.*, "Swift-heavy ion irradiation response and annealing behavior of A_2TiO_5 (A = Nd, Gd, and Yb)," *J. Solid State Chem.*, vol. 258, pp. 108–116, 2018.

[88] R. D. Aughterson *et al.*, "The influence of crystal structure on ion-irradiation tolerance in the $Sm_{(x)}Yb_{(2-x)}$TiO5 series," *J. Nucl. Mater.*, vol. 471, pp. 17–24, Apr. 2016.

[89] A. T. Mottat and D. R. Olander, "Theory of electron-irradiation-induced amorphization," *Acta Met. mater*, vol. 38, no. 11, pp. 2175–2185, 1990.

[90] W. J. Weber, "Radiation Damage in a Rare-Earth Silicate With the Apatite Structure," *J. Am. Ceram. Soc.*, vol. 65, no. 11, pp. 544–548, Nov. 1982.

[91] S. Ellsworth, A. Navrotsky, and R. C. Ewing, "Energetics of radiation damage in natural zircon (ZrSiO4)," *Phys. Chem. Miner.*, vol. 21, no. 3, pp. 140–149, 1994.

[92] J. R. Dennis and E. B. Hale, "Crystalline to amorphous transformation in ion-implanted silicon: a composite model," *J. Appl. Phys.*, vol. 49, no. 3, pp. 1119–1127, Mar. 1978.

[93] W. J. Weber, “Models and mechanisms of irradiation-induced amorphization in ceramics,” *Nucl. Instruments Methods Phys. Res. Sect. B Beam Interact. with Mater. Atoms*, vol. 166–167, pp. 98–106, May 2000.

[94] W. Weber, “Models and mechanisms of irradiation-induced amorphization in ceramics,” *Nucl. Instruments Methods Phys. Res. Sect. B Beam Interact. with Mater. Atoms*, vol. 166–167, pp. 98–106, May 2000.

[95] A. C. D. and G. J. Dienes, “Point defects in metals,” *Acta Crystallogr.*, vol. 19, no. 3, pp. 490–490, Sep. 1965.

[96] W. Weber, J. W. Wald, and H. Matzke, “Effects of self-radiation damage in Cm-doped $Gd_2Ti_2O_7$ and $CaZrTi_2O_7$,” *J. Nucl. Mater.*, vol. 138, pp. 196–209, Apr. 1986.

[97] J. Lian, L. M. Wang, K. Sun, and R. C. Ewing, “In situ TEM of radiation effects in complex ceramics,” *Microsc. Res. Tech.*, vol. 72, no. 3, pp. 165–181, Mar. 2009.

[98] D. P. P. Reid *et al.*, “The structure of ion beam amorphised zirconolite studied by grazing angle X-ray absorption spectroscopy,” *Nucl. Instruments Methods Phys. Res. Sect. B Beam Interact. with Mater. Atoms*, vol. 268, no. 11–12, pp. 1847–1852, Jun. 2010.

[99] S. Lawson *et al.*, “Resistance to amorphisation in $Ca_{1-x}La_{2x/3}TiO_3$ perovskites – a bulk ion-irradiation study”, Ac. Mat., vol. 180, pp. 180 – 188, Nov., 2019

[100] M. Stennett *et al.*, “Heavy ion implantation combined with grazing incidence X-ray absorption spectroscopy (GIXAS): A new methodology for the characterisation of radiation damage in nuclear ceramics,” *MRS Proc.*, vol. 1193, p. 67, Jan. 2011.

[101] S. J. Zinkle and L. L. Snead, “Opportunities and limitations for ion beams in radiation effects studies: Bridging critical gaps between charged particle and neutron irradiations,” *Scr. Mater.*, vol. 143, pp. 154–160, Jan. 2018.

[102] D. Kanjilal, “Swift heavy ion-induced modification and track formation in materials,” *Curr. Sci.*, vol. 80, no. 12, pp. 1560–1566, 2001.

[103] F. Zeeshan, J. Hoszowska, L. Loperetti-Tornay, and J. C. Dousse, “In-house setup for laboratory-based x-ray absorption fine structure spectroscopy measurements,” *Rev. Sci. Instrum.*, vol. 90, no. 7, p. 073105, Jul. 2019.

[104] L. M. Mottram *et al.*, "A Feasibility Investigation of Laboratory Based X-ray Absorption Spectroscopy in Support of Nuclear Waste Management," *MRS Adv.*, vol. 5, no. 1–2, pp. 27–35, Jan. 2020.

[105] G. T. Seidler *et al.*, "A laboratory-based hard x-ray monochromator for high-resolution x-ray emission spectroscopy and x-ray absorption near edge structure measurements," *Rev. Sci. Instrum.*, vol. 85, no. 11, p. 113906, Nov. 2014.

[106] A. Iglesias-Juez, G. L. Chiarello, G. S. Patience, and M. O. Guerrero-Pérez, "Experimental methods in chemical engineering: X-ray absorption spectroscopy—XAS, XANES, EXAFS," *Can. J. Chem. Eng.*, vol. 100, no. 1, pp. 3–22, Jan. 2022.

[107] D. M. Sherman, C. L. Peacock, and C. G. Hubbard, "Surface complexation of U(VI) on goethite (α-FeOOH)," *Geochim. Cosmochim. Acta*, vol. 72, no. 2, pp. 298–310, Jan. 2008.

[108] L. Newsome, K. Morris, D. Trivedi, A. Bewsher, and J. R. Lloyd, "Biostimulation by Glycerol Phosphate to Precipitate Recalcitrant Uranium(IV) Phosphate," *Environ. Sci. Technol.*, vol. 49, no. 18, pp. 11070–11078, Sep. 2015.

[109] J. R. Bargar *et al.*, "Uranium redox transition pathways in acetate-amended sediments," *Proc. Natl. Acad. Sci. U. S. A.*, vol. 110, no. 12, pp. 4506–4511, Mar. 2013.

[110] A. Bourchy *et al.*, "The evolution of hydrated lime-based cementitious waste forms during leach testing leading to enhanced technetium retention," *J. Hazard. Mater.*, vol. 430, p. 128507, May 2022.

[111] A. S. Yorkshire *et al.*, "Spectroscopic evaluation of UVI-cement mineral interactions: Ettringite and hydro-talcite," *J. Synchrotron Radiat.*, vol. 29, no. 1, pp. 89–102, Jan. 2022.

[112] A. M. Scheidegger *et al.*, "The use of (micro)-X-ray absorption spectroscopy in cement research," *Waste Manag.*, vol. 26, no. 7, pp. 699–705, Jan. 2006.

[113] L. R. Blackburn *et al.*, "Influence of accessory phases and surrogate type on accelerated leaching of zirconolite wasteforms," *npj Mater. Degrad. 2021 51*, vol. 5, no. 1, pp. 1–11, May 2021.

[114] A. Y. Romanchuk, I. E. Vlasova, and S. N. Kalmykov, "Speciation of Uranium and Plutonium From Nuclear Legacy Sites to the Environment: A Mini Review," *Front. Chem.*, vol. 8, p. 630, Aug. 2020.

[115] S. T. Barlow *et al.*, "Thermal treatment of nuclear fuel-containing Magnox sludge radioactive waste," *J. Nucl. Mater.*, vol. 552, p. 152965, Aug. 2021.

[116] A. R. Mason, F. Y. Tocino, M. C. Stennett, and N. C. Hyatt, "Molten salt synthesis of Ce doped zirconolite for the immobilisation of pyroprocessing wastes and separated plutonium," *Ceram. Int.*, vol. 46, no. 18, pp. 29080–29089, Dec. 2020.

[117] F. Farges, "Coordination of Ti^{4+} in silicate glasses: A high-resolution XANES spectroscopy study at the Ti Kedge," *Am. Mineral.*, vol. 82, pp. 36–43, 1997.

[118] T. Yamamoto, "Assignment of pre-edge peaks in K-edge x-ray absorption spectra of 3d transition metal compounds: electric dipole or quadrupole?," *X-Ray Spectrom.*, vol. 37, no. 6, pp. 572–584, Nov. 2008.

[119] D. J. Bailey, M. C. Stennett, B. Ravel, D. E. Crean, and N. C. Hyatt, "A synchrotron X-ray spectroscopy study of titanium co-ordination in explosive melt glass derived from the trinity nuclear test," *RSC Adv.*, vol. 9, no. 23, pp. 12921–12927, Apr. 2019.

[120] L. M. Mottram, M. C. Stennett, S. K. Sun, and N. C. Hyatt, "Laboratory Based X-ray Absorption Spectroscopy of Iron Phosphate Glasses for Radioactive Waste Immobilisation: A Preliminary Investigation.," *IOP Conf. Ser. Mater. Sci. Eng.*, vol. 818, no. 1, p. 012020, Apr. 2020.

[121] K. Joseph, K. Jolley, and R. Smith, "Iron phosphate glasses: Structure determination and displacement energy thresholds, using a fixed charge potential model," *J. Non. Cryst. Solids*, vol. 411, pp. 137–144, Mar. 2015.

[122] G. K. Marasinghe *et al.*, "Structural features of iron phosphate glasses," *J. Non. Cryst. Solids*, vol. 222, pp. 144–152, Dec. 1997.

[123] S. Finkeldei *et al.*, "Insights into the fabrication and structure of plutonium pyrochlores," *J. Mater. Chem. A*, vol. 8, no. 5, pp. 2387–2403, Feb. 2020.

[124] M. A. Kim, J. H. Song, W. Um, N. Hyatt, S. K. Sun, and J. Heo, "Structure analysis of vitusite glass–ceramic waste forms using extended X-ray absorption fine structures," *Ceram. Int.*, vol. 43, no. 5, pp. 4687–4691, Apr. 2017.

[125] G. Calas, M. Le Grand, L. Galoisy, and D. Ghaleb, "Structural role of molybdenum in nuclear glasses: an EXAFS study," *J. Nucl. Mater.*, vol. 322, no. 1, pp. 15–20, Oct. 2003.

[126] F. Farges, G. E. Brown, and J. J. Rehr, “Coordination chemistry of Ti(IV) in silicate glasses and melts: I. XAFS study of titanium coordination in oxide model compounds,” *Geochim. Cosmochim. Acta*, vol. 60, no. 16, pp. 3023–3038, Aug. 1996.

[127] F. Farges, “Fivefold-coordinated Ti^{4+} in metamict zirconolite and titanite: A new occurrence shown by Ti K-edge XANES spectroscopy,” *Am. Mineral.*, vol. 82, no. 1–2, pp. 44–50, Feb. 1997.

[128] M. C. Stennett, N. Peng, E. R. Maddrell, B. Ravel, and N. C. Hyatt, “Probing radiation damage in ceramic wasteforms using X-ray absorption spectroscopy,” *Diam. ’10 Conf. Proceedings; Decommissioning, Immobil. Manag. Nucl. Waste Dispos.*, 2010.

[129] E. R. Aluri and A. P. Grosvenor, “An X-ray absorption spectroscopic study of the effect of bond covalency on the electronic structure of $Gd_2Ti_{2-x}Sn_xO_7$,” *Phys. Chem. Chem. Phys.*, vol. 15, no. 25, pp. 10477–10486, Jun. 2013.

[130] E. R. Aluri, J. R. Hayes, J. D. S. Walker, and A. P. Grosvenor, “Investigation of the structural stability of ion-implanted $Gd_2Ti_{2-x}Sn_xO_7$ pyrochlore-type oxides by glancing angle X-ray absorption spectroscopy,” *J. Phys. Chem. C*, vol. 118, no. 15, pp. 7910–7922, Apr. 2014.

[131] J. Lian, K. B. Helean, B. J. Kennedy, L. M. Wang, A. Navrotsky, and R. C. Ewing, “Effect of Structure and Thermodynamic Stability on the Response of Lanthanide Stannate Pyrochlores to Ion Beam Irradiation,” *J. Phys. Chem. B*, vol. 110, no. 5, pp. 2343–2350, Feb. 2006.

[132] G. Sattonnay *et al.*, “Phase transformations induced by high electronic excitation in ion-irradiated $Gd_2(Zr_xTi_{1-x})_2O_7$ pyrochlores,” *J. Appl. Phys.*, vol. 108, no. 10, p. 103512, Nov. 2010.

[133] R. B. Greegor, F. W. Lytle, R. J. Livak, and F. W. Clinard, “X-ray spectroscopic investigation of Pu-substituted zirconolite,” *J. Nucl. Mater.*, vol. 152, no. 2–3, pp. 270–277, May 1988.

[134] G. R. Lumpkin *et al.*, “Alpha-recoil damage in zirconolite ($CaZrTi_2O_7$),” *J. Mater. Res.*, vol. 1, no. 4, pp. 564–576, 1986.

[135] C. L. Dube, · M C Stennett, · A Ananthanarayanan, · C David, · J G Shah, and · N C Hyatt, “Radiation stability study on cerium loaded iron phosphate glasses by ion irradiation method,” vol. 323, pp. 1381–1386, 2020.

[136] X. Fang, C. S. Ray, A. Moguš-Milanković, and D. E. Day, “Iron redox equilibrium, structure and properties of iron phosphate glasses,” *J. Non. Cryst. Solids*, vol. 283, no. 1–3, pp. 162–172, May 2001.

[137] S. L. M. Schroeder, G. D. Moggridge, R. M. Ormerod, T. Rayment, and R. M. Lambert, “What determines the probing depth of electron yield XAS?,” *Surf. Sci.*, vol. 324, no. 2–3, pp. L371–L377, Feb. 1995.

[138] A. S. Gandy, M. C. Stennett, C. Brigden, and N. C. Hyatt, “Ion Beam Irradiation Induced Structural Modifications in Iron Phosphate Glasses: A Model System for Understanding Radiation Damage in Nuclear Waste Glasses,” *MRS Online Proc. Libr.*, vol. 1757, no. January, pp. 65–70, 2015.

3. Experimental methods

3.1 Ceramic Synthesis

The following section describes the methodology used to synthesise the ceramic samples used in these studies, from initial batching and milling to consolidation and densification. Additionally, the underpinning scientific principles of the of the experimental methods are discussed to provide context and justification for the methodology.

3.1.1 Lanthanide surrogates

Development of nuclear wasteforms requires a significant use of inactive surrogates. Due to the radiotoxic nature of many actinides, inactive and chemically safe lanthanide oxides were used in these studies to simulate chemical behaviour of actinide elements in a ceramic system. The lanthanide series provides an excellent source of surrogates for many actinide elements due to similar nature of their possible valence states, ionic radii in a given coordination environment and electronic configuration [1]. The entire series of lanthanides (La – Lu, Y) was used in these studies, except Ce and Pm, the former due to the difficulty in achieving a single-phase product and the later due the radioactive nature of all its isotopes. All synthesised Ln_2TiO_5 (where Ln = La – Lu, Y) will be discussed to some extent in this thesis but only a representative sub-set of compositions was used for further study due to time and accessibility constraints. The choice of lanthanide was informed by the crystal structure formed (influenced by the size of ionic radii and thermal history) in addition to being representative of different ionic radius size differences that can form the same crystal structure (refer to Figure 2.8 in chapter 2). Furthermore, the use of Y, which is not a lanthanide but does exhibit very similar chemical and physical properties, was chosen because Y^{90} is a decay product of Sr^{90}. Sr^{90} is a common fission product of U^{235}, as such Y radionuclides will be present in spent fuel and other HLW produced as a product of nuclear fuel reprocessing.

3.1.2 Solid-state synthesis

3.1.2.1 Batching and milling

One of the most common and well tested means of ceramic fabrication is the use of solid-state synthesis. A relatively simple synthesis route, it has been shown to be widely applicable and reliable to achieve dense, single-phase ceramic products. In the studies presented in this thesis the majority of sample fabrication utilised the solid-state method. Reagent grade (typically > 99.9% purity) oxide precursors were typically dried at 180 ^{o}C overnight and particularly hygroscopic precursors such as Gd_2O_3 were dried at 800 ^{o}C overnight to drive off any surface moisture. Precursors were then batched into stoichiometric proportions, informed by batch calculations, to an accuracy of 0.0001

g. The precursor materials (totalling 5 g) were transferred into a SiAlON milling jar along with SiAlON milling media and a carrier fluid (typically isopropanol) to be homogenised and size reduced in a Fritsch Pulverisette 6 planetary ball mill for 15 minutes at 400 rotations per minute (RPM). Size reduction of the precursor particles increases the associated surface energy and leaves the morphology of the particles in an altered state, promoting greater reactivity and thus resulting improved thermal treatment of ceramic materials. Planetary ball mills operate by rotating a milling jar, secured non-concentrically on a so-called 'sun wheel', at high frequencies around a center. This rotational movement generated from the rotation of the milling jar about its own axis and the rotation of the sun wheel in an opposite direction. The resultant motion of milling media, driven by centrifugal and coriolis forces, cause highly energetic collisions transferring compressive and sheer forces to the precursor material [2]. This acts to reduce the size of the batched precursor material and alter the morphology of the powder particulates in addition to well homogenising the mixture.

After undergoing size reduction and homogenisation routines, samples were retrieved from the planetary mill and allowed to dry completely at 80 ^{o}C in an oven for 4 hours to evaporate any excess solvent. The resultant dried powder was sieved to break up any agglomerates prior to further processing. Loose powder batches were pressed into pellets under 3 tonnes of pressure in a hardened steel 10 mm diameter die and reacted between 1300 – 1600 ^{o}C, for 24 hours, to achieve the high thermal energies needed to mix particle reagents on the atomic level resulting in the desired composition. Phase purity was checked post-reaction through various analytical techniques such as X-ray Diffraction (XRD). If targeted composition or phase assemblage were not achieved, samples would undergo additional heat treatments, with intermittent grinding and mixing. This process was iterated until no improvement to the observed phase assemblage could be detected. A typical synthesis route is shown schematically in Figure 3.1.

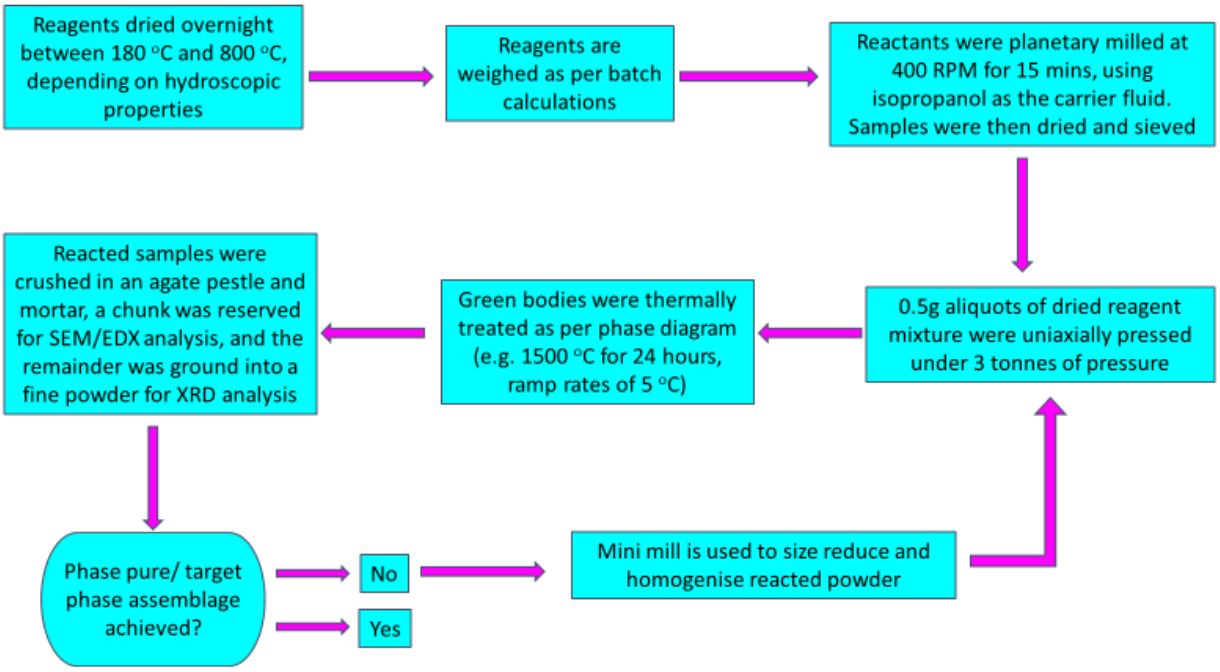

Figure 3.1: Flowchart of typical solid state synthesis route used throughout thesis.

3.1.2.2 Cold pressing and sintering

High density ceramics, a desirable property to be considered in wasteform design, can be achieved relatively simply through Cold Pressing and Sintering (CPS) of ceramic powders. This is a two-step process: the consolidation of calcined powders into green body pellets and the subsequent sintering at high temperatures and/or pressures. Green bodies are compacted precursors or reacted materials with roughly 35-50 % porosity [3], formed by uniaxially pressing precursor materials or reacted powders at 3 tonnes of pressure in a hardened steel 10 mm diameter die. The pressure exerted on the material reduces the volume of granular voids formed between loose collections of particles. Prior to the initial reaction of precursor material, it can be beneficial to form the unreacted powders into green bodies as this can aid the diffusion mechanics necessary for reaction by shortening diffusion paths, reducing the time necessary for a complete reaction to take place during sintering.

Sintering is the process by which ceramic material is densified into a single mass through the application of heat and/or pressure below the melting point of constituent materials, improving mechanical and microstructural properties. The driving force of sintering is a reduction in the total particle surface area achieved through atomic diffusion. This will result in two competing processes: densification and microstructure coarsening, the latter does not reduce porosity and as such does not increase density. The dominant behaviour can be influenced by the material's properties and processing conditions. As such it is important to consider particle size and morphology, sintering atmosphere, and applied pressures during fabrication. Six different mechanisms contribute to the

sintering of ceramic material and are related to the diffusional transport of matter along definite paths. A schematic can be seen in figure 3.2 for a three-particle system. Not all mechanisms contribute directly to densification. Surface diffusion, lattice diffusion and vapor transport (mechanism 1, 2 and 3 in Figure 3.2) from the particle surface to the neck (point of contact between grains) are non-densifying mechanisms and lead to neck growth without densification [4]. (bothThese mechanisms cannot be ignored, however, as they reduce the rate of densification. The most important mechanisms that contribute to densification are grain boundary diffusion and lattice diffusion from the grain boundary (Mechanisms 4 and 5 in Figure 3.2). Plastic flow, mechanism 6, is not typically a concern for non- metallic systems [4]. Chemical diffusion occurs due to the movement of an atom into within a from one lattice site to another. The energy needed for this process typically comes from thermal sources (such as a furnace). Lattice diffusion occurs by the movement of point defects through the bulk of the lattice. This process can occur more rapidly in areas of increased defects such as at grain boundaries of the surface of a material. Vapor transport is the process of evaporation and condensation of matter during heating processes. This can cause potentially unwanted neck growth and particle coarsening during solid state sintering of ceramics and metals and inhibit, or eliminate, densification [4].

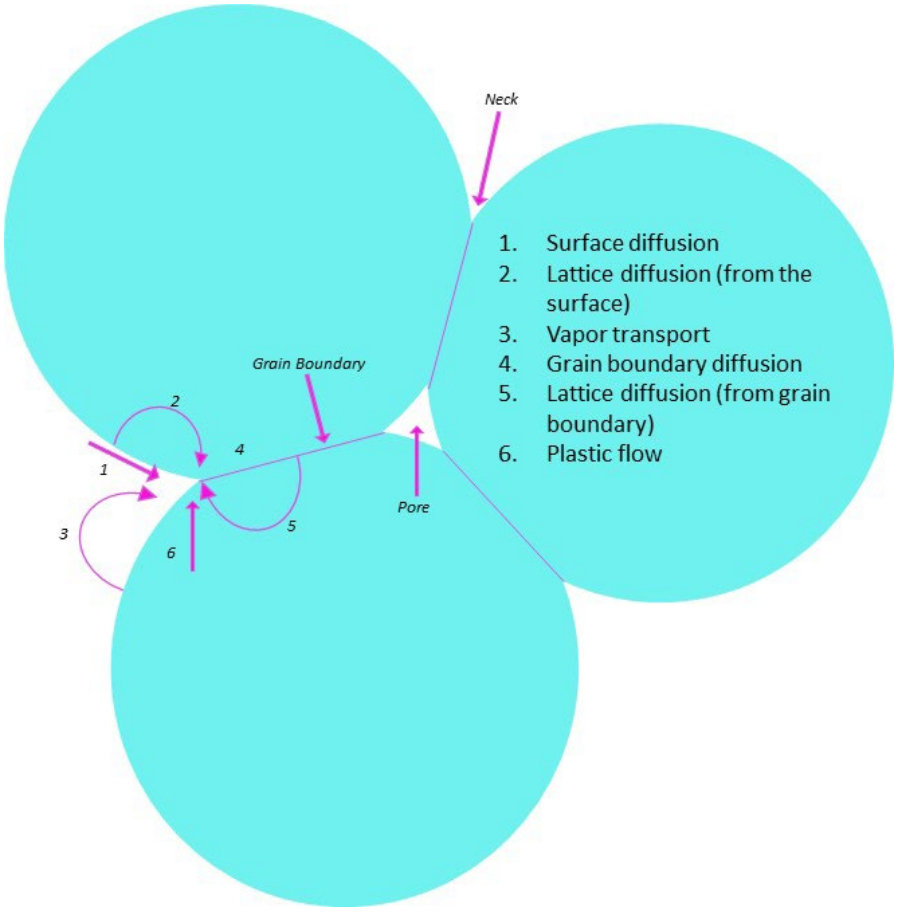

Figure 3.2: Schematic diagram showing the six mechanisms that contribute to the sintering process in an example three-particle system (Adapted from [4]).

3.1.3 Molten Salt synthesis

The feasibility of a Molten Salt (MS) synthesis route was examined for producing single phase Gd_2TiO_5 ceramics at lower reaction temperatures and reduced dwell durations when compared to a solid-state route. The MS method exploits a salt, or eutectic mixture of salts, to create a liquid medium to assist with the diffusion of reactants. This facilitates the production of homogenous products at lower temperatures over shorter durations by increasing the contact area of reactants and increasing mobility of reactant species dissolved into the liquid medium (in a SS route material mobility is of the order 10^{-18} cm^2 sec^{-1}, whereas in a MS route the mobility of species is typically in the range of 10^{-5} – 10^{-8} cm^2 sec^{-1}) [5]. Depending upon the relative dissolution rates of reactants, the particle growth mechanism is typically observed to be either a solution-precipitation or solution-dissolution mechanism, the latter of which is an effective means of controlling particle size and morphology [5].

Solution-precipitation occurs when the dissolution rates of reactants are comparable, both reactants dissolve into the molten salt and product phases precipitate out of the salt under a high degree of super-saturation. Solution-diffusion, also known as template-growth, occurs when the dissolution rate of one the reactants is significantly different from that of the other. The more readily soluble reactant dissolves into the salt medium and then diffuses onto the surface of the less soluble reactant and reacts. Once reactants are consumed the resulting product will have a near identical shape to the less soluble reactant. The molten salt method can also be an effective means to minimise the formation of agglomerates. The molten salt flux covers the surface of all reactants and prevents the formation of necks between particles. Agglomerates can lead to a heterogenous packing of green bodies and can lead to differential sintering when fired. Differential sintering is the occurrence of different contraction rates across the body and can lead to increased porosity and cracking.

The following is a brief description of the MS synthesis route used for the fabrication of ceramic compounds. Batching and milling of initial oxide reagents followed the same routine as a solid-state route. After reagents are intimately mixed and milled, a salt or eutectic mixture of salt is added (e.g. NaCl:KCl in a 1:1 mole ratio) in a 7:1 mole ratio of molten salt to ceramic precursor. Salt and precursor mixture are milled together, using a non-polar solvent, cyclohexane, as a carrier fluid, at low frequency to allow for even distribution of the salt flux but minimising any alterations to initial particle morphology of reagents. Salt-ceramic mixtures were dried and pressed into pellets following the same procedure used in a SS route. Reacted samples are then washed in ultrapure water to remove molten salt medium and the product collected via vacuum filtration.

3.1.4 Bulk density measurements

The densification of sintered pellets was measured using the Archimedes method. That was to ensure that the sintered ceramic pellets were as close to their theoretical densities as reasonably producible through typical CPS routes. Highly dense ceramics, wherein porosity has been significantly reduced, are necessary to achieve reliable results from bulk measurements techniques such as GAXRD and GAXAS analysis.

The Archimedes method of measuring density is based upon the principle of buoyancy, where any body immersed into a liquid will be reduced by an amount equal to the weight of the liquid volume displaced by the body. By measuring the weight of a sample in air, mm_1, and in water, mm_2, the density of the can be calculated thusly:

$$\rho_{pellet} = \rho_{water} \frac{m_1}{m_1 - m_2} \qquad \textbf{Equation 3.1}$$

where ρ_{pellet} is the sample density and ρ_{water} is the density of the water. These measurements were conducted using distilled water.

3.2 Solid-state characterisation

The following section describes the charatersation methods used in this study to determine the physical properties of the ceramic materials produced, including: the crystal structure, phase assemblage, microstructure and elemental composition.

3.2.1 X-ray diffraction

X-ray diffraction (XRD) has been one the key analytical techniques used in crystallography and materials science. Its principal application is used for the identification and quantification of phases present in crystalline materials. When highly energetic, charged, particles (i.e., electrons) interact with matter they lose energy. This lost energy is expressed as the emission of X-rays. X-rays are a form of electro-magnetic radiation and have wavelengths between 10^{-11} to 10^{-9} m. In a typical laboratory X-ray diffractometer, X-rays are produced in an X-ray tube by heating a tungsten filament cathode to cause the emission of electrons into a vacuum towards a water-cooled anode, accelerated by a high voltage power source. Interactions between the accelerated electrons and anode cause the emission of X-rays in all directions. The X-rays leave the X-ray tube *via* a window, made of elements with low atomic numbers so as to minimise loss of energy through scattering. The X-rays emitted in this manner fall into two categories, Bremsstrahlung (or braking) X-rays and characteristic X-rays. Bremsstrahlung radiation is the continuous spectrum of X-rays emitted by electrons that have been decelerated through collisions with another charged particle. The incident electrons will continue to lose energy in a series of collisions with the atoms that make-up the anode, emitting X-rays of varying wavelengths. Electrons that have sufficient energy can ionise a core electron, ejecting an electron from the inner orbital of a target atom, leaving the atom in an excited state. As the atom relaxes and fills the electron-hole a corresponding X-ray of energy equal to the difference between electron energy levels is emitted [6]. The wavelength of this X-ray is characteristic of the anode material. Characteristic X-rays are primarily used in XRD, though continuous X-rays are sometimes used, for example in the Lau method. A copper (Cu) anode was used throughout the work presented in this thesis. A Cu anode will produce X-rays of 1.5405 Å (*2p* → *1s* transition, Kα) and 1.3922 Å (*3p* → *1s* transition, Kβ). The two possible spin states of the *2p* electron actually causes the emission of both 1.5405 Å ($K\alpha_1$) and 1.5443 Å ($K\alpha_2$) wavelength X-rays.

The wavelength of monochromatic X-rays is of the same order as the typical internal lattice spacing in crystal structures. As such, incident X-rays will interact with a crystalline target and diffract, the interference patterns produced through diffraction are characteristic of a materials crystal structure, as indicated by Bragg's Law [6]. Bragg's Law relates the wavelength of an X-ray to the angle, θ, of the indent X-ray beam and the lattice spacing *d* of a crystalline structure. Consider two X-rays scattered from crystal planes separated by a spacing d. For the transmitted X-rays to be in phase with one another the additional distance, xyz, travelled by X-ray two must equal the wavelength, λ, of the

incident X-ray, or some integer n thereof. This is mathematically expressed in Equations 3.2 – 3.5 and graphically in Figure 3.3. When Bragg's law is satisfied incident X-rays are in phase and constructive interference results. When not satisfied, destructive interference occurs.

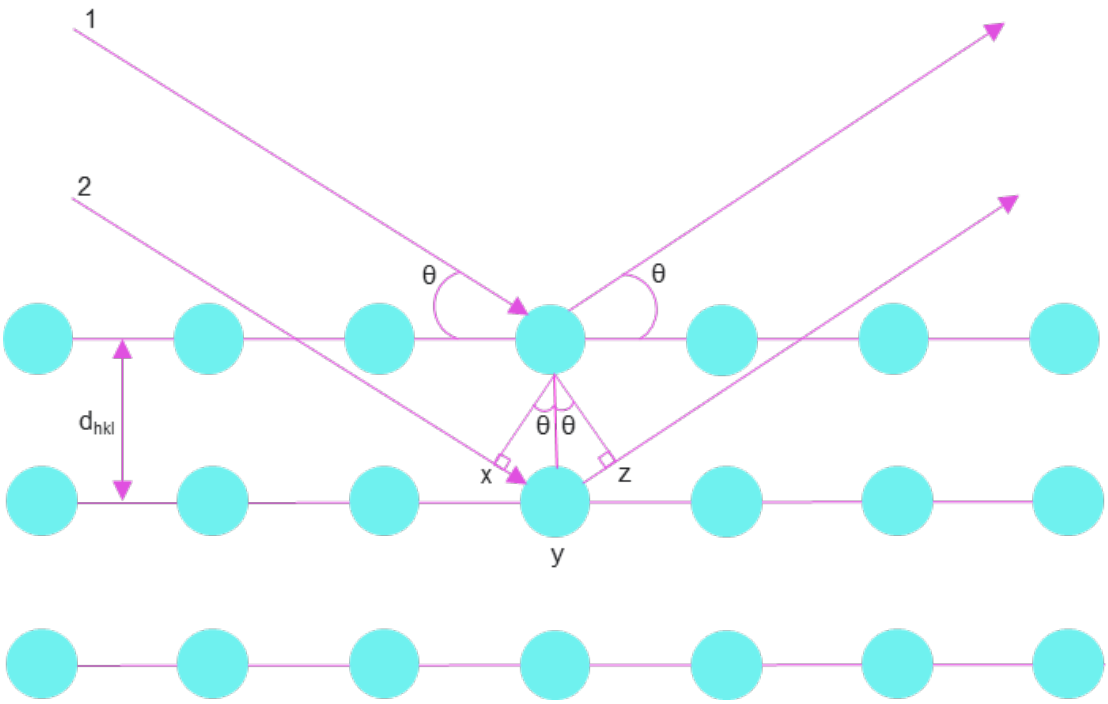

Figure 3.3: Diffraction of X-rays in a crystal lattice. Incoming and outgoing lines (1 and 2) indicate the path of diffracted X-rays by angle θ. The diffracted X-rays constructively interfere when the distance between paths differs by an integer number of wavelengths.

$$xy = yz = d\ sin\ (\theta)$$ **Equation 3.2**

$$xy + yz = 2d\ sin\ (\theta)$$
Equation 3.3

$$xyz = n\lambda$$ **Equation 3.4**

$$n\lambda = 2d\ sin\ (\theta)$$ **Equation 3.5**

The intensity of diffracted X-rays is collected by a detector, generally scintillation or gas-filled detectors, converting the X-rays into an electrical signal [6]. In X-ray diffractometers utilising a Bragg-Brentano parafocusing geometry the X-ray source is fixed, and the sample and detector are scanned through a range of angles, rotating around an axis perpendicular to the incident X-ray beam. The profile and position of peaks in each diffraction pattern are a consequence of various microstructural properties such as lattice defects and lattice parameters observed in the average long-range ordering of the crystal structure. An example of the XRD pattern for La_2TiO_5 and Gd_2TiO_5 is shown in Figure 3.4. Here it can be seen that both samples crystallise in a cubic *Fd-3m* symmetry but the relative peak position in 2θ changes due to difference in ionic radii of Yb^{3+} (0.985) and Lu^{3+} (0.977) This reflects the

changes in the relative lattice plane spacing between the two chemistries (lattice parameters). It should be noted that an amorphous material, wherein long-range order is absent, does not give rise to diffraction peaks but instead a continuous region of diffuse scattering is observed.

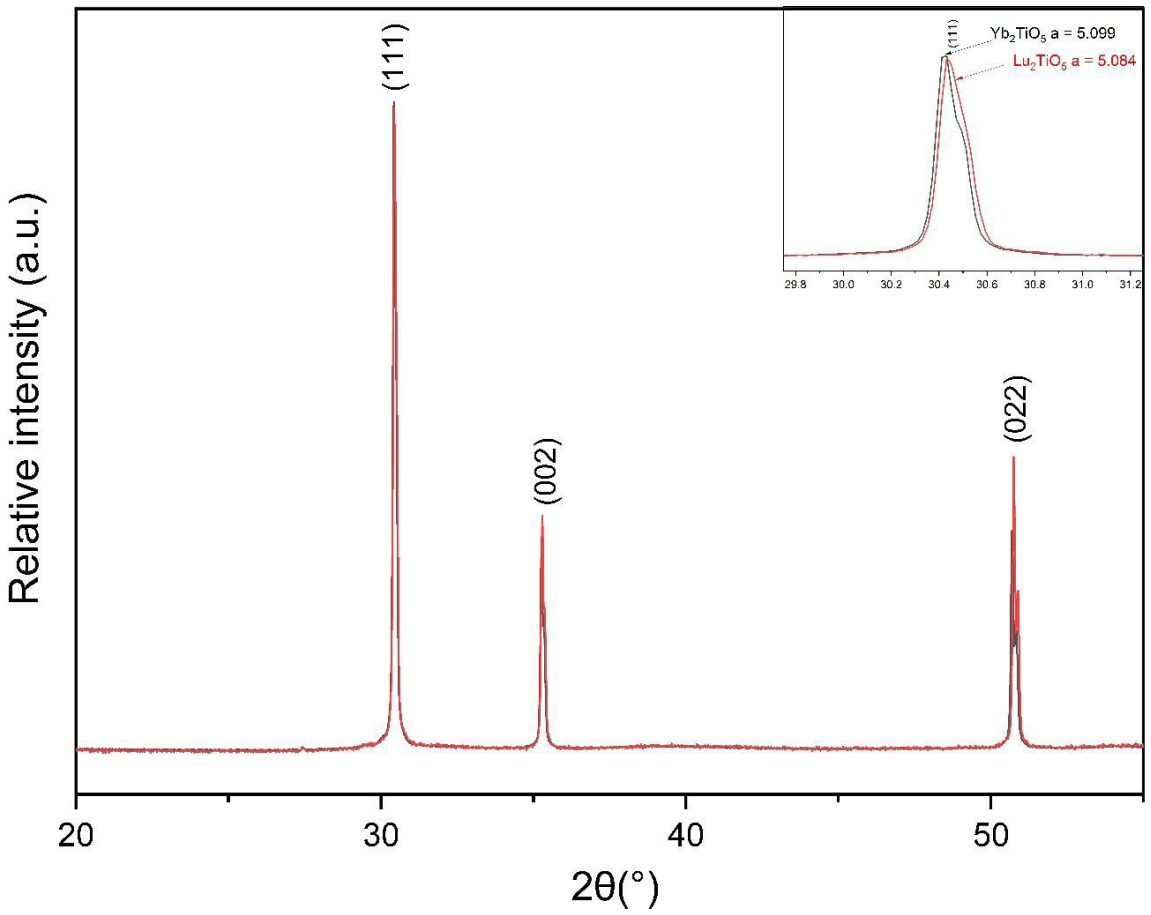

Figure 3.4: Example XRD pattern of Yb_2TiO_5 and Lu_2TiO_5 indexed in a *Fm-3m* space group. Inset shows the deviation in peak position as a result of increased lattice parameter, a (a=b=c)

XRD analysis of samples synthesised in this thesis were prepared by finely grinding ceramic powder in an agate pestle and mortar with isopropanol to reduce the size of crystallites. Once samples were dried, they were mounted in a zero-background holder. A glass slide, with a smooth surface, was pressed atop on the powder in the sample well to flatten the surface, limiting the effects of surface roughness and preferred orientation on the data. Routine diffraction analysis was collected on a Bruker D2 Phaser diffractometer, which operates in a Bragg Brentano geometry and utilises a Cu Kα X-ray source (λ = 1.5405 Å) with a 10 mA current and 30 kV accelerating voltage and a Lynxeye position sensitive detector. A Ni foil was used to filter out Cu Kβ radiation. Unless otherwise noted, data were collected with a step size of 0.02°, counting for 1.8 seconds per step detector over a range of $10^o \leq 2\theta \leq 70^o$.

3.2.2 Glancing-angle X-ray diffraction

The penetration depth of an X-ray is dependent upon the angle of incidence on a sample. Lowering this angle, and thereby reducing the penetration depth, allows for the study of surface layers of bulk samples. This is particularly useful for the study of materials irradiated by heavy-ion implantation where only the damaged surface region (around 100 - 700 nm) is of interest. Glancing-angle X-ray diffraction (GAXRD) makes use of this principle by using a small angle slightly greater than the critical angle of total reflectance of a material, such that X-rays propagate into the sample [7]. The penetration depth is dependent on the linear attenuation coefficient, μ, of the material which is defined as the fraction of attenuated X-rays in a beam per unit thickness of a material. The angle necessary to study a particular region can be given by:

$$\alpha_i = \frac{x}{3\varepsilon} \quad \textbf{Equation 3.6}$$

where α is the angle of incidence, x is the region depth and ε is the attenuation length (μ^{-1}). This value can be computed for a relevant absorption edge using the Hephaestus software [8]. The attenuation length is defined as the depth travelled before the intensity of the X-ray reaches e^{-1} (~40%) of its incident intensity. At 3ε the attenuation of incident X-rays is 95%.

A typical GAXRD geometry is shown in Figure 3.5. In the studies presented here a Philips PANalytical X'Pert3 diffractometer operating in glancing-angle parallel beam configuration with Cu Kα (λ = 1.5405 Å) operating in a Bragg-Brentano geometry was used. These experiments aided in identifying and characterising damaged regions of bulk samples, which was used to inform further XAS experiments making use of glancing angle setups. Incident angles used were 1°, 3° and 5° (see Figure 3.6 penetration depths of each sample with increasing incident angle and Table 3.1 for the corresponding penetration depths at these angles), scanning through a range of 20 – 40 2θ with a step size of 0.04° and a step time 20 s.

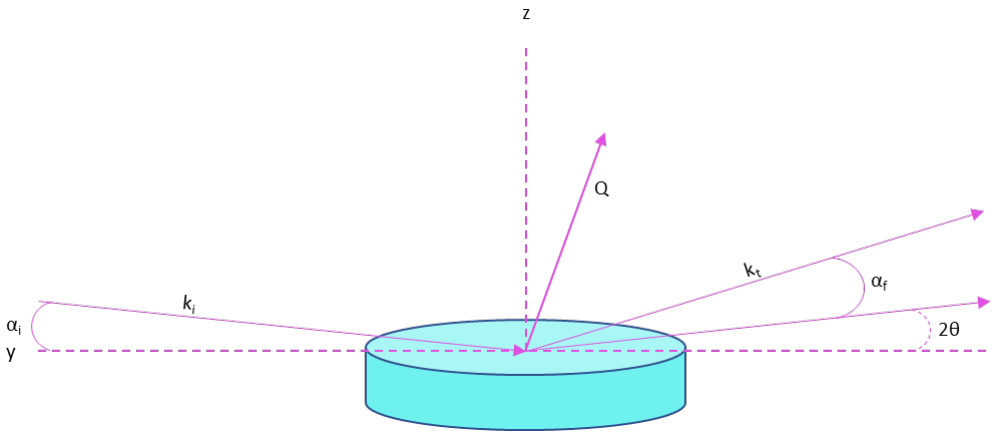

Figure 3.5: Schematic of the X-ray glancing angle diffraction geometry. The incident wave vector is denoted as k_i and diffracted wave vector by k_t, respectively; Q is the momentum transfer defined by the angle of incidence α_i, the transmitted angle α_t of the X-ray and in-plane angle 2θ. Adapted from [9].

Sample	Penetration Depth (nm)		
	1°	3°	5°
Gd2TiO5	87	235	498
Dy2TiO5	118	342	570
Yb2TiO5	171	437	780

Table 3.1: X-ray penetration depths for incident angles (1°, 3°, and 5° degrees) used in GAXRD measurements of Ln_2TiO_5 (Ln = Gd, Dy, Yb) ceramics.

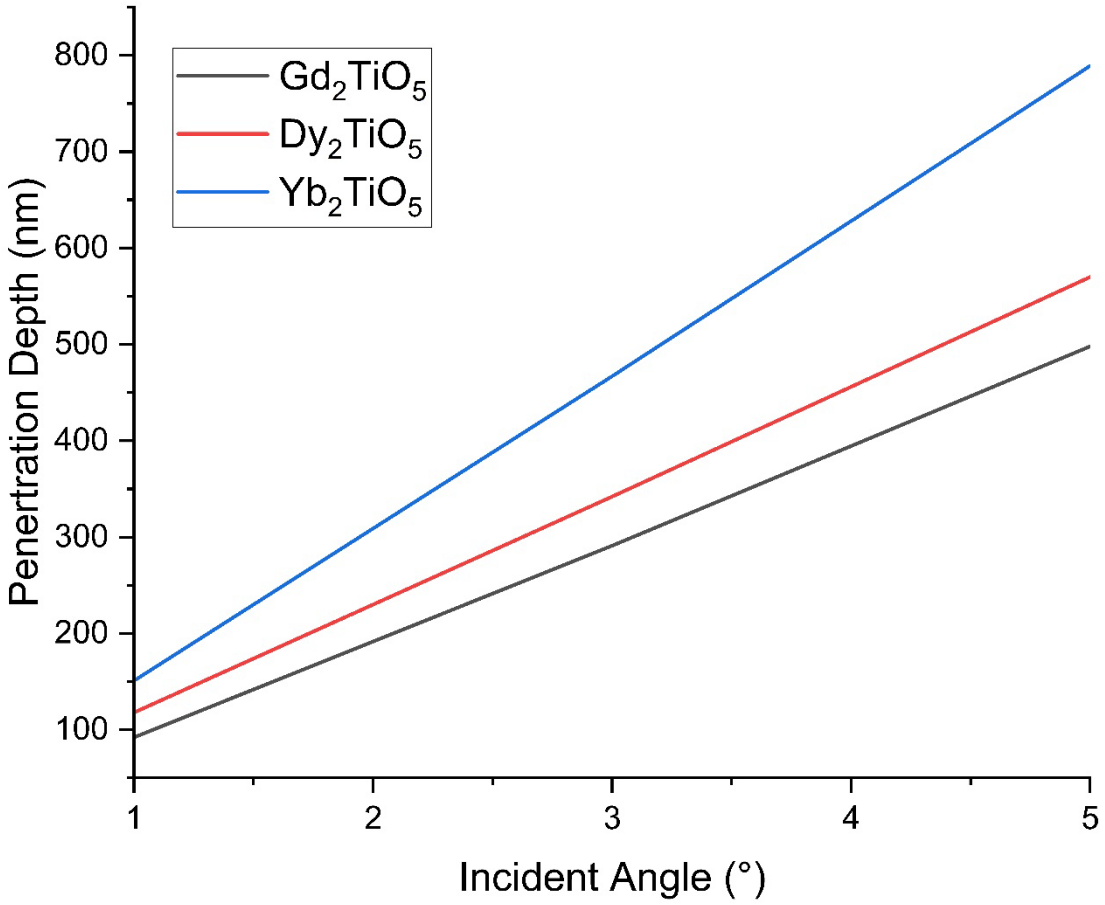

Figure 3.6: X-ray penetration depths with GAXRD incident angle for Gd_2TiO_5, Dy_2TiO_5 and Yb_2TiO_5.

3.2.3 Scanning electron microscopy and energy dispersive X-ray spectrometry (SEM-EDX)

Along with XRD, scanning electron microscopy is a fundamental technique of materials characterisation. Scanning electron microscopy is a technique that enables imaging of a materials surface at enhanced magnification compared to that of traditional optical microscopes. In combination with an energy dispersive X-ray spectrometer (EDX), a complementary technique which can be used to construct elemental distributions and collect semi-quantitative data regarding a sample's average elemental composition, a detailed account of a sample's surface topography, phase assemblage and phase distribution can be built.

Though optical microscopes have important applications for materials characterisation, the resolution achievable is limited due to the wavelengths associated with the visible spectrum. Electrons have wavelengths determined by the de Broglie principle, which postulates that any matter with a given momentum also has an associated wavelength. This implies that an electron with 1 eV of energy has a wavelength four orders of magnitude smaller than that of a corresponding photon with the same energy. This allows electron microscopes to achieve resolutions on the nano scale. An SEM operates by generating an electron beam, produced under vacuum at the top of a column by accelerating electrons produced by thermionic emission from a filament, often made from tungsten, or from a field emission gun (FEG) to a positively charged anode. The entire column must be under vacuum to prevent contamination of the electron source and other components in addition to aiding in the quality of data collection. Atoms or molecules that would otherwise be in the electron beams path would deflect the beam, reducing the resolution of an image. Electromagnetic lenses, condenser, and objective, control the path of the electron beam by adjusting the applied current and as such define the observed resolution [10]. A simplified schematic can be seen in Figure 3.6. A scanning coil is used to raster the beam across the surface of a sample. The penetration depth, *R*, of the electron beam is limited due to energy losses arising from elastic and inelastic scattering processes. *R* is a function of both the density of a sample and accelerating voltage and is typically within the range of 10 nm – 10 µm. Surface interactions between the beam and sample generate different types of electrons and X-rays which, once collected by a detector, can be translated into an image displayed onto a screen.

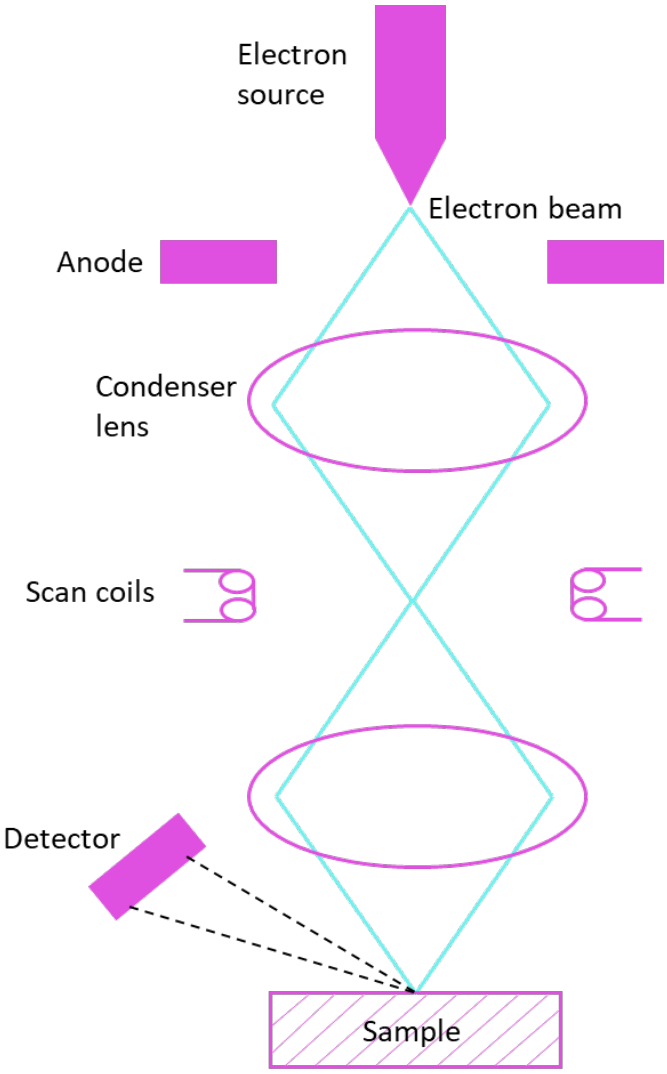

Figure 3.6: Schematic diagram of the basic components of a scanning electron microscope. Adapted from [10].

In addition to X-rays, the electrons used for imaging and compositional analysis are secondary electrons (SE) and backscattering electrons (BSE) (Figure 3.7 demonstrates the origin of each over a penetration depth, R [10]. SE have relatively little energy (typically 2 – 5 eV) and originate from inelastic collisions with surface atoms and the incident electron beam, wherein the work function of low energy electrons is overcame, as well as from backscattered electrons which are returning towards the surface. The yield of SE's is dependent upon, the angle of the incident electron beam, accelerating voltage and the work function of constituent atoms in a sample. SE are particularly well suited for the study of surface topology given that they are produced at penetration depths of only the first few nm. BSE are produced at greater penetration depths by elastic collisions, scattering the incident electrons [10]. The intensity of BSE's is dependent on the atomic number of a sample and, despite having less resolutions than SE's, they can provide detailed compositional analysis of sample, particularly when used in combination with EDX spectroscopy. EDX is a technique which utilises the

principle that electrons with sufficient energy can eject a core electron from a constituent atom of a sample (ionisation). When the core is filled by electronic transitions from an outer shell electron a characteristic X-ray is emitted. With appropriate calibration, the characteristic X-rays, and their intensities, can be used to collect semi-quantitative information regarding a sample's elemental composition [10]. This technique is limited in effectiveness for atoms with A < 20, due to the weakness of the characteristic X-rays produced by lighter elements.

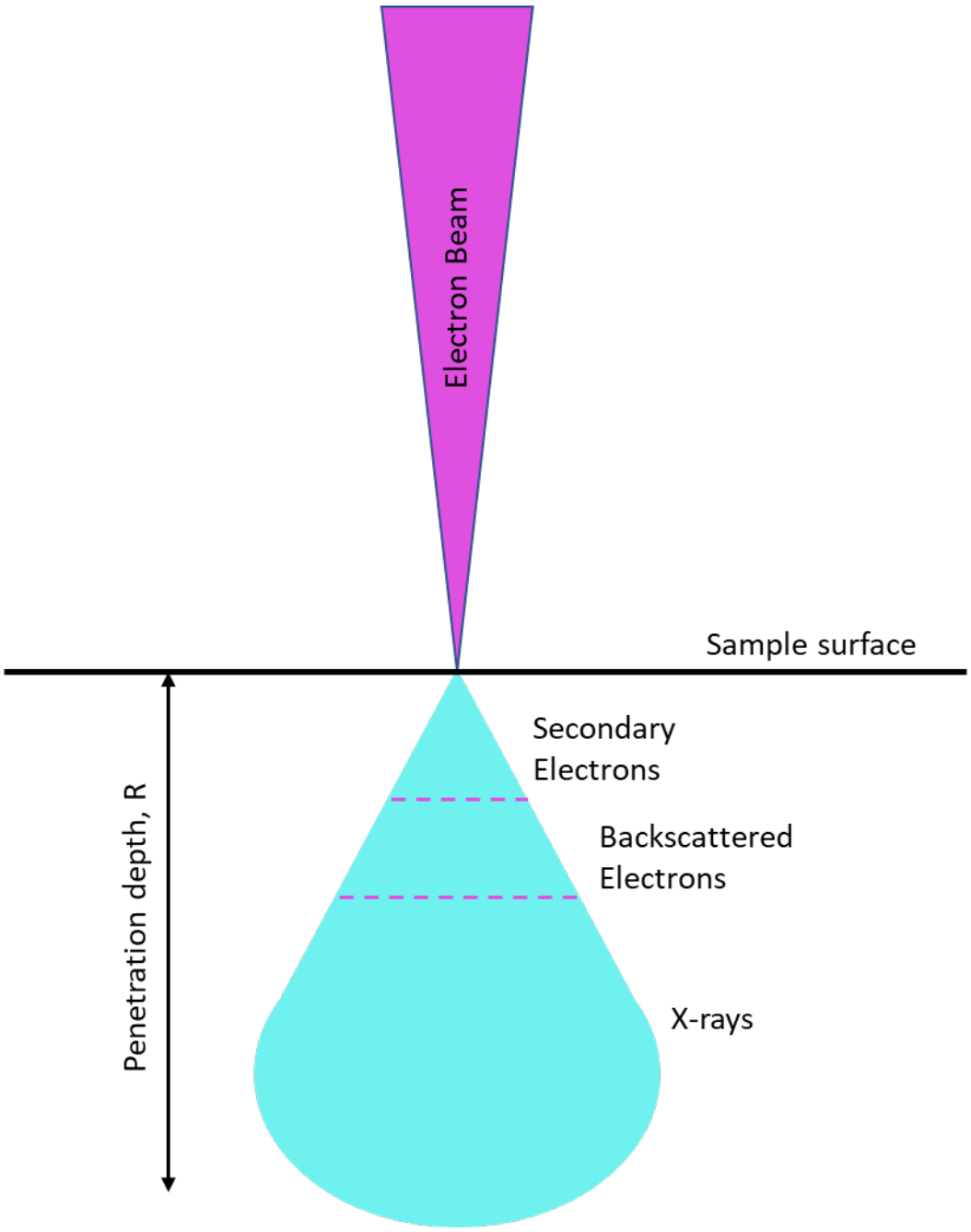

Figure 3.7: Origin of Backscattered electrons, Secondary electrons and characteristic X-rays over a penetration depth, *R*, as a result of interactions between the electron beam and a sample.

To prepare sintered ceramic samples for SEM-EDX analysis, samples were embedded in in cold setting epoxy resin poured into circular plastic moulds and allowing them to cure overnight. Resin blocks were liberated from their moulds and the surface ground in incremental stages using SiC pads (P400 – P600 – P800 – P1200) using a Kemet 300 Lapping and Polishing Wheel. Once a desired finish had been achieved, samples were polished to an optical finish using successively finer grades of diamond pastes (6 μm – 3 μm – 1 μm). Samples were carbon coated using an Agar Scientific Carbon Coater and conductive silver paint was applied. All SEM images were, unless otherwise stated, collected on a Hitachi TM3030 SEM, with an accelerating voltage of 15kV. Elemental analysis was carried out with a Bruker Quantax 30 Energy Dispersive X-ray Spectrometer (EDX). EDX analysis was applied in mapping and spot mode to characterise element distributions and perform semi-quantitative microanalysis. Spot analyses were integrated over a 20 x 20 micron area for 180 s, with element compositions determined using standardless quantification; at least six measurements were averaged to yield reported compositions and the error was taken as the standard deviation of the averaged set. Oxygen stoichiometry was inferred from quantification of other elements since this element cannot be determined reliably due to the surface sensitivity of the O K emission.

3.2 Radiation damage

The following section details the methods used to simulate radiation damage in samples of Ln_2TiO_5 (Ln = Gd, Dy, Yb) ceramic monoliths. This includes descriptions of the Dalton Accelerator For Nuclear Experiments, which was used to implant heavy ions onto the surface of samples to simulate α-decay damage, experimental procedures used during heavy ion implantation and the simulation of atomic displacements

3.2.1 Heavy-ion implantation

The use of heavy ion implantation to simulate α-decay damage is a common technique which provides a rapid and safe means to investigate a materials response to radiation damage compared to other methods such as using readily available metamict minerals or *via* the incorporation of radioactive isotopes directly into synthetic samples, where there is a risk of radiation exposure, as discussed previously in section 2.4.3. Implantation is generally achieved by accelerating ions (Kr, Au, Ni, Fe etc) to high energies; typically, between 1 – 15 MeV, depending on the nature of experiment and ion being used, though higher and lower energies are occasionally called for. Radiation damage experiments conducted through this thesis made use of facilities provided by the Dalton Cumbria Facility utilising the 5 MV tandem pelletron ion accelerator, which is commonly referred to as the Dalton Accelerator For Nuclear Experiments (DAFNE) [11]. Pelletron accelerators use a potential difference to accelerate oppositely charged particles. A schematic of DAFNE is given in Figure 3.8.

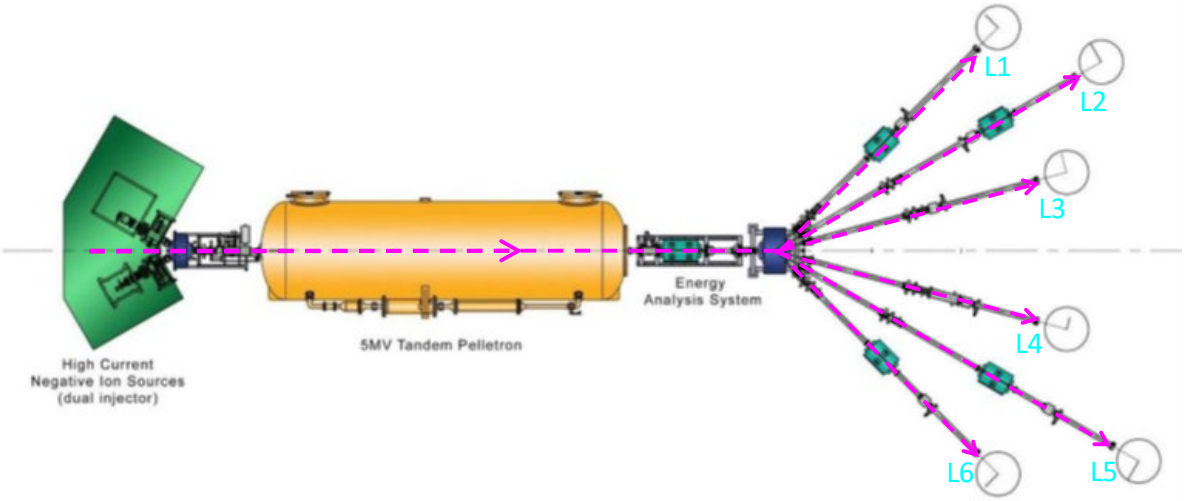

Figure 3.8: Schematic diagram of the Dalton Accelerator For Nuclear Experiments (DAFNE). Taken from: [12]. Pink dashed line represents the direction of the direction of the ions and L1, L2, L3, L4, L5 and L6 (Line 1 etc.) are the user end stations.

Heavy ions were produced from a multi-cathode source of negative ions by caesium sputter (MC-SNICS). Here, a reservoir of Cs is vaporised in an oven and flows from the Cs oven into an enclosed area. Some of the Cs will condense onto a cold cathode, forming a thin film of liquid Cs and the remainder will hit a heated spherical ionizing surface, ionising the Cs into Cs^+. The ionised Cs^+ is accelerated towards the negative cathode, which is made from the material intended to be implanted into a sample and focused on the front face of the cathode. The accelerated Cs^+ ions impart their momentum onto the surface of the negative cathode, sputtering particles through the condensed Cs layer which readily gives up its electrons to the sputter atoms, yielding a net negatively charged ion. The sputtered atoms flow into the Tandem pelletron unit to be further accelerated to the target energy. The ion current, whilst dependant on the cathode material, can generally achieve 10 – 100 nA but can potentially be pushed towards 1 -2 µA. The beam is focused and steered at the low energy beamline into the accelerator unit *via* a series of electric and magnetic fields generated by Einzel lenses, switching and injection magnets or quadrupole magnets [12].

The negatively charged ion beam is injected into the tandem accelerator to further increase the kinetic energy of the ions to the desired extent. A tandem accelerator, where both ends of the accelerator are grounded, has a high voltage positively charged central terminal. A tandem pelletron system is shown schematically in Figure 3.9. The high voltage terminal is generated by using a pelletron charging system consisting of a series of metal pellets forming a chain connected by insulation nylon links. A

negative inductor electrode induces a positive charge in the pellets whilst they are in contact with the grounded drive pulley. As the pellets leave the pulley, they retain a positive charge as they are still within the inductor field. As the chain moves towards the central terminal, the positive charge is conducted away from the pellets, giving the central terminal a net positive charge. This is typically referred to as 'up-charging'. The chain of pellets are then cycled back around the terminal, passing through a positive inductor electrode, inducing a negative charge in the pellets. The pellets are then transferred back towards the beginning of this cycle, transferring a negative from the terminal *via* a charging column. This is typically called 'down-charging' [13]. This dual charging regime effectively acts to double the charging capacity of the chain and therefore allows greater accelerating energies to be achieved.

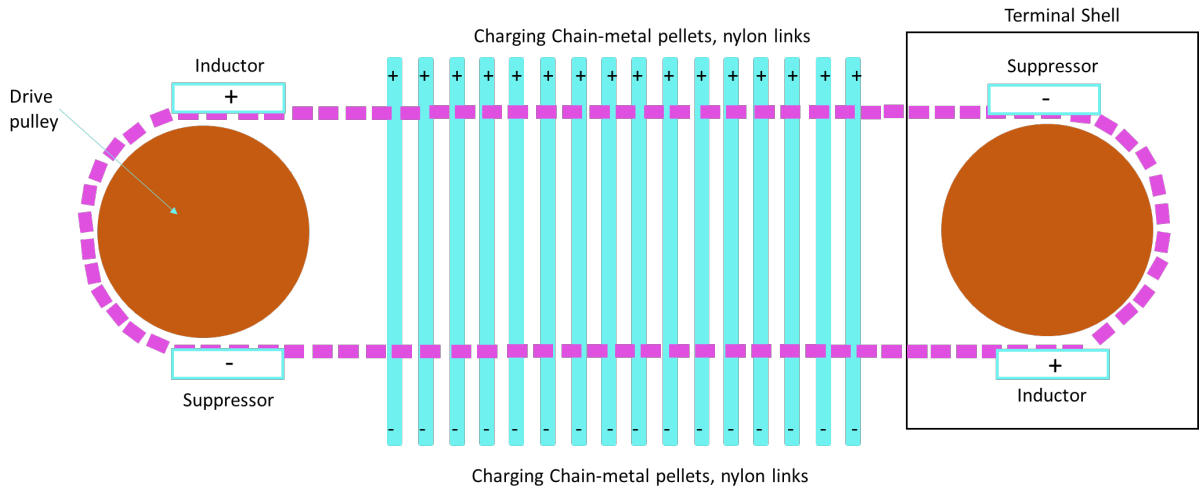

Figure 3.9: Pelletron charging system used in a tandem accelerator, showing the ground to terminal section. Adapted from: [12]

The negatively charged ion beam is accelerated towards the positively charged central terminal. Ar gas in the central tandem terminal strips electrons from the ions as they are accelerated through the chamber, becoming positively charged in the process. The efficiency of the electron stripping is dependant upon the ion energy and the binding energy of electrons. Ar gas can be pumped in and out of the chamber for more efficient stripping however an excess of Ar gas could lead to attenuation of the beam [12]. The now positively charged ion beam is repelled towards the end of the tandem accelerator by the positively charge central terminal, further increasing the kinetic energy of the ions. Magnetic optics are then used to further steer and focus the beam end station and user's sample. The beam can also be rastered across a pre-determined area of the sample's surface through careful steering.

Ion beam irradiations were carried out using a 5 MV Pelletron at Dalton Cambria Facility (DCF), University of Manchester. Dense, single phase ceramic monoliths of Gd_2TiO_5, Dy_2TiO_5 and Yb_2TiO_5, with dimensions 5 x 5 mm, were polished to 1 µm finish and mounted on a NIMONIC75 alloy block and secured in place using carbon sticky pads. Irradiation was carried in focused raster mode out using

ion beams of 1 MeV Kr^+ with fluence of 5 x 10^{15} ions cm^{-2} and 5 MeV Au^+ with a fluence of 1.2 x 10^{15} ions cm^{-2}. The beam current was maintained at 0.5 µm to avoid heating of the sample, the sample temperature was monitored by a K-type thermocouples fixed to the sample stage and a pyrometer camera mounted above the sample which continually records 2D thermal images throughout the experiments.

3.3.2 Determining displacements per atom (dpa) over depth (SRIM)

Irradiating particles are able to displace other atoms that are bound within the target structure as long as the irradiating particle has sufficient energy to overcome the electrostatic bonds. This energy is threshold is known as the displacement energy E_D, below which the probability of such a displacement is 0. The number of displacements caused by the incident irradiating particle is often defined as:

$$N_d = \frac{E_c}{2E_D} \qquad \textbf{Equation 3.7}$$

Where N_d is the number of displaced atoms, assuming no recombination events, E_c is the critical energy level for electron energy loses, defined as the incident ion's mass. The Norgett-Robinson-Torrens modification takes into consideration the electronic excitation that occur as displaced atoms travel through the crystal structure:

$$N_d = 0.8\frac{E_c}{2E_D} \qquad \textbf{Equation 3.8}$$

If the irradiating particle, or the first initial displaced ion (commonly referred to as the primary knock-on atom, PKA) has sufficient energy ($> 2E_D$) it can continue after the initial collision to cause further displacements, culminating in a cascading effect where secondary knock-on atoms can further displace additional atoms, if they are energetic enough. The damage caused due to these cascading atoms is often measured using the unit of displacements per atom (dpa) and is calculated as:

$$dpa = \frac{Irradiating\ Fluence \times Number\ of\ Displacement}{Target\ Density} \qquad \textbf{Equation 3.9}$$

Damage events (primary knock-on collisions and subsequent cascades etc.) caused by heavy-ion irradiation occur over sub-nanosecond timescales, making experimental measurements of the phenomenon highly impractical. As such, computer simulations are often used give a greater understanding of damage events and predict the behaviour of a material exposed to radiation.

One of the most frequently used programs for this purpose is Stopping Range of Ions in Matter (SRIM) [14]. The program generates simulations using a Monte Carlo binary collision approximation (BCA) approach to approximate ion ranges and damage distributions. In this approach the distance to, and impact parameter of, the next colliding atom is chosen randomly from a probability distribution. An

example of the simulated displacement cascades of 1 MeV Kr^+ ion in Gd_2TiO_5 can be found in Figure 3.10.

Both Kr^+ and Au^+ heavy ions were used in this thesis to simulate different damage profiles at varying depths and determine the efficacy of glancing angle X-ray absorption spectroscopy characterisation at different depths. Simulations performed using the SRIM [14] software showed that a similar dpa could be expected at depths of ∼300 nm and ∼700 nm when irradiated with Kr^+ or Au^+, respectively.

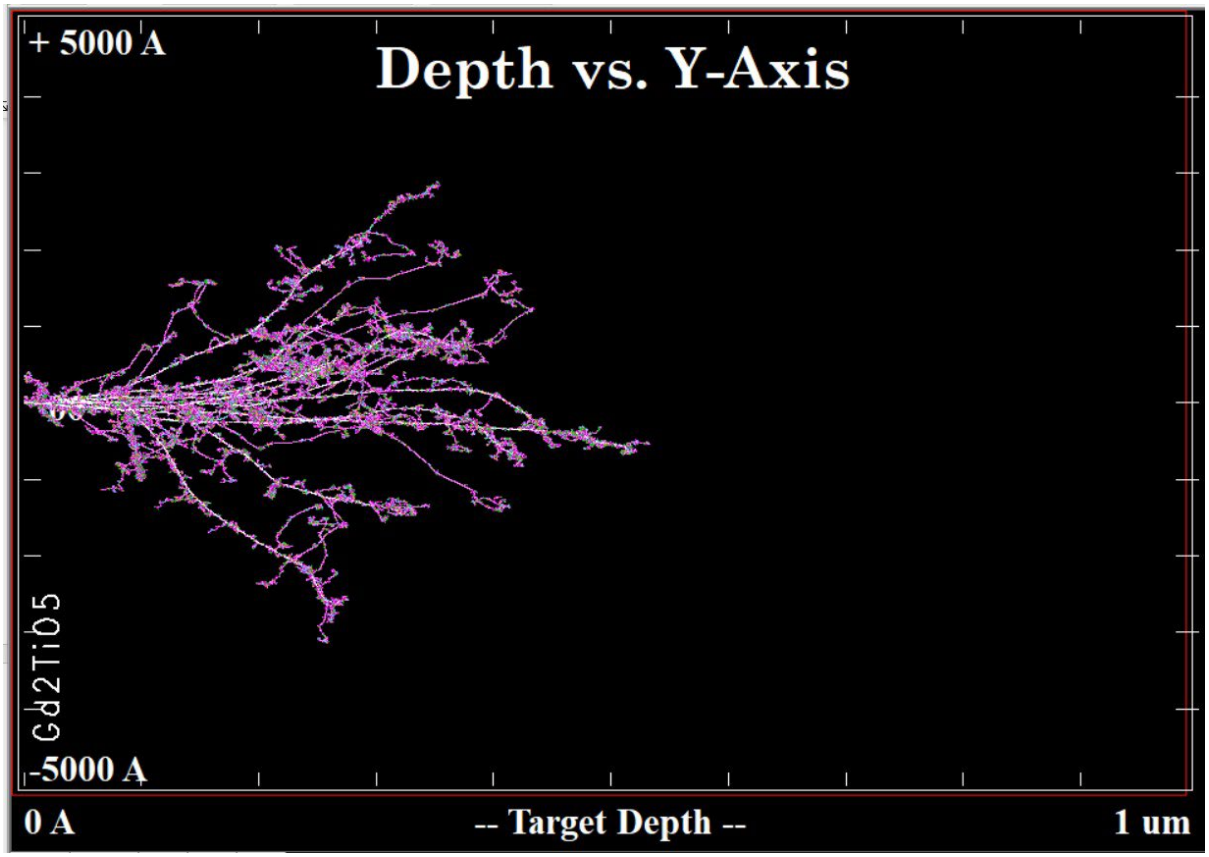

Figure 3.10: Simulated ion path of 10 1 MeV Kr^+ ions into a target layer of Gd_2TiO_5. White lines show the path travelled by Kr^+ ions and pink lines show the paths that displaced atoms travel. Green, blue, and purple show positions where atoms have stopped.

SRIM has a multitude of applications and can be used to calculate electronic and nuclear stopping powers, the former relating to inelastic collisions of projected ions with the bound electrons of the target atoms electrons and the later relating to the elastic collisions of an ion with the nucleus of the target atoms, the angular deflection of atoms, energy distribution, the trajectory of irradiation ions, displaced atoms and cascade products, and the distribution of defects over a given depth. An example of the damage depth profile of 1 MeV Kr ions into Yb_2TiO_5 can be found in Figure 3.10. The average total number of displacements can be determined by integrating the area under the curve, for the dpa vs depth plot; in Figure 3.10 this was 3.32 dpa. It should be considered however that SRIM does have limitations on how well it can predict a material's behaviour as it does not consider point defect recombinations (leading to an over estimation of total defects cause through collisions), crystal structure (instead, SRIM assumes that the target layer is amorphous) and recrystallisation processes induced by temperature and/or ion-irradiation. Nevertheless, SRIM has been shown to a vital tool in predicting a materials radiation damage behaviour and has been used to inform the design of many experiments [15], [16].

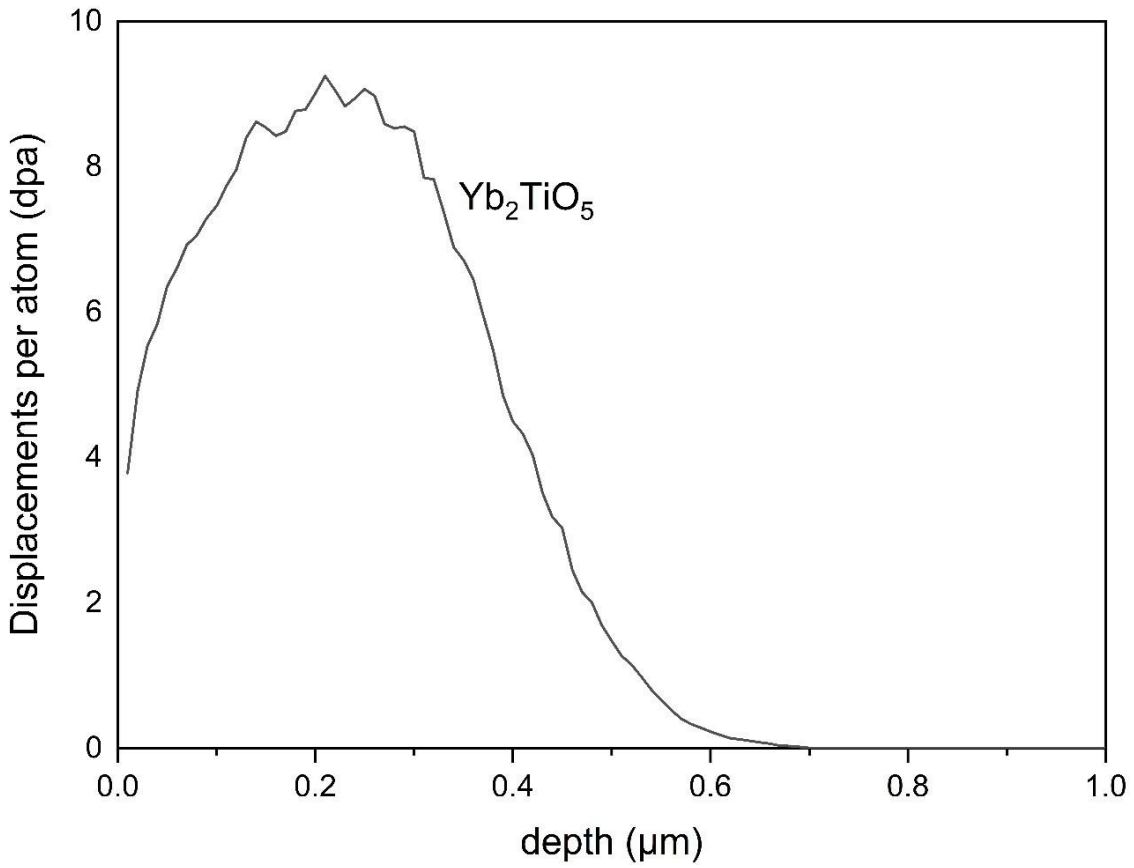

Figure 3.11: Showing simulated displacements per atom (dpa) over a depth of up to a 1 μm depth. performed in SRIM. In this example1 MeV Kr^{+} ions at a fluence of 1 x 0^{15} ions cm^{-2} are implanted into the surface of a Yb_2TiO_5 ceramic.

All SRIM simulations at different energies and ion fluences were also used in the design of initial irradiation experiments to predict the ideal parameters prior to actual irradiation experiments taking place. In this thesis, SRIM was used to calculate the damage vs depth profile of 1 MeV Kr^{+} ions and 5 MeV Au^{+} ions in bulk samples of Gd_2TiO_5, Dy_2TiO_5, and Yb_2TiO_5. These simulations were vital as they were used to select the angle of incidence of X-ray beams used in glancing angle X-ray absorption characterisation of irradiated materials wherein the most highly damaged (maximum of the displacement curve in Figure 3.11) depth was targeted.

3.4 X-ray absorption spectroscopy (XAS)

Since its development in 1971, by Dale Sayers, Ed Stern and Farrell Lytle [17] who gave a description of the physical origins of the features seen in the X-ray absorption fine structure (XAFS) by applying Fourier analysis to a theoretical XAFS model, X-ray absorption spectroscopy (XAS) has become a widely utilised tool for probing the structure and chemical speciation of a material at the atomic scale. Following the inception of the theoretical analysis of XAFS, synchrotron light sources began conducting experiments utilising high energy X-rays, providing rapid and highly accurate measurements. XAS experimental techniques have since been further developed to allow measurements under variety of experimental requirements such as studying samples over a wide range of thermal conditions (e.g. high/low temperatures and pressure), examination of atomistic properties of samples in gaseous, liquid or solid phases, to conduct long-term *in-situ* experiments and facilitate highly localised measurements of topographical features on the micron scale (μ-XAS), to name but a few.

3.4.1 XAS fundamentals

3.4.1.1 X-ray absorption

In an XAS experiment a sample is bombarded with X-rays of a definite energy. As the energy of the incoming X-rays increases and becomes commensurate with the electron binding energy the likelihood of absorption (i.e., annihilation) by a bound electron increases. The energy of the lowest accessible electron orbital is termed the Fermi energy. When an X-ray is absorbed by a core electron, the core electron is promoted to a higher, unoccupied orbital or is ejected into the continuum where the photoelectron no longer has any association with the atom (it is termed a photoelectron due it being an electron emitted from interactions between the atom and the X-ray photon) [18]. This process is known as the photoelectric effect and is visualised in Figure 3.12.

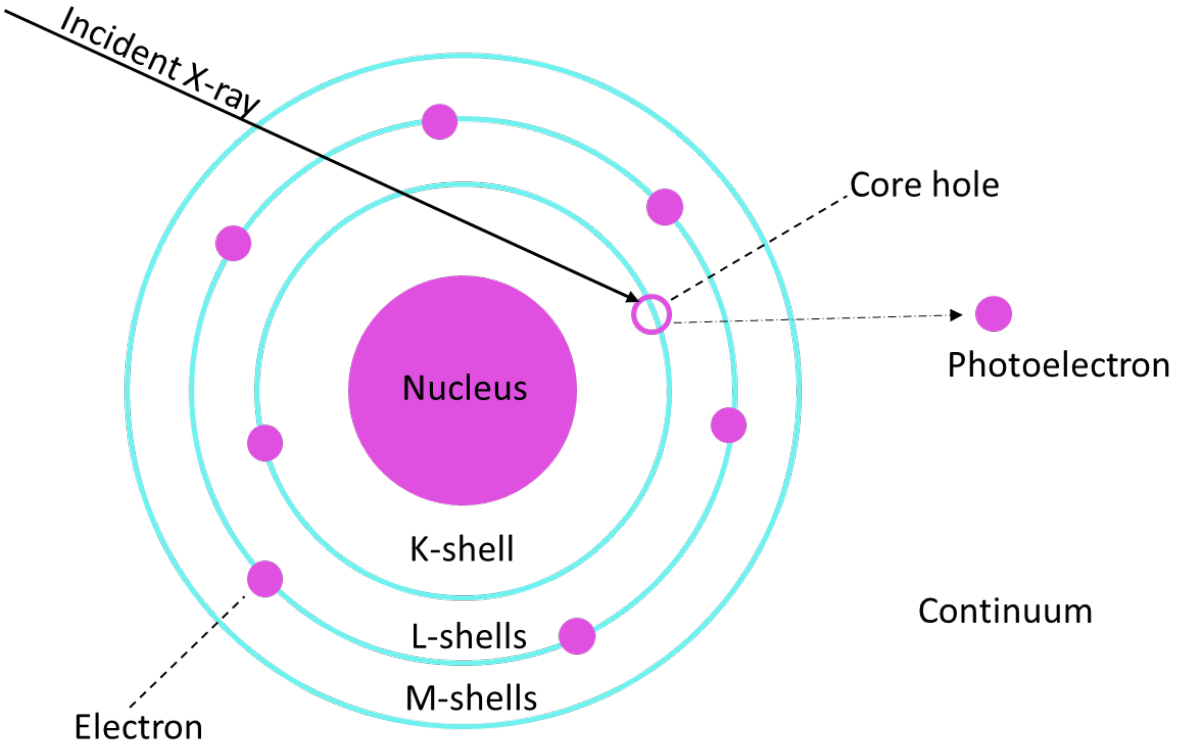

Figure 3.12: Emission of photoelectron due to X-ray absorption (photoelectric effect) based upon Bohr's model of an atom.

The core hole left behind by the excited electron is filled by an electron that relaxes from a higher orbital, accompanied by the emission of fluorescent X-rays where its energy is equal to the difference between the two orbitals. X-ray fluorescence is the predominant relaxation process for hard X-rays (energies > 2 keV) however for softer X-rays the production of Auger electrons is more probable. Auger electrons occur when higher energy orbital electrons drop to fill a core hole. The relaxation is accompanied by the emission of another electron from the same or different atomic shell into the continuum. This typically takes place over timescales on the order of 10^{-15} s (femtoseconds) [19]. Both X-ray fluorescence and Auger electrons can be used in XAS experiments to measure a sample's structural properties.

Electronic transitions are subject to restrictions of the dipole selection rule such that transitions can occur only between energy states that differ in azimuthal quantum numbers (l) ± 1, in order to conserve angular momentum (j).

3.4.1.2 X-ray absorption coefficient

An XAS experiment is primarily designed for measuring the X-ray absorption coefficient, μ [18]. This can be expressed as the fraction of photons that are absorbed when an X-ray passes through a given thickness of a particular material:

$$\mu(Ex) \equiv -\frac{dI}{dx} \quad \textbf{Equation 3.10}$$

where *I* is the intensity of transmitted X-rays and x is the thickness of the sample. As can be seen in Equation 3.10, the absorption coefficient is dependent upon the energy of X-rays absorbed. At higher energies, fewer X-rays are likely to be absorbed, however when the energy of the incoming X-rays equals the energy required to excite orbital electrons the absorption increases sharply. These sharp steps in absorption are known as absorption edges (e.g., for the Ti K-edge at X-ray energies of 4966 eV the probability of absorption is high, just above this energy the probability slowly decays). Given that absorption coefficient is dependent on thickness too, the density of a sample will also have an effect as a material with a higher density will be able to pack more atoms into a given thickness [18]. As such it can often be practical to express $\mu\mu$ in terms of mass:

$$\mu_m(E) \equiv \frac{\mu(E)}{\rho} \quad \textbf{Equation 3.11}$$

where ρ is the density of the sample. The probability that an X-ray, of a given energy, will be absorbed is directly proportional to μ_m. The relationship between transmitted intensity and initial intensity of an X-ray for a given is found by integrating the equation for the absorption coefficient giving:

$$I_t = I_0 e^{-\mu_m \rho x} \quad \textbf{Equation 3.12}$$

where I_t is the transmitted intensity of the X-rays and I_0 is the initial intensity of the X-rays. This equation is known as the Beer-Lambert-Bouguer law. The thickness of a sample prepared for XAS measurements is informed by rearranging Equation 3.12:

$$\mu_m \rho x = \mu x = ln\left(\frac{I_0}{I_t}\right) \quad \textbf{Equation 3.13}$$

where μx is the absorption length. This allows calculation of the mass needed of a given sample to correspond to the desired number of absorption lengths.

As the relaxation of excited electrons into core holes is dependent on the X-ray absorption, the intensity of fluorescent X-rays can be derived from the absorption coefficient:

$$\mu x \propto \frac{I_f}{0} \quad \textbf{Equation 3.14}$$

where I_f is the intensity of fluorescent X-rays.

3.4.2 Sample thickness

An XAS spectrum is a measurement of the probability of X-ray absorption at a given X-ray energy, taken as the function of the ratio intensity of outgoing X-rays over the intensity of incoming X-rays. In an ideal measurement this is all that would need to be considered but in practical application it is found that there are a number of issues that further effect the measurement. These effects on measurements are often called 'thickness effects' [18] and can potentially affect the amplitude of XAS spectra. The most common effects are:

- Scattered X-rays: those that have not been absorbed by the sample but nonetheless are deflected in such a way that they are detected regardless, leading to the measurement of X-rays that have no direct relation to the structure of the sample.
- Harmonics: in instances where X-rays are allowed through that have integer multiples they can be harmful to the measurement and are usually controlled by the use harmonic suppression methods such as harmonic rejection mirrors or by detuning the monochromator (the device used to selectively choose a particular X-ray energy for a relevant sample). Harmonics can lead to distortions of data collected in transmission mode, particularly for thick samples, and can degrade the signal-to-noise ratio of fluorescent measurements.
- Distribution tails: most monochromators have a resolution function that will have a tail overlapping the lower-energy region below edges. The spread of energy around the desired energy is typically ± 1 or 2 eV. The tailing energies are not attenuated to same extent as the central energy and as such can contribute significantly to the background for thick samples.
- Sample preparation: poorly prepared samples can lead to significant distortions in the data. Non-uniform samples, where part of the sample is thickness than another can lead to varied transmitted intensities (as can be seen in Equation 3.9 I_t is dependent on thickness x), pinholes in the sample can allow unabsorbed X-rays to pass through and the morphology of the particles in the sample can also lead to the X-ray beam being incident on regions of various thickness (Figure 3.13). These effects can be 84eneraliz through careful preparation of samples and, if possible, one could also scan the X-ray beam as a function of position across the sample to find the most uniform region.

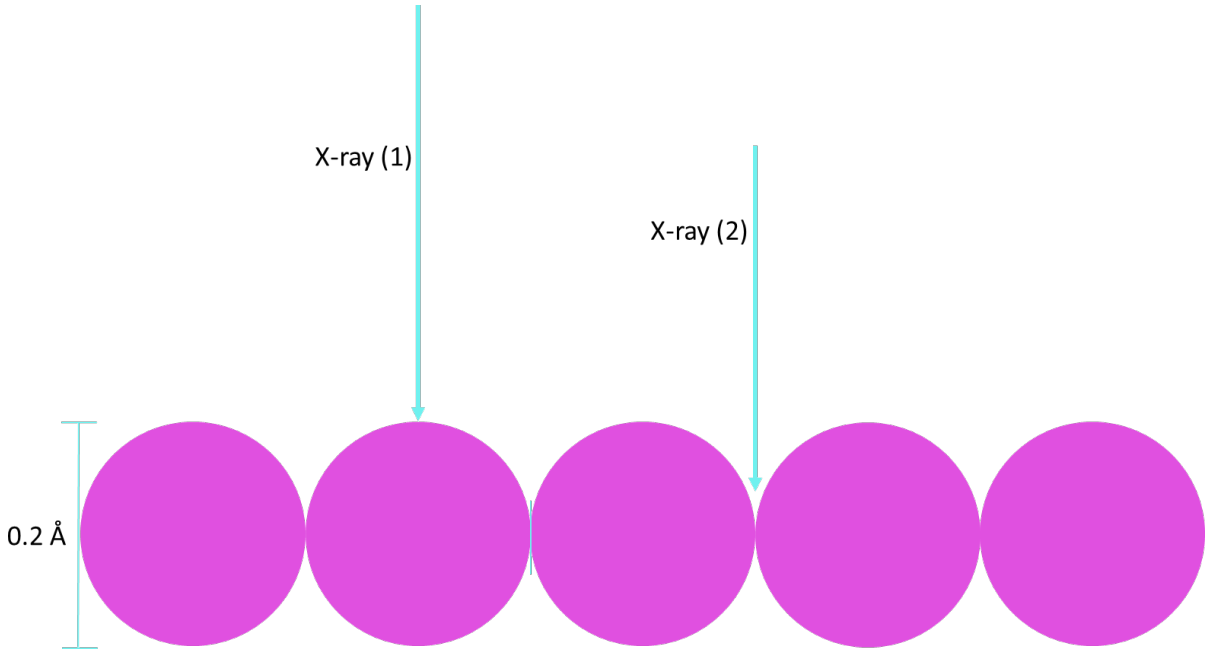

Figure 3.13: Single layer of spherical particles of diameter 0.2 Å. Incident X-ray (1) sees a thicker layer (0.2 Å) compared to X-ray (2) which sees a sample with thickness of 0.06 Å. This variation in thickness can lead to significant variations of the transmitted intensity.

3.4.3 X-ray absorption spectra

X-ray absorption spectra are typically measured from ~ 200 eV below to 1000 eV above the absorption edge of the element of interest [19]. The regions of the spectra can be seen in Figure 3.14 and are 85eneralized as the:

- Pre edge – the energy region below the absorption energy of the targeted elemental edge. This region is typically featureless as the probability of absorption below such energies is extremely low. However, a weak pre-edge feature can be observed, particularly for XAS spectra collected at the K-edge of the first row of transition metals [19]. Pre-edge features will be discussed in more detail in Section 3.6.3.1.
- Absorption edge – commonly referred to as the white line, is the point at which the energy of incident X-rays is equal to that of the electron binding energy where the probability of absorption increases dramatically. An edge is named according to the principal quantum number of the excited electron (Figure 3.15), e.g., the K-edge represents electron transitions from the *1s* orbital. Each element has characteristic absorption edge energies associated with the electron binding energy of a particular electron shell in the element. As atomic number increases so does the energy of specific edges as the greater proton content necessitates an increase in electron binding energy. For example, the Ti K-edge has an absorption energy of 4966 eV and the V K-edge has an absorption energy of 5465

eV, reflecting the greater electron binding energy of the K-shell electrons of V atoms. The shape of an absorption edge is dependent upon the binding geometry and oxidation state of the atom, which is reflected in the available density of states of the atom being measured [19]. Atoms with higher oxidation states usually have absorption energies several eV greater than that of an equivalent neutral atom (the inverse is the case for atoms with lower oxidation states), reflecting the changes in available energy states, requiring greater energy to excite the remaining electrons.

- XANES – (X-ray absorption near edge structure) is the region of ~ –50 to +200 eV about the absorption edge energy. This region, which is sensitive to changes in coordination and oxidation state, often refers to both the pre-edge and the white line in addition to the peaks and shoulders near the white line.
- EXAFS – (Extended X-ray absorption fine structure) is the region ~50 – 1000 eV above the absorption edge and consists of weak oscillations that result from interference of the emitted photoelectron scattering off nearby atoms and returning, out- or in-phase, to the absorbing atom (Figure 3.14). In phase results in an increase in amplitude to the features of the EXAFS region, out of phase results in a decrease. EXAFS will be discussed in more detail in Section 3.6.3.2.

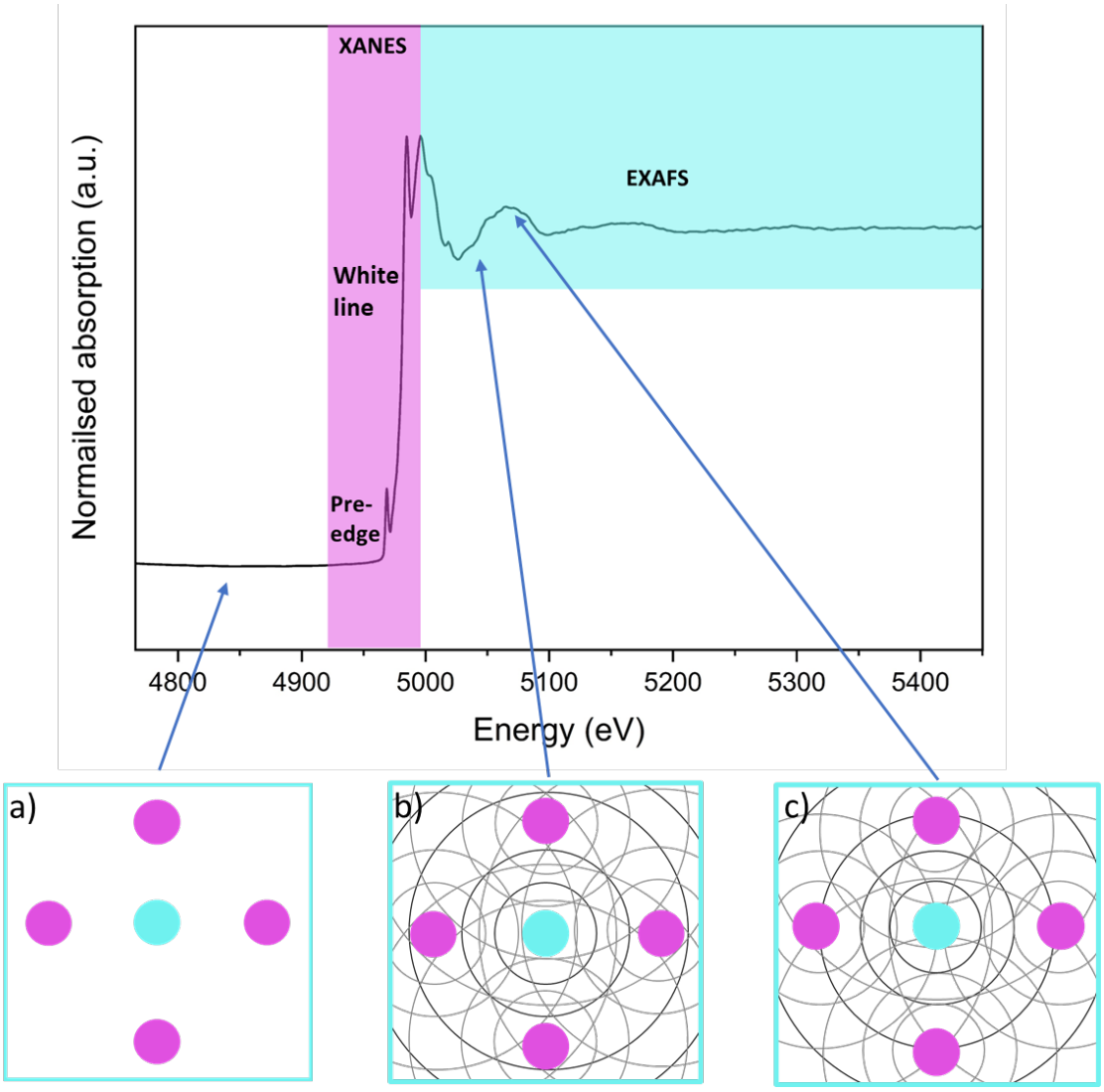

Figure 3.14: Normalised Ti K-edge spectra of Ho_2TiO_5, with the pre-edge, white line (absorption edge) and XANES and EXAFS regions highlighted. Also shown is the 87eneralized X-ray absorption process, where the absorber atom is in blue, nearest neighbour atoms are pink, photoelectron wave is black, and the backscattered photoelectric waves are grey. A) no absorption takes place as the incident X-ray energy is below the absorption energy of the target atoms, b) X-rays are absorbed and photoelectric wave propagates out from the absorber, backscattered waves return out of phase, resulting in a decrease in EXAFS amplitude (trough), c) X-rays are absorbed and photoelectric wave propagates out from the absorber, backscattered waves return in phase resulting in an increase in EXAFS intensity (peak).

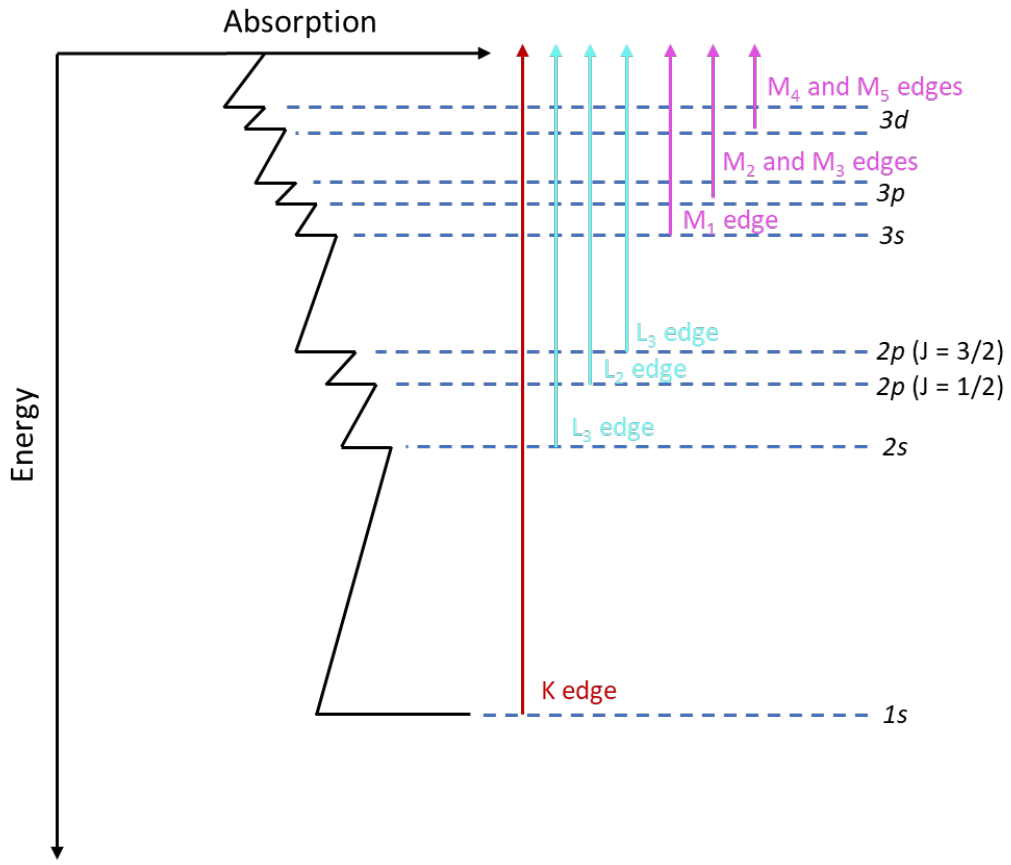

Figure 3.15: Electron transitions that contribute to XAS absorption edges.

3.4.3.1 Pre-edge

The features in the pre-edge are attributed to electron transitions from the 1s energy level in the core of absorber atoms to hybridised 3d / O 2p molecular orbitals, and as such information about the local coordination environment of the absorbing atoms can be obtained. A *1s* (l = 0) to 3d (l = 2) transition is usually forbidden due to selection rules ($\Delta l = \pm 1$), however, this rule is relaxed when an absorbing atom is located in a non-centrosymmetric coordination and *d-p* mixing occurs. This is frequently observed when atoms are 4-, 5- and 6-fold coordinated where *d-p* mixing is stronger than compared to other coordination motifs such as octahedral coordination. The intensity of the pre-edge feature is governed by the degree of *d-p* mixing in the molecular orbitals, which increases with site-distortion from regular octahedral, and the position is relatively insensitive to changes in the mean Ti-O distance. Changes in the height of the pre-edge are related to changes in centro-symmetry (*senso-stricto*) although both height and position are used in concert to derive indicative information about the local coordination environment. Tetrahedrally coordinated atoms will tend to have much strong *p-d* mixing compared to 5- and 6-fold coordinated atoms. The specific geometry of coordination can also affect the pre-edge intensity, even when the absorber atom has the same coordination number, and the pre-edge position remains the same. For instance, when Ti is in a trigonal bipyramidal coordination the

intensity of the pre-edge will much reduced compared to that of Ti in a square pyramidal coordination geometry, reflecting the changes in *d-p* mixing strength.

3.4.3.2 Extended X-ray absorption fine structure (EXAFS)

As described in Figure 3.13, EXAFS occurs from the elastic scattering of the photoelectron emitted into the continuum at energies above the absorption edge [18]. The photoelectron, when considered as a plane wave propagating in all directions from the absorber atom will have a wavelength:

$$\lambda = \frac{h}{p} \qquad \textbf{Equation 3.15}$$

where h is Planck's constant (6.626 x 10^{-34} m^2 kg s^{-1}) and p is the momentum of the electron. The photoelectron wave will elastically scatter off neighbouring atoms and return to the original absorbing atom. Upon returning to the original absorber atom the emitted photoelectron wave and backscattered wave can interfere constructively or destructively. Constructive interference occurs when the absorber-neighbour distance is an integer value of the photoelectron wavelength such that:

$$2D = n\lambda \qquad \textbf{Equation 3.16}$$

where D is the distance between an absorber-scatterer pair and n is some integer.

The probability of an incident X-ray being absorbed is modulated by a value χ, such that if Equation 3.16 is satisfied, where constructive interference occurs, the probability is increased in:

$$\chi \propto cos\,(2\pi \frac{2D}{\lambda}) \qquad \textbf{Equation 3.17}$$

If the wave number, k, is given by:

$$k = \frac{2\pi}{\lambda} \qquad \textbf{Equation 3.18}$$

Then Equation 3.17 becomes:

$$\chi \propto cos\,(2kD) \qquad \textbf{Equation 3.19}$$

The kinetic energy of the photoelectron can be expressed as:

$$T = \frac{p^2}{2m_e} \qquad \textbf{Equation 3.20}$$

where m_e is the mass of an electron and the momentum, p, is:

$$p = \hbar k \qquad \textbf{Equation 3.21}$$

where $\hbar$ is the modified Planck's constant ($\hbar = \frac{h}{2\pi}$). If the kinetic energy of the photoelectron is equal to the difference between the energy of the incident X-ray, E, and the energy necessary to eject an electron from the absorbing atom, E_0:

$$T = E - E_0 \qquad \textbf{Equation 3.22}$$

then Equations 3.20 and 3.22 can be combined to give the result:

$$k = \frac{1}{\hbar}\sqrt{2m_e(E - E_0)} \qquad \textbf{Equation 3.23}$$

As X-ray energy is increased, so does the wavenumber. It is now possible to see that the oscillations observed in the EXAFS region are not only dependent upon the wavenumber but also the distance between the absorbing atom, the larger the spacing between atoms causes the oscillations to have a larger frequency, occurring more quickly as a function of wavenumber and energy [18].

It should be noted, however, that in the model considered thus far all photoelectrons are effectively scattered by surrounding atoms. However, the photoelectron may scatter inelastically (loss of kinetic energy) which would cause a change in the wavelength of the backscattered photoelectron wave (and as such effect the interference pattern) or it could potentially not scatter at all, due to quantum mechanical probabilities [18]. Further, the current model only considers scattering between an absorber and one other atom, whereas in most systems multiple atoms are likely to have multiple neighbours. Both of these are considered by summing over multiple atoms:

$$\chi(k) = \sum_i N_i f_i(k) \cos(2kD_i) \qquad \textbf{Equation 3.24}$$

where N_i is the degeneracy (the number of atoms found in the same coordination shell), $f_i(k)$ is the proportionality constant of neighbouring atoms, i, which is proportional to probability of a photoelectron scattering elastically off of a nearby atom, dependent upon the momentum of the photoelectron (or wavenumber). When an atom has a larger number of electrons (such as U), the probability that the photoelectron wave will be scattered is much higher than compared to an atom with relatively fewer electrons (such as O) [18]. This shows that the EXAFS region can give information relevant to a specific chemical species and the number of scattering atoms, in addition to their distances.

So far, the photoelectron electron has been considered as a wave scattering as if it occurs in a 'soft boundary' wherein the photoelectron wave scatters, changing direction, without changing phase. However,

as the photoelectron is ejected from the absorber atom it must overcome the potential well created by the absorber atom, travelling faster once it escapes the potential well (Figure 3.14). The conservation of energy means that it will have a higher wavenumber, k, once it escapes the potential well (as k is dependent on energy). Likewise, as the photoelectron is scattered by it descends into the potential well of the scattering atom, gaining speed and correspondingly decreasing the wavenumber, k. This can be likened to a body leaving Earth's orbit and subsequently entering the orbit of another planet, being 'pulled in' by its gravitational forces. The phase shift is accounted for by including the term $\delta(k)$ into equation 3.24:

$$\chi(k) = \sum_i N_i f_i(k) \sin(2kD_i + \delta_i(k)) \qquad \textbf{Equation 3.25}$$

It should be noted that cosine has been switched to sine so as to be more consistent with how the EXAFS equation is typically expressed in literature.

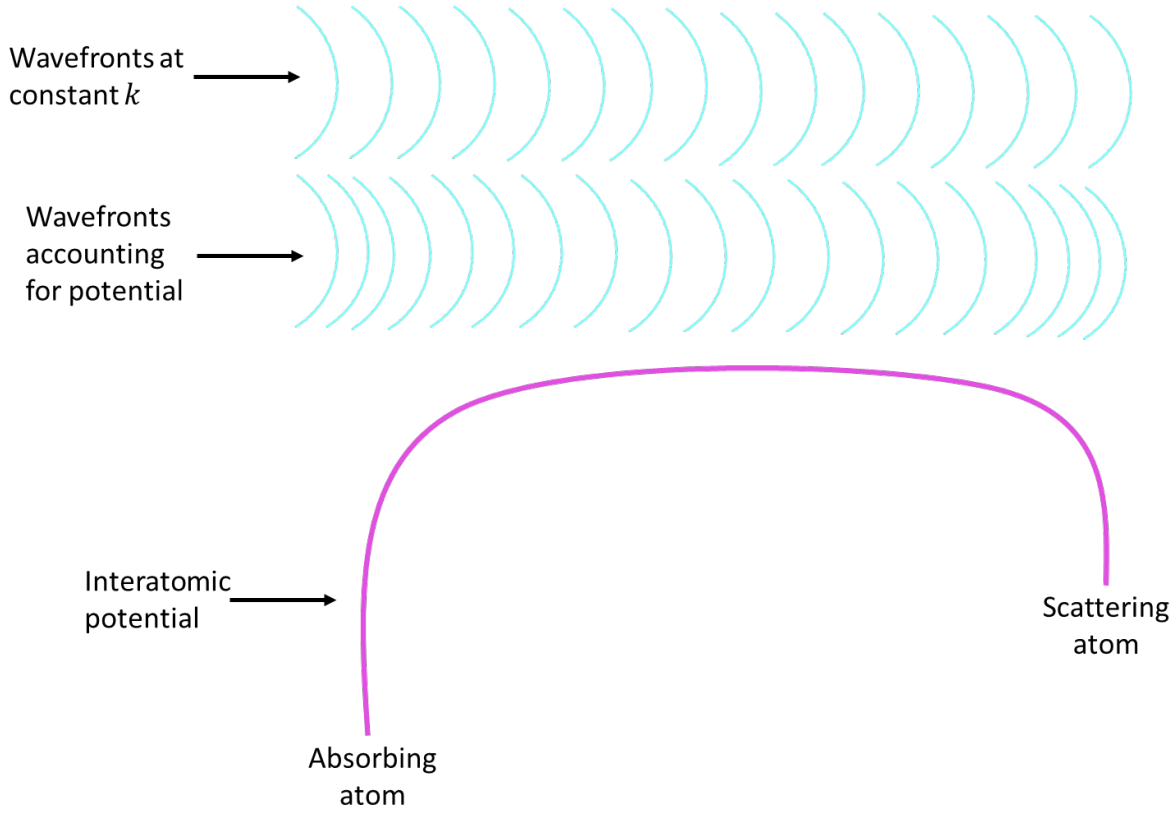

Figure 3.16: Schematic representation of the phase shift of a photoelectron as it is ejected from an absorbing atom and approaches a scattering atom.

It is important to also consider the photoelectron wave as it propagates isotropically in all directions, whereas previously we have been considering it as a plane wave. Accounting for spherical wave effects as the wave spreads out, the probability of absorption reduces by D^2:

$$\chi(k) = \sum_i N_i \frac{f_i(k)}{kD_i^2} \sin(2kD_i + \delta_i(k))$$ **Equation 3.26**

As the absorber atom ejects the photoelectron, leaving behind a core hole, orbitals must adjust as the remainder of the electrons experience a stronger positive charge from the protons in the nucleus. This leaves the absorber atom in a different final state than its initial state. This incomplete overlap can be modelled in the EXAFS equation by using an amplitude reduction term s_0^2:

$$\chi(k) = s_0^2 \sum_i N_i \frac{f_i(k)}{kD_i^2} \sin(2kD_i + \delta_i(k))$$ **Equation 3.27**

s_0^2 will typically have values between 0.7 to 1.1, though this value can be lower in fluorescence measurements due to self-absorption effects [18]. Self-absorption effects in fluorescence measurements refers to the absorption of fluorescent X-rays emitted as a higher orbital electron fills the core hole by other atoms of the same species (or elements with edge energies close to that of the target element). This effectively reduces I_f as fewer desired X-rays are able to escape from the sample. This can be avoided by have sufficiently dilute or thin samples, correcting for self-absorption in software or by using different XAS geometries.

Events, such as inelastic scattering, that remove energy from the photoelectron will ultimately change its wavelength. As discussed, changes in wavelength can result in changes to the interference condition. The likelihood of these events happening is dependent on the distance, D, the photoelectron travels, as the further it travels the more likely it is to encounter a scenario that will reduce its wavelength. Also, the further the photoelectron travels, the more likely it is that the core hole will be filled, changing the final state of the absorbing atom [18]. Both of these effects can suppress the EXAFS signal and are accounted for by the introduction of a mean free path term, $\lambda(k)$:

$$\chi(k) = s_0^2 \sum_i N_i \frac{f_i(k)}{kD_i^2} e^{-\frac{2D_i}{\lambda(k)}} \sin(2kD_i + \delta_i(k))$$ **Equation 3.28**

The variation due to disorder, both static and thermal, where the local environments of individual atoms are found to be different due possibly to defects or variations in atomic positions due to chemical bond vibrations can cause the photoelectron to scattered in many different manners and distances. Where these variations in scattering are not significant enough to alter the interference from one condition to the another, cumulant expansion term can be used to model the variation; often called the mean square radial displacement or Debye-Waller factor, σ^2, and is expressed in the EXAFS equation as:

$$\chi(k) = s_0^2 \sum_i N_i \frac{f_i(k)}{kD_i^2} e^{-\frac{2D_i}{\lambda(k)}} e^{-2k^2\sigma_i^2} \sin(2kD_i + \delta_i(k))$$ **Equation 3.29**

Equation 3.29 is often cited as the 'EXAFS equation' and is the principal tool used for analysing the EXAFS signal to derive information about the local structure of an absorbing atom. From the preceding discussion, it is plain to see how many physical properties of the local structure of an atom contribute to the EXAFS equation and serves to highlight the importance of understanding where each term in the EXAFS equation originates from and their physical meanings as these aids not only in the analysis of data but also interpretation of the results.

3.6.4 Glancing angle X-ray absorption spectroscopy (GAXAS)

In typical XAS experiments, the X-ray beam is focused onto one face of a thin sample and transmitted through the other side. The thickness of the sample is usually defined to be some value of the absorption length calculated based upon the elemental constituents of the sample. To study the surface layer of a bulk monolith, as one may want to if the surface has been damaged, a glancing angle geometry can be used as the penetration is otherwise restricted by absorption. Reducing the angle of incidence, φ, of the X-ray beam by tilting the sample such that φ is below the critical angle for totalinternal reflection, ϕ_c, causes the production of a damped evanescent wave [20]. This allows the X- ray beam to be restricted to only the surface monolayer of the sample, where X-ray fluorescence, generated as a product of higher orbital electrons filling the core hole left behind by the ejected electron that was excited by the X-ray beam, is able to escape from the samples surface in significant enough intensity to be measured and yield a XAS spectra pertaining to the absorbing atoms in the surface region. The depth of the penetrating X-ray beam is angularly dependent, reaching a minimum at:

$$z_{min} = \frac{\lambda}{4\pi\phi_c} \qquad \textbf{Equation 3.30}$$

z_{min} is around 1 – 10 nm for near perfectly flat specimens measured with hard X-rays. As φ is increased, the penetration depth also increases, reaching a maximum value that is dependent of the absorption coefficient. At values of $\phi > \phi_c$the penetration depth of the X-ray beam increases, allowing for XAS measurements at a greater penetration depth [20]. A desired penetration depth, x, can be calculated to ensure that at least 95% of the incident X-rays are absorbed using the Equation 3.6 [21].

3.6.5 X-ray synchrotron sources

In most XAS experiments high energy X-rays are needed to facilitate measurements. This can be achieved by utilising X-rays generated from synchrotron radiation. This requires the use of large particle accelerators found at central facilities. An example of the NSLS-II synchrotron facility is shown in Figure 3.17.

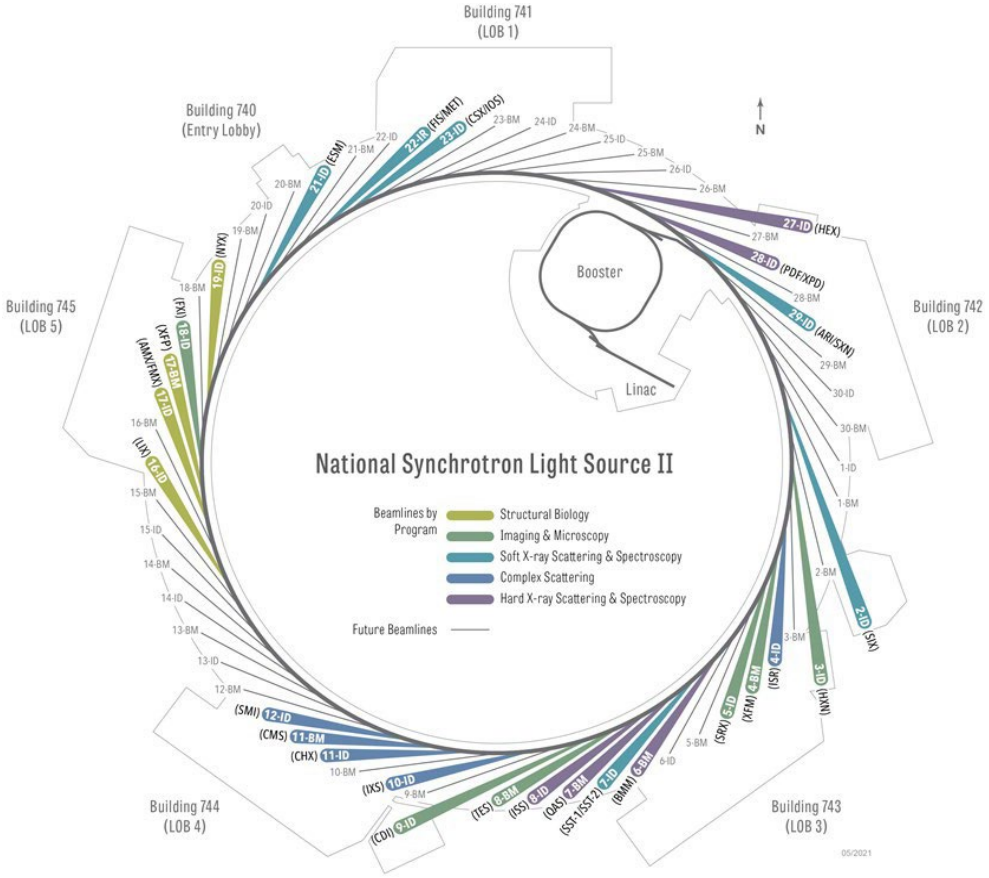

Figure 3.17: NSLS-II beamline diagram. Showing the various experimental beamlines hutches. Taken from [22].

Synchrotrons produce radiation by injecting electrons of near relativistic speeds (approaching the speed of light, c = 3 x 10^8 m s^{-1}) that have been produced by an electron gun and accelerated by a linear accelerator (LINAC) the booster. The booster subsequently uses a series of bending magnets to further increase the energy of the electrons to 3 GeV before injecting them into the storage ring [23]. The storage rings have both straight and curved sections, in the curved sections bending magnets are used to accelerate electrons perpendicular to their velocity in a circular path, producing high intensity X-rays emitted across a broad spectrum of wavelengths tangential to the direction of acceleration. In straight sections, an array of magnets called wigglers and undulators, collectively called insertion devices.

Insertion devices, where electrons are forced to oscillate back and forth by passing through electromagnetic fields of opposite polarity, causing the emission of X-rays in the process. Undulators only cause small deflections, allowing for the emission of X-rays that can overlap with those produced on the next lap. This overlap can cause constructive interference and increase the intensity of X-rays at energies that the undulator is tuned to and, at energies it is not tuned for, the almost complete cancelation of the waves (deconstructive interference) [18]. The emitted X-rays can be collimated by

a series of mirrors and focused onto a sample by travelling down beamline 'hutches'. In the optics hutch, monochromators are used to selectively tune the energy of the X-ray beam, or alternatively diffraction gratings are frequently used for softer X-rays, and mirrors are used to focus the beam footprint and scan across specific energies. The treated beam is then passed onto the experimental hutch where it interfaces with a sample and XAS occurs.

3.6.6 XAS experimental setup

XAS data collected at the Ti K-edge (4966 eV), La L_3-edge (5483 eV), Pr L_3-edge (5964 eV), Nd L_3-edge (6208 eV), Sm L_3-edge (6716 eV), Eu L_3-edge (6977 eV), Gd L_3-edge (7243 eV), Tb L_3-edge (7514 eV), Dy L_3-edge (7790 eV), Ho L_3-edge (8071 eV), Er L_3-edge (8358 eV), Tm L_3-edge (8648 eV), Yb L_3-edge (8944 eV), Lu L_3edge (9244 eV) and Y K-edge (17038 eV) were acquired at beamline 6-BM at the National Synchrotron Light Source II (NSLS-II), Brookhaven National Laboratory (Upton, New York). The NSLS-II storage ring operates at 3 GeV and 400 mA and delivers X-rays in the energy range between 4.5 and 23 keV using a 3-pole wiggler. The optical system consists of a parabolic collimating mirror, Si(111) and Si(311) monochromators, a toroidal focussing mirror, and an harmonic rejection mirror [24]. The beamline offers several modes of operation; in this study the Si(111) monochromator and an unfocussed beam were used. Samples were analysed either solely in transmission mode or simultaneously in transmission and fluorescence mode. In both cases the beam size was collimated using slits, to 1 mm in the vertical and 6 mm in the horizontal. Ionisation chambers were utilised to measure the incident (I_0) and transmitted (I_t) X-ray energies, and a 4-element Si drift detector (SII Vortex ME4, Hitachi) was used to collect the fluorescence signal. The samples were mounted between the incident and transmission ionisation chambers either perpendicular to the direction of the beam (transmission mode), or at 45^o to both the incident and the vortex detector (combined transmission and fluorescence). A photo of the experimental setup can be found in Figure 3.18. Dead-time correction was performed on the fluorescence signal using the method previously described by *Woicik et al.* [25].

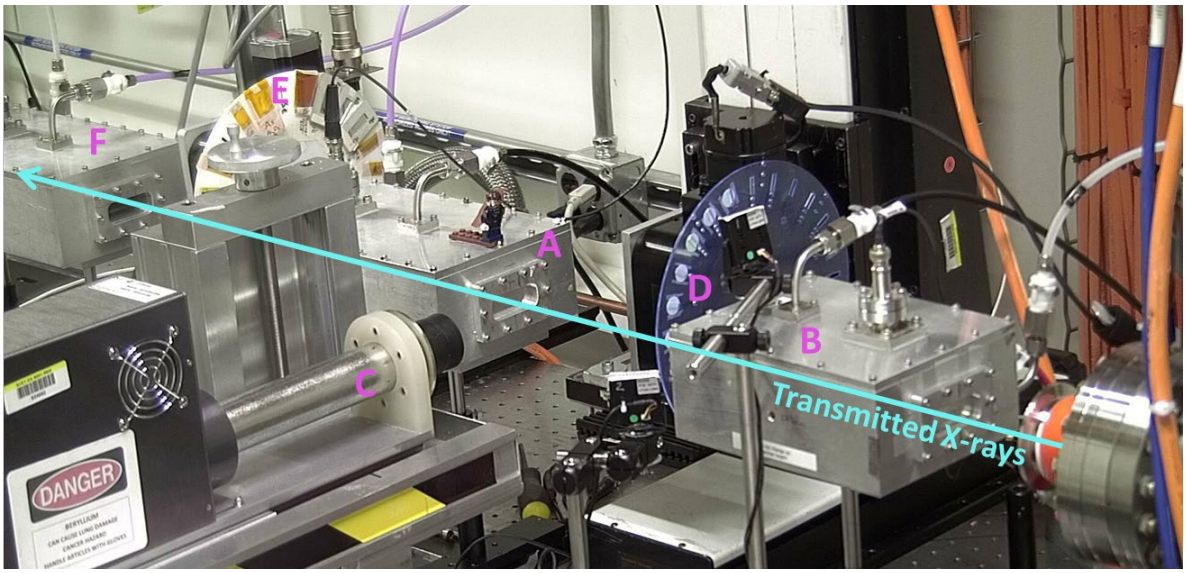

Figure 3.18: Photograph of XAS experimental setup. Major components are labelled A) incident ionisation chamber, I_0, B) transmission ionisation chamber, I_t, C) fluorescence detector, I_f, positioned at 45° to the incident X-ray beam and detector, D) sample wheel, allowing automated changing of samples, E) reference wheel and F) reference ionisation chamber, I_r

Data were acquired at the Ti K-edge, Ln L_3-edge, and the Y K-edge as appropriate. At the Ln L_3 and Y K-edges, spectra were collected over four regions between -200 eV and 16k (values relative to E0) with energy steps of 10 eV (-200 to -30), 2 eV (-30 to -10), 0.5 eV (-10 to 20), and 0.05k (20 – 16k). At the Ti K-edge spectra were collected between -200 and 12k with energy steps of 10 eV (-200 to -30), 2 eV (-30 to -10), 0.25 eV (-10 to 20), and 0.05k (20 – 12k). the data accumulation time was 1 s step-1 for all regions and for each sample multiple scans were averaged to improve signal to noise ratio. To ensure accurate energy calibration and reproducibility (± 0.05 eV), transmission spectra of metal foils (Ti, Cu, Y) were acquired simultaneously with the samples. The foils were placed downstream of the sample between the transmission (I_t) and reference (I_r) ion chambers. The position of the first inflection point for each foil was set to the absolute energy values given by *Bearden and Burr* [26]. Data reduction and analysis was performed using the Demeter suite of programmes [8], [27].

Samples and standards were prepared by homogeneously mixing finely ground powder specimens with polyethylene glycol (PEG) and uniaxially pressing them to form 13mm diameter pellets with a thickness of ca. one absorption length. PEG, which is transparent to X-rays of the energies used in these experiments, is used to act as a binder, securing the homogenously distributed powder samples in a shape and size appropriate for measurement.

3.6.7 GAXAS experimental setup

To probe the surface layer of irradiated bulk monoliths, the angle of incidence of the X-ray beam was determined using Equation 3.6 such that the penetration depth was set to 300 – 700 nm, depending on the region on interest, ensuring at least 95 % of the incident X-rays were absorbed within a thickness xx. Samples were placed on a motor-driven stage permitting translation in the x-, y-, z-axis and rotation about z- and x-axis. The sample was moved in the x and y directions to bisect the X-ray beam and was tilted about the z- and x-axis in relation to the plane of the incoming X-ray beam until flat (the maxima of the transmitted X-ray intensity). The incident angle of the X-ray beam was then set to a value corresponding to a chosen penetration depth. An example of the experimental setup can be found in Figure 3.19.

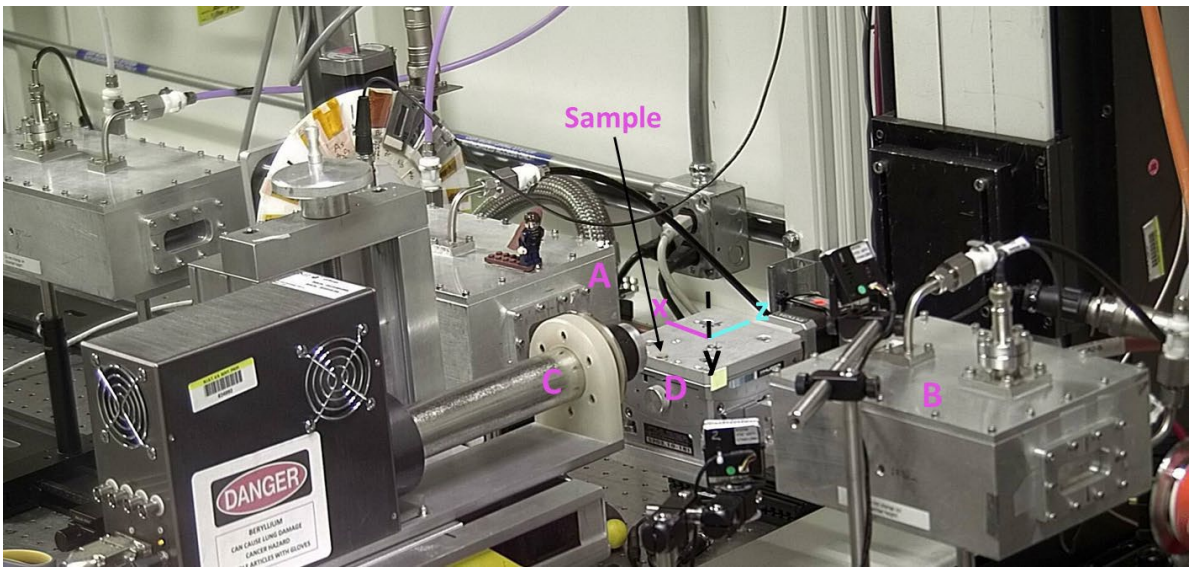

Figure 3.19: Photograph of GAXAS experimental setup. Major components are labelled A) incident ionisation chamber, I_0, B) transmission ionisation chamber, I_t, C) fluorescence detector, I_f, positioned at 45° to the incident X-ray beam and detector and D) the motor driven goniometer permitting translation through the x-, y-, z-axis and rotation about the x- and z-axis

3.6.8 XAS Data analysis

3.6.8.1 XANES and pre-edge analysis

Initial raw data processing involved a background subtraction (modelled with a cubic spline) and normalisation procedure outlined by [8], [28]. This procedure was required to allow direct comparison between data from different samples and the reference compounds. This was achieved by defining two regions of the data, the pre-edge range and the normalisation range, which are defined as before and after the edge, E_0, respectively. Lines are regressed through the data, a straight line through the data in the pre-edge range and a three term quadratic polynomial through the normalisation range (see Figure 3.20. The normalisation parameters are then varied until good normalisation is achieved

(typically through visual inspection of the data, aiming to have the lines pass through the middle of the data). In order to extract qualitative diagnostic information from the pre-edge regions of the spectra, modelling using a methodology similar to that described previously in the literature was performed [29], [30]. The spectral region in the 4965 – 5040 eV range was deconvoluted into a step-like arctangent function and a set of Gaussian components. The arctangent function was used to model the photoelectric edge step that represents the transition of ejected photoelectrons into the continuum [29]. The Gaussian components were included to model the pre-edge features (located ca. 20 eV before the crest on the absorption edge), features on the steeply sloped side of the absorption edge, and features between the edge and the second major absorption crest at ca. 5000 eV [29]. In oxides, the features in the pre-edge are attributed to electron transitions from the 1s energy level in the core Ti atoms to hybridised Ti *3d* / O *2p* molecular orbitals and they contain information about the local coordination environment of the absorbing Ti atoms. The other features on the main part of the absorption edge are dominated by multiple scattering of the photoelectric wave with the local neighbouring atomic shells and are sensitive to details of the ligand arrangement around the central absorber [29]–[31]. The position and normalised height for each pre-peak component were extracted from the spectra by fitting the arctangent and Gaussians using the nonlinear least–square fitting routine SOLVER in Microsoft Excel. The position of the pre-edge was assigned by taking the intensity weighted average of the energy positions for the first four fitted Gaussian components. An example of a fit using the above procedure for Ti K-edge data of Y_2TiO_5 is shown in Figure 3.21. Here the energy position was determined to be 4970.63 eV with a normalized pre-edge peak height of 0.196.

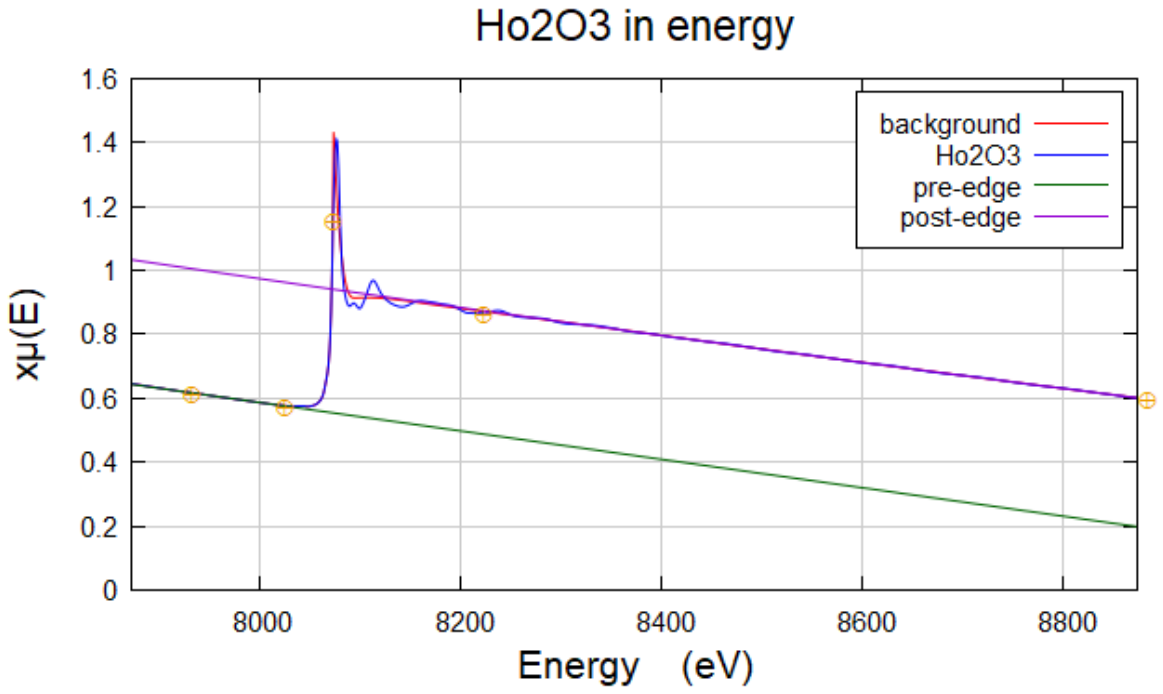

Figure 3.20: Ho_2O_3 XAS spectrum of the Ho L_3-edge (8071 eV) with pre- and post-edge normalisation lines

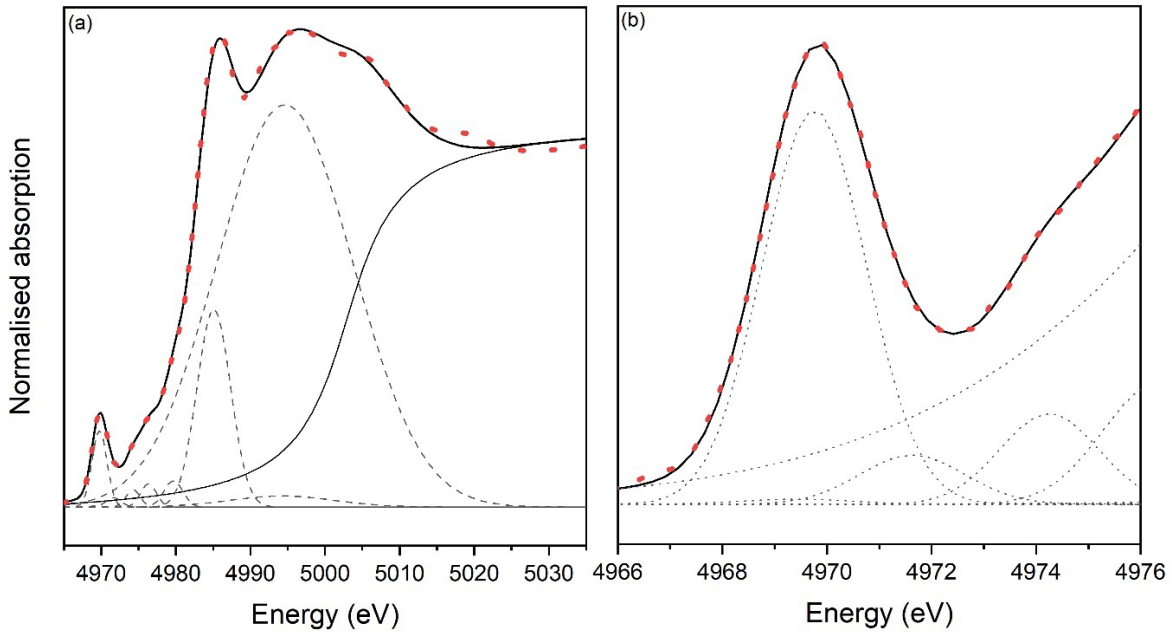

Figure 3.21: Fitting of XANES features for Y2TiO5 (Q). (a) XANES region (b) pre-edge features. The data were fit using combinations of Gaussian and arctangent functions (shown as grey lines); data are shown by red dashed lines, fit is shown by a solid black line

To complement the spectral fitting procedure described above, linear combination fitting (LCF) was performed on the pre-edge region of the data. The LCF routine in the Athena package uses least-squares minimisation, to fit linear combinations of various reference compounds, to a narrow region around the pre-edge features in the aligned and normalised sample data.

3.6.8.2 EXAFS analysis

Information about the local structural environment around the cations was obtained by fitting the extended X-ray fine structure (EXAFS) region of the XAS spectra. The features in the EXAFS region are extracted by subtracting the photoelectric edge step from the data and converting the energy values (eV) to wavenumber *k* ($Å^{-1}$). Applying a Fourier Transform (FT) to the data will then generate a function where peaks represent the position of shells of atoms surrounding the central absorber atom. The fitting process requires the generation of appropriate scattering paths to model the interactions between the ce-ntral absorber cation and the surrounding anions and cations, in the nearest neighbour atom shells. Scattering paths were generated by applying the FEFF6 algorithm in Artemis [27], [28], which uses *ab initio* theory, to an appropriate structural model. The model is taken from a Crystallographic Input File [32] which can be modified, as required, to correctly represent the

stoichiometry of the samples being analysed. Individual scattering paths can be added to the model of the local structure to represent the core absorber – neighbour backscattering contributions. Contribution specific parameters, such as path length (*R*), degeneracy (*N*), thermal parameter (σ^2), and global parameters, such as the amplitude reduction factor (S^2) and shift in absorption edge energy (δE_0), are applied to each path and allowed to refine.

The construction of models specific to each dataset is discussed in more detail in the results section as they were pivotal to informing the interpretation of data collected.

A detailed understanding of the experimental methods used in any piece of work is crucial for facilitating reliable reproduction of results, the accurate interpretation of results and errors and, ultimately, the successful application of any research outside of laboratory environments. The aim of this chapter was to such given credibility to the results discussed in the following chapters (4 – 7), necessary for any future potential application of the Ln_2TiO_5 ceramics for HLW immobilisation, or any other application. This chapter has covered the synthesis of Ln_2TiO_5 ceramics, through both solid-state and molten salt methods, characterisation methods (XRD, SEMD/EDX, XAS etc.) and the techniques used to simulate and characterize the damage caused by α-decay events in crystalline matrices. The following chapters make frequent use of these experimental techniques and were pivotal in developing a more detailed understand of the local coordination of the orthorhombic, hexagonal and cubic structures of Ln_2TiO_5 stuffed pyrochlores and the mechanisms and responses of these materials to intense radiation damage

3.6.8.3 Bond Valence Sum

The bond valence sum (BVS) provides a method of validation of a crystal structure model. Distances of neighbouring anions and cations are considered as bonds, though not of necessarily of equal strength. The bond valence s_{ij}, which is the number attributed to the bond between atoms *i* and *j*, is inversely proportional to bond distance. The summation of s_{ij} over all pairs in in a coordination shell is equal to the formal oxidation state of the absorber cation. The bond valence sum is given by (Brown and Altermatt 1985)

$$V_i = \sum_j \exp\left(\frac{r_0 - r_{ij}}{B}\right) \qquad \textbf{Equation 3.31}$$

Where r_0 and r_{ij} are the observed and tabulated bond lengths, between the atoms *I* and *j* and B is an empirical parameter (typically 0.37 for most oxides). Reference bond lengths were taken from (Brown and Altermatt 1985). BVS's were used throughout the EXAFS analysis as a tool to independently validate models as they are determined independently of S_0^2 and *N*, using only the absorber-scatterer pair distance, *D*, of cations in the first coordination shell. As an example, if the refined coordination

number for Yb^{3+} in a model is 8, but the BVS returns a value of 4.3 valence units (v.u.) (it is expected that the BVS for an accurate model will return a value of 3 v.u. for Yb^{3+} as this is the formal valence of the Yb) then the model is incorrect as the bond lengths for the Yb-O first coordination shell are too short and such a structure would be too physically unstable to exist.

3.7 Summary

A detailed understanding of the experimental methods used in any piece of work is crucial for facilitating reliable reproduction of results, the accurate interpretation of results and errors and, ultimately, the successful application of any research outside of laboratory environments. The aim of this chapter was to such given credibility to the results discussed in the following chapters (4 – 7), necessary for any future potential application of the Ln_2TiO_5 ceramics for HLW immobilisation, or any other application. This chapter has covered the synthesis of Ln_2TiO_5 ceramics, through both solid-state and molten salt methods, characterisation methods (XRD, SEMD/EDX, XAS etc.) and the techniques used to simulate and characterize the damage caused by α-decay events in crystalline matrices. The following chapters make frequent use of these experimental techniques and were pivotal in developing a more detailed understand of the local coordination of the orthorhombic, hexagonal and cubic structures of Ln_2TiO_5 stuffed pyrochlores and the mechanisms and responses of these materials to intense radiation damage.

3.8 References

[1] C. Lopez, X. Deschanels, J. M. Bart, J. M. Boubals, C. Den Auwer, and E. Simoni, "Solubility of actinide surrogates in nuclear glasses," *J. Nucl. Mater.*, vol. 312, no. 1, pp. 76–80, 2003.

[2] M. Broseghini, M. D'Incau, L. Gelisio, N. M. Pugno, and P. Scardi, "Effect of jar shape on high-energy planetary ball milling efficiency: Simulations and experiments," *Mater. Des.*, vol. 110, pp. 365–374, Nov. 2016.

[3] E. N. Lightfoot, "Fundamentals of ceramic powder processing and synthesis," *Chem. Eng. Sci.*, vol. 53, no. 1, p. 187, Jan. 1998.

[4] M. N. Rahaman, "Ceramic processing and sintering, second edition," *Ceram. Process. Sintering, Second Ed.*, pp. 426–472, Jan. 2017.

[5] T. Kimura, "Molten Salt Synthesis of Ceramic Powders," in *Advances in Ceramics - Synthesis and Characterization, Processing and Specific Applications*, InTech, 2011, pp. 75–100.

[6] R. Guinebretière, '*X-Ray Diffraction by Polycrystalline Materials*'. Wiley-ISTE, pp. 3-77, 2010.

[7] A. J. London, B. K. Panigrahi, C. C. Tang, C. Murray, and C. R. M. Grovenor, "Glancing angle XRD analysis of particle stability under self-ion irradiation in oxide dispersion strengthened alloys," *Scr. Mater.*, vol. 110, pp. 24–27, Jan. 2016.

[8] B. Ravel and M. Newville, “ATHENA, ARTEMIS, HEPHAESTUS: Data analysis for X-ray absorption spectroscopy using IFEFFIT,” in *Journal of Synchrotron Radiation*, 2005, vol. 12, no. 4, pp. 537–541.

[9] Y. Wang *et al.*, “Real-time synchrotron x-ray studies of low- and high-temperature nitridation of c -plane sapphire,” *Phys. Rev. B - Condens. Matter Mater. Phys.*, vol. 74, no. 23, p. 235304, Dec. 2006.

[10] P. J. Goodhew, J. Humphreys, and R. Beanland, *Electorn Microscopy and Analysis*, vol. 3rd. Taylor & Francis, pp. 1-133, 2001.

[11] L. Leay *et al.*, “Resurgence of a nation’s radiation science driven by its nuclear industry needs,” *Appl. Sci.*, vol. 11, no. 23, Dec. 2021.

[12] N. Mason, “Acceleration Operations & Theory, DAFNE Masterclass (Presentation), Dalton Cumbrian Facility.” 2019.

[13] “Pelletron Charging System - National Electrostatics Corp.” [Online]. Available: https://www.pelletron.com/products/pelletron-charging-chains/. [Accessed: 30-Mar-2022].

[14] J. F. Ziegler, M. D. Ziegler, J. P. Biersack, J. F. Ziegler, M. D. Ziegler, and J. P. Biersack, “SRIM - The stopping and range of ions in matter (2010),” *NIMPB*, vol. 268, no. 11–12, pp. 1818–1823, Jun. 2010.

[15] R. E. Stoller, M. B. Toloczko, G. S. Was, A. G. Certain, S. Dwaraknath, and F. A. Garner, “On the use of SRIM for computing radiation damage exposure,” *Nucl. Instruments Methods Phys. Res. Sect. B Beam Interact. with Mater. Atoms*, vol. 310, pp. 75–80, Sep. 2013.

[16] W. J. Weber and Y. Zhang, “Predicting damage production in monoatomic and multi-elemental targets using stopping and range of ions in matter code: Challenges and recommendations,” *Curr. Opin. Solid State Mater. Sci.*, vol. 23, no. 4, p. 100757, Aug. 2019.

[17] D. E. Sayers, E. A. Stern, and F. W. Lytle, “New Technique for Investigating Noncrystalline Structures: Fourier Analysis of the Extended X-Ray—Absorption Fine Structure,” *Phys. Rev. Lett.*, vol. 27, no. 18, pp. 1204–1207, Nov. 1971.

[18] S. Calvin, *XAFS for Everyone*. CRC Press, pp. 1-40, 2013.

[19] S. D. Kelly, D. Hesterberg, and B. Ravel, “Analysis of Soils and Minerals Using X-ray Absorption Spectroscopy,” John Wiley & Sons, Ltd, 2015, pp. 387–463.

[20] S. Pizzini *et al.*, “Instrumentation for glancing angle x-ray absorption spectroscopy on the Synchrotron Radiation Source,” *Rev. Sci. Instrum.*, vol. 60, no. 7, p. 2525, Aug. 1998.

[21] C. Maurizio, M. Rovezzi, F. Bardelli, H. G. Pais, and F. D'Acapito, "Setup for optimized grazing incidence x-ray absorption experiments on thin films on substrates," *Rev. Sci. Instrum.*, vol. 80, no. 6, p. 063904, Jun. 2009.

[22] BNL, "BNL | NSLS-II Beamline Map." [Online]. Available: https://www.bnl.gov/nsls2/beamlines/map.php. [Accessed: 04-Apr-2022].

[23] "BNL | NSLS-II Accelerator Complex." [Online]. Available: https://www.bnl.gov/nsls2/accelerator/machine.php. [Accessed: 05-Apr-2022].

[24] C. Weiland *et al.*, "NIST HAXPES at NSLS and NSLS-II," *Synchrotron Radiat. News*, vol. 31, no. 4, pp. 23–28, Jul. 2018.

[25] J. C. Woicik, B. Ravel, D. A. Fischer, and W. J. Newburgh, "Performance of a four-element Si drift detector for X-ray absorption fine-structure spectroscopy: Resolution, maximum count rate, and dead-time correction with incorporation into the ATHENA data analysis software," *J. Synchrotron Radiat.*, vol. 17, no. 3, pp. 409–413, 2010.

[26] J. A. Bearden and A. F. Burr, "Reevaluation of X-ray atomic energy levels," *Rev. Mod. Phys.*, vol. 39, no. 1, pp. 125–142, Jan. 1967.

[27] B. Ravel and M. Newville, "ATHENA and ARTEMIS: Interactive graphical data analysis using IFEFFIT," *Phys. Scr. T*, vol. T115, no. T115, pp. 1007–1010, 2005.

[28] M. Newville, "IFEFFIT: Interactive XAFS analysis and FEFF fitting," *J. Synchrotron Radiat.*, vol. 8, no. 2, pp. 322–324, Mar. 2001.

[29] A. G. Waychunas, "Synchrotron radiation xANES spectroscopy of Ti in minerals: Effects of Ti bonding distances, Ti valence, and site geometry on absorption edge structure," *American Min.,* vol. 72, no. 1-2, pp. 89-101 1987.

[30] F. Farges, G. E. Brown, and J. J. Rehr, "Coordination chemistry of Ti(IV) in silicate glasses and melts: I. XAFS study of titanium coordination in oxide model compounds," *Geochim. Cosmochim. Acta*, vol. 60, no. 16, pp. 3023–3038, Aug. 1996.

[31] P. Behrens, J. Felsche, S. Vetter, B. Schulz-Ekloff, N. 1 Jaegerb, and W. Niemannc, "A XANES and EXAFS Investigation of Titanium Silicalite," *J. CHEM. SOC., CHEM. COMMUN*, 1991.

[32] S. R. Hall, F. H. Allen, and I. D. Brown, "The crystallographic information file (CIF): a new standard archive file for crystallography," *Acta Crystallogr. Sect. A*, vol. 47, no. 6, pp. 655–685, Nov. 1991.

4. Draft paper: Probing the local coordination of Ln_2TiO_5 (Ln = Yb, Y) through multi-element X-ray absorption techniques

In this chapter, the structure of cubic Ln_2TiO_5 stuffed pyrochlores is explored *via* XAS. Whilst the long-range or Ln_2TiO_5 crystal structures is relatively well characterised, the short-range ordering is not. This has led to conflicting accounts regarding the local structures of cubic Ln_2TiO_5 compounds, where they are identified as having either pyrochlore-like or orthorhombic ordering. This section will investigate the effects different cooling regimes have on the local structure of cubic Yb_2TiO_5 and Y_2TiO_5 stuffed pyrochlores. These two compounds were selected on the basis of having significantly differently sized Ln ionic radii (0.985 Å and 1.019 Å, respectively), within the limits of Ln_2TiO_5 compounds that can crystalise in a cubic symmetry, facilitating a comparison of the effects on ionic radius on the local structural ordering.

The work presented here is the form of a manuscript that has been submitted to Acta Materialia, and as such is written in the appropriate style for that journal. Supporting information for each paper follows the refences sections.

The author's contribution was the synthesis of samples, X-ray diffraction, analysis of XANES and EXAFS data and writing of the manuscript. XAS data were acquired by the author in collaboration with M. C. Stennett, N. C. Hyatt. Manuscript proofing and editing were assisted by R. J. Hand, L. T. Townsend, B. Ravel and M. C. Stennett. All authors contributed to the discussion and interpretation of data.

Probing the local coordination of Ln_2TiO_5 (Ln = Yb, Y) through multi- element X-ray absorption techniques

Daniel A. Austin[1], Luke T. Townsend[1], Martin C. Stennett[1], Daniel J. Bailey[1], Bruce Ravel[2], Russell J. Hand[1], Neil C. Hyatt[1]

[1] *Immobilisation Science Laboratory, Department of Materials Science and Engineering, University of Sheffield, Sheffield S1 3JD, United Kingdom*

[2] *National Institute of Standards and Technology, 100 Bureau Drive, Gaithersburg, MD 20899, USA*

Abstract

The design and application of ceramic wasteforms for nuclear waste immobilisation requires extensive knowledge of structure and behaviour in order to understand how their properties will be affected by waste disposal conditions such as radiation damage and corrosion. One of the ceramic materials for nuclear waste immobilisation that is of significant current interest is the 'stuffed' pyrochlore (Ln_2TiO_5 (Ln = Yb, Y) and whilst previously investigated, there still exists a paucity of structural information from a local coordination environment up to a supercell scale. In this study, we comprehensively probe the local structural environment in Ln_2TiO_5 (Ln = Yb, Y) stuffed pyrochlores with varied thermal histories by X-ray absorption spectroscopy (XAS), trialling multiple different XAS fitting models in order to establish the most accurate and robust model that describes these phases. The difference in short- and long-range ordering of these materials is demonstrated through a combination of XAS and X-ray diffraction, clearly showing that the local structure exhibits a structure closely related to the cubic $Ln_2Ti_2O_7$ phase, wherein the Ti is reduced to 5-fold coordination, but the Ln cations remain well described as an 8-fold coordinated structural motif. The results of this study provide a key underpinning structural model for stuffed pyrochlore phases, providing clarity on the short- and long-range order of the structures, whilst acting as a foundation for more information to be gleaned from further studies, such as dissolution or irradiation experiments.

1. Introduction

Rare-earth titanates, with nominal stoichiometry Ln_2TiO_5 have received significant interest as potential application in the nuclear industry as ceramic wasteforms for actinide waste immobilisation, additives in inert matrix fuels and alloy additives in oxide dispersion strengthened (ODS) steels due to their chemical flexibility and high tolerance for radiation induced damage [1]–[7]. Ln_2TiO_5 compounds can be considered as a derivative of the $Ln_2Ti_2O_7$ pyrochlore phase, wherein additional lanthanides are 'stuffed' onto the B-site (i.e. $Ln_2(Ln_{0.66}Ti_{1.33})O_{6.67}$), with charge compensation achieved through the formation of vacancies in the anionic array [1]. Ln_2TiO_5 compounds are referred to as stuffed pyrochlores throughout. These compounds have been reported to adopt various different structures based on the ionic radius of the Ln cations and the compound's thermal history. Compounds

containing relatively large lanthanides (Ln = La – Sm, where the ionic radii vary between 1.16 Å – 1.08 Å) are reported to crystallise in an orthorhombic *Pnma* phase, which is best described as a framework of intersecting columns of edge sharing LnO_7 polyhedra [8], with Ti cations occupying interstices within the tunnels forming TiO_5 square pyramids (Figure A1a). The smaller lanthanides (Ln = Er - Lu) are reported to adopt a defect-fluorite *Fm-3m* structure, where the disordering of the cation and anion vacancy sites yield average 7-fold coordination polyhedra (Figure A1c) [8], compared to the ordered LnO_8 and TiO_6 sites, respectively, in the parent pyrochlore ($Ln_2Ti_2O_7$) structure (Figure A1d) [8]. Furthermore, various studies have shown that the defect-fluorite compounds show complex structural modulations commensurate with pyrochlore *Fd-3m* ordering as observed in Ho_2TiO_5, Yb_2TiO_5 and $Sm_{2-x}Yb_xTiO_5$ (x = 0 – 2) or alternatively observed in Yb_2TiO_5 [9]–[12].

The short-range ordering of cubic Ln_2TiO_5 has been the topic of various studies utilising different experimental techniques, however, there appears to be a lack of consensus on the particular structure that is observed. Recently, studies have shown that defect-fluorite phases can exhibit different ordering on the short-range compared to the long-range. X-ray and neutron diffraction studies have reported weak diffuse reflections in diffraction patterns of defect fluorite type Ln_2TiO_5 compounds (with Ln = Ho, Yb), which can be indexed as a pyrochlore super-cell. Neutron diffraction studies on Ho_2TiO_5 and Yb_2TiO_5 heat treated in argon at 1700°C and fast cooled (~ 60 °C min^{-1}) were conducted by *Lau et al.* The structures were refined using a model with cubic fluorite symmetry (*Fm-3m*), although the presence of diffuse scattering was attributed to short range pyrochlore ordering [9], [13]. In the same study, slow cooled samples synthesised using a floating zone furnace showed longer-range pyrochlore ordering, as confirmed by transmission electron microscopy, although the presence of streaking and additional weak reflections indicate the existence of more complex structural modulations [9]. *Shlyakhtina et al.* synthesised Ln_2TiO_5 (Ln = Ho – Lu) at 1600 °C and investigated the effect of cooling rate on the structure using X-ray diffraction [14]. Fast cooled samples (~ 130 °C min^{-1}) adopted the defect-fluorite *Fm-3m* structure whilst in patterns acquired from slow cooled samples (~ 0.1 °C min^{-1}) superstructure reflections were observed consistent with stabilisation of the pyrochlore *Fd-3m* structure. These studies serve to highlight the complexity surrounding the possible differences between short- and long-range ordering and the necessity of further investigations which are ideally suited to probe the short-range ordering of these materials.

Further investigations utilising electron diffraction (ED) have demonstrated that short-range pyrochlore domains are present in samples of Yb_2TiO_5, which do not exhibit any additional weak reflections. The size of these domains decreases as the size of the lanthanide decreases, for $Sm_{0.6}Yb_{1.6}TiO_5$ the size of the domains was measured to be 6 nm and for Yb_2TiO_5 2 nm [10]. The small size of these domains likely mean that they cannot be detected through XRD due to the technique's low sensitivity to local ordering effects. Neutron diffraction pair distribution function (PDF) analysis have also indicated the possibility of orthorhombic ordering demonstrated through pair distribution functions analysis of Yb_2TiO_5. In this work, it was found that there was better evidence for

orthorhombic symmetry than cubic pyrochlore [12]. *Mullens et al.* demonstrated that the Crystal Field Splitting (CFS) energies of Ti *3d* orbitals indicate a progressive 6 to 7-fold coordinated Ti as lanthanides are incorporated into the $Ln_2(Ti_{2-x}Ln_x)O_{7-x/2}$ solution, where Ln = Yb or Tm [15], [16]. Given the lack of clarity in literature whether 7-fold coordinated Ti exists and that as, Pauling's first rule stipulates, the coordination number of a cation is directly related to the ratio of ionic radii of the cation and the surrounding anions, (r_c/r_a) , as such there is difficulty in satisfying this rule for Ti in a 7-fold coordination as r_{Ti}/r_O would be would be much smaller than the minimum stability radius ratio given by Pauling [17]. Evidently, due to the lack of coherent findings in the literature it's important to develop a robust and consistent understanding of the structure of these stuffed pyrochlores. This contribution aimed to pursue that aim by using X-ray absorption spectroscopy (XAS) techniques.

Compounds with intermediate sized cations (Eu – Ho, Y, with ionic radii between 1.07 Å – 1.02 Å) demonstrate polymorphism, and apart from the previously discussed structures, can also adopt a hexagonal *$P6_3/mmc$* structure (Figure A1b) [3]. This structure consists of edge-sharing LnO_6 octahedra, separated by TiO_5 trigonal bipyramids. Stabilisation of these polymorphs was achieved through rapid cooling of the ceramic sample, synthesis of single crystal samples or by the addition of lanthanides of different ionic radii. Aughterson *et al.* synthesised a single crystal of cubic Dy_2TiO_5 through the addition of MoO_3 as a flux to facilitate rapid cooling [18]. In the same study, it was shown that a hexagonal polymorph of Dy_2TiO_5 was possible to obtain through a combination of multiple sintering steps along with rapid cooling of the ceramic product. Furthermore, it was shown that a hexagonal polymorph can be synthesised by substituting a lanthanide of sufficiently different ionic radius into the structure, with the ionic radii ratio of cations (r_A/r_B,) then tailored to achieve different crystal symmetries [19].

Insight into the structural properties of stuffed pyrochlores is fundamental to understanding and predicting how these materials will behave in high intensity radiation fields or in long-term, geological disposal. This study was devised to explore the structure of Ln_2TiO_5 (Ln = Yb or Y) stuffed pyrochlores synthesised with varying thermal histories by utilising a variety of applied X-ray techniques. The local coordination environment (i.e., short-range order) of samples was studied using XAS by considering XANES pre-edge peak fitting, linear combination fitting (LCF), and extended X-ray absorption fine structure (EXAFS) modelling. XRD was used to examine the effects of the processing conditions on the mid-to-long range order of stuffed pyrochlores. Given the strong structural relationship between structure types in the Ln_2TiO_5 series and conflicting descriptions of the short-range order of cubic Ln_2TiO_5 stuffed pyrochlores in literature (as pyrochlore-like or orthorhombic), this contribution will explore different possible local descriptions. As such, multiple EXAFS models were considered, including the space groups *Fd-3m*, *$P6_3$-mmc*, and *Pnma*, to determine the best fitting model for these systems, with the most accurate description of the local environment.

2. Materials and methods

2.1 Ceramic synthesis

Y_2TiO_5 and Yb_2TiO_5 samples were prepared via a solid-state synthesis route. Samples were batched using the component oxides Ln_2O_3 (>99.9 %, Alfa Aesar) and TiO_2 (>99.99 %, Alfa Aesar), according to target stoichiometry. Ln_2O_3 and Y_2O_3 were dried at 800 °C and TiO_2 was dried at 180 °C overnight prior to weighing. The batches of reagents were planetary ball milled (Pulverisette 6, Fritsch) at 500 rpm, for 15 minutes, using isopropanol as a carrier fluid and the resulting slurry was dried in an 80 °C oven. After drying, the powder cake was broken up and passed through a 63 µm (250 mesh) stainless steel sieve. 0.5 g aliquots of the master batch were pressed into 10 mm diameter pellets under 4 tonnes of uniaxial pressure.

Pellets of unreacted Y_2TiO_5 and Yb_2TiO_5 were subject to different heating schedules in a chamber furnace under an air atmosphere. All programmed schedules involved a ramp to 1500 °C at a rate of 5 °C min^{-1} and were held at temperature for 24 hours. After the dwell, samples were either quenched in water from 1500 °C or allowed to cool at a rate of 5 °C min^{-1} or 1 °C min^{-1}.

2.2 X-ray diffraction (XRD)

All samples and standards were analysed using powder X-ray diffraction (XRD) analysis to ascertain the phase assemblage. XRD data were acquired using a Bruker D2 Phaser diffractometer, operating with Cu Kα radiation and a Lynxeye solid state detector. Data were acquired over the range $0° < 2\theta < 70^o$, with a step size of 0.02^o, counting for 1.8 s $step^{-1}$, and rotation of the sample at 30 rpm. Diffraction data were analysed for phase composition using the PDF -4+ database and the lattice parameters determined by Le Bail analysis [20] using the DIFFRAC.SUITE TOPAS software [21].

2.3 X-ray absorption spectroscopy

X-ray absorption spectroscopy (XAS) data were acquired on a series of samples at beamline 6-BM at the National Synchrotron Light Source II (NSLS-II), Brookhaven National Laboratory (Upton, New York). Samples were measured either in transmission mode, or simultaneously in both transmission and fluorescence mode at room temperature using a 1 mm (vertical) by 6 mm (horizontal) beam. Ionisation chambers were utilised to measure the incident (I_0) and transmitted (I_t) X-ray energies, and a 4-element Si drift detector (SII Vortex ME4, Hitachi) was used to collect the fluorescence signal. Samples were prepared by homogeneously mixing finely ground powder specimens with polyethylene glycol and uniaxially pressing them to form 13 mm diameter pellets with a thickness of one absorption length. In order to aid interpretation, data was also acquired from several groups of standards: Y_2O_3

and Yb_2O_3, $Y_2Ti_2O_7$ and $Yb_2Ti_2O_7$, Dy_2TiO_5 and Gd_2TiO_5, $Ba_2SiTi_2O_8$ (fresnoite, Junnila Mine, California), and $Ni_{2.6}Ti_{0.7}O_4$. The syntheses of standards followed procedures outlined by previous authors [2], [7], [17], [26] and are outlined in the Supplementary information (SI), section B). All standards were confirmed to be phase pure by X-ray diffraction (Figure B1 of the SI).

Data were acquired at the Ti K-edge (4966 eV), Yb L_3-edge (8944 eV), and the Y L_3-edge (17038 eV) and energy calibration of the data was achieved by measuring metal foils (Ti, Cu, Y) simultaneously with the samples and adjusting absolute energy as necessary. Data reduction and analysis was performed using the Demeter suite of programmes with FEFF6 [22]–[24].

2.3.1 Ti pre-edge analysis

Initial raw XAS data processing utilised Athena of the Demeter software package and involved a background subtraction (modelled with a cubic spline) and normalisation procedure outlined previously by Newville *et al.* [22]–[24]. Fluorescence data were self-absorption corrected using an algorithm implemented within the Athena package [23]. In order to extract quantitative information, the pre-edge data of the Ti K-edge spectra were fit using the methodology described by Farges *et al.* [25], [26]. The spectral region in the 4965 – 5040 eV range was deconvoluted into a step-like arctangent function and a set of Gaussians components. The position of the pre-edge peak was assigned by taking the intensity weighted average of the energy positions for the first four fitted Gaussian components (an example of this fit can be found in the SI, section C).

To complement the spectral fitting procedure described above, linear combination fitting (LCF) was performed on the pre-edge region of the data using the Athena software package [23]. The reference compounds used include: pyrochlore $Ln_2Ti_2O_7$, Ln = Y or Yb, (octahedral TiO_6), Dy_2TiO_5 (trigonal bi-pyramidal TiO_5), Gd_2TiO_5 (square pyramidal TiO_5), fresnoite ($Ba_2SiTi_2O_8$, square pyramidal TiO_5), and $Ni_{2.6}Ti_{0.7}O_4$ spinel (tetrahedral TiO_4). All reference compounds were included as possible components and a combinatorial approach was adopted allowing the weighting parameter of each reference to vary, in order to reduce the misfit between the absorption data and the total fit. A constraint was applied that each variable weighting parameter (w_i) should be in the range $0 \leq w_i \leq 1$. The fitting range was fixed to be the pre-edge region, between -20 eV and -7 eV (relative to E_0), as this feature is robustly correlated to electronic and local structure of the Ti cation.

2.3.2 EXAFS analysis

Information about the local structural environment around the cations was obtained by fitting the EXAFS region of the XAS spectra. Models utilised Crystallographic Input Files [27] which were modified as required to correctly represent the stoichiometry of the samples being analysed. In models based on a cubic pyrochlore structure the Ti coordination number was refined, all other degeneracies of the scattering paths used were set in accordance with the stoichiometry. Global parameters amplitude reduction factor (S_0^2) and shift in absorption edge energy (ΔE_0) were applied to each path. S_0^2 parameters were fixed at values determined from appropriate standards and ΔE_0 was allowed to refine. Additionally, contribution specific parameters path length (R) and Debye-Waller factor (σ^2) were allowed to refine independently for each patch. Sequential improvement to the total fit can be assessed by comparing the reduction in the misfit (R-factor) between the fit and the data. Starting structures for EXAFS were informed by observations in literature [10], [28]–[30] and pre-edge analysis results. Bond valence sums were used as heuristic measurement of the accuracy of a crystal structure model as they are determined indepenantly from the coordination number (and S_0^2) and rely on the bond lengths of atoms in the first coordination shell and were a key metric used to understand the quality of fits in this study. BVS were calculated based on methods established by previous authors [31].

2.3.2.1 Refinement of Ti-O coordination

Application of the crystallographic models based on the *Fd-3m* $Y_2Ti_2O_7$ and $Yb_2Ti_2O_7$ structures (taken from [32], [33], respectively) to the data acquired from the Ln_2TiO_5 (recast as $Ln_2(Ln_{0.66}Ti_{1.33})O_{6.67}$) compounds required appropriate manipulation of the scattering paths generated by FEFF to reflect the differences in stoichiometry and site occupancy when compared to the $Ln_2Ti_2O_7$ standards. The amplitude reduction factor, S_0^2, was fixed at values refined from fitting Y Ti O (0.58 ± 0.07) and $Yb_2Ti_2O_7$ (0.54 ± 0.1) and the oxygen stoichiometry was refined to produce a satisfactory fit to the data (see section D of the SI).

2.3.2.2 Adjustment of structural model to account for Ln incorporation on the B-site

Multiple FEFF calculations were used to adjust the $Ln_2Ti_2O_7$ (Ln = Y, Yb) stoichiometry to reflect that of the target Ln_2TiO_5 stoichiometry and the distribution of Ln across the A- and B-site. Each single scattering path was weighted appropriately to account for the relative contribution to the signal from each of the two Ln central absorbers, found on the A- and B-sites (the S_0^2 for Ln(A) scattering paths were weighted by 0.75 and for Ln(B) by 0.25). The starting structures were again taken from *Haile et al.* and *Shlyakhtina et al.* [32], [33]. The initial iterations of this model included both A- and B-site

scattering paths, with the Ln(B)-O_1 degeneracy set to 5 (based on the results of the Ti K-edge model) and all other degeneracies were set appropriately. The resultant model was unable to be fit to a consistently satisfactory degree using a Ti coordination of 5, whilst the S ^{2} value was weighted by the appropriate signal contribution factor. To investigate the relative contribution of Ln(A) and Ln(B) oxygen paths the signal weighting factor was refined within a restraint and the weighting of the Ln(A) environment was found to approach unity, indicating that the contribution to the average EXAFS signal is dominated by A-site Ln cations. An example of this fit can be found in the SI (Figure E1, Table E1).

3. Results and Discussion

3.1 X-ray diffraction

All products were characterised by XRD to determine if any secondary phases were present. Figure 1 shows the XRD patterns of Y_2TiO_5 and Yb_2TiO_5 samples synthesised using different cooling regimes. All reflections were indexed on the cubic *Fm-3m* space group. Le Bail refinements were carried out using a defect-fluorite *Fm-3m* structure for all sample sets, with the determined unit cell parameters (Table 1) showing a steady decrease in unit cell volume as the cooling rate decreases., likely due to possible growth in the nanodomain sizes, as is seen in samples of Ho_2TiO_5 and Yb_2TiO_5 where the larger Ho cations afford both a larger unit cell volume and larger pyrochlore-like nanodomains, sufficiently so that weak reflections are observable in the XRD pattern, compared to [11], [30], [34] . Additional reflections at 15^o 2θ were observed for the Y_2TiO_5 furnace cooled sample and Y_2TiO_5 and Yb_2TiO_5 slow cooled samples that could be indexed on a *Fd-3m* pyrochlore supercell ($a_{py} = 2a_{df}$), as shown by the Miller indices labelled on the slow cooled samples. These reflections are attributed to a pyrochlore superstructure, thought to consist of randomly oriented pyrochlore nanodomains which give rise to an average long-range defect-fluorite structure [9], [10], [30], [34]. Here, a possible tripling of the pyrochlore unit cell in the <111> planes has also been reported to be observed through selected area ED [30]. The inset of Figure 1 shows the <111> reflection (indexed in the pyrochlore structure), which is pronounced for the slow cooled samples and transitions to diffuse for the quenched samples, indicating a change in the length of the short-range ordering [30]. *Aughterson et al.* determined that samples with composition $Sm_{0.6}Yb_{1.4}TiO_5$, which exhibited additional superstructure peaks, was most appropriately modelled through this structure due to the increased occupancy of the O(2) site [10].

The size of these pyrochlore nanodomains, observed to be 2 nm in Yb_2TiO_5 and 3 nm in Ho_2TiO_5 [13], gives rise to the detection of these weak supercell reflections, as such weak reflections are only observable *via* XRD in Ho_2TiO_5. Similar observations have been shown to occur when the thermal history of these compounds consists of slow cooling to 840 °C and then quenching in liquid nitrogen [35]. The size of nanodomains was reported to be due to a liquid-assisted growth of the nanodomains at high temperatures [35]. In our study, the cooling regime appears to influence the size of these

nanodomains given the appearance in both slow cooled samples and absence of in both quenched samples, as the slower cooling rate likely allows for the local ordering to anneal into larger domains [10] but would need to be confirmed through other experimental techniques (e.g., transmission electron microscopy (TEM)).

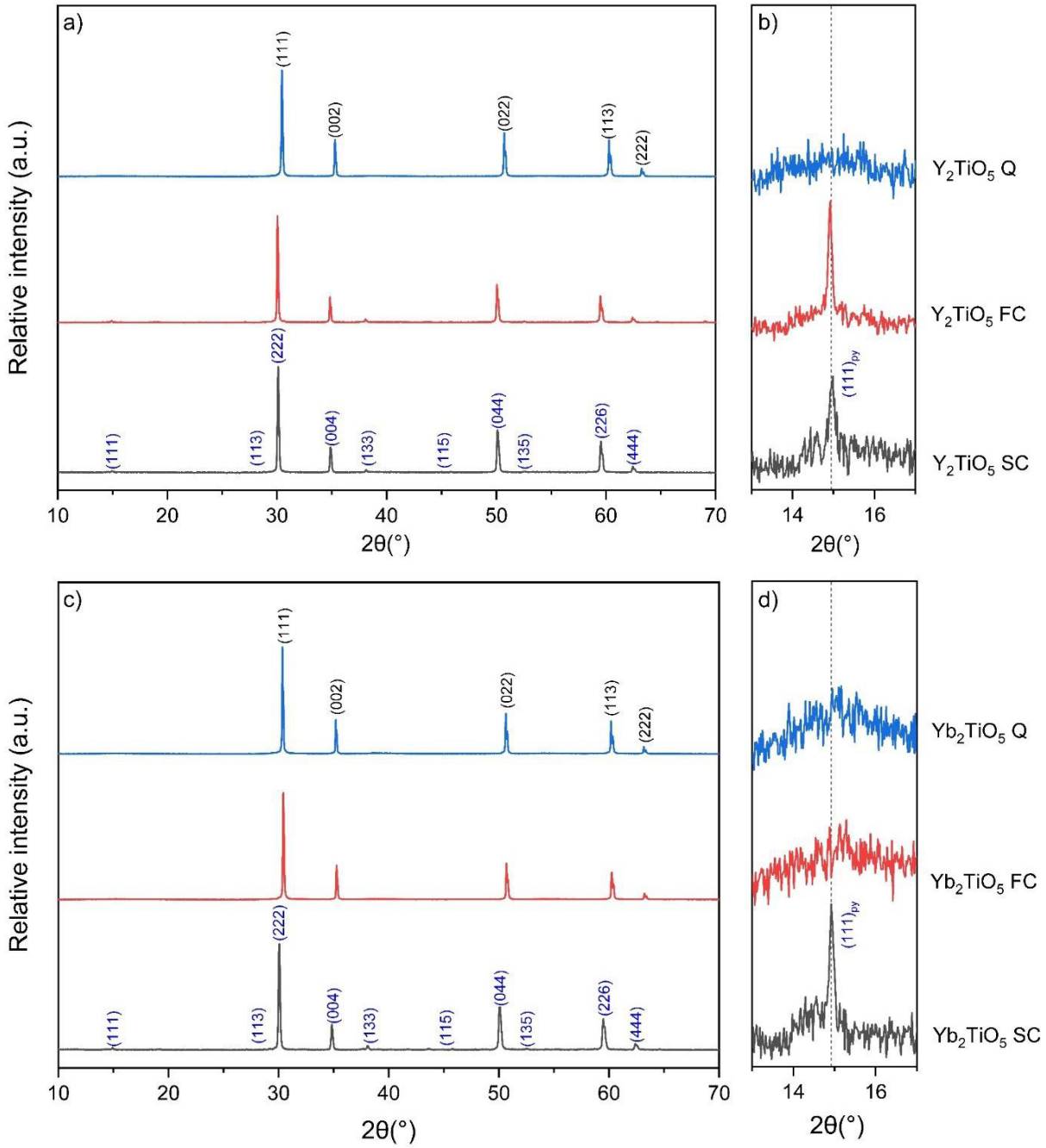

Figure 1: X-ray diffraction data for (a) Y_2TiO_5 and (c) Yb_2TiO_5 samples, showing the single-phase nature of the samples. Labels refer to cooling regime, Q – quenched, FC – furnace cooled and SC – slow cooled. Miller indices for quenched samples and furnace cooled Yb_2TiO_5 are indexed in the *Fm-3m* space group. Those for the slow cooled samples and furnace cooled Y_2TiO_5 are indexed in the *Fd-3m* space group. Panels b) and d) show a magnified region of the plot containing the pyrochlore (111) superstructure reflections.

Table 1: Refined sample unit cell parameters of Y_2TiO_5 and Yb_2TiO_5 obtained using the Le Bail method. Labels in brackets refer to cooling regime: Q – quench, FC – furnace cooled, and SC – slow cooled. a refers to the lattice parameter value (a = b = c), V refers to the lattice volume and R_{wp} refers to the weighted profile R-factor.

Sample	a (Å)	V (Å3)	R_{wp}
Y_2TiO_5 (Q)	5.1514(1)	136.70(4)	8.18
Y_2TiO_5 (FC)	5.1529(7)	136.82(11)	9.85
Y_2TiO_5 (SC)	5.1539(4)	136.90(8)	10.45
Yb_2TiO_5 (Q)	5.0945(6)	132.22(9)	7.75
Yb_2TiO_5 (FC)	5.0950(8)	132.26(10)	8.08
Yb_2TiO_5 (SC)	5.0953(4)	132.28(8)	8.35

3.2 X-ray absorption spectroscopy

3.2.1 Pre-edge feature & XANES analyses

The normalised Ti K-edge XANES spectra of the synthesised samples and standards are shown in Figure 2. All Ti cations in the samples and standards used in this study were of 4+ speciation, as such suitable comparisons can be made independent of Ti oxidation state. In oxides, the features in the pre-edge are attributed to electron transitions from the 1s energy level in the core Ti atoms to hybridised Ti 3d / O 2p molecular orbitals, therefore containing information about the local coordination environment of the absorbing Ti atoms [26], [36], [37]. A 1s to 3d transition is usually forbidden due to selection rules ($\Delta l = \pm 1$) however, this rule is relaxed when Ti is located in a non- centrosymmetric coordination and *d-p* mixing occurs. The intensity of the pre-edge feature is governed by the degree of *d-p* mixing in the molecular orbitals which increases with a greater degree of site-distortion from regular octahedral, and the position is relatively insensitive to changes in the mean Ti-O distance. Changes in the height of the pre-edge are related to changes in centro-symmetry although both height and position are used in concert to derive indicative information about the local coordination environment. Other key features in the XANES (A_1, A_2, and A_3 in Figure 2b) are dominated by multiple scattering of the photoelectric wave with the local neighbouring atomic shells and are sensitive to details of the ligand arrangement around the central absorber [25], [26], [38].

Visual inspection of Figure 2 yields qualitative information about the Ti local coordination environment. The position of the pre-edge feature (4969 – 4972 eV) in the Ln_2TiO_5 (where Ln = Y or Yb) spectra indicates that the local anion geometry is similar to the five-fold coordination environment observed in Ln_2TiO_5 (where Ln = Gd or Dy) and the mineral fresnoite ($Ba_2SiTi_2O_8$). As previously

discussed, the intensity of the pre-edge feature provides additional diagnostic information with the shape and height for the Ln_2TiO_5 (where Ln = Y or Yb) samples appearing more consistent with Dy_2TiO_5, which adopts the hexagonal *P6₃/mmc* symmetry. The hexagonal structure model (Figure A1b) for Ln_2TiO_5 was first proposed based on analysis of powder X-ray diffraction data for Y_2TiO_5 [39], although it has been shown that this structure can be stabilised for a range of intermediate sized lanthanide cations in samples prepared with a carefully controlled thermal history or chemical composition [8], [10], [18]. The Ti cations sit in trigonal bi-pyramidal polyhedral layers, which share oxygen atoms in the equatorial plane, and possess a centre of symmetry. Comparatively, the pre-edge features are more intense for Gd_2TiO_5 and fresnoite where the Ti cations sit in square pyramidal polyhedral [8], [40] which lack a centre of symmetry. These observations are consistent with the distinction between spectra for compounds with Ti in highly symmetric octahedral environments and spectra for compounds with tetrahedral coordinated Ti, which lack inversion symmetry [41]. The pre-edge features of $Ln_2Ti_2O_7$ and anatase TiO_6 octahedra are characterised by 3 distinct features A_1-A_3; A_1 is associated with dipolar transitions from *1s* to t_{2g} orbitals; A_2 is associated with local *1s* to e_g excitations or *1s* to d-state transitions of overlapping *4p* states of next-nearest neighbour atoms, depending on coordination and disorder of the local polyhedra; A_3 is attributed to local *1s* to *4p* transitions or possibly a dipolar transition to the e_g orbital of the next-nearest neighbour cation [36], [42]. The Ti pre-edge features in both Yb_2TiO_5 and Y_2TiO_5 lack these distinctive TiO_6 octahedra (Figure 2b).

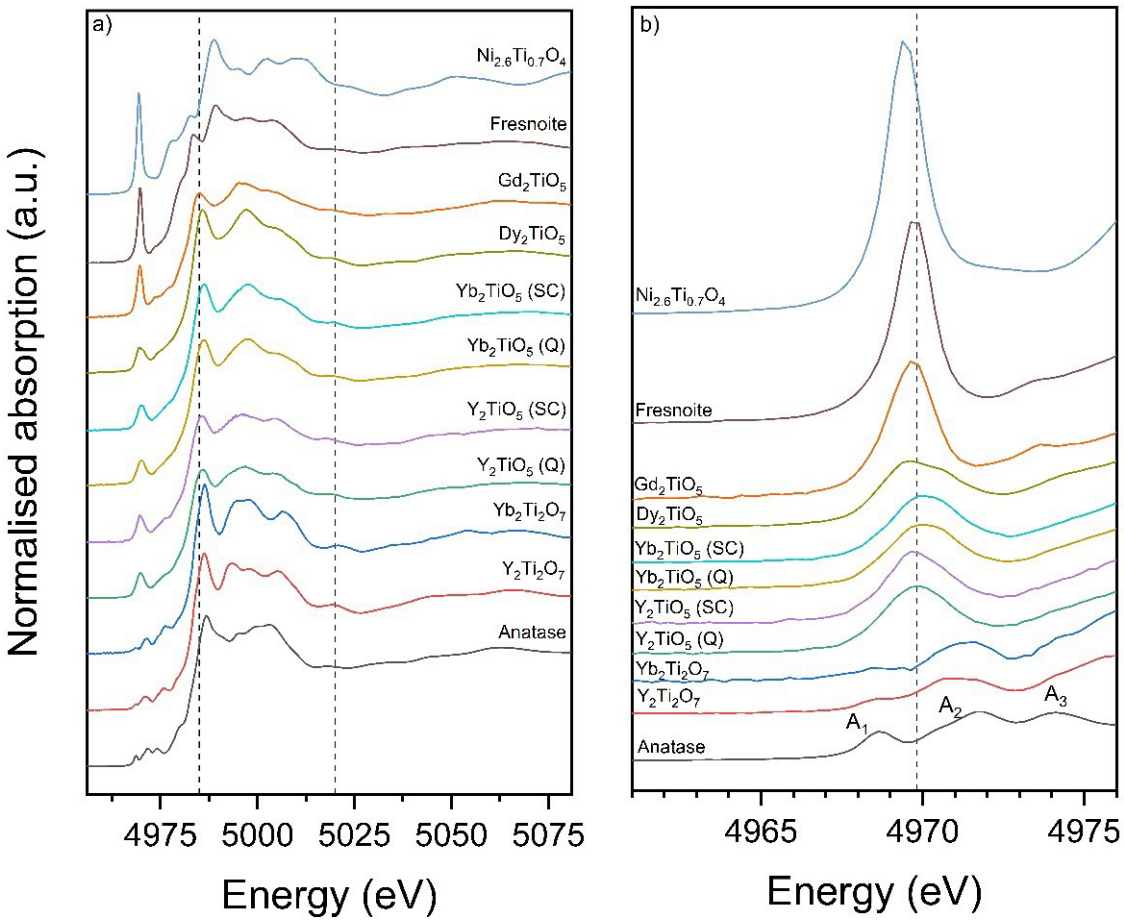

Figure 2: (a) Normalised Ti K-edge XANES data for Y_2TiO_5 and Yb_2TiO_5 samples measured in fluorescence mode. Spectra for reference materials are included. Dashed lines are included to highlight the region just beyond the main crest approximately 4985 eV to 5020 eV (b) The pre-edge region is shown magnified (4961 – 4975 eV). Points of interest are labelled A_1, A_2 and A_3. A dashed line is included to guide the eye. Labels in brackets refer to cooling regime: (Q) – quench, (FC) – furnace cooled, and (SC) – slow cooled.

The derived values from quantitative pre-edge analysis were compared to previously published data and reference compounds with defined Ti coordination, as shown in Figure 3 [43], [44]. Fitted values for standard compounds measured in this work were found to be in good agreement with literature values providing confidence in the comparability of data sets. As can be seen in Figure 3, the data points for the Ln_2TiO_5 (where Ln = Y or Yb) samples are all clustered in the region of the plot consistent with five-fold coordinated titanium with a trigonal bipyramid structural motif (Dy_2TiO_5) [45]. The reduction in normalised height, which relates to the degree of *p-d* mixing of orbitals, of Ln_2TiO_5 where Ln = Dy, Yb or Y compared to other 5-fold standards with a square pyramidal coordination is consistent with that of the 6-fold coordinated Ti standards. This region has also been identified as being related to mixtures of 4- and 6-fold coordinated Ti. However, given the qualitative similarities between the

pre-edge features of standards with 5-fold coordinated Ti and these samples, this seems unlikely but further investigation of the local coordination through quantitative analysis of the EXAFS region is needed. The pre-edge normalised height and position are also consistent with observations from *Farges et al.* where Ti^{4+} coordination environment is identified as trigonal bipyramidal in metamict zirconolite and the 5-fold coordination Ti^{4+} site in crystalline zirconolite [37]. Corroboratory evidence for the similarities with Dy_2TiO_5 beyond the first oxygen neighbour shell can be obtained from comparison of the features between the crest on the absorption edge and 5020 eV, highlighted as the region between the dotted lines in Figure 3a. The features observed in the Ln_2TiO_5 (where Ln = Y or Yb) stuffed pyrochlores are very similar in shape, intensity, and position to those seen in Dy_2TiO_5; these features are due to multiple scattering events and are sensitive to details of the medium range order around the central absorber [25], [26], [46].

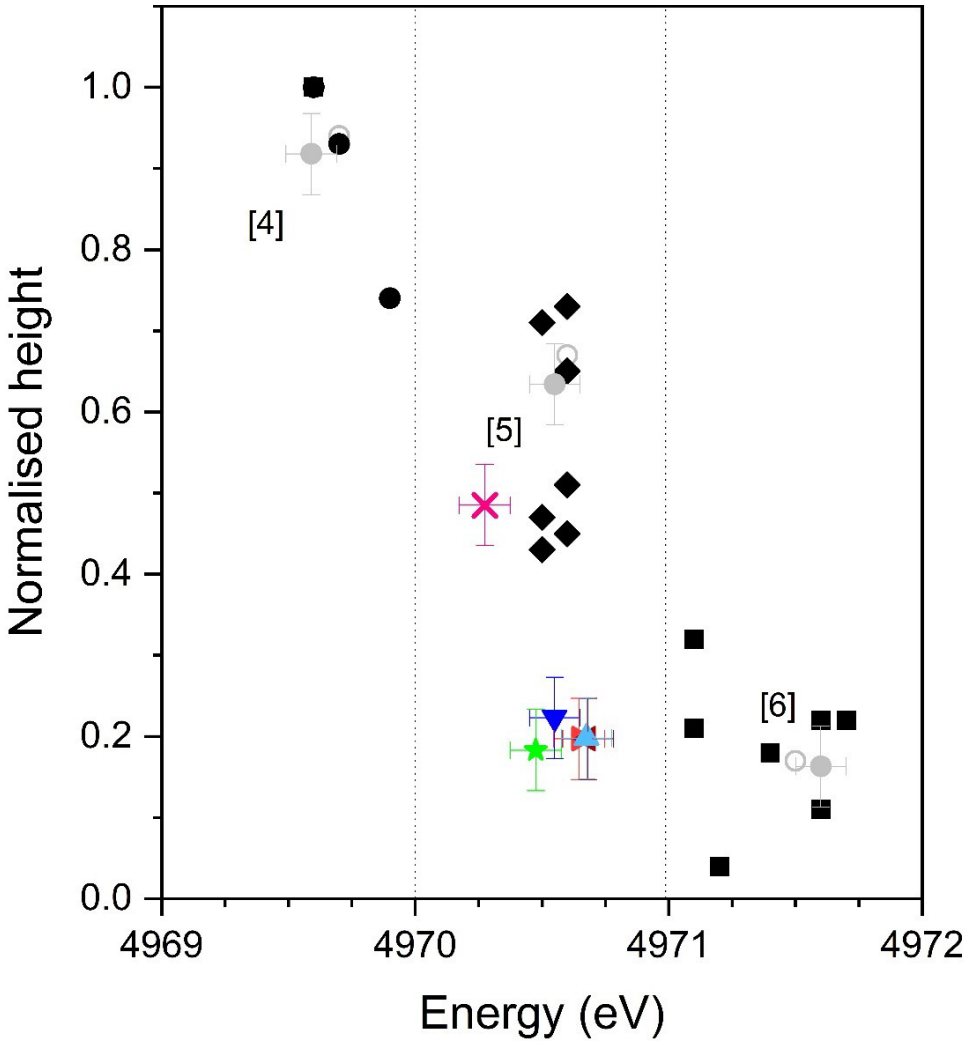

Figure 3: Ti coordination environment as specified by pre-edge energy position and normalised height of pre-edge feature in Ti K-edge XANES. Black solid squares show data for 6-fold coordination standards from previous studies; solid diamonds show data for 5-fold coordination standards and solid black circles show 4-fold coordination standards from previous studies [44]. Data points in solid grey circles represent standards. Going from left to right are: $Ni_{2.6}Ti_{0.7}O_4$ (4969.6 eV), fresnoite (4970.5 eV) and, anatase (4971.6 eV) data points outlined in grey are the corresponding standards collected from previous studies. The downward pointing dark blue triangle and upwards pointing light blue triangle are Yb_2TiO_5 (SC) and Yb_2TiO_5 (Q), respectively; the dark red leftwards pointing triangle and light red rightward pointing triangle are Y_2TiO_5 (SC) and Y_2TiO_5 (Q), respectively; the pink cross and green star are Gd_2TiO_5 and Dy_2TiO_5, respectively. Regions associated with 4-, 5- and 6-fold coordination polyhedra are labelled [4], [5] and [6], respectively.

The pre-edge region of the spectra (-20 eV to -7 eV relative to E_0) was also modelled using linear combinations of the standard compounds. The results of the LCF are shown in Table 2. Excellent fits (R-factors < 1%) were achieved for all samples as can be seen in the example in Figure C1. In all cases

the dominant contribution (≥ 75%) to the overall fit was from Ti in a trigonal bi-pyramidal environment (Dy_2TiO_5); this is consistent with the observations from the pre-edge analysis discussed in the previous section. Minor components with square pyramidal TiO_5 and octahedral TiO_6 were also determined as shown in Table 2. Despite not giving an exact match to a trigonal bi-pyramidal environment the results clearly indicate there are similarities between the local coordination of Ti in Dy_2TiO_5 and cubic Ln_2TiO_5 (Ln = Yb or Y), as such the latter must retain some unique properties that can't be reproduced by a trigonal bipyramidal structural motif. The analysis of the XANES region using a combination of pre-edge fitting and LCF of the Ti K-edge spectra for Yb_2TiO_5 and Y_2TiO_5 samples shows a definite trend towards a 5-fold coordination environment.

Table 2: Contributions to the linear combination fitting for the pre-edge region from model compounds with different Ti coordination environments. Labels in brackets refer to cooling regime: Q – quench, FC – furnace cooled, and SC – slow cooled.

Component	**Y_2TiO_5 (Q)**	**Y_2TiO_5 (SC)**	**Yb_2TiO_5 (Q)**	**Yb_2TiO_5 (SC)**
	% ± 5	% ± 5	% ± 5	% ± 5
$(Y/Yb)_2Ti_2O_7$	-	-	9	11
$Ba_2SiTi_2O_8$	4	5	10	13
Dy_2TiO_5	87	85	81	76
Gd_2TiO_5	9	8	-	-
$Ni_{2.6}Ti_{0.7}O_4$	-	2	-	-
R-factor	0.004	0.006	0.005	0.009

3.3 Extended X-ray-absorption fine-structure (EXAFS) analysis

Despite XRD data indicating a long-range cubic structure there are conflicting reports of the short-range order of cubic Ln_2TiO_5. Descriptions have varied between cubic pyrochlore or orthorhombic, based on TEM/ED and neutron PDF analyses, respectively. Alternatively, the XANES analysis in this study indicate a local Ti environment commensurate with that of the hexagonal Dy_2TiO_5 (trigonal bipyramidal). As such, quantitative EXAFS modelling was used to investigate the local environments of both slow cooled and quenched cubic stuffed pyrochlores to further elucidate short-range structural features. The data, therefore, were modelled using relevant structures (orthorhombic, hexagonal, and cubic) to determine which is the most representative based on interpretation of statistical and physical results. Although all three structures were modelled, the cubic model was

found to be the most appropriate and is subsequently the only model covered in detail here (see sections F – G of the SI for a more thorough discussion of the other models).

3.3.2 Ti K-edge EXAFS

The results of Ti K-edge EXAFS fitting are shown in Figure 4 and Table 3. Ti-O coordination was refined by the methods detailed above and the refined coordination number of the Ti core absorber for both chemistries was found to be 5.3 ± 0.6 for the quenched samples, 4.9 ± 0.6 for the slow cooled sample Y_2TiO_5, and 5.3 ± 0.6 for slow cooled Yb_2TiO_5. These results (Figure 4 and Table 3) can be taken with a good degree of confidence given reasonable R-factors of below 3.7% and that the calculated bond valence sum (BVS) came within 10 % of the formal valence of Ti (4 v.u.) for both the quenched (4.01 v.u. for both chemistries) and slow cooled (3.81 v.u. and 3.99 v.u. for Y_2TiO_5 and Yb_2TiO_5, respectively) samples (Table 3). Although in agreement with results from the XANES analysis, these results are not consistent with either the cubic pyrochlore or defect-fluorite Ti coordination environments (CN = 6, 7 respectively). They are, however, consistent with the Ti coordination of other Ln_2TiO_5 structures adopted by the larger lanthanides, incorporating either trigonal bipyramidal TiO_5 (hexagonal) or square pyramidal TiO_5 (orthorhombic), [8], [10]. The refined bond distances (Table 3) indicate that there is an increase in the size of the local environment of slow cooled samples, which is consistent with the observations that the intensity of supercell reflections corresponds to an increase in the size of local nanodomains as the cooling regime changes [10], [11], [30].

Structural refinements of XRD data based on a defect-fluorite *Fm-3m* symmetry of Yb_2TiO_5 and $Sm_{0.6}Yb_{1.4}TiO_5$ samples found that the Ti-O bond distances were 2.21 Å and 2.22 Å, respectively, whereas this study consistently refines to Ti-O distances between 1.90 – 1.92 Å, consistent with a 5-fold coordination environment. A bond distance of 2.224 Å is consistent with a significantly higher coordination number (CN = 8) found in defect-fluorite structures. This difference may arise from XAS techniques being significantly more sensitive to short-range ordering than XRD, wherein long-range ordering is more dominant and was observed to have an average defect-fluorite structure in Yb_2TiO_5 and $Sm_{0.6}Yb_{1.4}TiO_5$. As such the short-range pyrochlore-like ordering would not be detected or considered in the XRD refinements.

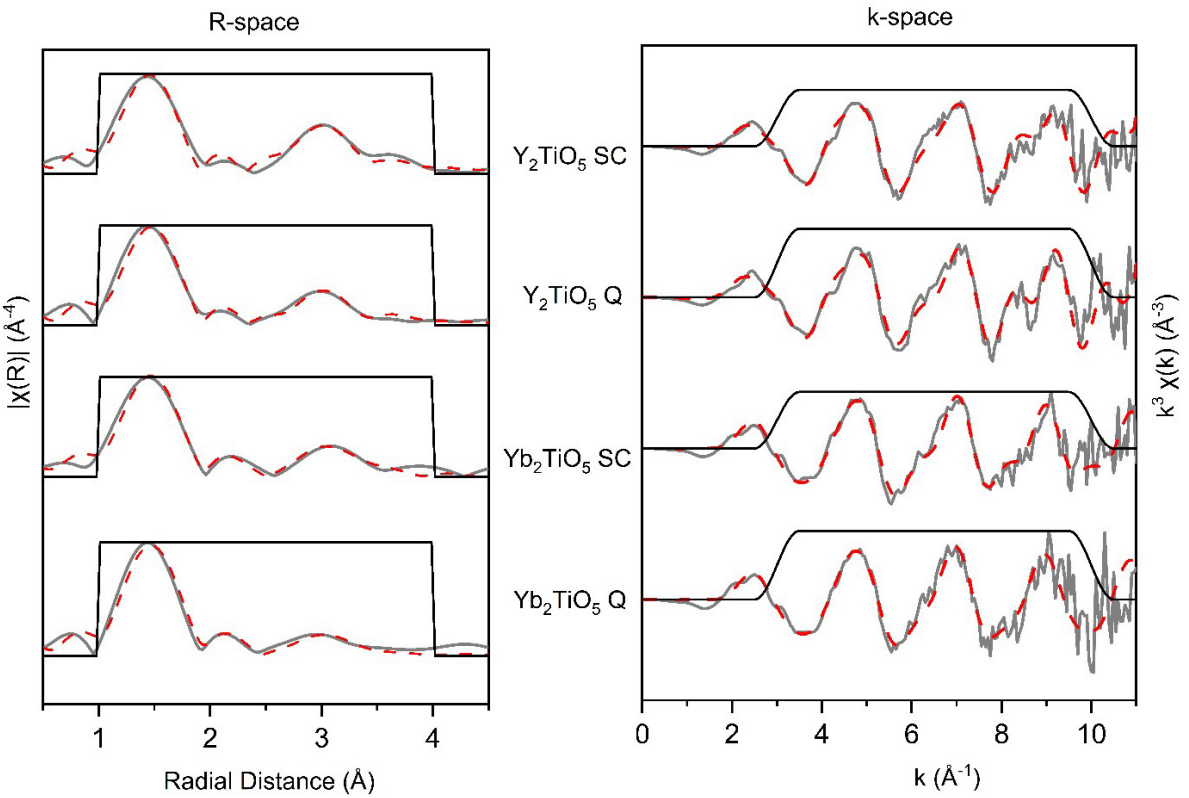

Figure 4: a) Fourier transform of Ti K-edge waveform of Yb_2TiO_5 and Y_2TiO_5 in R-space; b) k^3 weighted waveform. Solid grey line represents experimental data, red dashed line represents the theoretical cubic fit and the black line indicates the fitting window. SC – Slow cooled; Q – Quenched

Table 3: Refined structural parameters for the Y_2TiO_5 and Yb_2TiO_5 samples measured at the Ti k-edge modelled using a cubic *Fd-3m* structure. The average change in scattering path distance for a given absorber-scatterer pair is denoted as R, the Debye–Waller factor is denoted as σ^2, the degeneracy of the path is denoted as N and Ln represents the corresponding metal cation (Ln = Y, Yb) The fitting range in R was 1–4 Å and 3–10 in k.

Cubic		Y_2TiO_5 (Q)	Y_2TiO_5 (SC)	Yb_2TiO_5 (Q)	Yb_2TiO_5 (SC)
	E_o (eV)	-2.0(13)	-2.6(15)	-1.7(14)	-1.6(15)
Ti-O	*R (Å)*	1.91(1)	1.92(3)	1.91(1)	1.92(1)
	σ^2 *(Å²)*	0.004(2)	0.003(2)	0.003(2)	0.003(2)
	N	5.3(6)	4.9(6)	5.3(6)	5.3(6)
Ti-Ln N = 8	*R (Å)*	3.44(2)	3.44(2)	3.38(2)	3.40(3)
	σ^2 *(Å²)*	0.009(2)	0.012(2)	0.011(2)	0.014(4)
Ti-Ti N = 4	*R (Å)*	3.85(5)	3.89(5)	3.58(2)	3.57(2)
	σ^2 *(Å²)*	0.013(8)	0.015(8)	0.022(12)	0.023(15)
R-factor		0.027	0.023	0.020	0.031
BVS (v.u.)		4.01	3.81	4.01	3.99

3.3.3 Yb L_3- and Y K-edge EXAFS

The results of Y K-edge and Yb L_3 edge EXAFS fitting is shown in Figure 5 and Table 4. Good fits to the data were achieved using a cubic model for both Y_2TiO_5 and Yb_2TiO_5The calculated BVS were within 10 % of the formal valence (3 v.u.) of Y for the Y_2TiO_5 samples. This gives confidence in the conclusion that the average local Y environment in Y_2TiO_5 adopts 8-fold coordination characteristic of the pyrochlore A-site. Similarly, the calculated BVS were 3.16 v.u. and 3.28 v.u., respectively for the quenched and slow cooled samples, which are within 10 % of the formal valence of Yb. The bond distance of the Ln-O_2 (N = 6) in quenched samples is 0.2 Å shorter than that of the change in bond distance of Ln-O_2 in slow cooled samples. This smaller change in bond distance is the cause for smaller BVS values and suggests greater disorder is present in the structures for compounds that were quenched. Indeed, similar conclusions have been reached by other authors from interpretation of thermal parameters in structure refinements against neutron diffraction data [9]. As with cubic based models of the Ti K-edge, the refined bond distances for both chemistries yielded results that indicate an average expansion of bond distances in slow cooled samples compared to quenched samples. On closer inspection of Figure

5a, the fit can be seen to accurately map onto the trend of the data between 2.6 – 3.7 Å, which is the region predominantly consisting of contributions from more distant Ln-cation scatters, that some of the other models have failed to account for (see SI Figure F1).

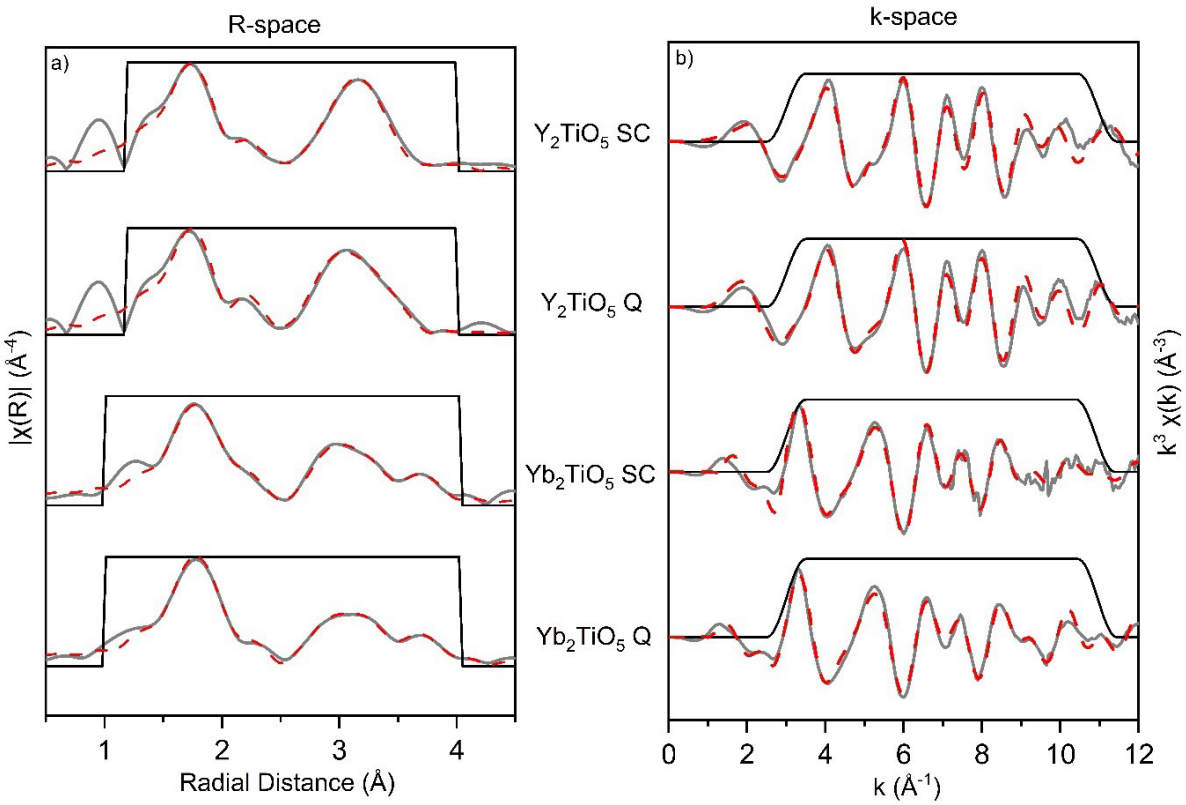

Figure 5: a) Fourier transform of Yb L_3-edge and Y K-edge waveforms of Yb_2TiO_5 and Y_2TiO_5, respectively, in R-space; b) k^3 weighted waveform. Solid grey line represents experimental data, red dashed line represents the theoretical cubic fit and the black line indicates the fitting window. SC – Slow cooled; Q – Quenched.

Table 4: Refined structural parameters for the Y_2TiO_5 and Yb_2TiO_5 samples measured at the Y K-edge and Yb L_3-edge, respectively, modelled using a cubic *Fd-3m* structures. The average change in scattering path distance for a given absorber-scatterer pair is denoted as R, the Debye–Waller factor is denoted as σ^2, the degeneracy of the path is denoted as N and Ln represents the corresponding metal cation (Ln = Y, Yb). The fitting range in R was 1–4 Å and 3–11 in k.

Cubic		**Y_2TiO_5 (Q)**	**Y_2TiO_5 (SC)**	**Yb_2TiO_5 (Q)**	**Yb_2TiO_5 (SC)**
	E_0 (eV)	-2.9(20)	-1.9(13)	4.5(7)	6.7(5)
Ln-O(1) N = 2	*R (Å)*	2.23(1)	2.24(2)	2.20(1)	2.20(2)
	σ^2 (Å^2)	0.002(1)	0.003(2)	0.004(1)	0.004(2)
Ln-O(2) N = 6	*R (Å)*	2.36(3)	2.38(2)	2.31(1)	2.33(1)
	σ^2 (Å^2)	0.011(2)	0.013(2)	0.018(2)	0.017(1)
Ln-Ti N = 4	*R (Å)*	3.39(1)	3.45(2)	3.40(1)	3.41(2)
	σ^2 (Å^2)	0.007(1)	0.009(3)	0.018(3)	0.017(2)
Ln-Ln N = 8	*R (Å)*	3.66(2)	3.65(2)	3.56(1)	3.56(2)
	σ^2 (Å^2)	0.012(2)	0.012(2)	0.013(1)	0.012(1)
Ln-O(3) N = 12	*R (Å)*	3.80(2)	3.85(4)	4.09(2)	4.12(3)
	σ^2 (Å^2)	0.011(2)	0.013(2)	0.017(3)	0.019(3)
R-factor		0.010	0.016	0.006	0.003
BVS (v.u.)		3.22	3.30	3.16	3.30

3.4 Comparison with orthorhombic and hexagonal models

Determination of the short-range ordering of cubic Ln_2TiO_5 stuffed pyrochlores is a complex task, particularly given the body of literature which reports conflicting assessments. This study aimed to consider many different possible structures, which have been highlighted by in this study and literature, as possible descriptions. Without a comprehensive and considered understanding of the local coordination of Yb_2TiO_5 it would not be possible to correctly infer the impact intrinsic (e.g., mixed cation doping) and extrinsic (e.g., radiation) effects have.

As previously mentioned, the local coordination of Ti cations has been described as either hexagonal or orthorhombic structures. *Shamblin et al.* indicated a possible orthorhombic ordering, demonstrated through neutron PDF analysis of Yb_2TiO_5, where fitting of the data based on orthorhombic symmetry had a better fit (Rwp = 0.111) than the cubic pyrochlore symmetry (Rwp = 0.306) [29]. The orthorhombic structure is characterised as having arrays of TiO_5 square based polyhedra, similar to the hexagonal structure (TiO_5 trigonal bipyramidal polyhedra) indicated through our XANES analysis. It should be noted, however that a fit using *$P6_3/mmc$* hexagonal structure was not attempted by *Shamblin et al.*, consequently it remains to be seen if this structure would also have given a satisfactory fit in their study. The pre-edge, XANES, and EXAFS analysis of the Ti K-edge demonstrated that Ti was 5-fold coordinated with O, in good agreement with *Shamblin et al.*, and is well described using a structural model based on a cubic pyrochlore structure. Similarly, the Yb and Y local coordinating environments were also well described by using the same basis for the structural model. As such, analysis of the Ti K-edge, Y K-edge and Yb L_3-edge EXAFS regions was carried out using hexagonal and orthodromic structures as the basis for the models. The results of these models are discussed and presented in sections F and G of the SI.

Though the attempts to fit orthorhombic and hexagonal structures did not yield entirely poor fits, it was found that the most consistent and reliable fit across all absorption edges (Yb L_3-edge, Y K-edge and Ti K-edge) based upon R-factor values, refined parameters, BVS and physical interpretations, was from that of a cubic pyrochlore structure with 5-fold coordinated Ti. The refined bond distances in the cubic models are also the most consistent and follow the most physically sensible trend with relation to each other. Cations in hexagonal and orthorhombic models swap distances as to which, Ti or Ln, is closer to the core absorber or the distances vary significantly between thermal history and chemistries, indicating that the models are somewhat less consistent than the cubic model. In orthorhombic models at the Yb L_3- and Y K-edges the two Ln core absorbers yielded quite disparate BVS, both of which deviated significantly from the formal valence of the absorber.

Based upon the EXAFS refinements of the Ti K-edge, Y K-edge, and Yb L_3-edge data, it is apparent that the short-range order of these materials is well described by a model based on a pyrochlore *Fd-3m* structure, however Ti is found to be in 5-fold coordination (a reduction of the typical 6-fold Ti coordination found in pyrochlore structure). TEM/ED studies of these types of materials have reported observing short-range modulation commensurate with pyrochlore-like structures [10], [11], [30]. These EXAFS results appear to agree with this observation of a cubic-like short-range order. Though, it should also be considered that neutron PDF analysis of the short-range order of cubic Yb_2TiO_5 reported that a *Fd-3m* pyrochlore structure poorly modelled the Ti-O coordination [29]. Here, fitting of the experimental XANES and EXAFS data with an orthorhombic *Pnma* (TiO_5) structure yielded more accurate results, better representing the Ti-O coordination. The discrepancy between the two results may well satisfied by our conclusion of a short-range order of pyrochlore-like nanodomains, with a reduced Ti coordination.

Therefore, the cubic model was selected as the most robust model in this contribution of the local coordination of cations and will aid in facilitating further studies into studying the changes to local structural environments of Ln_2TiO_5 compounds post irradiation through the application of Glancing Angle X-ray absorption spectroscopy (GA-XAS) [47], [48].

4. Conclusions

Y_2TiO_5 and Yb_2TiO_5 stuffed pyrochlores were fabricated under different cooling regimes to facilitate the growth of nanodomain features. XRD results found the samples to have a long-range ordering equivalent to a defect-fluorite *Fm-3m* structure, but the presence of weak or diffuse peaks that can be indexed in the pyrochlore *Fd-3m* structure indicated a difference in the short-range ordering. The local structural environment was further investigated through XAS, with the analysis of the Ti K-edge XANES showing that Ti was best represented as 5-fold coordinated Ti in a trigonal bipyramidal motif. Quantitative analysis of the Ti K-edge, Y K-edge and Yb L_3-edge EXAFS region was undertaken through the fitting of experimental data, with the Ti coordination number refined to 5-fold O coordination, which is in good agreement with the results from the XANES analysis. This result is consistent with fitting of other 5-fold coordinated Ti in orthorhombic and hexagonal structures. Models based upon orthorhombic and hexagonal structures were deemed less reliable and robust than the model for the cubic structure when accounting for statistical assessments and physical interpretation of the refined parameters. Though hexagonal and orthorhombic models are not entirely without merit, further studies utilising more distant scatterers and multiple scattering in combination with computational modelling would be necessary to finely differentiate between them. For the purposes of producing a robust and coherent local and long-range structural model that may also be used in future studies to assess changes in the local coordination at both the Ln- and Ti-sites, the cubic models were deemed the most viable. The results of this study, therefore, indicate that Y_2TiO_5 and Yb_2TiO_5 stuffed pyrochlores have a short-range order commensurate with the *Fd-3m* pyrochlore structure but with a reduced Ti coordination (from 6 to 5). These findings will be pivotal in developing a better understanding of how processes, such as radiation damage and dissolution impact the structure of stuffed pyrochlores, therefore informing future uses of these nuclear-relevant ceramic compounds.

Acknowledgments

DAA is grateful to the Engineering and Physical Sciences Research Council (EPSRC) for funding. This research utilised the HADES/MIDAS facility at The University of Sheffield established with financial support from EPSRC and BEIS, under grant EP/T011424/1 and was supported by grant EP/S01019X/1. This research used 6-BM of the National Synchrotron Light Source II, a U.S. Department of Energy (DOE) Office of Science User Facility operated for the DOE Office of Science by Brookhaven National Laboratory under Contract No. DE-SC0012704

References

[1] Y. F. Shepelev, M. A. Petrova, and A. S. Novikova, "Crystal structure of the hexagonal modification of lutetium-stabilized gadolinium titanate $Gd_{1.8}Lu_{0.2}TiO_5$," *Glas. Phys. Chem.*, vol. 30, no. 4, pp. 342–344, Jul. 2004.

[2] R. D. Aughterson *et al.*, "Ion-irradiation resistance of the orthorhombic Ln_2TiO_5 (Ln = La, Pr, Nd, Sm, Eu, Gd, Tb and Dy) series," *J. Nucl. Mater.*, vol. 467, pp. 683–691, 2015.

[3] S. Park *et al.*, "A_2TiO_5 (A = Dy, Gd, Er, Yb) at High Pressure," *Inorg. Chem.*, vol. 57, no. 4, pp. 2269–2277, Feb. 2018.

[4] R. D. Aughterson, G. R. Lumpkin, K. L. Smith, G. J. Thorogood, and K. R. Whittle, "Synthesis and Characterisation of Ln_2TiO_5 Compounds," *MRS Proc.*, vol. 1107, p. 365, Jan. 2008.

[5] V. D. D. Risovany, E. E. E. Varlashova, and D. N. N. Suslov, "Dysprosium titanate as an absorber material for control rods," *J. Nucl. Mater.*, vol. 281, no. 1, pp. 84–89, Sep. 2000.

[6] A. Sinha and B. P. Sharma, "Development of Dysprosium Titanate Based Ceramics," *J. Am. Ceram. Soc.*, vol. 88, no. 4, pp. 1064–1066, Apr. 2005.

[7] Y. Jiang, J. R. Smith, and G. Robert Odette, "Prediction of structural, electronic and elastic properties of Y_2Ti2O_7 and Y_2TiO_5," *Acta Mater.*, vol. 58, no. 5, pp. 1536–1543, Mar. 2010.

[8] Y. F. Shepelev and M. A. Petrova, "Crystal structures of Ln_2TiO_5 (Ln = Gd, Dy) polymorphs," *Inorg. Mater.*, vol. 44, no. 12, pp. 1354–1361, Dec. 2008.

[9] G. C. Lau, T. M. McQueen, Q. Huang, H. W. Zandbergen, and R. J. Cava, "Long- and short-range order in stuffed titanate pyrochlores," *J. Solid State Chem.*, vol. 181, no. 1, pp. 45–50, Jan. 2008.

[10] R. D. Aughterson *et al.*, "Crystal structures of orthorhombic, hexagonal, and cubic compounds of the $Sm_{(x)}Yb_{(2-x)}TiO_5$ series," *J. Solid State Chem.*, vol. 213, pp. 182–192, May 2014.

[11] G. C. Lau *et al.*, "Structural disorder and properties of the stuffed pyrochlore Ho_2TiO_5," *Phys. Rev. B*, vol. 76, no. 5, p. 054430, 2007.

[12] J. Shamblin *et al.*, "Structural and magnetic short-range order in fluorite Yb_2TiO_5," *Phys. Rev. B*, vol. 96, p. 174418, 2017.

[13] G. C. C. Lau, B. D. D. Muegge, T. M. M. McQueen, E. L. L. Duncan, and R. J. J. Cava, "Stuffed rare earth pyrochlore solid solutions," *J. Solid State Chem.*, vol. 179, no. 10, pp. 3126–3135, Oct. 2006.

[14] A. V. Shlyakhtina, D. A. Belov, S. Y. Stefanovich, and L. G. Shcherbakova, "Nanostructuring phenomena in oxygen-conducting complex oxides of heavy REE," *Russ. J. Electrochem.*, vol. 47, no. 5, pp. 620–627, May 2011.

[15] B. G. Mullens *et al.*, “Average and local ordering of $Yb_2(Ti_{2-x}Yb_x)O_{7-x/2}$ ‘stuffed’ pyrochlores: The development of a robust structural model,” *J. Solid State Chem.*, vol. 302, p. 122412, Oct. 2021.

[16] B. G. Mullens *et al.*, “Effect of Long- And Short-Range Disorder on the Oxygen Ionic Conductivity of $Tm_2(Ti_{2-x}Tm_x)O_{7-x/2}$"stuffed" Pyrochlores,” *Inorg. Chem.*, vol. 60, no. 7, pp. 4517–4530, Apr. 2021.

[17] L. Pauling, “The principles determining the structure of complex ionic crystals,” *J. Am. Chem. Soc.*, vol. 51, no. 4, pp. 1010–1026, Apr. 1929.

[18] R. D. Aughterson, N. J. Zaluzec, and G. R. Lumpkin, “Synthesis and ion-irradiation tolerance of the Dy_2TiO_5 polymorphs,” *Acta Mater.*, vol. 204, p. 116518, Feb. 2021.

[19] R. D. Aughterson, G. R. Lumpkin, K. L. Smith, and J. M. Cairney, “Novel complex ceramic oxides, Ln_2TiO_5 (Ln = La, Sm, Gd, Tb, Dy, Ho, Er, and Yb), for polyphase nuclear waste-forms,” *J. Am. Ceram. Soc.*, vol. 103, pp. 5536–5545, Jun. 2020.

[20] A. Le Bail, H. Duroy, and J. L. Fourquet, “Ab-initio structure determination of $LiSbWO_6$ by X-ray powder diffraction,” *Mater. Res. Bull.*, vol. 23, no. 3, pp. 447–452, Mar. 1988.

[21] A. A. Coelho, “TOPAS and TOPAS-Academic: An optimization program integrating computer algebra and crystallographic objects written in C++: An,” *J. Appl. Crystallogr.*, vol. 51, no. 1, pp. 210–218, Feb. 2018.

[22] B. Ravel and M. Newville, “ATHENA, ARTEMIS, HEPHAESTUS: Data analysis for X-ray absorption spectroscopy using IFEFFIT,” in *Journal of Synchrotron Radiation*, 2005, vol. 12, no. 4, pp. 537–541.

[23] B. Ravel and M. Newville, “ATHENA and ARTEMIS: Interactive graphical data analysis using IFEFFIT,” *Phys. Scr. T*, vol. T115, no. T115, pp. 1007–1010, 2005.

[24] M. Newville, “IFEFFIT: Interactive XAFS analysis and FEFF fitting,” *J. Synchrotron Radiat.*, vol. 8, no. 2, pp. 322–324, Mar. 2001.

[25] A. G. Waychunas, “Synchrotron radiation XANES spectroscopy of Ti in minerals: Effects of Ti bonding distances, Ti valence, and site geometry on absorption edge structure,” 1987.

[26] F. Farges, G. E. Brown, and J. J. Rehr, “Coordination chemistry of Ti(IV) in silicate glasses and melts: I. XAFS study of titanium coordination in oxide model compounds,” *Geochim. Cosmochim. Acta*, vol. 60, no. 16, pp. 3023–3038, Aug. 1996.

[27] S. R. Hall, F. H. Allen, and I. D. Brown, “The crystallographic information file (CIF): a new standard archive file for crystallography,” *Acta Crystallogr. Sect. A*, vol. 47, no. 6, pp. 655–685, Nov. 1991.

[28] R. D. Aughterson, G. R. Lumpkin, K. L. Smith, Z. Zhang, N. Sharma, and J. M. Cairney, "The crystal structures and corresponding ion-irradiation response for the $Tb_{(x)}Yb_{(2-x)}TiO_5$ series," *Ceram. Int.*, vol. 44, no. 1, pp. 511–519, Jan. 2018.

[29] J. Shamblin *et al.*, "Structural and magnetic short-range order in fluorite Yb_2TiO_5," *Phys. Rev. B*, vol. 96, no. 17, p. 174418, Nov. 2017.

[30] K. R. Whittle, M. G. Blackford, R. D. Aughterson, G. R. Lumpkin, and N. J. Zaluzec, "Ion irradiation of novel yttrium/ytterbium-based pyrochlores: The effect of disorder," *Acta Mater.*, vol. 59, no. 20, pp. 7530–7537, Dec. 2011.

[31] I. D. Brown and D. Altermatt, "Bond-valence parameters obtained from a systematic analysis of the Inorganic Crystal Structure Database," *Acta Crystallogr. Sect. B*, vol. 41, no. 4, pp. 244–247, Aug. 1985.

[32] S. M. Haile, B. J. Wuensch, and E. Prince, " Neutron Rietveld Analysis of Anion and Cation Disorder in the Fast-Ion Conducting Pyrochlore System $Y_2(Zr_xTi_{1-x})_2O_7$," *MRS Proc.*, vol. 166, 1989.

[33] A. V. Shlyakhtina *et al.*, "Effect of the Ca-doping on the electrical conductivity of oxide ion conductor $Yb_2Ti_2O_7$," *Solid State Ionics*, vol. 179, no. 21–26, pp. 1004–1008, Sep. 2008.

[34] R. D. Aughterson *et al.*, "The ion-irradiation tolerance of the pyrochlore to fluorite $Ho_{(x)}Yb_{(2-x)}TiO_5$ and Er_2TiO_5 compounds: A TEM comparative study using both in-situ and bulk ex-situ irradiation approaches," *J. Nucl. Mater.*, vol. 507, pp. 316–326, Aug. 2018.

[35] A. V. Shlyakhtina, D. A. Belov, O. K. Karyagina, and L. G. Shcherbakova, "Ordering processes in Ln_2TiO_5 (Ln = Dy-Lu): The role of thermal history," *J. Alloys Compd.*, vol. 479, no. 1–2, pp. 6–10, 2009.

[36] F. Farges and G. E. Brown, "Ti-edge XANES studies of Ti coordination and disorder in oxide compounds: Comparison between theory and experiment," *Phys. Rev. B - Condens. Matter Mater. Phys.*, vol. 56, no. 4, pp. 1809–1819, Jul. 1997.

[37] F. Farges, "Fivefold-coordinated Ti^{4+} in metamict zirconolite and titanite: A new occurrence shown by Ti K-edge XANES spectroscopy," *Am. Mineral.*, vol. 82, no. 1–2, pp. 44–50, Feb. 1997.

[38] P. Behrens, J. Felsche, S. Vetter, G. Schulz-Ekloff, N. I. Jaeger, and W. Niemann, "A XANES and EXAFS investigation of titanium silicalite," *J. Chem. Soc. Chem. Commun.*, no. 10, pp. 678–680, Jan. 1991.

[39] M. L. K. German, "Structural model of β-modification rare earth orthotitanates," *Zhurnal Neorg. Khimii*, vol. 29, no. 12, pp. 3024–3026, 1984.

[40] P. B. Moore and S. Johnlouisna'l'han, "The crystal structure of fresnoite. $Ba_2(TiO)Si_2O_7$,"

Zeitschrift für Krist. - Cryst. Mater., vol. 130, no. 1–6, pp. 438–448, Dec. 1969.

[41] R. B. Greegor, F. W. Lytle, D. R. Sandstrom, J. Wong, and P. Schultz, "Investigation of TiO_2SiO_2 glasses by X-ray absorption spectroscopy," *J. Non. Cryst. Solids*, vol. 55, no. 1, pp. 27–43, Apr. 1983.

[42] E. R. Aluri and A. P. Grosvenor, "An X-ray absorption spectroscopic study of the effect of bond covalency on the electronic structure of $Gd_2Ti_{2-x}Sn_xO_7$," *Phys. Chem. Chem. Phys.*, vol. 15, no. 25, pp. 10477–10486, Jun. 2013.

[43] G. E. Brown, G. Calas, G. A. Waychunas, and J. Petiau, "X-ray absorption spectroscopy and its applications in minerology and geochemistry," *Spectrosc. Methods Mineral. Geol.*, pp. 431–512, Dec. 1988..

[44] F. Farges, "Coordination of Ti^{4+} in silicate glasses: A high-resolution XANES spectroscopy study at the Ti Kedge," *Am. Mineral.*, vol. 82, pp. 36–43, 1997.

[45] M. C. Stennett, N. Peng, E. R. Maddrell, B. Ravel, and N. C. Hyatt, "Probing radiation damage in ceramic wasteforms using X-ray absorption spectroscopy," *Diam. '10 Conf. Proceedings; Decommissioning, Immobil. Manag. Nucl. Waste Dispos.*, 2010.

[46] P. Behrens, J. Felsche, S. Vetter, G. Schulz-Ekloff, N. I. Jaeger, and W. Niemann, "A XANES and EXAFS investigation of titanium silicalite," *J. Chem. Soc. Chem. Commun.*, no. 10, pp. 678–680, Jan. 1991.

[47] D. P. Reid *et al.*, "The structure of ion beam amorphised zirconolite studied by grazing angle X-ray absorption spectroscopy," *Nucl. Instruments Methods Phys. Res. Sect. B Beam Interact. with Mater. Atoms*, vol. 268, no. 11–12, pp. 1847–1852, Jun. 2010.

[48] M. Stennett *et al.*, "Heavy ion implantation combined with grazing incidence X-ray absorption spectroscopy (GIXAS): A new methodology for the characterisation of radiation damage in nuclear ceramics," *MRS Proc.*, vol. 1193, p. 67, Jan. 2011.

Supporting information

A: Crystal structures of Ln_2TiO_5 stuffed pyrochlores

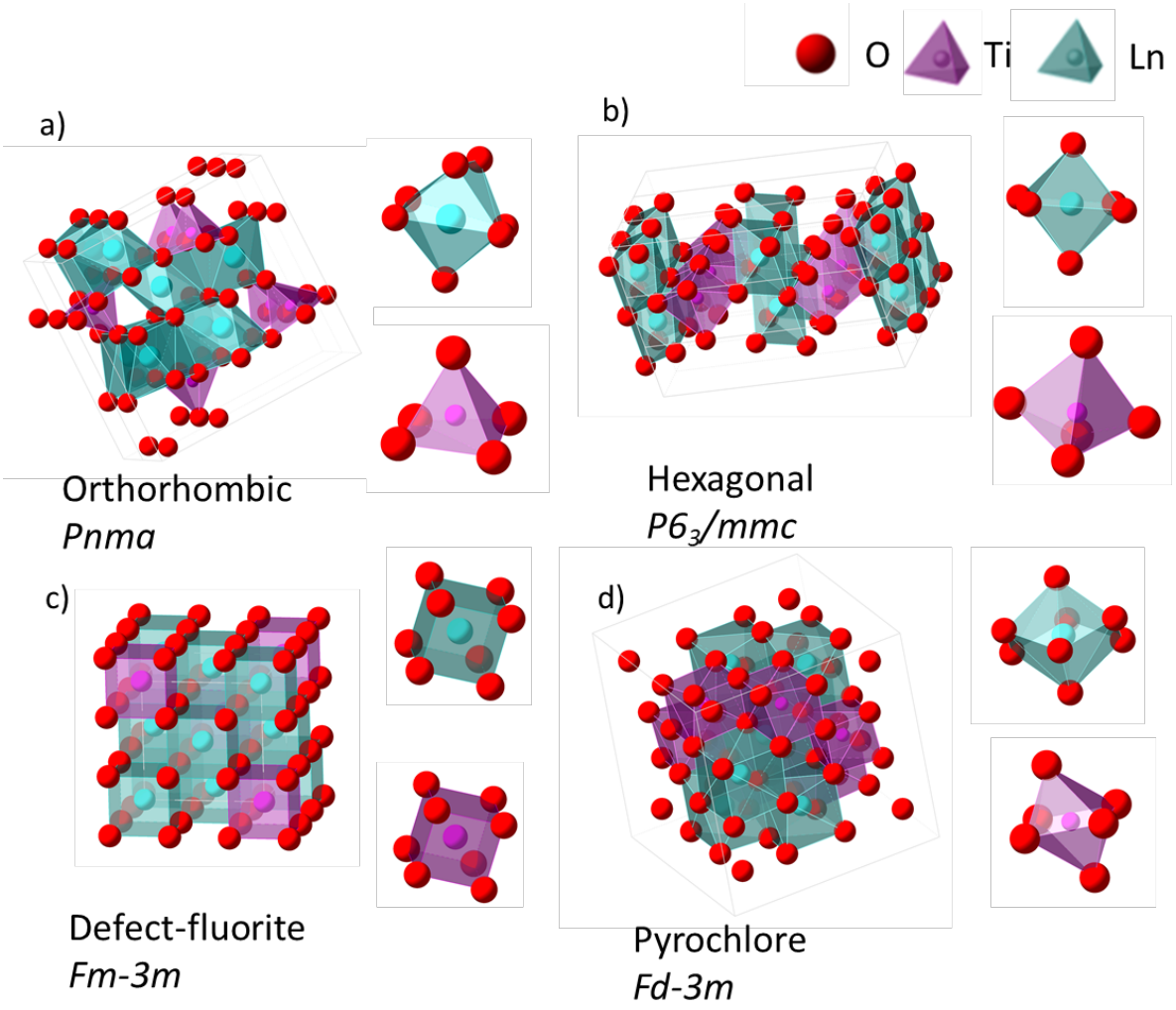

Figure A1: Schematic crystal structures and cation polyhedra of a) orthorhombic *Pnma* Ln_2TiO_5; LnO_7 octahedra and TiO_5 square pyramid polyhedra, b) Hexagonal *P6₃/mmc* Ln_2TiO_5; LnO_5 trigonal bipyramid polyhedra, c) defect fluorite *Fm-3m* Ln_2TiO_5 (A- and B-site cations are randomly distributed); MO_7 (M = cation) polyhedra and d) cubic *Fd-3m* $Ln_2Ti_2O_7$ pyrochlore; LnO_8 scalenohedra and TiO_6 trigonal antiprisms.

B: Synthesis and XRD characterisation of standards

To aid in the interpretation of data XAS data was collecting on a suite of samples. Standards used in this study were Y_2O_3 and Yb2O_3 (Alfa Aesar, 99.9 %), $YCrO_3$, $Y_2Ti_2O_7$, $Yb_2Ti_2O_7$, Dy_2TiO_5, Gd_2TiO_5 and $Ni_{2.6}Ti_{0.7}O_4$.

Samples of $Y_2Ti_2O_7$, $Yb_2Ti_2O_7$, Dy_2TiO_5, Gd_2TiO_5 and $Ni_{2.6}Ti_{0.7}O_4$ were prepared by solid-state routes. Oxide precursors of Ln_2O_3 (>9.9 %, Alfa Aesar), NiO (99.99 %, Alfa Aesar) and TiO_2 (99.99 %, Alfa Aesar) were weighed out according to target stoichiometry. Ln_2O_3 and Y_2O_3 were dried at 800 °C and TiO_2 was dried at 180 °C overnight prior to weighing. Samples were then intimately milled at 500 RPM, using isopropanol as carrier fluid, and the resulting powder slurries were dried at 80 °C. Dried powders were then consolidated into 10 mm diameter pellets using a uniaxial press (4 tonnes). $Y_2Ti_2O_7$, $Yb_2Ti_2O_7$ and Gd_2TiO_5 were heated between 1300 – 1500 °C for 24 hours and checked for phase purity *via* XRD. If any precursor remained, as indicated by presence of diagnostic peaks in XRD patterns, they were ground up, reconsolidated, and thermally treated again between 1300 – 1500 °C. This process was repeated until single-phase products were achieved (Figure A1). $Ni_{2.6}Ti_{0.7}O_4$ and Dy_2TiO_5 were heat treated in the same manner outlined by previous authors [1], [2]. This involved reactions at target temperatures (1500 °C and 1600 °C, respectively) for 24 hours, and then rapidly cooling the samples to room temperature. Phase purity is reported in Figure A1, where no additional reflections associated with secondary phases are present.

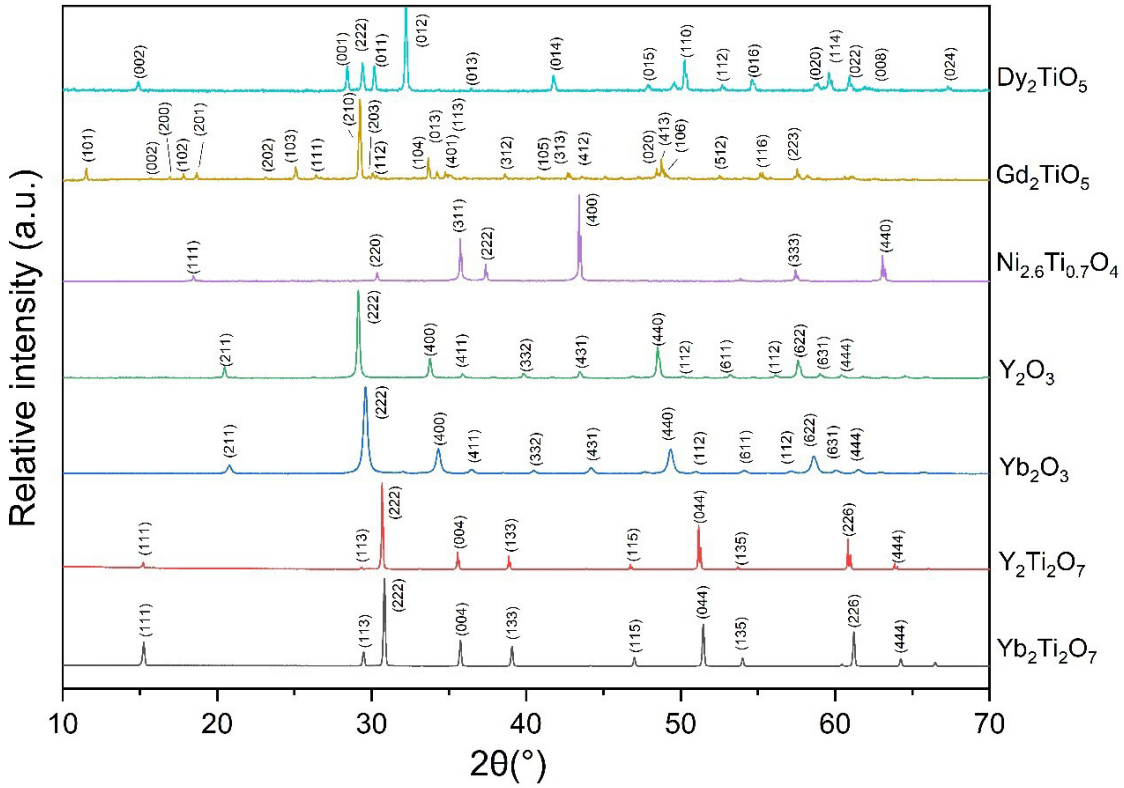

Figure B1: XRD data for standards used in analysis of XAS. Standards are indexed in the following space groups: $Yb_2Ti_2O_7$ = *Fd-3m*, $Y_2Ti_2O_7$ = *Fd-3m*, Yb_2O_3 = *Ia-3*, Y_2O_3 = *Ia-3*, Ni_2TiO_4 = *Fd-3m*, Gd_2TiO_5 = *Pnma* and Dy_2TiO_5 = *P6$_3$/mmc*.

C: Example fit to pre-edge features of Y_2TiO_5 quenched Ti K-edge

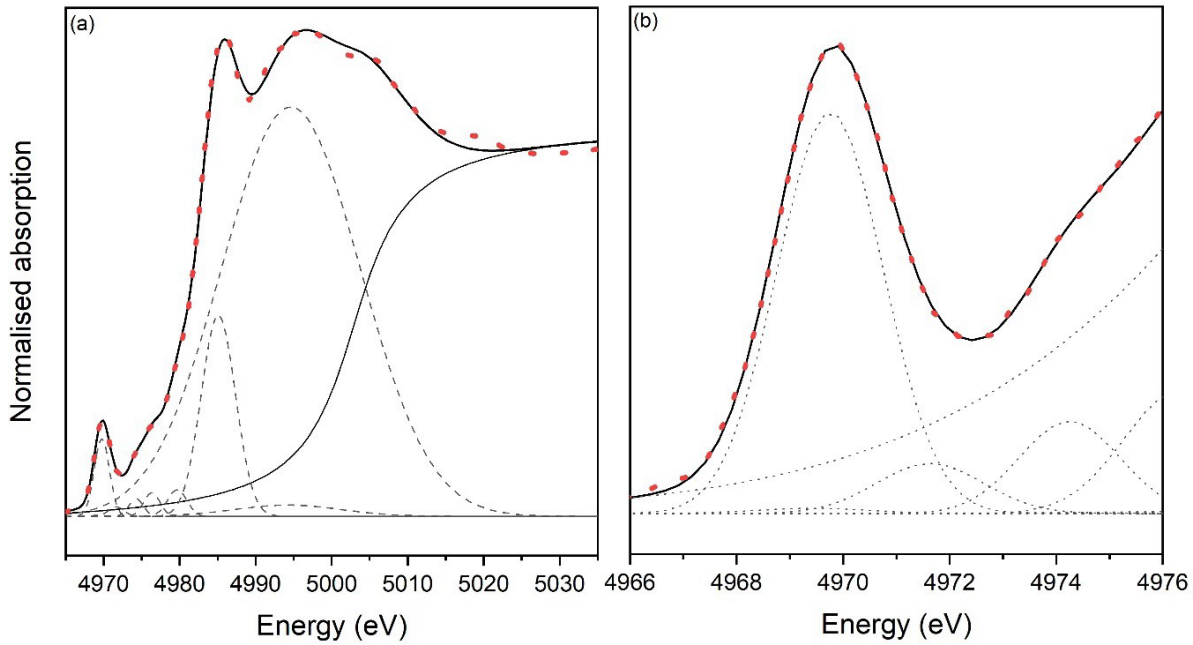

Figure C1: Fitting of XANES features for Y_2TiO_5 (Q). (a) XANES region (b) pre-edge features. The data were fit using combinations of Gaussian and arctangent functions (shown as grey lines); data are shown by red dashed lines, fit is shown by a solid black line

D: S_n^2 determination - fitting results of Ln$_2$Ti$_2$O$_7$ standards

Accurate determination of an unknown first oxygen shell coordination number (N_O) requires prior determination of the amplitude reduction factor (S_n^2) since these two parameters directly contribute to the signal intensity and are completely correlated. Therefore, a value of S_n^2 was determined through fitting of the first shell of the Ti K edge fluorescence XAS data for $Y_2Ti_2O_7$ (pyrochlore *Fd-3m* structure as confirmed by X-ray diffraction (Figure A1)).

The structure of $Y_2Ti_2O_7$ and $Yb_2Ti_2O_7$ pyrochlores have been reported *Haile et al.* and *Shlyakhtina et al.* [3], [4] and this was used to provide a basic model for fitting the Ti K-edge EXAFS data. FEFF calculations were performed to generate appropriate scattering paths between the central Ti absorber and shells of next nearest neighbours. Titanium cations on the B-site in the pyrochlore structure are characterised as having 6 Ti-O_1 nearest neighbours at a distance of ca. 1.96 Å, 6 Ti-Ln and 6 Ti-Ti bonds at ca. 3.57 Å (Table C1). Visual inspection of the k^3-weighted waveform and the corresponding Fourier transform show a major contribution to the amplitude arising at ca. 1.6 Å (uncorrected for phase shift), which arises from the nearest neighbour oxygen shell (Figures C1 and C2). Additional smaller contributions can be observed in the region between ca. 2.5 and 4.0 Å. This model gave a good fit

($Y_2Ti_2O_7$ R-factor 4.5% and $Yb_2Ti_2O_7$ R-factor 3.6%) to the $k^3\chi(k)$ waveform and the FT $k^3\chi(k)$ spectral envelope out to a k = 13 Å^{-1} and an R = 4.0 Å. The refined S_n^2 values were 0.58 ± 0.07 and 0.54 ± 0.10, respectively for $Y_2Ti_2O_7$ and $Yb_2Ti_2O_7$

A similar procedure was followed for Y K-edge and Yb L_3edge XAS data acquired from the $Y_2Ti_2O_7$ and $Yb_2Ti_2O_7$ standards. The structure reported by *Haile et al.* and *Shlyakhtina et al.* [3], [4] was used as the basis for the starting model. The nearest neighbour anion shell contains eight oxygen atoms, 2 Ln-O_{8b} are at a distance of ca. 2.19 Å and 6 Ln-O_{48f} at ca. 2.48 Å. This is followed by 6 of both Ln-Ti and Ln-Ln contacts at 3.57 Å. Scattering paths for each bond length were included in the structural model. The results of these fits can be seen in Figures C1 and C2 and Table C1. This produced good fits (R- factors 5.1 % (BVS = 3.03) and 2.2 % (BVS = 3.06), respectively for $Y_2Ti_2O_7$ and $Yb_2Ti_2O_7$ models) to the main features in the $k^3\chi(k)$ waveform and the FT $k^3\chi(k)$ spectral envelope out to a k = 14 Å^{-1} and an R = 4.0 Å, respectively. The bond valence sum, determined from the refined models, were 3.03 ± 0.1 v.u. for $Y_2Ti_2O_7$ and 3.06 ± 0.1 v.u. for $Yb_2Ti_2O_7$, in good agreement with the formal valence of Y (3 v.u.) and refined S_n^2 values of 0.75 ± 0.07 and 0.79 ± 0.09.

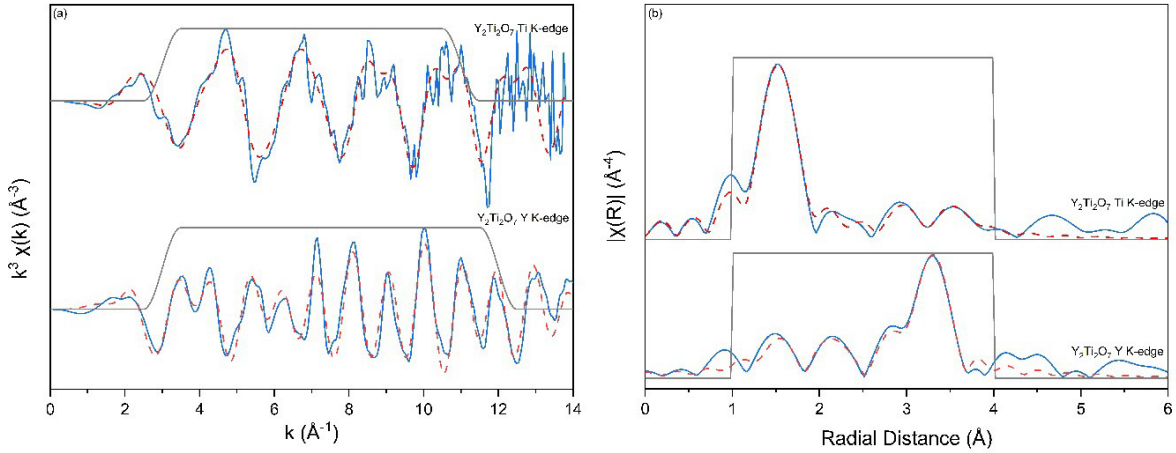

Figure D1: (a) k^3 weighted Ti and Y k-edge waveforms for the $Y_2Ti_2O_7$ samples; (b) the Fourier transform of the waveform in R space. Blue line represents the experimental data and the red line represents the theoretical fit. The grey lines indicate the fitting windows used.

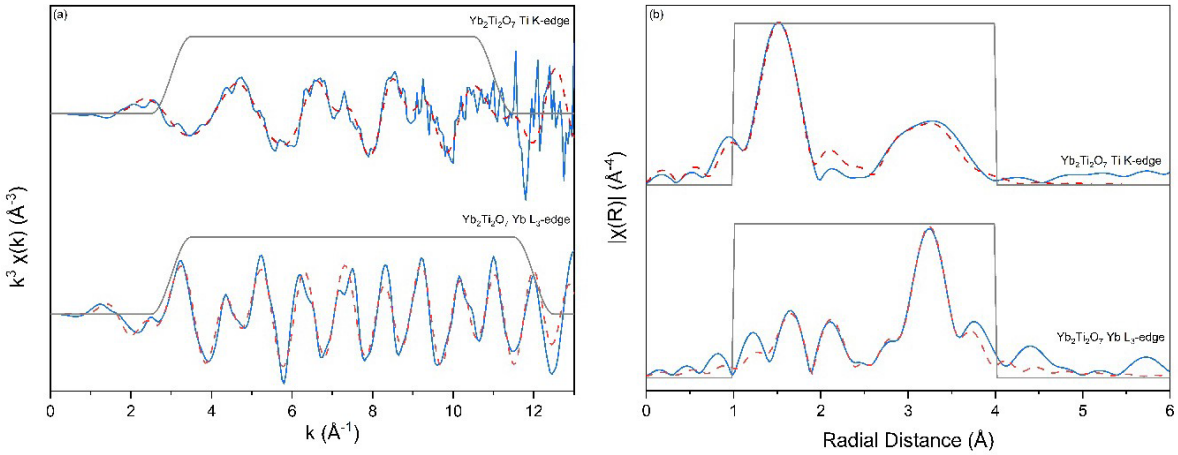

Figure D2: (a) k^3 weighted Ti and Yb L_3-edge waveforms for the $Yb_2Ti_2O_7$ samples; (b) the Fourier transform of the waveform in R space. Blue line represents the experimental data, and the red line represents the theoretical fit. The grey lines indicate the fitting windows used.

Table D1: Refined structural parameters for the $Y_2Ti_2O_7$ and $Yb_2Ti_2O_7$ standards measured at the Ti k-edge Yb L_3-edge and Y k-edge. The average change in the scattering path distance for a given absorber-scatterer pair is denoted as R, the Debye–Waller factor is denoted as σ^2, the number of scatters in the coordination shell is denoted as N and Ln = Yb or Y. The fitting range in R was 1–4 Å and 3.0–10 in k for Ti k-edge data. The fitting range in R was 1–4 Å at all edges. The fitting range in k was 3-12 for Y k-edge and Yb L_3-edge data.

Path		Y2Ti2O7 Ti k-edge	Yb2Ti2O7 Ti k-edge	Path		Y2Ti2O7 Y k-edge	Yb2Ti2O7 Yb L3-edge
	E_0 (eV)	-1.5(7)	-1.9(12)		E_0 (eV)	3.1(11)	3.7(10)
	S_0^2	0.58(7)	0.54(10)		S_0^2	0.75(7)	0.79(9)
Ti-O N = 6	*R (Å)*	1.97(1)	1.95(2)	**Ln-O_1 N = 2**	*R (Å)*	2.26(4)	2.17(2)
	σ^2 (Å^2)	0.003(1)	0.003(2)		*σ^2 (Å^2)*	0.007(1)	0.004(3)
Ti-Ln N = 6	*R (Å)*	3.92(9)	3.50(7)	**Ln-O_2 N = 6**	*R (Å)*	2.44(4)	2.44(2)
	σ^2 (Å^2)	0.006(3)	0.008(7)		*σ^2 (Å^2)*	0.010(8)	0.014(4)
Ti-Ti N = 6	*R (Å)*	3.89(7)	3.58(7)	**Ln-Ln N = 6**	*R (Å)*	3.65(3)	3.55(1)
	σ^2 (Å^2)	0.006(4)	0.003(2)		*σ^2 (Å^2)*	0.006(5)	0.006(1)
				Ln-Ti N = 6	*R (Å)*	3.68(5)	3.54(2)
					σ^2 (Å^2)	0.013(9)	0.012(3)
R-factor		0.045	0.036	**R-factor**		0.041	0.022
BVS (v.u.)		4.06	4.20	**BVS (v.u.)**		3.03	3.06

E: Yb_2TiO_5 A- and B-site contribution refinement: Example

Initial EXAFS models of Ln_2TiO_5 (where Ln = Yb or Y) using a cubic *Fd*-3m structure for Yb L_3- and Y K-edge data allowed contributions from B-site lanthanides (as per recast stoichiometry $Ln_2(Ln_{0.66}Ti_{1.33})O_{6.67}$) with the relative contributions to the signal from Ln(A)-O and Ln(B)-O paths weighted appropriately in a ratio of 3:1. Ln(A)-Ln, Ln(B)-Ln, Ln(A)-Ti and Ln(B)-Ti paths all had $R_{effective}$ path lengths of 3.56 Å and as such, to minimize unnecessary variables, Ln-Ln and Ln-Ti contributions were represented by one path each where the total path degeneracy was *N(A) + N(B)*. This failed to elicit a convincing fit, yielding large changes in σ^2 or *R* (the latter of which was reflected in unphysical BVS totals). The signal weighting factor, *y*, was allowed to refine to determine the relative contribution (and site occupancy) of B-site lanthanides. This refinement was done so with a restraint to prevent the value from becoming unphysically large or small (e.g. y >> 1). An example of a fit can be found below Figure D1, Table D1). Other variations on this model also gave a similar result.

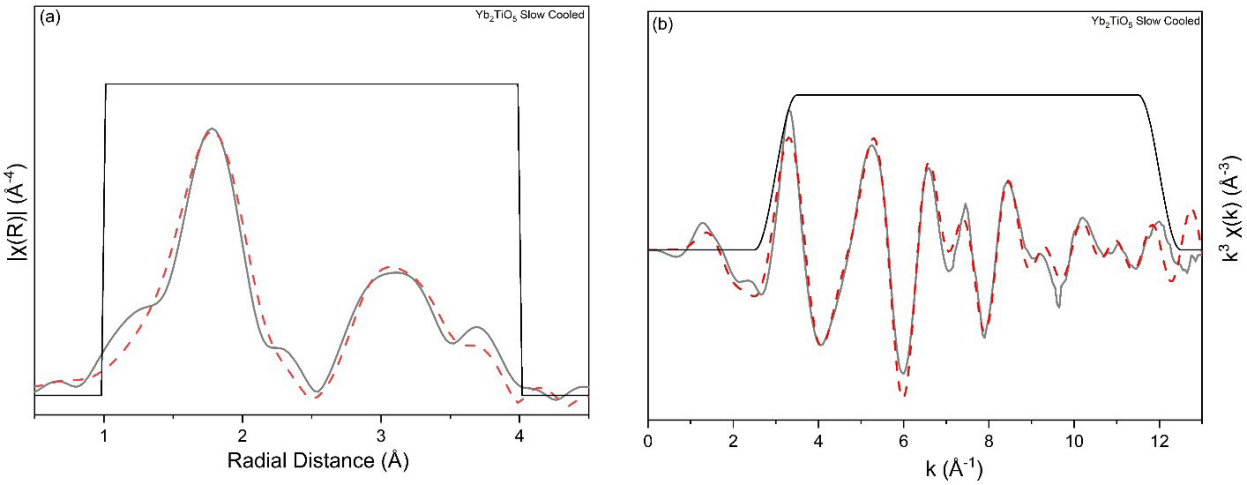

Figure E1: Example fit of a model that included Ln A- and B-site contributions. a) Fourier transform of Yb L_3-edge waveform of Yb_2TiO_5 Slow cooled in R-space; b) k^3 weighted waveform. Solid grey line represents experimental data, red dashed line represents the theoretical cubic fit, Black line indicates the fitting window.

Table E1: Refined structural parameters for the Yb_2TiO_5 Slow cooled measured at the Yb L_3-edge modelled using a both A- and B-site contributions in a cubic *Fd*-3m structure. The average change in scattering path distance for a given absorber-scatterer pair is denoted as R, the Debye–Waller factor is denoted as σ^2, the degeneracy of the path is denoted as N and Ln represents the corresponding metal cation (Ln = Yb) The fitting range in R was 1–4 Å and 3–12 in k

Cubic A- and B-site Yb		**Yb_2TiO_5 (SC)**
	Eo (eV)	2.1(25)
Ln-O(A) N = 8	*R (Å)*	2.23(10)
	σ^2 (Å^2)	0.011(10)
Ln-O(B) N = 5	*R (Å)*	2.09(30)
	σ^2 (Å^2)	-0.001(95)
Ln-Ln N = 8	*R (Å)*	3.58(1)
	σ^2 (Å^2)	0.007(5)
Ln-Ti N = 4	*R (Å)*	3.86(5)
	σ^2 (Å^2)	0.017(24)
	y	0.99(2)
R-factor		0.024
BVS (A) (v.u.)		3.71
BVS (B) (v.u.)		3.42

In the example the weighting parameter *y* refined to 0.99 +/- 0.02 (1 within error). This result was consistent for all data sets and models fit over different data ranges. Future fits excluding contributions from B-site Ln absorbers saw a marked improvement and are presented in the manuscript.

F: Orthorhombic model fits to Y_2TiO_5 and Yb_2TiO_5 (Slow cooled, Quenched)

The orthorhombic structure has been shown to well represent the local structure of Yb_2TiO_5 [9] as determined through neutron pair distribution function (PDF) studies and the coexistence of cubic and orthorhombic structures at different length scales has been established in related A_3BO_7 (where A = Ln and B = Os, Re, Ru, Re, Mo, Ir, Sb, Nb or Ta) compounds [5], [6]. As such, a model utilising an orthorhombic structure was attempted.

The orthorhombic structure of Y_2TiO_5 that was refined by *Mumme and Wadsley* [7] was used as the basis for this model. As no CIF exists for orthorhombic Yb_2TiO_5, the Y_2TiO_5 CIF refined by *Mumme and Wadsley*, which crystallises in an orthorhombic *Pnma* structure, was edited to accommodate Yb on the lanthanide sites for Yb_2TiO_5 models. From the Ti core absorber, the nearest neighbour anion shell consists of 1 O at 1.78 Å, 1 O at 1.88 Å and 3 O at 1.93 Å. The next shell consists of 5 Ln atoms (4 at 3.35 Å and 1 at 3.65 Å) and 2 Ti atoms at 3.70 Å. The associated σ^2 parameters of Ln-O single scattering paths were grouped together to reduce the number of variables being refined. The resultant fits can be found in Figure E1 along with the refined parameter values in Table E1. The model yielded a good fit with R-factor values (2.7 % - 4.5%) that indicated a slightly worse, but comparable, goodness of fit compared with those obtained at the Ti K-edge when fitting to a cubic structure. The BVS (3.73 – 3.85) were also considerably smaller than that for the cubic pyrochlore based model for both the Y_2TiO_5 and Yb_2TiO_5 samples. The majority of the bond lengths changed consistently and by an acceptable degree within the constraints of a local square pyramidal geometry. However, the Ti-Yb and Ti-Ti bonds moved by 0.2 Å and -0.44 Å, respectively, for the quenched Yb_2TiO_5 sample resulting in a reversal of which cation is found closest to the central absorber site. Whilst this could be a feature of the crystal structure it is not observed in Y chemistries nor in other structural models of the Ti K-edge and is more likely an indication that the model is not accurately representing the Ti-Cation paths. A visual inspection of the data and corresponding fits in Figure E1 shows that the model accurately represents the experimental data.

The Y K-edge and Yb L_3-edge were also fit using the orthorhombic structure by weighting each Ln core absorber by 0.5, as there are two Ln core absorbers occupying a 7-fold polyhedral coordination [8]. σ^2 parameters were shared between like-for-like elements. This led to a good fit for both the slow cooled and quenched samples, with R-factors of 2.3% and 1.8%, respectively for Y_2TiO_5 samples. The Yb_2TiO_5 samples also afforded acceptable goodness of fit values of 2.5% and 2.7%, respectively for the quenched and slow cooled samples. Results for the fit can be found in Figure E1 and Table E2. The bond valence sums, taken individually for the two Ln-O bonds for each Ln core, were between 15-25% off from the formal valence, 3 v.u., of Yb or Y. For all samples the BVS of each core was either significantly under-bonded or over-bonded, for instance the BVS for Ln(1)-O Y_2TiO_5 (SC) was 3.72 and for Ln-O(2) 2.57. This implies that the Ln coordination environment was not accurately represented by two 7-fold octahedra characteristic of orthorhombic *Pnma* Ln_2TiO_5. The refined bond distances for

the more distant cation shells were consistent with the orthorhombic structure. However, the Ln-Ti bond distances lacked some regularity. The refined bond distances of Ln-Ti(1) (N = 5) and Ln-Ti(2) (N = 3) were 3.03 Å and 3.36 Å, respectively, for quenched Y_2TiO_5. Whereas, for slow cooled Y_2TiO_5 the inverse can be seen with Ln-Ti(1) at a longer distance (3.30 Å) and Ln-Ti(2) at a shorter distance (3.01 Å). The opposite trend is observed in Yb_2TiO_5 models. (i.e. the refined bond distance of Yb-Ti(1) in quenched Yb_2TiO_5 is greater than that of Ln-Ti(2) path). It should be noted the refined bond distances are commensurate with those observed in the cubic models. This is likely due to the commonality of the distances and average degeneracies of cation shells around the two central absorbers in an orthorhombic structure and a cubic pyrochlore structure.

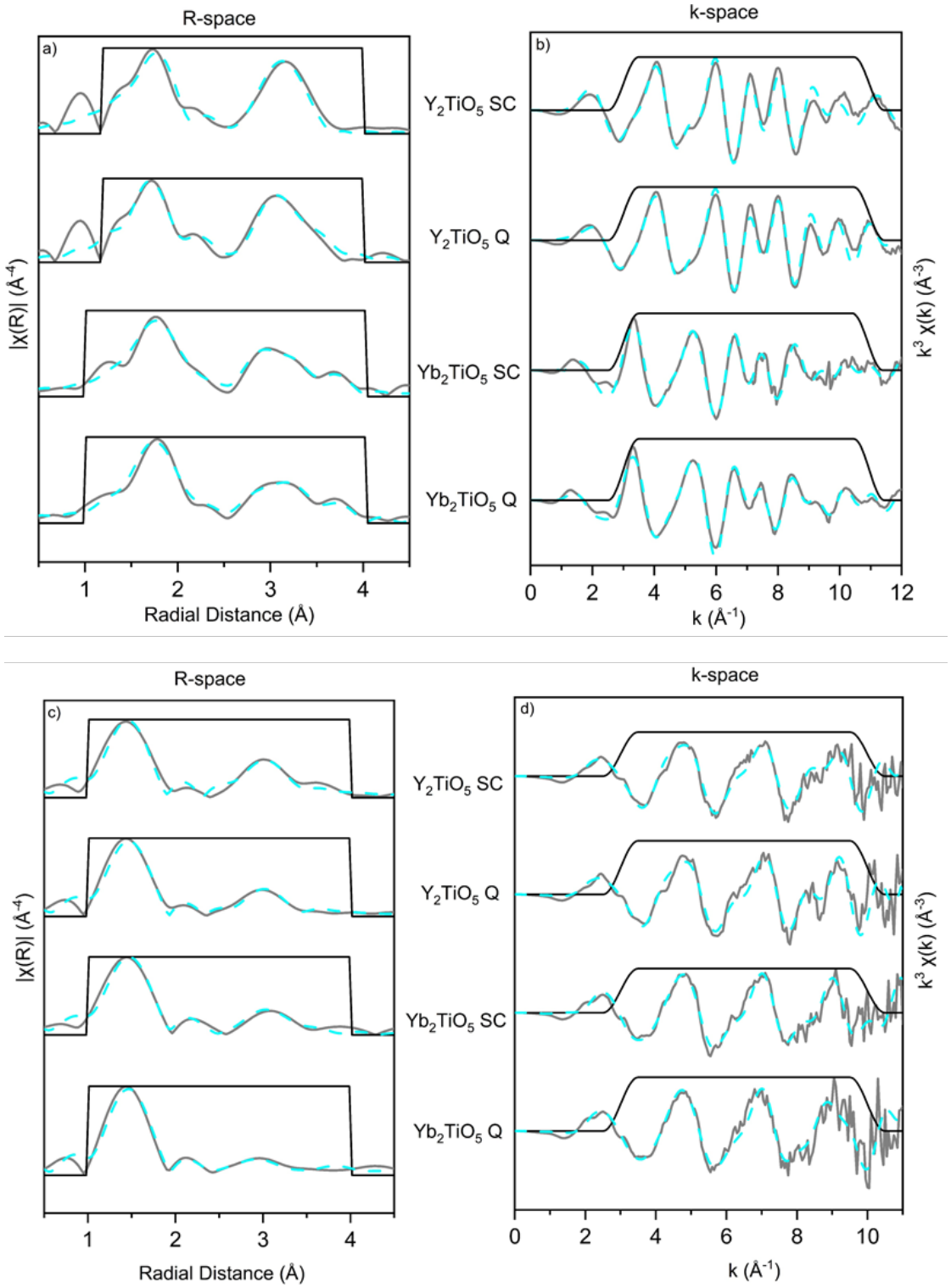

Figure F1: a) Fourier transform of Yb L_3-edge and Y K-edge waveforms of Yb_2TiO_5 and Y_2TiO_5, respectively, in R-space; b) k^3 weighted waveform of Yb L_3-edge and Y K-edge data; c) Fourier transform of Ti K-edge waveform of Yb_2TiO_5 and Y_2TiO_5 in R-space; d) k^3 weighted waveform of Ti K-

edge data Solid grey line represents experimental data, blue dashed line represents the theoretical orthorhombic fit and the black line indicates the fitting window. SC – Slow cooled; Q – Quenched.

Table F1: Refined structural parameters for the Y_2TiO_5 and Yb_2TiO_5 samples measured at the Ti k-edge modelled using an orthorhombic *Pnma* structure. The average change in scattering path distance for a given absorber-scatterer pair is denoted as R, the Debye–Waller factor is denoted as σ^2, the degeneracy of the path is denoted as N and Ln represents the corresponding metal cation (Ln = Y, Yb) The fitting range in R was 1–4 Å and 3–10 in k.

		Y_2TiO_5 (Q)	**Y_2TiO_5 (SC)**	**Yb_2TiO_5 (Q)**	**Yb_2TiO_5 (SC)**
	E_0 (eV)	-1.5(12)	-2.7(18)	-1.5(16)	-1.7(15)
Ti-O	*R (Å)*	1.90(1)	1.91(1)	1.92(1)	1.92(1)
N = 5	*σ^2 (Å²)*	0.003(1)	0.004(2)	0.002(1)	0.003(1)
Ti-Ln	*R (Å)*	3.43(2)	3.44(2)	3.55(15)	3.37(5)
N = 5	*σ^2 (Å²)*	0.007(2)	0.006(2)	0.026(31)	0.006(6)
Ti-Ti	*R (Å)*	3.80(4)	3.81(6)	3.26(4)	3.54(41)
N = 2	*σ^2 (Å²)*	0.003(6)	0.006(9)	0.008(5)	0.045(124)
R-factor		0.037	0.045	0.032	0.027
BVS (v.u.)		3.73	3.85	3.76	3.77

Table F2: Refined structural parameters for the Y_2TiO_5 and Yb_2TiO_5 samples measured at the Yb L_3-edge and Y K-edge modelled using an orthorhombic *Pnma* structure. The average change in scattering path distance for a given absorber-scatterer pair is denoted as R, the Debye–Waller factor is denoted as σ^2, the degeneracy of the path is denoted as N and Ln represents the corresponding metal cation (Ln = Y, Yb) The fitting range in R was 1–4 Å and 3–11 in k.

		Y_2TiO_5 (Q)	Y_2TiO_5 (SC)	Yb_2TiO_5 (Q)	Yb_2TiO_5 (SC)
	E_o (eV)	-3.2(1.4)	-3.9(15)	2.0(12)	4.7(10)
Ln-O(1) N = 7	*R (Å)*	2.24(2)	2.23(1)	2.21(2)	2.34(5)
	σ^2 (Å²)	0.004(2)	0.004(1)	0.009(5)	0.015(7)
Ln-O(2) N = 7	*R (Å)*	2.39(2)	2.38(2)	2.31(2)	2.31(3)
	σ^2 (Å²)	0.004(2)	0.004(1)	0.009(5)	0.015(7)
Ln-Ln(1) N = 7	*R (Å)*	3.58(2)	3.60(2)	3.20(4)	3.79(7)
	σ^2 (Å²)	0.005(2)	0.004(1)	0.005(6)	0.017(9)
Ln-Ln(2) N = 9	*R (Å)*	3.58(2)	3.56(2)	3.45(6)	3.47(4)
	σ^2 (Å²)	0.005(2)	0.004(1)	0.005(6)	0.017(9)
Ln-Ti(1) N = 5	*R (Å)*	3.03(4)	3.30(4)	3.45(8)	3.36(2)
	σ^2 (Å²)	0.012(3)	0.011(4)	0.005(13)	0.004(1)
Ln-Ti(2) N = 3	*R (Å)*	3.36(4)	3.01(4)	3.38(4)	3.51(1)
	σ^2 (Å²)	0.012(3)	0.011(4)	0.005(13)	0.004(1)
R-factor		0.023	0.018	0.025	0.027
BVS (v.u.) O(1)		3.72	3.68	2.59	3.47
BVS (v.u.) O(2)		2.57	2.48	3.72	2.36

G: Hexagonal model fits to Y_2TiO_5 and Yb_2TiO_5 (Slow cooled, Quenched)

Modelling of the pre-edge features of Ti K-edge data showed that the local Ti coordination environment is close to that of a five-fold trigonal bipyramid. This geometry is found in the hexagonal structure of certain Ln_2TiO_5 compounds wherein the A-site is occupied by intermediately sized Ln. Based on these results, hexagonal model was also fit to the experimental data.

The hexagonal structure was fit using a modified version of the $Yb_{0.6}Sm_{1.4}TiO_5$ (wherein the average Ln ionic radius of $Yb_{0.6}Sm_{01.4}$ is 0.895 Å, which allows for the stabilisation of the hexagonal structure) structure determined by *Aughterson et al*. [9] as the basis for the model, wherein all Sm dopants were

removed and the Yb or Y, Ti, O given appropriate site occupancies. From the Ti core absorber, a total 5 O atoms can be found constituting the first O shell (trigonal bipyramidal motif), with the first 2 O at 1.97 Å and the remaining 3 at 2.11 Å. This is followed by 6 Ln atoms at 3.63 Å and 6 Ti atoms at 3.65 Å. The resultant fit and refined parameter values, seen in Figure F1 and Table F1, show that Ti-Ln bond distances in the quenched sample of Y_2TiO_5 are contracting by 0.2 Å from their initial positions but in the slow cooled sample they are contracting by 0.6 Å. Given the smaller ionic radius of Yb and Y compared to the average ionic radius of $Yb_{0.6}Sm_{01.4}$, decreases in bond distances would be expected. However, this was not the case for all samples modelled. The R-factor values and BVS are consistent with the other Ti K-edge models. The refined bond distances are consistent with the cubic based model for the Ti K-edge data, given that the degeneracies are the same, this is not surprising.

The modified hexagonal structure from *Aughterson et al*. used to model the Y K-edge and Yb L_3-edge EXAFS regions [9] and set up in the same manner as previously described. Refinements of the site occupancies of Ln cations of hexagonal Dy_2TiO_5 [1] and $Yb_{2-x}Sm_xTiO_5$ [9] have shown the ratio of Ln:Ti on occupying the B-site position can vary depending on chemistry. This was accounted for by allowing a weighting factor, x, to refine to determine the relative contribution to the signal from each site. In each model this was found to approach unity This indicates that the contribution to the EXAFS signal is dominated by A-site Ln cations. The B-site occupancy of hexagonal Dy_2TiO_5 was shown to have a fractional occupancy of 0.24, or 12% of the total Dy atoms [1]. This low amount of Ln atoms found on the B-site may not be significant enough to contribute meaningfully to the average EXAFS signal, given the bulk measurement nature of transmission mode collected EXAFS. This model consisted of 6 O at 2.4 Å followed by 2 O at 3.0 Å. The metal cation shell consists of 4 Ti and 2 Ln atoms, both at 3.67 Å, on the B-site and 6 Ln atoms at 3.66 Å (Figure F1 and Table F2). The bond valence sums were calculated to be 3.05 v.u. for quenched Y_2TiO_5 and 2.97 v.u. for slow cooled Y_2TiO_5, well within 5% of the formal valence of Y, 3 v.u. Inspection of the Yb_2TiO_5 BVS, giving values of 3.06 v.u. for the quenched sample and 3.03 v.u. for the slow cooled, again, within 5% of the formal valence of Yb (3 v.u). The trends in refined bond distances of these models were found to be inconsistent between chemistries. The goodness of fit for the models were comparatively high compared to cubic models, between 2.8%-4.1% for all data sets. Visually there is notable mismatch between the experimental data and theoretical fit in regions between 2.5 - 4 Å, this region is predominately made up of contributions from cation-cation scattering paths.

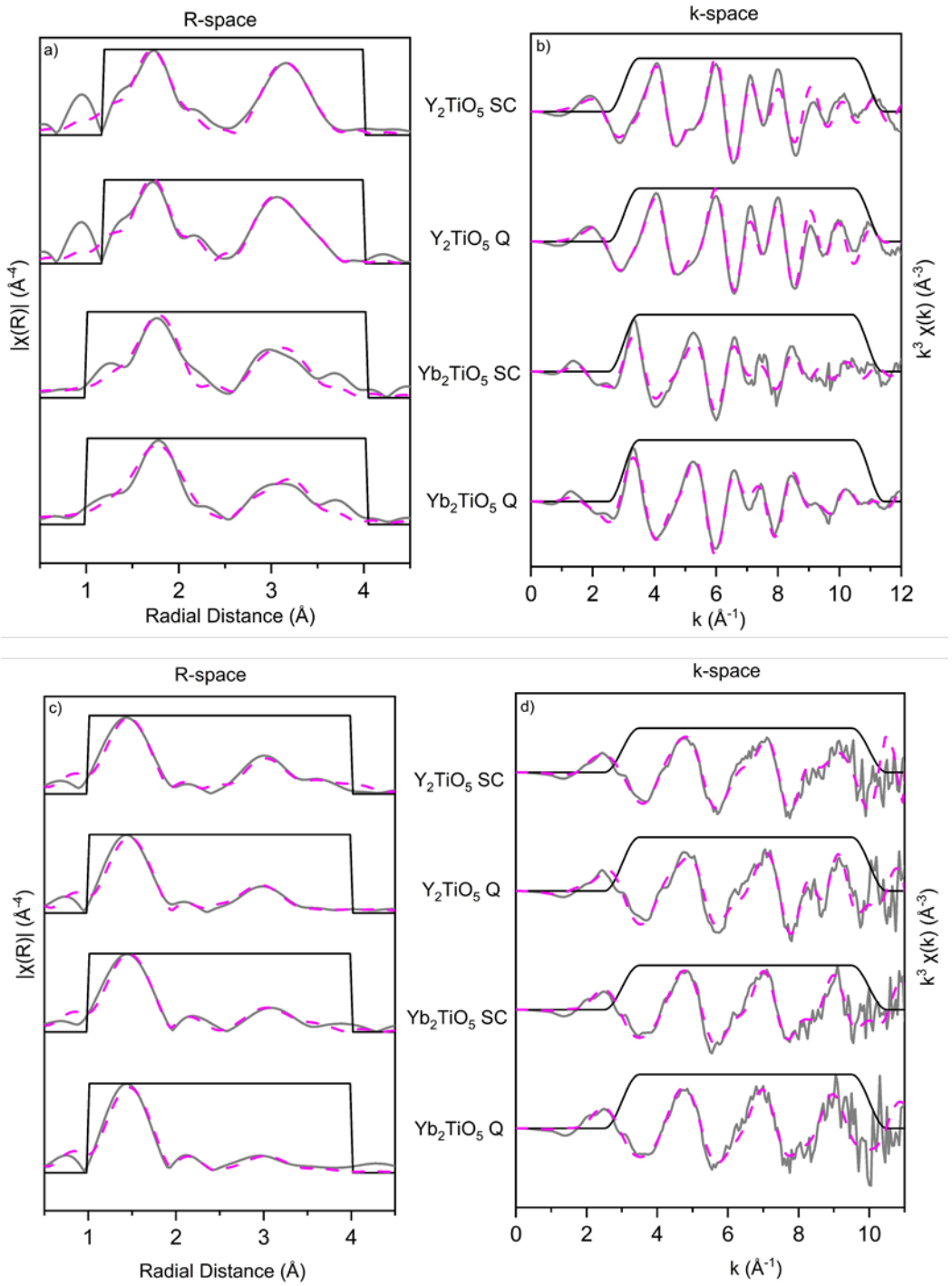

Figure G1: a) Fourier transform of Yb L_3-edge and Y K-edge waveforms of Yb_2TiO_5 and Y_2TiO_5, respectively, in R-space; b) k^3 weighted waveform of Yb L_3-edge and Y K-edge data; c) Fourier transform of Ti K-edge waveform of Yb_2TiO_5 and Y_2TiO_5 in R-space; d) k^3 weighted waveform of Ti K-edge data Solid grey line represents experimental data, pink dashed line represents the theoretical hexagonal fit and the black line indicates the fitting window. SC – Slow cooled; Q – Quenched.

Table G1: Refined structural parameters for the Y_2TiO_5 and Yb_2TiO_5 samples measured at the Ti k-edge modelled using a hexagonal *P6₃/mmc* structure. The average change in scattering path distance for a given absorber-scatterer pair is denoted as R, the Debye–Waller factor is denoted as σ^2, the degeneracy of the path is denoted as N and Ln represents the corresponding metal cation (Ln = Y, Yb) The fitting range in R was 1–4 Å and 3–10 in k.

Hexagonal		**Y_2TiO_5 (Q)**	**Y_2TiO_5 (SC)**	**Yb_2TiO_5 (Q)**	**Yb_2TiO_5 (SC)**
	E_0 (eV)	-2.7(14)	-1.6(19)	-2.1(16)	-2.1(15)
Ti-O N = 5	*R (Å)*	1.92(10)	1.92(2)	1.92(1)	1.92(1)
	σ^2 (Å²)	0.004(1)	0.039(1)	0.003(1)	0.003(1)
Ti-Ln N = 8	*R (Å)*	3.44(2)	3.09(3)	3.41(4)	3.39(3)
	σ^2 (Å²)	0.011(2)	0.017(5)	0.012(5)	0.009(3)
Ti-Ti N = 4	*R (Å)*	3.86(4)	3.64(3)	3.43(10)	3.42(9)
	σ^2 (Å²)	0.012(2)	0.012(2)	0.012(1)	0.013(1)
R-factor		0.039	0.065	0.042	0.029
BVS (v.u.)		3.74	3.8	3.8	3.78

Table G2: Refined structural parameters for the Y_2TiO_5 and Yb_2TiO_5 samples measured at the Yb L_3- edge and Y K-edge modelled using an hexagonal *$P6_3/mmc$* structure. The average change in scattering path distance for a given absorber-scatterer pair is denoted as R, the Debye–Waller factor is denoted as σ^2, the degeneracy of the path is denoted as N and Ln represents the corresponding metal cation (Ln = Y, Yb) The fitting range in R was 1–4 Å and 3–11 in k.

Hexagonal		**Y_2TiO_5 (Q)**	**Y_2TiO_5 (SC)**	**Yb_2TiO_5 (Q)**	**Yb_2TiO_5 (SC)**
	E_o (eV)	-6.1(18)	-4.3(17)	0.6(11)	1.4(11)
Ln-O(1)	*R (Å)*	2.28(1)	2.31(2)	2.22(1)	2.22(1)
N = 6	*σ^2 (Å²)*	0.009(1)	0.014(2)	0.010(1)	0.010(1)
Ln-O(2)	*R (Å)*	2.86(5)	2.79(3)	2.99(6)	2.96(1)
N = 2	*σ^2 (Å²)*	0.010(7)	0.014(4)	0.010(7)	0.010(5)
Ln-Ln	*R (Å)*	3.58(1)	3.57(2)	3.40(2)	3.51(2)
N = 8	*σ^2 (Å²)*	0.011(2)	0.011(2)	0.012(2)	0.014(2)
Ln-Ti	*R (Å)*	3.86(5)	3.33(4)	3.52(4)	3.38(3)
N = 4	*σ^2 (Å²)*	0.011(2)	0.010(4)	0.021(4)	0.015(5)
R-factor		0.028	0.037	0.030	0.041
BVS (v.u.)		3.05	2.97	3.06	3.03

H: References

[1] R. D. Aughterson, N. J. Zaluzec, and G. R. Lumpkin, "Synthesis and ion-irradiation tolerance of the Dy_2TiO_5 polymorphs," *Acta Mater.*, vol. 204, p. 116518, Feb. 2021.

[2] G. A. Lager, T. Armbruster, F. K. Ross, F. J. Rotella, and J. D. Jorgensen, "Neutron powder diffraction study of defect spinel structures: Tetrahedrally coordinated Ti^{4+} in $Ni_{2.62}Ti_{0.69}O_4$ and $Ni_{2.42}Ti_{0.74}Si_{0.05}O_4$," *J. Appl. Crystallogr.*, vol. 14, no. 4, pp. 261–264, Aug. 1981.

[3] S. M. Haile, B. J. Wuensch, and E. Prince, " Neutron Rietveld Analysis of Anion and Cation Disorder in the Fast-Ion Conducting Pyrochlore System $Y_2(Zr_xTi_{1-x})_2O_7$," *MRS Proc.*, vol. 166, 1989.

[4] A. V. Shlyakhtina *et al.*, "Effect of the Ca-doping on the electrical conductivity of oxide ion conductor $Yb_2Ti_2O_7$," *Solid State Ionics*, vol. 179, no. 21–26, pp. 1004–1008, Sep. 2008.

[5] J. Shamblin *et al.*, "Probing disorder in isometric pyrochlore and related complex oxides," *Nat. Mater.*, vol. 15, no. 5, pp. 507–511, May 2016.

[6] G. King, C. M. Thompson, J. E. Greedan, and A. Llobet, "Local structure of the vacancy disordered fluorite Yb_3TaO_7 from neutron total scattering," *J. Mater. Chem. A*, vol. 1, no. 35,

pp. 10487–10494, Sep. 2013.

[7] W. G. Mumme and A. D. Wadsley, “The structure of orthorhombic Y_2TiO_5, an example of mixed seven- and fivefold coordination,” *Acta Crystallogr. Sect. B Struct. Crystallogr. Cryst. Chem.*, vol. 24, no. 10, pp. 1327–1333, Oct. 1968.

[8] R. D. Aughterson, G. R. Lumpkin, G. J. Thorogood, Z. Zhang, B. Gault, and J. M. Cairney, “Crystal chemistry of the orthorhombic Ln_2TiO_5 compounds with Ln=La, Pr, Nd, Sm, Gd, Tb and Dy,” *J. Solid State Chem.*, vol. 227, pp. 60–67, Jul. 2015.

[9] R. D. Aughterson *et al.*, “Crystal structures of orthorhombic, hexagonal, and cubic compounds of the $Sm_{(x)}Yb_{(2-x)}TiO_5$ series,” *J. Solid State Chem.*, vol. 213, pp. 182–192, May 2014.

5. Draft paper: Characterisation of the local structure of Ln_2TiO_5 (Ln = La, Pr, Nd, Sm, Eu, Gd, Tb, Dy, Ho, Er, Tm, Yb, Lu) compounds through multi element XANES and EXAFS analyses

In this study a series of Ln_2TiO_5 (Ln = La, Pr, Nd, Sm, Eu, Gd, Tb, Dy, Ho, Er, Tm, Yb, Lu) stuffed pyrochlores are fabricated through solid-state synthesis, these compounds constitute the entire range of known stable Ln_2TiO_5 stuffed pyrochlores as well as the three crystal structures associated with the series (orthorhombic, hexagonal and cubic). The aim of this study was to characterise the short-range order associated with each crystal structure, not only giving for the first time a comprehensive description of said short-range order, but also forming the basis for further experiments investigating the radiation damage effects done to the short-range order, investigated through GAXAS in Section 6. A detailed understanding of the local structural ordering is a prerequisite for understanding, and comparing, radiation damaged samples investigated through this technique.

The work presented here is the form of a draft paper intended for submission to Dalton Transactions, and as such is written in the appropriate style for that journal. Supporting information for each paper follows the refences sections. References to draft paper from chapter 4 are given in the appropriate journal format to keep contintiuty with other references.

The author's contribution was the synthesis of samples, X-ray diffraction, analysis of XANES and EXAFS data and writing of the manuscript. XAS data were acquired by the author in collaboration with M. C. Stennett, N. C. Hyatt. Manuscript proofing and editing were assisted by R. J. Hand, L. T. Townsend, B. Ravel and M. C. Stennett. All authors contributed to the discussions and interpretations of data.

Characterisation of the local structure of Ln_2TiO_5 (Ln = La, Pr, Nd, Sm, Eu, Gd, Tb, Dy, Ho, Er, Tm, Yb, Lu) compounds through multi element XANES and EXAFS analyses

Daniel A. Austin[1], Luke T. Townsend[1], Martin C. Stennett[1], Bruce Ravel[2], Neil. C. Hyatt[1], Russell J. Hand[1]

[1] *Immobilisation Science Laboratory, Department of Materials Science and Engineering, University of Sheffield, Sheffield S1 3JD, United Kingdom*

[2] *National Institute of Standards and Technology, 100 Bureau Drive, Gaithersburg, MD 20899, USA*

Abstract

The Ln_2TiO_5 series of ceramics have seen significant interest for their application as ceramic hosts for actinide wastes arising from nuclear activities, however the local crystal structure of these compounds remains poorly understood. As such, the local structure of orthorhombic, hexagonal, and cubic Ln_2TiO_5 (Ln = La, Pr, Nd, Sm, Eu, Gd, Tb, Dy, Ho, Er, Tm, Yb, Lu) ceramics were investigated using X-ray absorption spectroscopy (XAS) techniques, for the first time. Qualitative and quantitative analyses of the X-ray absorption near edge structure (XANES) and extended X-ray absorption fine structure (EXAFS) regions were performed on data collected at both the Ln L_3-edge and Ti K-edge. The results give conclusive descriptions of the local structural environments of both the Ti and Ln cation sites, showing that Ti is found to be 5-fold coordination with O anions for all structures, and that the coordination geometry of hexagonal and cubic Ln_2TiO_5 compounds is more highly symmetrical than that of orthorhombic compounds. Further EXAFS analysis of both the Ti K- and Ln L_3-edges showed short-range ordering in orthorhombic and hexagonal Ln_2TiO_5 compounds equivalent to the ascribed long-range ordering, whereas cubic Ln_2TiO_5 compounds were well described by a pyrochlore-like structure, with a change in Ti coordination number from 6 to 5. These results will form the foundation for future XAS studies probing the to the local structure response of Ln_2TiO_5 compounds to radiation damage or other adverse conditions, such as aqueous dissolution.

1. Introduction

The $Ln_2O_3 – TiO_2$ binary system is well defined and subject of ongoing interest for potential application across a range of industries, such as nuclear waste immobilisation, semiconductor fabrication and in battery technologies. One such compound from this system, Ln_2TiO_5 (Ln = La – Lu, Y), has received particular interest for applications within the nuclear industry in large part due to their favourable physical and chemical properties (e.g. high thermal and mechanical) when employed in different nuclear environments [1]–[3]. The crystal structure of a particular Ln_2TiO_5 ceramic is dependent upon chemical composition and fabrication methods, with it being possible to obtain a wide range of crystal

phases, such as orthorhombic *Pnma,* hexagonal *P6$_3$/mmc* and cubic *Fm-3m* structures. For instance, orthorhombic Dy_2TiO_5 has been successfully utilised within Russian VVER-1000 and RBMK-1000 reactors, replacing boron steels and boron carbides. Dy is an ideal candidate for this replacement due to the high neutron cross-section of ^{164}Dy isotopes (^{164}Dy thermal neutron absorption cross section = 2780 barns) and the robust response of the material to neutron radiation damage [4], with other lanthanides such as samarium, europium, and gadolinium also under consideration for similar uses. Y_2TiO_5 nanoparticles have found application in oxide-dispersion-strengthened (ODS) steels used in the fabrication of nuclear reactor materials due to their excellent high temperature creep and tensile properties [5], in addition to their resistance to radiation induced swelling [6]. The resistance of damage (cracks, swelling, amorphization, etc.) caused through irradiation is also why Ln_2TiO_5 compounds have been suggested as potential ceramic wasteforms for the immobilisation of radioactive wastes arising from nuclear activities [3], [7]–[10]. Therefore, the importance of developing robust knowledge of the local structural ordering of these materials is vital to predicting and understanding their behaviours when exposed to potentially damaging reactor and disposal environments.

Ln_2TiO_5 compounds, of general formula A_2BO_5, can be considered as a derivative of the $Ln_2Ti_2O_7$ pyrochlore wherein additional lanthanides are 'stuffed' onto the B-site (i.e. $Ln_2(Ln_{0.66}Ti_{1.33})O_{6.67}$). In this case, the effective ionic radii of Ln^{3+} cations will heavily influence the available crystalline phases that these compounds can form. For instance, it has been shown that in the solid-state synthesis of Ln_2TiO_5 stuffed pyrochlores at atmospheric pressure (0.101 MPa), the observed crystal structure will be heavily influenced by the ionic radius of the lanthanide used in addition to the temperature of the reaction. This is illustrated in the structure-stability diagram constructed by *Shepelev and Petrova* (Figure 1) [11] and shows the range of crystallographic structures Ln_2TiO_5 stuffed pyrochlores can adopt. Larger, lower Z lanthanides (La – Eu) adopt an orthorhombic *Pnma* structure [12], first assigned by *Mumme and Wadsley* for Y_2TiO_5, and consists of two distinct edge-sharing LnO_7 polyhedra and titanium cations that are coordinated by five oxygens in a square-based pyramid motif (TiO_5) [13]. Smaller lanthanides (Ho – Lu) adopt a cubic long-range defect-fluorite *Fm-3m* structure, and exhibit short-range ordering that can be well described as a pyrochlore-like (*Fd-3m*) structure [14]–[16]. The pyrochlore structure is a 2 x 2 x 2 super-cell of the fluorite structure, where the A- and B-site cations are ordered (LnO_8, TiO_6 polyhedra) compared to the complete cation mixing found in the defect-fluorite structure (average $(Ln,Ti)O_7$ polyhedra). It has also been observed that intermediately sized lanthanides (Tb – Dy, Y) have been shown to exhibit polymorphism and can potentially crystallise in a cubic, orthorhombic or hexagonal symmetry [11]. The hexagonal *P6$_3$/mmc* structure consists of alternating layers of edge-sharing LnO_6 octahedra and basal corner-sharing TiO_5 trigonal bipyramids [11]. As the ionic radii of Gd – Dy and Y are more comparable to that of Ti^{4+} than the ionic radii of the larger, orthorhombic structured lanthanides, the closer size relationship allows for some of the lanthanide cations to partially occupy the same B-site as the titanium cations. Depending on ionic radii, between 20 – 30% of B-sites have been reported to be occupied by these lanthanides [3], [14], [17].

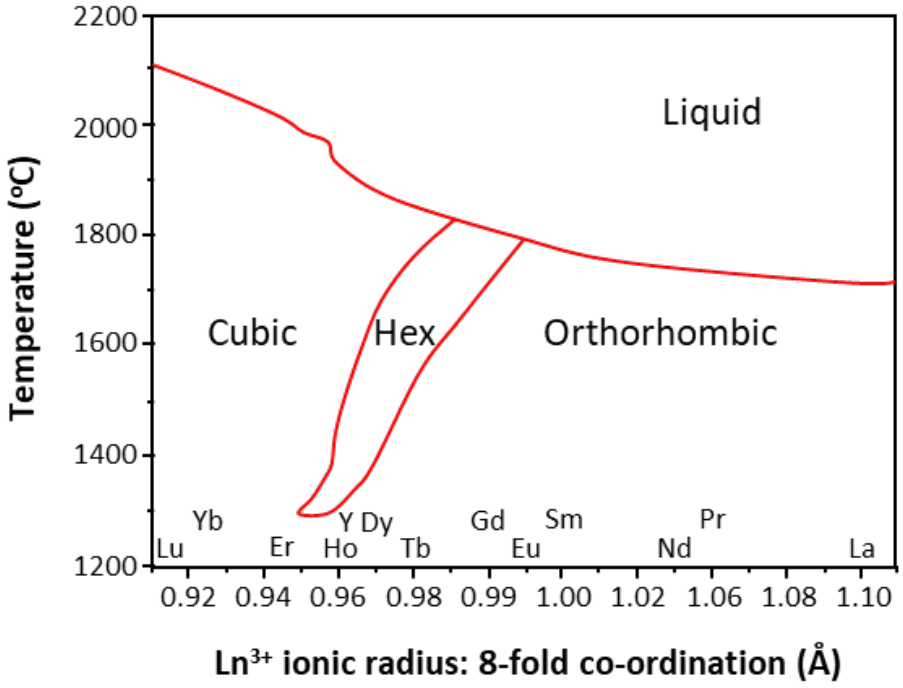

Figure 1: Pseudo-phase diagram showing the expected crystal structure based on the ionic radius of a lanthanide and reaction temperature under atmospheric pressure. This pseudo-phase diagram is based upon that proposed by *Shepelev and Petrova* [11].

Studies of cubic Ln_2TiO_5 stuffed pyrochlores have been shown to demonstrate pyrochlore-like nano-domains, as observed through detailed electron diffraction [14]–[16], [18]. It has been proposed that they are formed upon cooling from the fully disordered cation array found in defect-fluorite structures wherein the lanthanides nucleate onto the sublattice of corner-sharing tetrahedra into pyrochlore-like domains, approximately 200 – 500 nm in size. Any remaining lanthanides are forced onto the B-site and the average of these nano-domains gives rise to an average, long-range, defect-fluorite symmetry [16], [18]. The size of the nano-domain is dependent on the atomic radii of the Ln atom, with larger lanthanides having large nano-domains [14], [16]. Further study on cubic Ln_2TiO_5 through the application of neutron diffraction (ND) have also indicated a possible orthorhombic ordering, demonstrated through neutron pair distribution functions (PDF) analysis of Yb_2TiO_5 found that the orthorhombic symmetry had a better fit (Rwp = 0.111) than the cubic pyrochlore symmetry (Rwp = 0.306) [19].

Another highly accurate method for obtaining information about the local atomic environment of a structure is the application of X-ray Absorption Spectroscopy (XAS). XAS analysis of Yb_2TiO_5 and Y_2TiO_5 samples synthesised under different cooling regimes found that, through both the fitting of pre-edge features and Linear Combination Fitting (LCF) of Ti K-edge data, the titanium coordination environment had a close relationship to hexagonal Dy_2TiO_5. Modelling of the extended X-ray absorption fine structure (EXAFS) for the Yb L_3-, Y K- and Ti K-edges of these samples showed that they

were best described by a pyrochlore-like structure, wherein Ti was in a 5-fold coordination environment and the path degeneracies were representative of the $Ln_2(Ln_{0.66}Ti_{1.33})O_{6.67}$ chemistry [20].

In this work, the first X-ray Absorption Spectroscopy (XAS) study of the entire Ln_2TiO_5 (Ln = La, Pr, Nd, Sm, Eu, Gd, Tb, Dy, Ho, Er, Tm, Yb, Lu) series is presented. Here, the crystal structures of the Ln_2TiO_5 samples range between orthorhombic, hexagonal, and cubic, with X-ray absorption near edge spectroscopy (XANES) and EXAFS analyses proving integral in developing a description of the local structural environment. Building up a detailed account and description of the local structural order is important to understanding the effects nuclear conditions can have on the short-range ordering of a compound. Significant change of the local structure can lead to unknown, and perhaps detrimental, changes in physical and chemical qualities important to a wasteforms performance. The results here produce a thorough fundamental understanding of the structure and local environments within stuffed pyrochlores and as such, will be pivotal in underpinning future work on the alteration of stuffed pyrochlores in environments relevant to nuclear waste disposal (i.e. under irradiation or aqueous dissolution).

2. Methods

2.1 Sample fabrication

Ln_2TiO_5 (Ln = La, Pr, Nd, Sm, Eu, Gd, Tb, Dy, Ho, Er, Tm, Yb, Lu) was synthesised through a solid-state route. Samples were stoichiometrically batched from dried reagents according to batch calculations. Lanthanide oxide precursors: Ln_2O_3 (Ln = La, Sm, Nd, Eu, Gd, Dy, Ho, Er, Tm, Yb; Sigma Aldrich > 99.9% purity), Pr_6O_{11} (Alfa Aesar, 99.5% purity), Tb_4O_7 (Alfa Aesar 99.9% purity), Lu_2O_3 (Alfa Aesar 99.9% purity), were dried at 700 °C and TiO_2 (Alfa Aesar 99.99% purity) at 200 °C, both for 24 hours. Batches were planetary milled at 500 RPM for 15 minutes, using isopropanol carrier fluid. The subsequent powder slurry was dried out at 90 °C and passed through a 63 µm (250 mesh) sieve. 0.5 g samples were uniaxially pressed under 4 tonnes of pressure in a 10 mm diameter stainless steel die. Samples were subsequently reacted between 1275 – 1500 °C for 48 hours (with ramp rates of 5 °C min^{-1}), as per the pseudo-phase diagram (Fig. 1). Further reaction was carried out at intervals of 500 °C from initial reaction temperature until single phase products were achieved. In order to successfully synthesise single phase hexagonal Dy_2TiO_5 (and remove any orthorhombic Dy_2TiO_5 impurities) a ramp of at 5 °C min^{-1} to 1600 °C, a 48 hour dwell, and a rapid quench to room temperature with water was used. This method was based on similar work that has previously been used to obtain single phase hexagonal Dy_2TiO_5 [3].

2.2 X-ray diffraction

Crystalline phase identification was undertaken *via* X-ray diffraction (XRD). A Bruker D2 Phaser instrument was used to acquire the XRD data, operating with Cu Kα radiation and a Lynxeye solid state detector. Data was collected over a range of $0 < 2\theta < 70°$, with a step size of 0.02°, counting for 1.8 s, step^{-1}. Phase composition and diffraction data were analysed using the PDF -4+ database. Le Bail analysis [21] was applied to determine the lattice parameters of each dataset using the DIFFRAC.SUITE TOPAS software [22].

2.3.1 Ln L_3-edge and Ti K-edge measurements

XAS measurements were conducted at beamline 6-BM at the National Synchrotron Light Source II (NSLS-II), Brookhaven National Laboratory (Upton, New York). The optical system at 6-BM configured with a parabolic collimating mirror, Si(111) and Si(311) monochromators, a toroidal focussing mirror, and an harmonic rejection mirror [23]. Transmission and fluorescent measurements were collected using samples of finely ground Ln_2TiO_5 dispersed in polyethylene glycol (PEG) to achieve a thickness of one absorption length. To assist in the interpretation, data was also collected for several sets of standards at the Ln L_3-edge and/or Ti K-edge, prepared for XAS measurements in the same manner as the samples. Standards measured were $Pr(OH)_3$, $Nd(OH)_3$, $Sm_2Ti_2O_7$, $Eu_2Ti_2O_7$, Gd_2O_3, Dy_2O_3, Tm_2O_3 and Lu_2O_3. $Eu_2Ti_2O_7$ and $Sm_2Ti_2O_7$, and were synthesised in-house following methods outlined by previous authors [24], [25]. $Nd(OH)_3$, $Pr(OH)_3$, standards were synthesised by exposing Nd_2O_3 and Pr_6O_{11} reagents exposed to air for 7 – 10 days until they had fully hydrated, with the phase assemblage monitored periodically *via* XRD.

Simultaneous transmission and fluorescence mode data were collected by mounting samples at a 45° angle to the incident X-ray beam and fluorescence detector. The beam size was collimated using slits to 6 mm x 1 mm. Ionisation chambers were utilised to measure the incident (I_0) and transmitted (I_t) X-ray energies, and a 4-element Si drift detector (SII Vortex ME4, Hitachi) was used to collect the fluorescence signal. Data were collected at room temperature at the Ti K-edge (4966 eV), Pr L_3-edge (5964 eV), Nd L_3-edge (6208 eV), Sm L_3-edge (6716 eV), Gd L_3-edge (7243 eV) Dy L_3-edge (7790 eV), Tm L_3-edge (8648 eV) and the Lu L_3-edge (9244 eV). An accumulation time of 1 s step^{-1} was used for all regions, multiple scans were collected as needed and averaged to reduce the signal to noise ratio. Calibration of the data was performed using a series of inline reference foils (Ti, Cr, Fe, Ni, Cu) that were acquired simultaneously with the samples. The first inflection point was set as the absolute energy value, as given by *Bearden and Burr* [26], for each foil. Analysis of the XANES and EXAFS region was undertaken using the Demeter software package with FEFF6, using standard background subtraction and normalisation procedures [27]–[30].

2.3.2 Pre-edge fitting methods

To derive information about the local coordination environment of Ti the pre-edge feature was fit in an energy range of 4965-5040 eV following a similar procedure previously described in literature [31],

[32]. Fits to Ti pre-edge data of Ln_2TiO_5 samples, along with values obtained in previous studies, allow for a direct comparison of different Ti coordination environments. This was achieved by fitting an arctangent function to model the photoelectric edge step and set gaussians were used to fit the pre-edge components. The intensity weighted average of the energy positions of the first four gaussians was used to determine the pre-edge position and normalised intensity.

2.3.3 EXAFS analysis

Quantitative analysis of the EXAFS region of Pr_2TiO_5, Nd_2TiO_5, Sm_2TiO_5, Dy_2TiO_5, Ho_2TiO_5, and Lu_2TiO_5 Ln L_3-edge and Ti K-edge XAS spectra was conducted, with these samples being selected on the basis that they were a representative spread of crystal structures and ionic radii of lanthanide cations across the Ln_2TiO_5 series. Scattering paths were generated using the FEFF algorithm [30] and analysis was undertaken using the Artemis software [27], [29]. The structural models used were taken from Crystallographic Information Files (CIF) [33] [3], [12], [34], [35]. Multiple structural models (Ln_2TiO_5 orthorhombic, hexagonal structures and the $Ln_2Ti_2O_7$ cubic pyrochlore structure) were applied to all samples at both Ti and Ln edges to determine the most appropriate modelled description. Where a CIF was not available for a specific sample (i.e., orthorhombic Lu_2TiO_5 or cubic $Sm_2Ti_2O_7$) the most appropriate CIF, that described the structure of interest and had an original Ln of closest size to the targeted Ln, was edited such that the targeted Ln was substituted in place of the original Ln. In the case of the $Ln_2Ti_2O_7$ CIFs, the stoichiometry was altered to be more representative of the Ln_2TiO_5 chemistry (alternately written as $Ln_2(Ln_{0.66}Ti_{1.33})O_{6.67}$).

As the structure was treated to be initially unknown, the amplitude reduction factor S_0^2 for each Ln and Ti needed to be fixed at a previously determined value. This was achieved through the fitting of a set of appropriate standards as the S_0^2 value for chemically and structurally similar compounds collected at the same beamline is generally accepted to be transferable. Interatomic distances (R) and Debye-Waller factors (σ^2) were refined for each individual contribution in addition to the global parameter ΔE_0, the shift in the absorption energy. Degeneracy (N) was fixed when attempting to fit both the orthorhombic and hexagonal structures as both these structures possess 5-fold coordinated Ti. When fitting the 6-fold coordinated Ti using an $Ln_2Ti_2O_7$ based model the degeneracy of Ti was allowed to refine. The determination of the most appropriate EXAFS model to describe a structure was based upon a metric that considered of both statistical parameters such as the R-factor value of a fit, and the comparison of the reduced χ^2 of individual datasets when alternate structure models are applied over the same data range. Other considerations for determining the best fits were the calculated uncertainty in refined experimental variables, the degree of correlation between those variables, and the bond valence sum (BVS). The BVS is a method relating the formal valence of an absorbing cation to the degeneracy and bond distances of the nearest neighbour anions [36], [37]. BVS were calculated using methods previously outlined by other authors [36], [37]. Interpretation of returned refinements was also used in determining the quality of a model; if a model returned sensible statistical results but gave refined values that made no physical sense (such as a negative σ^2 value or

an unreasonably large change in bond distance, Δ*R*) then model was rejected. The results presented here will reflect the models that most satisfied the metrics previously discussed.

3 Results and Discussion

3.1 Solid-state characterisation

All synthesised products were characterised by XRD to determine whether a single phase Ln_2TiO_5 stuffed pyrochlore had formed and what structure it had crystallised in. Figure 2 shows the XRD patterns (indexed with the appropriate space group) for all samples after a single-phase product had been achieved. Also reported are the XRD patterns for the standards ($Pr(OH)_3$, $Nd(OH)_3$, $Sm_2Ti_2O_7$, $Eu_2Ti_2O_7$, Gd_2O_3, Dy_2O_3,Tm_2O_3 and Lu_2O_3) (Figure A2 of the SI). La_2TiO_5 to Tb_2TiO_5 all crystalise in the orthorhombic structure *Pnma*, Dy_2TiO_5 crystalised in the hexagonal *P6₃/mmc* polymorph and Ho_2TiO_5 – Lu_2TiO_5 crystallise with an observed long-range defect-fluorite structure *Fm-3m*. Weak reflections observable in the XRD pattern of Ho_2TiO_5 are indexable in a pyrochlore unit cell, with such reflections having previously been observed in Ho_2TiO_5, and are attributed to small pyrochlore-like nano-domains [14], [15], [38]. The relative size of these nano-domains has been suggested to related to the prevalence of observable weak reflections in XRD patterns of other cubic Ln_2TiO_5 stuffed pyrochlores, with their size being influenced by the ionic radius of the lanthanide as well as the synthesis method [14]–[16].

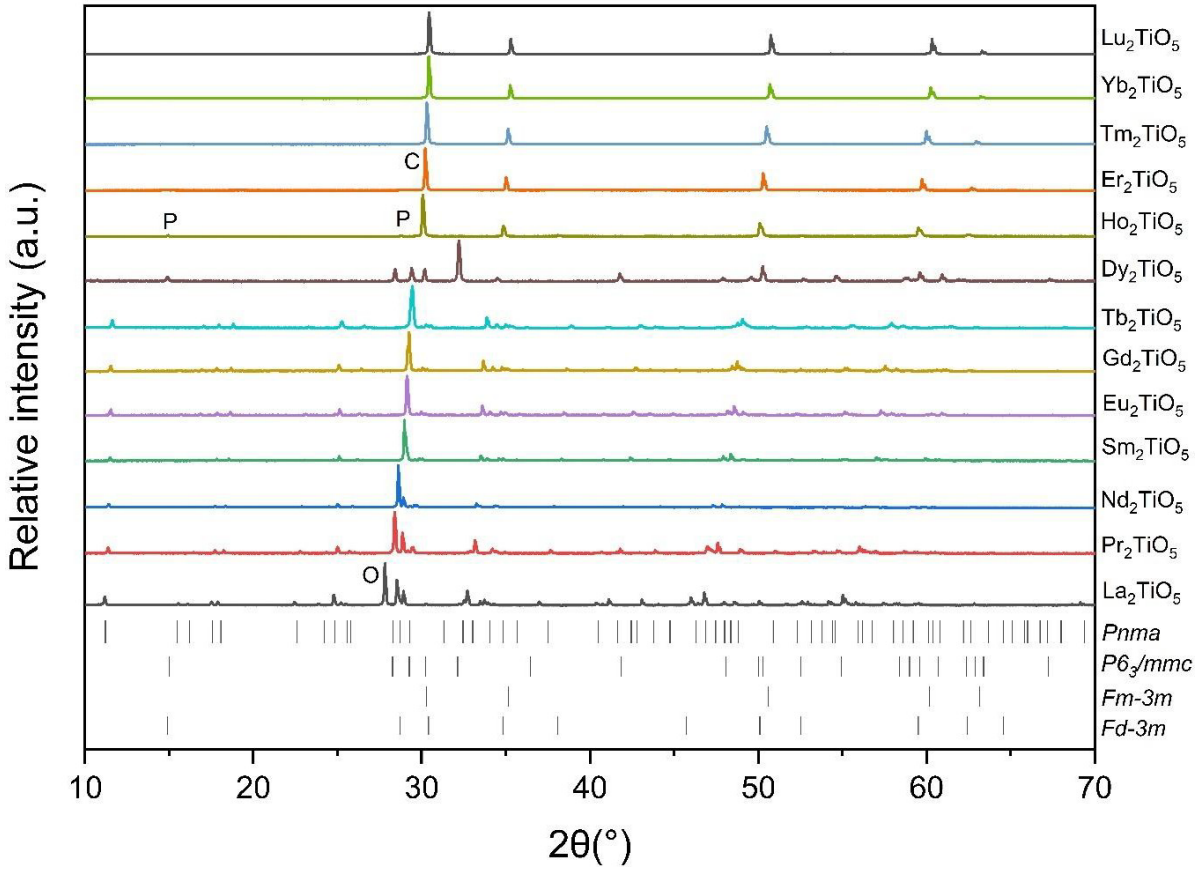

Figure 2: Powder X-ray diffraction data of Ln_2TiO_5 (Ln = La – Lu) stuffed pyrochlores. Vertical marks indicate Bragg positions of: Pr_2TiO_5, chosen as the representative *Pnma* orthorhombic structure (ICSD – 195208); $Sm_{1.40}Yb_{0.60}TiO_5$ representative of the *P6₃/mmc* hexagonal structure (ICSD – 191144); $(Yb_{2.67}Ti_{1.33})O_{6.67}$ (which can be recast as Yb_2TiO_5) to be representative of the defect-fluorite structure *Fm-3m* (ICSD – 191146); and Ho_2TiO_5 representative of cubic Ln_2TiO_5 compounds where supercell reflections are visible, indexed in as having *Fd-3m* symmetry (ICSD – 245792). Selected major reflections of the orthorhombic *Pnma* and defect-fluorite *Fm-3m* structures are labelled as O and C, respectively. Weak reflections indexable on a pyrochlore *Fd-3m* unit cell are labelled P.

Uniform shifts in the main peaks in the orthorhombic stuffed pyrochlores (Figure 2: point O) La_2TiO_5 – Tb_2TiO_5 and cubic (Figure 2, point C) Ho_2TiO_5 – Lu_2TiO_5 stuffed pyrochlores indicate a contraction of the crystal lattice. The change in the unit cell parameters, as determined through Le Bail refinement, can be found in Table A1 of the supporting information (SI) and are consistent with the lattice parameters determined in previous studies for these materials [3], [15], [16], [34], [38], [39]. Refinements of XRD patterns for cubic Ln_2TiO_5 stuffed pyrochlores utilised a defect-fluorite structure, consistent with the methodology used in previous studies [38]. As Ho_2TiO_5 exhibited weak reflections (Figure 2, point P) indexable on the pyrochlore supercell ($a_{py} = 2a_{df}$) it was also refined using a *Fd-3m* structure [38]. The relationship between a lanthanides ionic radius and change in unit cell volume can

be seen in Figure 3, the orthorhombic unit cell volume decreases by 11 % from La_2TiO_5 to Tb_2TiO_5 and the defect-fluorite unit cell volume decreased by 3.8 % from Ho_2TiO_5 to Lu_2TiO_5

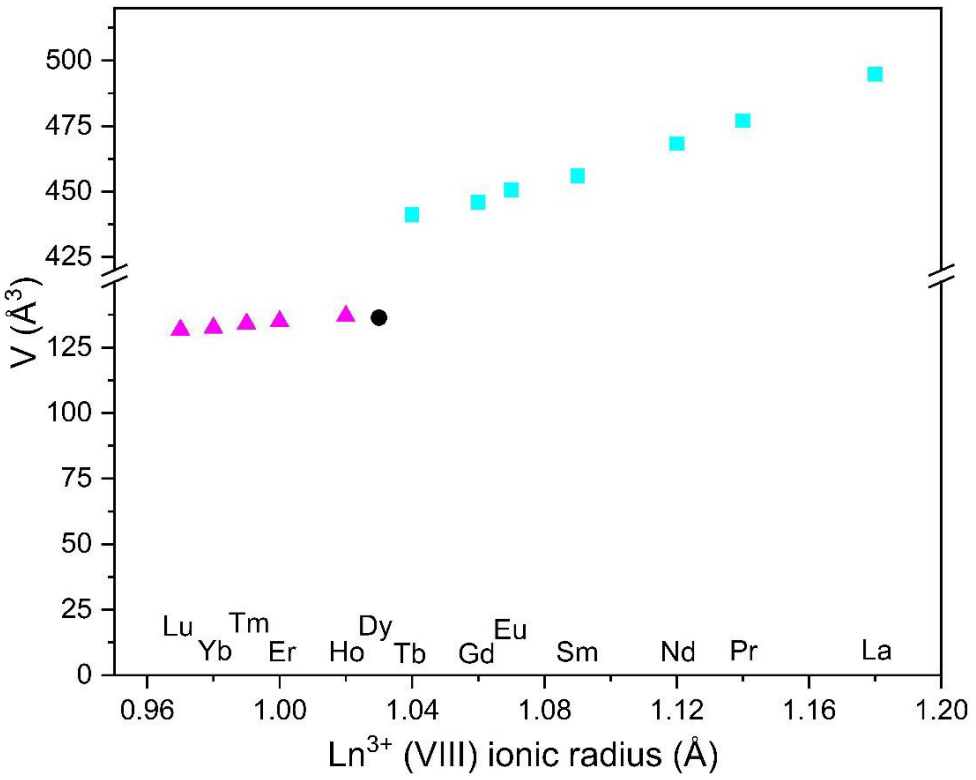

Figure 3: Showing the relationship between unit cell volume and ionic radius of the lanthanide in Ln_2TiO_5 stuffed pyrochlores over different structures. Ionic radii were taken from *Shannon and Prewitt* [40]. Blue squares are representative of orthorhombic Ln_2TiO_5 (La – Tb), from right to left; the black circle is representative of hexagonal Dy_2TiO_5; pink triangles are representative of cubic Ln_2TiO_5 (Ho – Lu) refined using a *Fm-3m* structure.

Representative SEM micrographs can be found in Figure A1 of the SI. Even with heat treatments at 1500 °C the resultant ceramic microstructure lacks appreciable density. Due to the refractory nature of these ceramics, multiple heat treatments, at high temperatures would be needed to aid in the densification process. Despite the porous nature of these materials, no areas of contrasting greyscale were detected, indicating a homogenous distribution of elements. The chemical composition of the materials was confirmed to be single phase through EDX measurements over multiple areas of the ceramic (Table A2 of the SI).

3.2 XAS: Pre-edge and XANES analysis

The normalised Ti K-edge and Ln L_3-edges XANES spectra for all Ln_2TiO_5 compounds shown in Figure 4. A qualitative trend can be seen in Figure 4a whereby all the Ln L_3-edge spectra exhibit similarities in profile, but the features A and B (~20 eV and ~75 eV above the edge, respectively) become significantly less intense as the structure transitions from orthorhombic to hexagonal and cubic. The intensity of feature A has been related to contributions from more distant coordination shells, and as such originating from the promotion of a photoelectron to the continuum states of *d* symmetry [41]. Changes in bond lengths and multiple scattering events from nearest neighbour anions have been reported to contribute significantly to the intensity and position of feature B in Ln^{3+} L_3-edge spectra collected on $LnTp_3$ (Ln = La, Pr, Nd, Sm, Eu; Tp is a ligand of chemical formula $HB(C_3N_2H_3)_3$) complexes [42]. It is therefore apparent that the local coordination and more distant coordination shells of hexagonal and cubic Ln_2TiO_5 stuffed pyrochlores share some structural commonality, particularly when compared to more distinct profile of these features observed in orthorhombic Ln_2TiO_5 compounds.

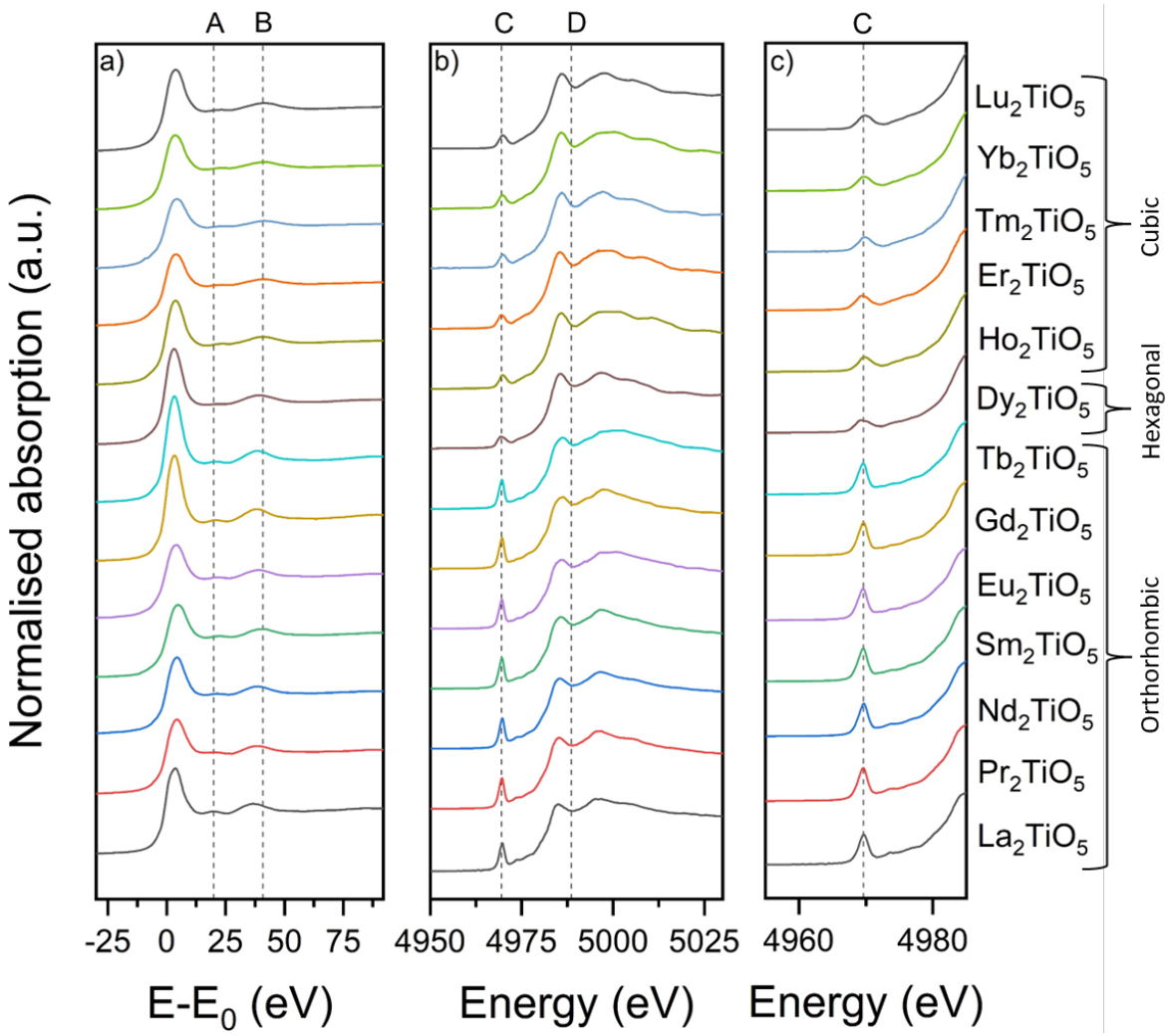

Figure 4: a) Normalised Ln L_3-edge XAS spectra of Ln_2TiO_5 (Ln = La – Lu), all spectra are shifted to their corresponding E_0 positions to aid comparisons; b) Normalised Ti K-edge XAS spectra of Ln_2TiO_5 (Ln = La – Lu). Labels A, B C and D, as well as the dotted lines, are included to identify key features and aid discussion; c) shows an enhanced view of the pre-edge feature's profile.

In Figure 4b, feature D of Ti K-edge spectra becomes more dampened in orthorhombic Ln_2TiO_5 (Ln = La – Tb) stuffed pyrochlores and becomes sharper as the crystal structure moves to a hexagonal or cubic symmetry. Likewise, the intensity of the characteristic pre-edge feature (labelled C in Figures 4b and c), ~20 eV below the white line, of the Ti K-edge spectra varies significantly as the crystal structure changes. The pre-edge feature offers insight into both the oxidation state and local coordination environment of Ti within the structure and arises due to the electronic transitions from 1s energy levels to hybridised Ti *3d*/O *2p* molecular orbital [32], [43]. The intensity of this feature is indicative of any changes in the centrosymmetric environment around the central Ti atom. Given the 1s -> 3d transition is formally forbidden, the further a structure deviates from centrosymmetry (and the greater degree of ligand p/Ti d hybridisation), the more intense the pre-edge feature and, when considered along with the position, can give detailed information about the local coordination environment [32], [43], [44].

Qualitative inspection of the spectra of the Ti K-edge pre-edge features of Ln_2TiO_5 (Ln = Pr – Lu) samples appears to indicate a 5-fold coordination as the position of the pre-edge features are consistent with that of 5-fold coordinated fresnoite ($Ba_2SiTi_2O_8$) (Figure 5). The long-range structures identified through XRD for Ln_2TiO_5 (Ln = La – Tb) and Dy_2TiO_5 were orthorhombic *Pnma* and hexagonal *$P6_3/mmc$*. As both of these structures are characterised by TiO_5 polyhedra, this suggests that there is some agreement between the observed local- and long-range Ti environments, as the pre-edge positions are consistent with that of other 5-fold Ti standards (Figure 5a). Through use of XRD, the Ln_2TiO_5 (Ln = Ho – Lu) were identified as having a defect fluorite *Fm-3m* structure which is characterised by the presence of an average $(Ln,Ti)O_7$ polyhedra, with O vacancies randomly distributed through the structure. Furthermore, the parent pyrochlore $Ln_2Ti_2O_7$ structure is found to have *Fd-3m* symmetry with Ti in 6-fold coordination, with pre-edge positions manifesting at at higher energy values (1 – 2 eV) for compounds with this Ti coordination. However, the position of the pre-edge features of Ln_2TiO_5 (Ln = Ho – Lu) suggests a 5-fold Ti coordination, which is consistent with observations of the pre-edge features of 5-fold Ti standards and Yb_2TiO_5 and Y_2TiO_5 synthesised through varied cooling regimes [20].

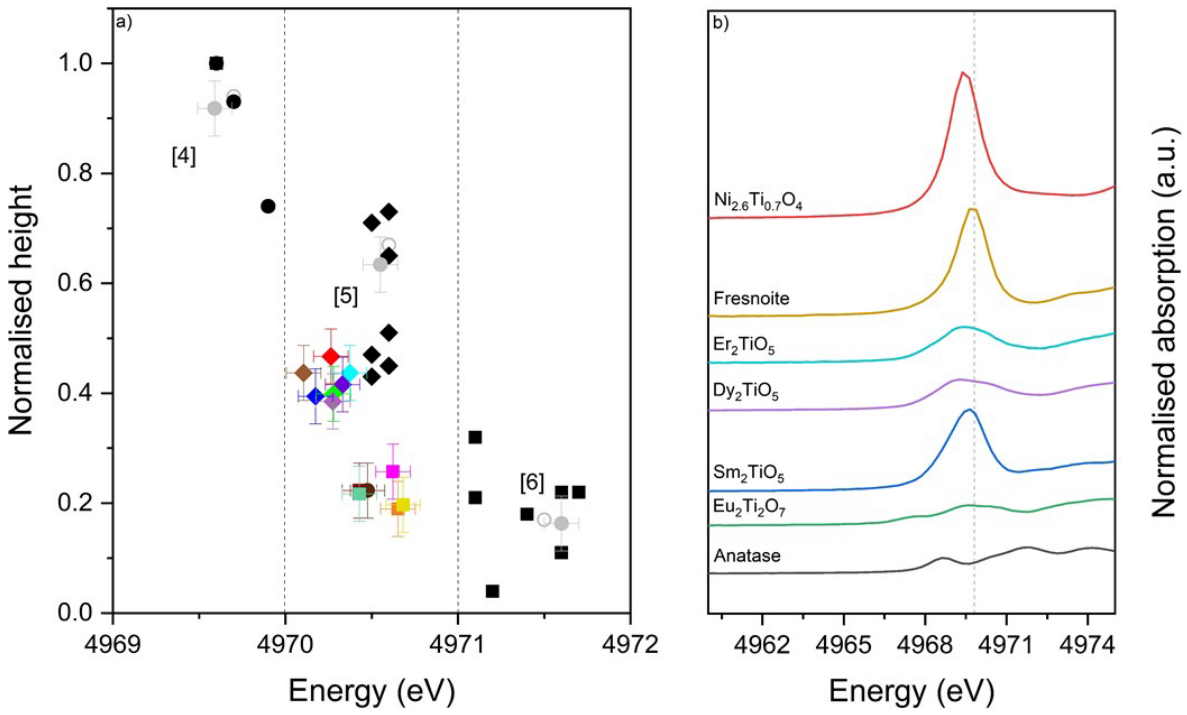

Figure 5: a) Normalised heighet and energy position of the pre-edge features of the Ti K-edge XANES. Black solid squares show data for 6-fold coordination standards from previous studies; solid diamonds show data for 5-fold coordination standards and solid black circles show 4-fold coordination standards from previous studies [32]. Data points in solid grey circles represent standards. Going from right to left are: anatase (4971.6 eV), fresnoite (4970.5 eV) and $Ni_{2.6}Ti_{0.7}O_4$ (4969.6 eV), data points outlined in grey are the corresponding standards collected from previous studies. Orthorhombic Ln_2TiO_5 (Ln = La – Tb) are denoted as diamonds; Hexagonal Dy_2TiO_5 is denoted by a circle; and cubic Ln_2TiO_5 are denoted as squares. Regions corresponding to 4, 5- and 6-fold Ti coordination are indicated by [4], [5] and [6], respectively; b) an enhanced view of pre-edge features of normalised Ti K-edge XAS spectra of a 4-fold Ti standard ($Ni_{2.6}Ti_{0.7}O_4$), 5-fold Ti standard (Fresnoite), 6-fold Ti standards ($Eu_2Ti_2O_7$ and anatase), and selected Ln_2TiO_5 (Ln = Sm, Dy, Er) spectra for comparison. A dotted line is included to aid qualitative interpretation.

The pre-edge features for all samples were further characterised by quantitative analysis of both the position and intensity. Figure 5a shows the correlation between pre-edge intensity and position of Ln_2TiO_5 samples along with reference compounds for four-, five- and six-fold coordinated Ti as well as published data from literature [32]. The tabulated results from this study as well as from those results from previous studies can be found in the supporting information (Table B1). Prior to the analysis of the sample pre-edges, the fitting procedure employed in this study was validated through comparison of the fitted values for both model compounds (Fresnoite and $Ni_{2.6}Ti_{0.7}O_4$) with those previously reported in literature for similar compounds [45]. A clear consistency of results was observed confirming the validity of the fitting method. As can be seen in Figure 5a, the data points for

orthorhombic-Ln_2TiO_5 samples are clustered in a region consistent with 5-fold coordinated fresnoite wherein Ti cations are found to be in a square pyramidal polyhedra [32]. These polyhedra lack a centre of symmetry resulting in the breaking of inversion symmetry rules and therefore giving rise to a more intense pre-edge feature due to strong *p-d* mixing. Hexagonal Dy_2TiO_5 and cubic-Ln_2TiO_5 are all centred around a point consistent with 5-fold coordination Ti in a trigonal bipyramidal geometry [44] and the pre-edge features are comparatively less intense compared to Ln_2TiO_5 (Ln = La – Tb) . The reduction of intensity of pre-edge features where Ti is nominally found in a trigonal bipyramidal structural motif relates to the lesser degree of *p-d* orbital mixing (i.e. a higher degree of centrosymmetry compared to a square pyramidal motif) [44]. Further similarities, in both shape and position, between the XAS spectra for cubic-Ln_2TiO_5 and hexagonal-Dy_2TiO_5 can be found in the features beyond the main crest of the white line (~5020 eV) which are responsive to the details of the medium range order (i.e. next-nearest neighbours) around the central absorber (Figure 4b).

The results from the pre-edge modelling and qualitative inspection of XANES spectra indicates a 5-fold coordination environment for all Ln_2TiO_5 compounds. Differences in the pre-edge intensity and XAS spectra above the white line of orthorhombic samples compared with hexagonal and cubic samples suggests that the local Ti geometries are more highly symmetrical in the latter and that there are similarities between hexagonal and cubic local structures. It has been shown previously that the short-range ordering of materials can have direct effects on a materials response to radiation damage [3], [15], [46], [47], as such characterisation of the local coordination will further assist the interpretation of future results regarding the response of Ln_2TiO_5 compounds to radiation.

3.3 EXAFS

Modelling of the EXAFS was used to provide detailed structural models of each central absorbing atom (Ln and Ti for each sample). Based on the observations from the XRD and XANES analysis of the Ln_2TiO_5 stuffed pyrochlores various EXAFS models were developed. Due to the complex local ordering exhibited by cubic-Ln_2TiO_5 stuffed pyrochlores documented in literature [14]–[16], models based upon the 3 structure types (orthorhombic *Pnma*, hexagonal *P6$_3$/mmc* and cubic *Fd-3m*) of Ln_2TiO_5 stuffed pyrochlores were used for EXAFS analysis of data collected at the Ln L_3-edge and Ti K-edge for all Ln_2TiO_5 samples. This methodology was employed to examine whether any strong deviations from the observed long-range order can be detected through EXAFS analysis. The models that returned the best structural fit, based upon statistical metrics (such as R-factor) and interpretation of refined physical parameters (such as the calculated BVS) are presented here. An extended discussion as to how these models were constructed is presented in section C of the SI.

As both degeneracy (N) and amplitude reduction factor (S_0^2) are entirely correlated, models of known and well-characterised standards that are chemically and structurally similar to the Ln_2TiO_5 samples

were fit to determine S_0^2 parameters (see Figures D1 and D2 and Tables D1 and D2 in section D of the SI for the results of these models). As these values are generally considered chemically transferable, the parameters can be fixed at this value in the Ln_2TiO_5 models to allow refinement of the Ti coordination number (CN).Titanium K-edge EXAFS.

EXAFS models of the Ti K-edge were based on refined structures established by previous authors [14], [35], [39], [48]. Further details on how these models were constructed can be found in section C of the SI. The fits for all datasets are shown in Figure 6 and the refined model parameters can be found in Table 1. The Ti K-edge models produced for Pr_2TiO_5 – Gd_2TiO_5 were fit using an orthorhombic *Pnma* structure, Dy_2TiO_5 was fit using a hexagonal *P6₃/mmc* structure and Ho_2TiO_5 and Lu_2TiO_5 were fit using a modified $Ln_2Ti_2O_7$ pyrochlore *Fd-3m* structure produced the fits with the lowest statistical values (R-factor ≤2.5 %) and returned sensible physical parameters (i.e. positive Debye-Waller factors and calculated BVS). The local coordination environments of Ti in Pr_2TiO_5, Nd_2TiO_5, Sm_2TiO_5 and Gd_2TiO_5 were all well described by a square pyramidal (CN = 5) motif, where the average refined Ti-O bond length (1.90 – 1.92 Å) was consistent with the weighted mean Ti-O bond distances from the crystal structures published by other authors (also found to be within the range of 1.90 – 1.92 Å) [3], [12], [35], [48]. Further validation of the bond lengths can be seen in the calculated BVS which are 3.81 ± 0.1 v.u., 3.79 ± 0.1 v.u., 3.75 ± 0.1 v.u. and 3.81 ± 0.1 v.u. for Pr_2TiO_5, Nd_2TiO_5, Sm_2TiO_5 and Gd_2TiO_5, respectively. These values are within 7 % of the formal valence of Ti (4 v.u.), suggesting good agreement in the ascribed square pyramidal coordination environment and experimentally determined values.

Furthermore, a linear decrease in bond distance of more distant cations was observed (from 3.91 to 3.77 Å for the Ti-Ti bond distance of Pr_2TiO_5 to Gd_2TiO_5, for example), consistent with the lanthanide contraction as the series progresses. Within error, this is in agreement with the refined bond distance determined from XRD data (3.87 – 3.76 Å) [12], suggesting an agreement between the short- and long-range ordering of orthorhombic Ln_2TiO_5. The Ti local coordination of Dy_2TiO_5 appears to be well described by a trigonal bipyramidal (CN = 5) motif given an R-factor of 2.5% and BVS of 3.83 ± 0.1 v.u., differing by less than 5% of the formal Ti valence. The refined Ti coordination number of both Ho_2TiO_5 and Lu_2TiO_5 were 5.25 ± 0.4 and 5.20 ± 0.4, respectively, indicating (within error) that Ti has a CN of 5. Further confirmation of a 5-fold coordinated Ti environment is given by the BVS, which is dependent on both CN and bond distance of oxygen coordinators, of 4.14 ± 0.1 v.u and 4.13 ± 0.1 v.u, respectively, for Ho_2TiO_5 and Lu_2TiO_5 both within 5% of the formal Ti valence. It is noteworthy that a 6-fold coordinated Ti environment, as the case in $Ho_2Ti_2O_7$ and $Lu_2Ti_2O_7$, would typically necessitate Ti-O bond distances on the order of 1.954 Å and 1.943 Å to achieve BVS of similar values [34], [35]. A 5-fold Ti-O coordination, as indicated by EXAFS refinements, is consistent with observations from both a qualitative inspection and comparison of pre-edge features of 5-fold coordinated Ti in other compounds in addition to previously observed coordination number refinements of cubic Yb_2TiO_5 and Y_2TiO_5. Given that the refined CN in both studies were 5 ± 9% observed for both Ln_2TiO_5 stuffed pyrochlores where the lanthanide ionic radius is larger (Ln = Ho, Y) and smaller (Ln = Lu, Yb), it would

be sensible to assume this trend would be consistent across all cubic Ln_2TiO_5 (Dy – Lu, Y) stuffed pyrochlores. These conclusions are further reinforced by the consistent trend in Ti pre-edge features previously discussed.

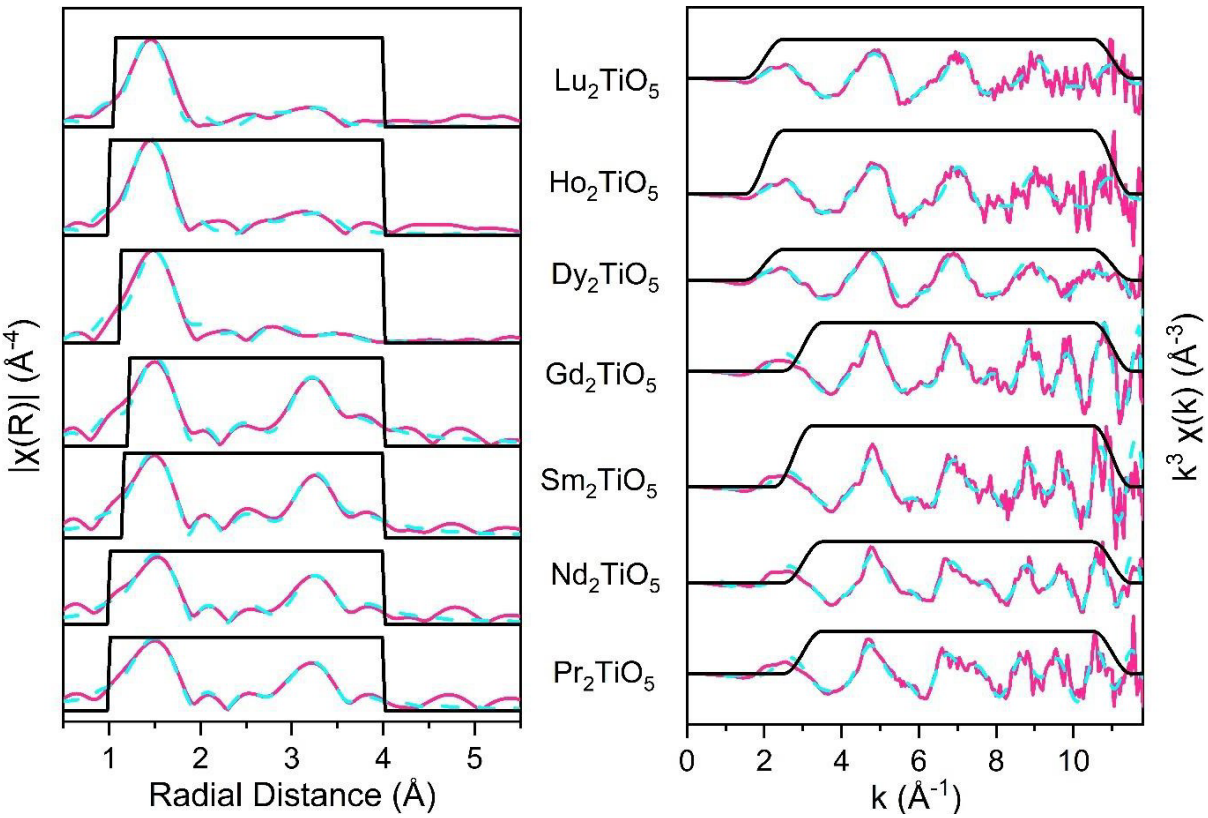

Figure 6: Fourier transform of Ti K-edge waveform of Ln_2TiO_5 (Ln = Pr, Nd, Sm, Gd, Dy, Ho, Lu) in R-space along with the residual difference between experimental data and theoretical fits; b) k^3 weighted waveform. Data from Pr_2TiO_5 – Gd_2TiO_5 are fit using an orthorhombic *Pnma* structure, Dy_2TiO_5 was fit using a hexagonal *P6₃/mmc* structure and Ho_2TiO_5 and Lu_2TiO_5 were fit using a modified $Ln_2Ti_2O_7$ pyrochlore *Fd-3m* structure. Solid pink lines represent the experimental data, blue dashed lines represent the theoretical fit and solid black line represents the fitting window.

Table 1: Refined structural parameters for Ln_2TiO_5 (Ln = Pr, Nd, Sm, Gd, Dy, Ho, Lu) samples measured at the Ti K-edge modelled using orthorhombic *Pnma*, hexagonal *P6₃/mmc* and cubic *Fd-3m* structures (Figure 6). The average change in scattering path distance for a given absorber-scatterer pair is denoted as R, the Debye–Waller factor is denoted as σ^2, the degeneracy of the path denoted as N and Ln represents the corresponding metal cation. The fitting range in R space was 1– 4 Å for all samples, 3 – 11 $Å^{-1}$ in k space for Pr_2TiO_5 to Gd_2TiO_5, and 2 – 11 $Å^{-1}$ in k space for the Dy_2TiO_5 to Lu_2TiO_5. A dash denotes that there was no corresponding path included in a specific model.

Path		**Pr_2TiO_5**	**Nd_2TiO_5**	**Sm_2TiO_5**	**Gd_2TiO_5**	**Dy_2TiO_5**	**Ho_2TiO_5**	**Lu_2TiO_5**
Space group		*Pnma*	*Pnma*	*Pnma*	*Pnma*	*P6₃/mmc*	*Fd-3m*	*Fd-3m*
	E_0 (eV)	1.6(8)	3.5(12)	2.4(18)	1.6(14)	-3.9(11)	-2.4(8)	-1.9(8)
	S_0^2	0.59	0.59	0.59	0.59	0.59	0.59	0.59
	R (Å)	1.91(2)	1.92(1)	1.90(3)	1.91(3)	1.91(1)	1.90(1)	1.91(1)
Ti-O(1)	*σ^2 (Å²)*	0.005(1)	0.006(1)	0.006(2)	0.006(2)	0.003(1)	0.003(1)	0.004(1)
	N	5	5	5	5	5	5.25(5)	5.2(4)
	R (Å)	3.53(1)	3.51(3)	3.48(2)	3.44(3)	3.60(6)	3.39(2)	3.36(8)
Ti-Ln(1)	*σ^2 (Å²)*	0.003(1)	0.003(2)	0.003(2)	0.003(2)	0.008(6)	0.011(3)	0.012(7)
	N	4	4	4	4	2	8	8
	R (Å)	3.75(2)	3.74(6)	3.70(4)	3.66(4)	3.50(5)	-	-
Ti-Ln(2)	*σ^2 (Å²)*	0.003(1)	0.005(2)	0.003(2)	0.003(2)	0.006(1)	-	-
	N	3	3	3	3	6	-	-
	R (Å)	3.91(5)	3.87(3)	3.81(7)	3.77(8)	3.32(8)	3.51(11)	3.38(3)
Ti-Ti(1)	*σ^2 (Å²)*	0.003(1)	0.005(2)	0.003(2)	0.003(2)	0.004(2)	0.016(7)	0.014(3)
	N	2	2	2	2	4	4	4
R-factor		0.023	0.018	0.030	0.025	0.025	0.0243	0.025
BVS (v.u.)		3.81	3.78	3.75	3.81	3.83	4.14	4.13

3.3.1 Lanthanide L_3-edge EXAFS

The models shown here of the Ln L_3-edge EXAFS were based on the same structures used to fit the Ti K-edge EXAFS. Quantitative analysis of the local structural environment around Ln atoms showed that models based upon the same structure that was assigned to the long-range ordering observed in XRD data provided good fits (R-factor < 3 %). Specifically, the local structure of Ln_2TiO_5 (Ln = Pr, Nd, Sm, Gd) stuffed pyrochlores were well described by an orthorhombic *Pnma* structure, Dy_2TiO_5 was well described by a hexagonal *P6₃/mmc* structure, and Ln_2TiO_5 (Ln = Ho, Lu) were well described by a modified $Ln_2Ti_2O_7$ *Fd-3m* structure. The tabulated results of the refined physical parameters can be found in Table 2 and fits are shown in Figure 7. All data sets were fit up to 4.5 Å in R-space and over a range of 10 – 11 $Å^{-1}$ in k-space. The local Ln coordination of Ln_2TiO_5 (Ln = Pr, Nd, Sm, Gd) was well

described by a 7-fold polyhedron and is supported by the calculated BVS for all datasets which came within 5 % of the formal Ln (3 v.u.). Coordination environments with either a LnO_6 or LnO_8 polyhedron would require the Ln-O bond distances to be significantly different than those obtained in the models shown here. For example, when Pr_2TiO_5 was fit using a structural model that necessitates a higher Ln coordination number (e.g., CN = 8, as is the case in the hexagonal *$P6_3/mmc$* structure), a refined Ln-O bond distance of 2.43 Å and a BVS of 3.60 ± 0.1 v.u. was obtained. In the orthorhombic *Pnma* model of Pr_2TiO_5, with a CN = 7, the refined Ln-O bond distance was determined to be 2.42 Å with a calculated BVS of 3.15 v.u. ± 0.1. For Ln_2TiO_5 (Ln = Pr, Nd, Sm, Gd) to support an 8-fold local coordination, Ln-O bond distance on the order of 2.50 Å would be necessitated to return a BVS of 3 v.u., indicating that the local coordination can only be satisfactorily fit using a 7-fold coordinated polyhedron based upon the refined bond distances.

The local coordination of Dy_2TiO_5 and Ln_2TiO_5 (Ln = Ho, Lu) were both well represented by being surrounded by 8 O anions, where the calculated BVS of all datasets came within 5 % of the formal valence of Ln (3 v.u.). In the hexagonal Dy_2TiO_5, this constituted two Ln-O paths, where Ln(1)-O had a degeneracy of 6 (2.32 Å) and Ln(2)-O had a degeneracy of 2 (2.56 Å). In the cubic pyrochlore models of Ln_2TiO_5 (Ln = Ho, Lu) this relationship was inverted, where Ln(1)-O (2.22 – 2.25 Å) had a degeneracy of 2 and Ln(2)-O (2.32 – 2.39 Å) had a degeneracy of 6. Models attempting to fit the entire O coordination shell as one distinct Ln-O (N = 8) path failed to return a good fit, with higher R-factors (most notably a fit mismatch to the first coordination peak in the Fourier transform k^3 χ(k) spectral envelope) and negative σ^2 values. This implies that the nearest neighbour O shell is significantly distorted, requiring multiple paths to represent a broader spread of O bond lengths to satisfactorily fit the spectral features of the first coordination shell.

A general trend of a decrease in bond distances of more distant Ln-Ti and Ln-Ln next nearest neighbours across individual structure is also observed. For example, the Ln-Ln(1) path of Pr_2TiO_5 – Gd_2TiO_5 fit using an orthorhombic structure decreases from 3.87 – 3.81 Å and Ln-Ln(1) path of Ho_2TiO_5 and Lu_2TiO_5 fit with a cubic structure decreases from 3.64 – 3.50 Å. Such a trend is the expected behaviour as a decrease as lanthanide ionic radii (from Pr = 1.13 Å to Gd = 1.05 Å and Ho = 1.02 to Lu = 0.99 Å) will result in a shortening of path distances. This finding is also consistent with the observed behaviour of Ln-O/Ti/Ln bond distances in structural refinements of XRD data by other authors [12].

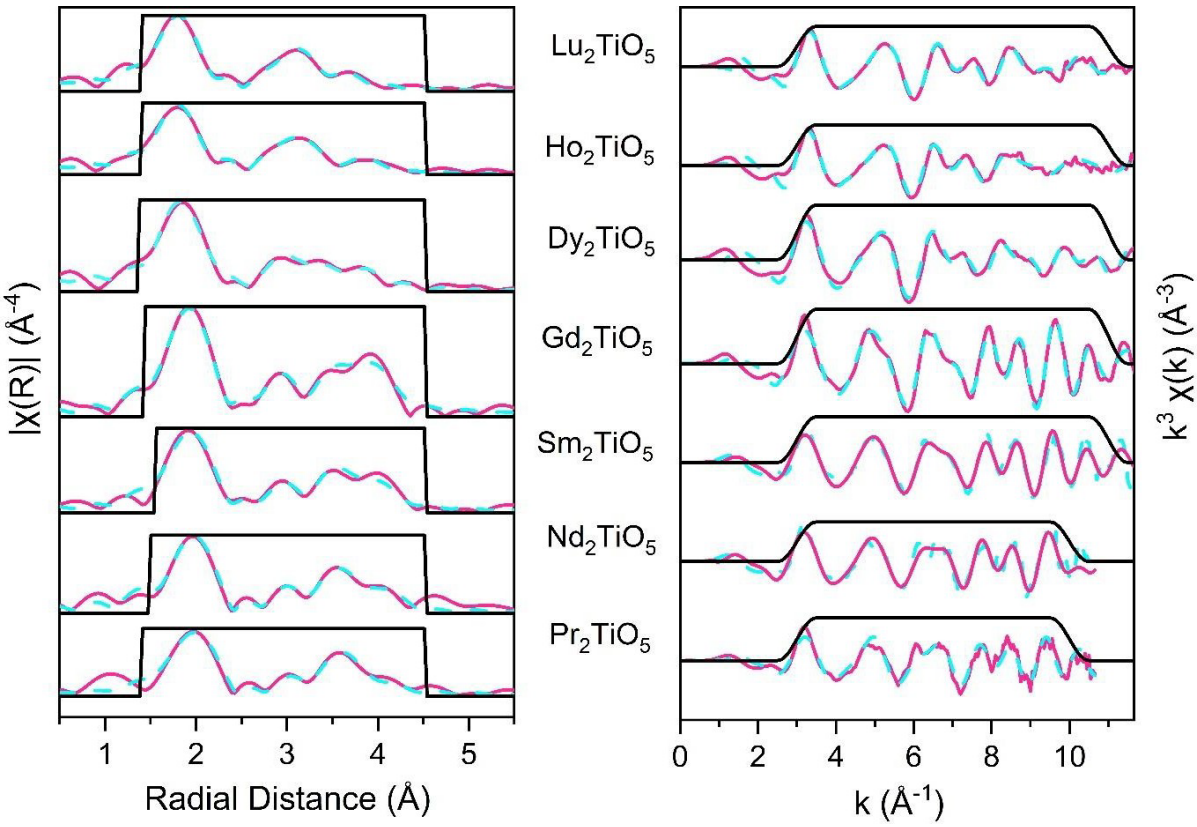

Figure 7: Fourier transform of Ln L_3-edge waveform of Ln_2TiO_5 (Ln = Pr, Nd, Sm, Gd, Dy, Ho, Lu) in R-space along with the residual difference between experimental data and theoretical fits; b) k^3 weighted waveform. Data from Pr_2TiO_5 – Gd_2TiO_5 are fit using an orthorhombic *Pnma* structure, Dy_2TiO_5 was fit using a hexagonal *P6₃/mmc* structure and Ho_2TiO_5 and Lu_2TiO_5 were fit using a modified $Ln_2Ti_2O_7$ pyrochlore *Fd-3m* structure. Solid pink lines represent the experimental data, blue dashed lines represent the theoretical fit and solid black line represents the fitting window.

Table 2: Refined structural parameters for Ln_2TiO_5 (Ln = Pr, Nd, Sm, Gd, Dy, Ho, Lu) samples measured at the Ln L_3-edge modelled using orthorhombic *Pnma*, hexagonal *$P6_3/mmc$* and cubic *Fd-3m* structures (Figure 7). The average change in scattering path distance for a given absorber-scatterer pair is denoted as R, the Debye–Waller factor is denoted as σ^2, the degeneracy of the path denoted as N and Ln represents the corresponding metal cation. The fitting range in R-space for all samples was 1– 4.5 Å, and 3 – 10 $Å^{-1}$ in k-space for Pr_2TiO_5 and Nd_2TiO_5, and 3 – 11 $Å^{-1}$ in k space for the remainder. A dash denotes that there was no corresponding path included in a specific model.

Path		**Pr_2TiO_5**	**Nd_2TiO_5**	**Sm_2TiO_5**	**Gd_2TiO_5**	**Dy_2TiO_5**	**Ho_2TiO_5**	**Lu_2TiO_5**
Space group		*Pnma*	*Pnma*	*Pnma*	*Pnma*	*$P6_3/mmc$*	*Fd-3m*	*Fd-3m*
	E_0 (eV)	1.6(8)	3.5(12)	2.4(18)	1.6(14)	-3.9(11)	-2.4(8)	-1.9(8)
	S_0^2	0.59	0.59	0.59	0.59	0.59	0.59	0.59
	R (Å)	1.91(2)	1.92(1)	1.90(3)	1.91(3)	1.91(1)	1.90(1)	1.91(1)
Ti-O(1)	*σ^2 (Å²)*	0.005(1)	0.006(1)	0.006(2)	0.006(2)	0.003(1)	0.003(1)	0.004(1)
	N	5	5	5	5	5	5.25(5)	5.2(4)
	R (Å)	3.53(1)	3.51(3)	3.48(2)	3.44(3)	3.60(6)	3.39(2)	3.36(8)
Ti-Ln(1)	*σ^2 (Å²)*	0.003(1)	0.003(2)	0.003(2)	0.003(2)	0.008(6)	0.011(3)	0.012(7)
	N	4	4	4	4	2	8	8
	R (Å)	3.75(2)	3.74(6)	3.70(4)	3.66(4)	3.50(5)	-	-
Ti-Ln(2)	*σ^2 (Å²)*	0.003(1)	0.005(2)	0.003(2)	0.003(2)	0.006(1)	-	-
	N	3	3	3	3	6	-	-
	R (Å)	3.91(5)	3.87(3)	3.81(7)	3.77(8)	3.32(8)	3.51(11)	3.38(3)
Ti-Ti(1)	*σ^2 (Å²)*	0.003(1)	0.005(2)	0.003(2)	0.003(2)	0.004(2)	0.016(7)	0.014(3)
	N	2	2	2	2	4	4	4
R-factor		0.023	0.018	0.030	0.025	0.025	0.0243	0.025
BVS (v.u.)		3.81	3.78	3.75	3.81	3.83	4.14	4.13

4. Conclusions

The use of Ln_2TiO_5 ceramics as wasteforms for actinide wastes, as well as broader applications within the nuclear industry, requires a detailed and comprehensive understanding of the complex local structure in order to more fully interpret their responses to radiation damage and other adverse conditions. This work presents the first XAS study, collected at the Ti K- and Ln L_3-edges, of the short-range ordering of the entire Ln_2TiO_5 (Ln = La – Lu) series, across a range of the most common crystal structures observed in the Ln_2TiO_5 system. As has been noted, the local structure of these compounds is complex, however through structural characterisation of the short-range ordering exhibited by these compounds, a quantitative description of the local structure and confirmation of the assigned crystal structures is provided. It has been shown, through both qualitative interpretation of the XANES region and quantitative analysis of pre-edge features of the Ti K-edge spectra, that Ln_2TiO_5 (Ln = La – Tb) stuffed pyrochlores contain 5-fold coordinated Ti in a square pyramidal motif, consistent with observations of the long-range order exhibited by these stuffed pyrochlores. Pre-edge features of Ti K-edge spectra of Dy_2TiO_5 and Ln_2TiO_5 (Ln = Ho – Lu) were comparatively less intense, consistent with a coordination geometry with a higher degree of centrosymmetry, such as TiO_5 trigonal bipyramid motif. The EXAFS region (for both Ln and Ti central atoms) of the spectra for Pr_2TiO_5, Nd_2TiO_5, Sm_2TiO_5, Gd_2TiO_5, Ho_2TiO_5 and Lu_2TiO_5 were modelled to fit a description of the local structural environment. The best modelled fits of the Ti EXAFS showed all structures were well described using models based upon the assigned long-range structure and that the local coordination of Ti in all stuffed pyrochlores studied here have a coordination number of 5. The local coordination of Ln and Ti cations was shown to be highly dependent upon the ionic radii of Ln cations, which also influences the crystal symmetry observed in the long-range ordering. In orthorhombic compounds, the EXAFS suggested that the Ln central atom was coordinated by 7 O anions, whilst in both hexagonal and cubic models the Ln central atom was shown to be 8-fold coordinated. However, it should be noted that multiple paths were required to satisfactorily fit the spectral features related to O coordination in the 8-fold coordinated systems, indicating greater levels of distortion to the local coordination than what is seen in the 7-fold coordinated species. Overall, the results presented here provide key fundamental information on the structure of stuffed pyrochlores at both the Ti and Ln sites. This information will be pivotal in developing robust models that will underpin the application of XAS analysis in probing the local coordination Ln_2TiO_5 stuffed pyrochlores that have been degraded by radiation damage and/or aqueous dissolution in the future, therefore informing radioactive waste disposal techniques.

Acknowledgments

DAA is grateful to the Engineering and Physical Sciences Research Council (EPSRC) for funding. This research utilised the HADES/MIDAS facility at The University of Sheffield established with financial support from EPSRC and BEIS, under grant EP/T011424/1 and was supported by grant

EP/S01019X/1.This research used 6-BM of the National Synchrotron Light Source II, a U.S. Department of Energy (DOE) Office of Science User Facility operated for the DOE Office of Science by Brookhaven National Laboratory under Contract No. DE-SC0012704.

References

[1] X. Liu *et al.*, "Insights into the radiation behavior of Ln2TiO5(Ln = La-Y) from defect energetics," *Comput. Mater. Sci.*, vol. 139, pp. 295–300, 2017.

[2] H. Niu, H. Gou, R. C. Ewing, and J. Lian, "First principles investigation of structural, electronic, elastic and thermal properties of rare-earth-doped titanate Ln2TiO5," *AIP Adv.*, vol. 2, no. 3, p. 032114, Sep. 2012.

[3] R. D. Aughterson, N. J. Zaluzec, and G. R. Lumpkin, "Synthesis and ion-irradiation tolerance of the Dy2TiO5 polymorphs," *Acta Mater.*, vol. 204, p. 116518, Feb. 2021.

[4] W. Anderson, *Neutron absorber materials for reactor control.* Washington: Naval Reactors Division of Reactor Development U.S. Atomic Energy Commission, 1962.

[5] Y. Jiang, J. R. Smith, and G. Robert Odette, "Prediction of structural, electronic and elastic properties of Y2Ti2O7 and Y2TiO5," *Acta Mater.*, vol. 58, no. 5, pp. 1536–1543, Mar. 2010.

[6] M. Dholakia, S. Chandra, and S. M. Jaya, "Properties of Y2TiO5 and Y2Ti2O7 crystals: Development of novel interatomic potentials," *J. Alloys Compd.*, vol. 739, pp. 1037–1047, Mar. 2018.

[7] X. Liu *et al.*, "Insights into the radiation behavior of Ln 2 TiO 5 (Ln = La-Y) from defect energetics," *Comput. Mater. Sci.*, vol. 139, pp. 295–300, Nov. 2017.

[8] J. Zhang, F. Zhang, M. Lang, F. Lu, J. Lian, and R. C. Ewing, "Ion-irradiation-induced structural transitions in orthorhombic Ln2TiO5," *Acta Mater.*, vol. 61, no. 11, pp. 4191–4199, Jun. 2013.

[9] R. D. Aughterson *et al.*, "The influence of crystal structure on ion-irradiation tolerance in the Sm(x)Yb(2-x)TiO5 series," *J. Nucl. Mater.*, vol. 471, pp. 17–24, Apr. 2016.

[10] S. Park *et al.*, "Swift-heavy ion irradiation response and annealing behavior of A2TiO5(A = Nd, Gd, and Yb)," *J. Solid State Chem.*, vol. 258, pp. 108–116, 2018.

[11] Y. F. Shepelev and M. A. Petrova, "Crystal structures of Ln 2TiO 5 (Ln = Gd, Dy) polymorphs," *Inorg. Mater.*, vol. 44, no. 12, pp. 1354–1361, Dec. 2008.

[12] R. D. Aughterson, G. R. Lumpkin, G. J. Thorogood, Z. Zhang, B. Gault, and J. M. Cairney, "Crystal chemistry of the orthorhombic Ln 2 TiO 5 compounds with Ln =La, Pr, Nd, Sm, Gd, Tb and Dy," *J. Solid State Chem.*, vol. 227, pp. 60–67, Jul. 2015.

[13] W. G. Mumme and A. D. Wadsley, "The structure of orthorhombic Y2TiO5, an example of mixed seven- and fivefold coordination," *Acta Crystallogr. Sect. B Struct. Crystallogr. Cryst. Chem.*, vol. 24, no. 10, pp. 1327–1333, Oct. 1968.

[14] R. D. Aughterson *et al.*, “Crystal structures of orthorhombic, hexagonal, and cubic compounds of the Sm(x)Yb(2−x)TiO5 series,” *J. Solid State Chem.*, vol. 213, pp. 182–192, May 2014.

[15] K. R. Whittle, M. G. Blackford, R. D. Aughterson, G. R. Lumpkin, and N. J. Zaluzec, “Ion irradiation of novel yttrium/ytterbium-based pyrochlores: The effect of disorder,” *Acta Mater.*, vol. 59, no. 20, pp. 7530–7537, Dec. 2011.

[16] G. C. Lau, T. M. McQueen, Q. Huang, H. W. Zandbergen, and R. J. Cava, “Long- and short-range order in stuffed titanate pyrochlores,” *J. Solid State Chem.*, vol. 181, no. 1, pp. 45–50, Jan. 2008.

[17] R. D. Aughterson, G. R. Lumpkin, K. L. Smith, Z. Zhang, N. Sharma, and J. M. Cairney, “The crystal structures and corresponding ion-irradiation response for the Tb(x)Yb(2−x)TiO5 series,” *Ceram. Int.*, vol. 44, no. 1, pp. 511–519, Jan. 2018.

[18] G. C. Lau *et al.*, “Structural disorder and properties of the stuffed pyrochlore Ho 2 TiO 5,” *Phys. Rev. B*, vol. 76, no. 5, p. 054430, 2007.

[19] J. Shamblin *et al.*, “Structural and magnetic short-range order in fluorite Yb 2 TiO 5,” *Phys. Rev. B*, vol. 96, p. 174418, 2017.

[20] D. A. Austin, L. T. Townsend, M. C. Stennett, B. Ravel, and R. J. Hand, “Probing the local coordination of Ln2TiO5 (Ln = Yb, Y) through multi-element X-ray absorption techniques [Unpublished manuscript],” *Dep. Mater. Sci. Eng. Univ. Sheff.*, 2022.

[21] A. Le Bail, H. Duroy, and J. L. Fourquet, “Ab-initio structure determination of LiSbWO6 by X-ray powder diffraction,” *Mater. Res. Bull.*, vol. 23, no. 3, pp. 447–452, Mar. 1988.

[22] A. A. Coelho, “TOPAS and TOPAS-Academic: An optimization program integrating computer algebra and crystallographic objects written in C++: An,” *J. Appl. Crystallogr.*, vol. 51, no. 1, pp. 210–218, Feb. 2018.

[23] C. Weiland *et al.*, “NIST HAXPES at NSLS and NSLS-II,” *Synchrotron Radiat. News*, vol. 31, no. 4, pp. 23–28, Jul. 2018.

[24] M. Jafar, P. Sengupta, S. N. Achary, and A. K. Tyagi, “Phase evolution and microstructural studies in CaZrTi2O7 (zirconolite)–Sm2Ti2O7 (pyrochlore) system,” *J. Eur. Ceram. Soc.*, vol. 34, no. 16, pp. 4373–4381, Dec. 2014.

[25] A. Bayart, A. Katelnikovas, J. F. Blach, J. Rousseau, and S. Saitzek, “Synthesis, structural and luminescence properties of (La1−xLnx)2Ti2O7 (Ln=lanthanides) solid solutions,” *J. Alloys Compd.*, vol. 683, pp. 634–646, Oct. 2016.

[26] J. A. Bearden and A. F. Burr, “Reevaluation of X-ray atomic energy levels,” *Rev. Mod. Phys.*, vol. 39, no. 1, pp. 125–142, Jan. 1967.

[27] B. Ravel and M. Newville, “ATHENA and ARTEMIS: Interactive graphical data analysis using IFEFFIT,” *Phys. Scr. T*, vol. T115, no. T115, pp. 1007–1010, 2005.

[28] M. Newville, “IFEFFIT: Interactive XAFS analysis and FEFF fitting,” *J. Synchrotron Radiat.*, vol. 8, no. 2, pp. 322–324, Mar. 2001.

[29] B. Ravel and M. Newville, “ATHENA, ARTEMIS, HEPHAESTUS: Data analysis for X-ray absorption spectroscopy using IFEFFIT,” in *Journal of Synchrotron Radiation*, 2005, vol. 12, no. 4, pp. 537–541.

[30] A. L. Ankudinov, B. Ravel, J. J. Rehr, and S. D. Conradson, “Real-space multiple-scattering calculation and interpretation of x-ray-absorption near-edge structure,” *Phys. Rev. B*, vol. 58, no. 12, p. 7565, Sep. 1998.

[31] A. G. Waychunas, “Synchrotron radiation xANES spectroscopy of Ti in minerals: Effects of Ti bonding distances, Ti valence, and site geometry on absorption edge structure,” 1987.

[32] F. Farges, G. E. Brown, and J. J. Rehr, “Coordination chemistry of Ti(IV) in silicate glasses and melts: I. XAFS study of titanium coordination in oxide model compounds,” *Geochim. Cosmochim. Acta*, vol. 60, no. 16, pp. 3023–3038, Aug. 1996.

[33] S. R. Hall, F. H. Allen, and I. D. Brown, “The crystallographic information file (CIF): a new standard archive file for crystallography,” *Acta Crystallogr. Sect. A*, vol. 47, no. 6, pp. 655–685, Nov. 1991.

[34] O. Knop, F. Brisse, and L. Castelliz, “Pyrochlores. V. Thermoanalytic, X-ray, neutron, infrared, and dielectric studies of A2Ti2O7 titanates,” *https://doi.org/10.1139/v69-155*, vol. 47, no. 6, pp. 971–990, Mar. 2011.

[35] K. Baroudi, B. D. Gaulin, S. H. Lapidus, J. Gaudet, and R. J. Cava, “Symmetry and light stuffing of Ho2Ti2O7, Er2Ti2O7, and Yb2Ti2O7 characterized by synchrotron x-ray diffraction,” *Phys. Rev. B - Condens. Matter Mater. Phys.*, vol. 92, no. 2, p. 024110, Jul. 2015.

[36] I. D. Brown and D. Altermatt, “Bond-valence parameters obtained from a systematic analysis of the Inorganic Crystal Structure Database,” *Acta Crystallogr. Sect. B*, vol. 41, no. 4, pp. 244–247, Aug. 1985.

[37] D. Altermatt and I. D. Brown, “The automatic searching for chemical bonds in inorganic crystal structures,” *Acta Crystallogr. Sect. B*, vol. 41, no. 4, pp. 240–244, Aug. 1985.

[38] R. D. Aughterson *et al.*, “The ion-irradiation tolerance of the pyrochlore to fluorite Ho(x)Yb(2-x)TiO5 and Er2TiO5 compounds: A TEM comparative study using both in-situ and bulk ex-situ irradiation approaches,” *J. Nucl. Mater.*, vol. 507, pp. 316–326, Aug. 2018.

[39] R. D. Aughterson, G. R. Lumpkin, G. J. Thorogood, Z. Zhang, B. Gault, and J. M. Cairney, "Crystal chemistry of the orthorhombic Ln2TiO5 compounds with Ln=La, Pr, Nd, Sm, Gd, Tb and Dy," *J. Solid State Chem.*, vol. 227, pp. 60–67, Jul. 2015.

[40] R. D. Shannon and C. T. Prewitt, "Effective ionic radii in oxides and fluorides," *Acta Crystallogr. Sect. B*, vol. 25, no. 5, pp. 925–946, May 1969.

[41] F. Bartolomé, M. H. Krisch, D. Raoux, and J. M. Tonnerre, "Quadrupolar excitation channels at the L3 edge of rare-earth ions probed by resonant inelastic x-ray scattering," *Phys. Rev. B*, vol. 60, no. 19, p. 13497, Nov. 1999.

[42] P. Zasimov, L. Amidani, M. Retegan, O. Walter, R. Caciuffo, and K. O. Kvashnina, "HERFD-XANES and RIXS Study on the Electronic Structure of Trivalent Lanthanides across a Series of Isostructural Compounds," *Inorg. Chem.*, vol. 61, no. 4, pp. 1817–1830, Jan. 2022.

[43] T. Yamamoto, "Assignment of pre-edge peaks in K-edge x-ray absorption spectra of 3d transition metal compounds: electric dipole or quadrupole?," *X-Ray Spectrom.*, vol. 37, no. 6, pp. 572–584, Nov. 2008.

[44] F. Farges, "Fivefold-coordinated Ti4+ in metamict zirconolite and titanite: A new occurrence shown by Ti K-edge XANES spectroscopy," *Am. Mineral.*, vol. 82, no. 1–2, pp. 44–50, Feb. 1997.

[45] F. Farges, "Coordination of Ti4+in silicate glasses: A high-resolution XANES spectroscopy study at the Ti Kedge," *Am. Mineral.*, vol. 82, pp. 36–43, 1997.

[46] M. Stennett *et al.*, "Heavy ion implantation combined with grazing incidence X-ray absorption spectroscopy (GIXAS): A new methodology for the characterisation of radiation damage in nuclear ceramics," *MRS Proc.*, vol. 1193, p. 67, Jan. 2011.

[47] D. P. Reid *et al.*, "The structure of ion beam amorphised zirconolite studied by grazing angle X-ray absorption spectroscopy," *Nucl. Instruments Methods Phys. Res. Sect. B Beam Interact. with Mater. Atoms*, vol. 268, no. 11–12, pp. 1847–1852, Jun. 2010.

[48] A. V. Shlyakhtina *et al.*, "Effects of the synthesis procedure, doping and non-stoichiometry on the order–disorder transformation in Ln2Ti2O7 (Ln = Tm–Lu) oxygen-ion conductors," *Solid State Ionics*, vol. 176, no. 29–30, pp. 2297–2304, Sep. 2005.

Supporting Information

A: Solid-state characterisation

Table A1: Showing the Le Bail refinements of the unit cell parameters (*a, b,* and *c*; θ = 90 ° for all) of Ln_2TiO_5 (Ln = La – Lu) using orthorhombic *Pnma*, hexagonal *P6₃/mmc*, *Fd-3m* and *Fm-3m* structures.

Ln_2TiO_5	*a* (Å)	*b* (Å)	*c* (Å)	*V* (Å³)	R_{wp}
La_2TiO_5	11.0087(2)	3.9456(1)	11.3913(2)	494.80(2)	8.205
Pr_2TiO_5	10.8437(3)	3.8736(1)	11.3581(2)	477.08(1)	8.020
Nd_2TiO_5	10.7347(2)	3.8457(1)	11.3449(2)	468.34(2)	7.280
Sm_2TiO_5	10.5980(2)	3.7999(1)	11.3247(2)	456.04(1)	4.923
Eu_2TiO_5	10.5302(2)	3.7793(1)	11.3240(2)	450.65(1)	4.006
Gd_2TiO_5	10.4813(1)	3.7575(1)	11.3115(2)	445.96(1)	3.038
Tb_2TiO_5	10.4226(3)	3.7369(1)	11.2654(3)	441.23(2)	7.057
Dy_2TiO_5	3.6334(1)	3.6334(1)	11.9258(4)	136.34(1)	4.722
Ho_2TiO_5 *(Fd-3m)*	10.3062(2)	10.3062(2)	10.3062(2)	1094.70(6)	8.090
Ho_2TiO_5 (*Fm-3m)*	5.1539(1)	5.1539(1)	5.1539(1)	136.90(9)	7.580
Er_2TiO_5	5.1292(1)	5.1292(1)	5.1292(1)	134.94(1)	6.194
Tm_2TiO_5	5.1169(1)	5.1169(1)	5.1169(1)	133.98(1)	6.738
Yb_2TiO_5	5.0976(1)	5.0976(1)	5.0976(1)	132.47(6)	9.723
Lu_2TiO_5	5.0881(1)	5.0881(1)	5.0881(1)	131.70(1)	6.497

SEM/EDX was used for the purposes of confirming the absence of secondary phases to confirm observations from XRD data. As can be seen in Figure A1, except for obvious porosity, the back scattered electron micrographs exhibited a homogeneous contrast, with no obvious second phase. The lack of consistent microstructure between samples is indicative of the refractory nature of these materials, the multiple heat treatments at various temperatures required to achieve single phase products for some samples (e.g., Tm_2TiO_5), and the sensitivity of different chemistries to temperature (which would necessitate higher reaction temperatures to achieve single phase products and, as a by-product, aid in the sintering densification process). Table A2 reports the microanalytical composition determined from EDX analysis, excluding oxygen, and normalised to a Ln content of 2.00 formula units (f.u.). Within the margin of precision, the calculated and expected compositions are in good agreement, as expected for formation of the desired Ln_2TiO_5 compound. The Ti Kα and La Lα X-ray

emission lines show considerable overlap and hence it was necessary to use a narrow energy window to quantify these elements.

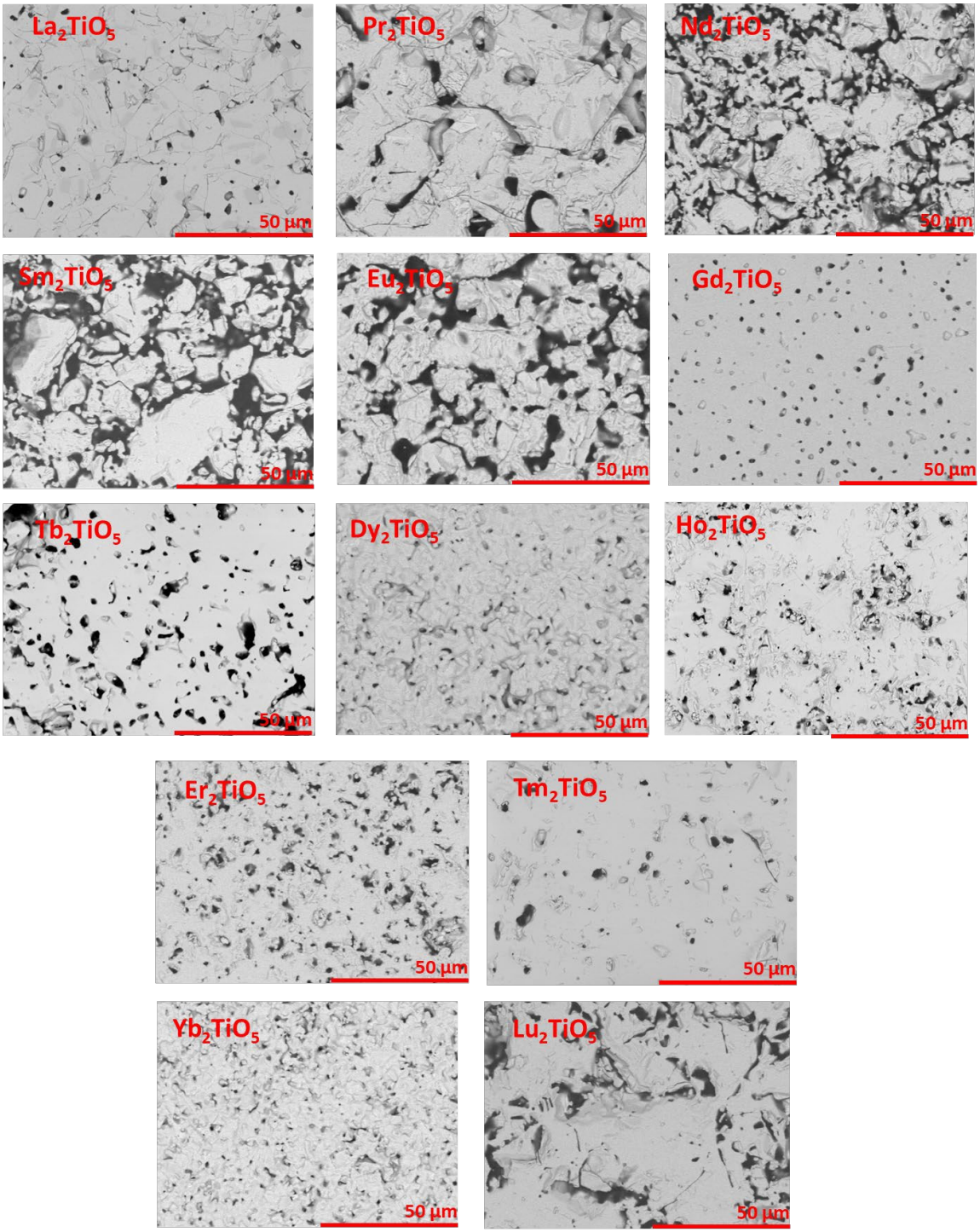

Figure A1: Back scattered electron images of Ln_2TiO_5 (Ln = La – Lu). Dark grey regions are indicative of grain pullout. Black areas are porosity. Due to the refractory nature of these materials, densification was difficult to achieve in some samples (e.g., Eu_2TiO_5)

Table A2: EDX determined microanalytical compositions for Ln_2TiO_5 (Ln = La – Lu), normalised to 2.00 f.u. of Ln

Ln_2TiO_5	Ln		Ti	
	Calc.	*Obs.*	*Calc.*	*Obs.*
La_2TiO_5	2.00	2.00(11)	1.00	1.00(5)
Pr_2TiO_5	2.00	2.00(2)	1.00	1.06(4)
Nd_2TiO_5	2.00	2.00(7)	1.00	1.06(7)
Sm_2TiO_5	2.00	2.00(9)	1.00	1.05(4)
Eu_2TiO_5	2.00	2.00(10)	1.00	1.03(10)
Gd_2TiO_5	2.00	2.00(5)	1.00	1.05(6)
Tb_2TiO_5	2.00	2.00(7)	1.00	1.07(9)
Dy_2TiO_5	2.00	2.00(9)	1.00	1.01(6)
Ho_2TiO_5	2.00	2.00(11)	1.00	1.03(6)
Er_2TiO_5	2.00	2.00(9)	1.00	1.02(7)
Tm_2TiO_5	2.00	2.00(5)	1.00	1.02(3)
Yb_2TiO_5	2.00	2.00(14)	1.00	1.01(6)
Lu_2TiO_5	2.00	2.00(9)	1.00	1.00(6)

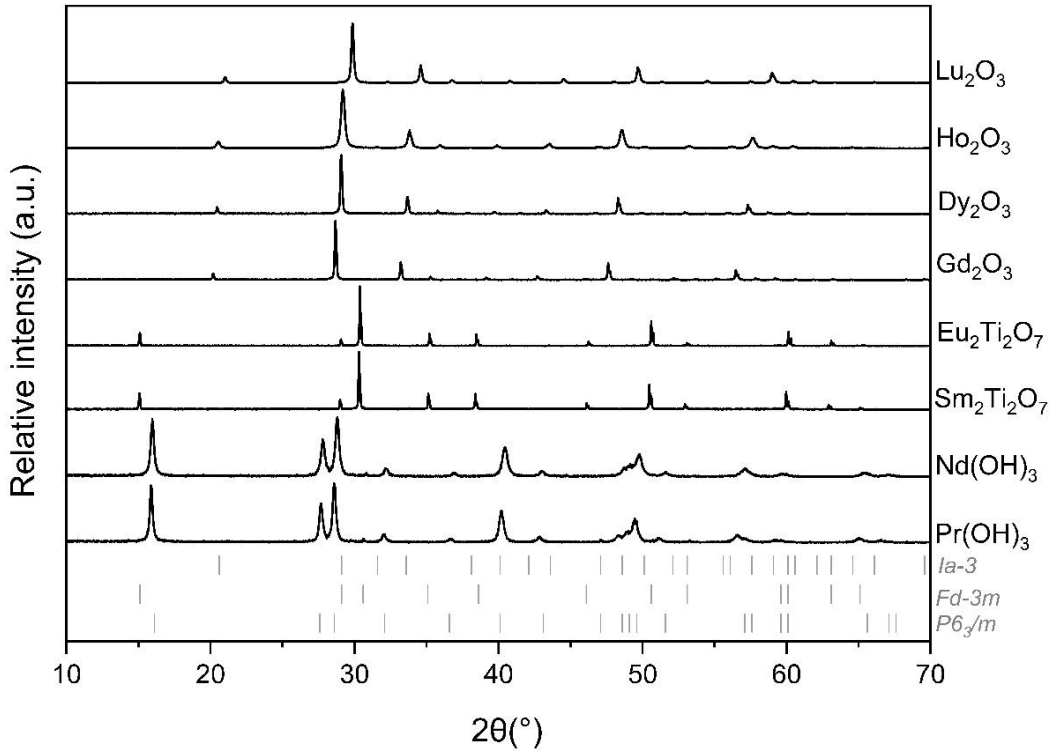

Figure A2: Powder X-ray diffraction data of standards used for XAS analysis. Vertical marks indicate Bragg positions of: $Nd(OH)_3$ *P6₃/m* (ICSD – 167481); $Eu_2Ti_2O_7$ *Fd-3m* (ICSD – 92767); and Ho_2O_3 *Ia-3* (ICSD – 82423). Samples $Nd(OH)_3$ and $Pr(OH)_3$, $Eu_2Ti_2O_7$ and $Sm_2Ti_2O_7$ are isostructural as are Gd_2O_3, Dy_2O_3, Ho_2O_3 and Lu_2O_3

B: XANES Pre-edge Analysis

Table B1: Normalised height and potion (eV) of pre-edge features for Ln_2TiO_5 (Ln = La – Lu) and selected standards taken from previous studies [1].

Sample	Ti coordination	Position (eV)	Normalised height	Source
$Ni_{2.6}Ti_{0.7}O_4$	4	4969.7	0.94	[1]
$Ni_{2.6}Ti_{0.7}O_4$	4	4969.59	0.918	NSLS-II
Ba_2TiO_4	4	4969.6	1	[1]
$K_6Ti_2O_7$	4	4969.7	0.93	[1]
Y_2TiMoO_8	4	4969.9	0.74	[1]
Rb_2TiO_3	4	4969.6	1	[1]
$KNaTiO_3$	5	4970.6	0.73	[1]
$Ba_2TiSi_2O_8$	5	4970.6	0.67	[1]
$Ba_2TiSi_2O_8$	5	4970.55	0.634	NSLS-II
$Sr_2TiSi_2O_8$	5	4970.5	0.71	[1]
$Ba_2TiGe_2O_8$	5	4970.6	0.65	[1]
$Na_2Ti_4O_9$	5	4970.5	0.43	[1]
$K_2Ti_4O_9$	5	4970.6	0.45	[1]
$Rb_2Ti_4O_9$	5	4970.5	0.47	[1]
$K_2Ti_2O_5$	5	4970.6	0.51	[1]
Rutile	6	4971.6	0.22	[1]
Anatase	6	4971.5	0.17	[1]
Anatase	6	4971.6	0.163	NSLS-II
$CaTiO_3$	6	4971.6	0.11	[1]
$BaTiSi_3O_9$	6	4971.2	0.04	[1]
$KNa_2LiFe_2Ti_2Si_8O_{24}$	6	4971.1	0.32	[1]
$FeTiO_3$	6	4971.7	0.22	[1]
$CaTiSiO_5$	6	4971.4	0.18	[1]
$TiZrO_4$	6	4971.1	0.21	[1]
La_2TiO_5	5	4970.275	0.385	This study
Pr_2TiO_5	5	4970.264	0.467	This study
Nd_2TiO_5	5	4970.175	0.394	This study
Sm_2TiO_5	5	4970.279	0.399	This study
Eu_2TiO_5	5	4970.363	0.437	This study
Gd_2TiO_5	5	4970.331	0.416	This study
Tb_2TiO_5	5	4970.105	0.437	This study

Dy_2TiO_5	5	4970.476	0.223	This study
Ho_2TiO_5	5	4970.652	0.189	This study
Er_2TiO_5	5	4970.428	0.217	This study
Tm_2TiO_5	5	4970.428	0.223	This study
Yb_2TiO_5	5	4970.682	0.197	This study
Lu_2TiO_5	5	4970.476	0.223	This study

C: EXAFS fitting methods

The observed long-range order in Pr_2TiO_5, Nd_2TiO_5, Sm_2TiO_5 and Gd_2TiO_5 was shown to have long-range orthorhombic *Pnma* symmetry (graphically represented in Figure C1a). The orthorhombic structure has two distinct Ln sites where both LnO_7 polyhedra form a distorted cube. Here, one oxygen position is vacant, and the remaining oxygens rearrange their positions accordingly. Despite the difference in the two Ln absorber sites, the variation of Ln-O paths distances was not significant (<0.01 Å) and so the Ln first oxygen shells were assigned a shared oxygen path in the fitting models. Given the available data range (up to 10 – 11 $Å^{-1}$ in k-space depending on the sample), Ln-Ln and Ln-Ti scattering paths were grouped together based upon the average spread of bond distances (e.g., Gd_2TiO_5 average Ln(1)-Ln = 3.807 Å, Ln(2)-Ln = 3.841 Å, Ln(1)-Ti = 3.473 Å. The more distant next-nearest neighbour coordination shells were modelled using Ln-Ln and Ln-Ti contributions from Ln site 1, given the similarities in cation degeneracies and distances between the two Ln sites. A Ln(1)-Ln scattering path was used to represent the closer Ln-Ln(1) scatters (e.g.,3.666 – 3.748 Å, average N of 5 between Ln sites, for Gd_2TiO_5) and a more distant Ln-Ln(2) scatterers (e.g., 3.810 – 4.067 Å , average N of 3 between the two Ln sites for Gd_2TiO_5). In the models for the Ti K-edge data, the Ti-O paths are grouped together into one path due to the tight spread of oxygen atoms (e.g., 1.872 – 1.970 Å for the Ti-O bonds in Gd_2TiO_5). Two Ti-Ln paths have been included to account for the relatively broad spread of Ln distances (e.g., 3.390 – 3.666 Å and 3.742 – 3.946 Å for Gd_2TiO_5) and a single Ti-Ti path to account for the more distant Ti cation shell (3.757 Å for Gd_2TiO_5. It was found, based upon our previously defined metrics of statistical and physical interpretations, that the EXAFS of Pr_2TiO_5, Nd_2TiO_5, Sm_2TiO_5 and Gd_2TiO_5 all were satisfactorily described by an orthorhombic *Pnma* model at both the Ln L_3-edges and Ti K-edge.

Initial hexagonal models were setup to include stoichiometric amounts of B-site Ln atoms as per the crystallographic description of Dy_2TiO_5 [2]. A-site lanthanides (Ln_A) and B-site lanthanides (Ln_B) contributions to the signal were weighted appropriately by applying weighting factors to scattering paths, where S_0^2 of Ln_A was multiplied by 0.75 and Ln_B was defined to be 1-Ln_A, based upon the recast stoichiometry $Ln_2(Ln_{0.66}Ti_{1.33})O_{6.67}$ where 75 % of Ln cations occupy A-site positions. However, addition of the Ln_B-O increased the R-factor value, showing that its contribution to the fit was not statistically meaningful. The weighting factor was allowed to refine, and it was found that the overall weighting of Ln_A environment approached unity for all models, implying Ln_B scattering paths were not contributing

meaningfully to the model. Subsequent models excluded B-site features (whilst retaining the appropriate stoichiometry) and found both an improvement in R-factor and reduced χ^2 values. In some instances, this also improved other aspects of the fit, yielding positive σ^2 values, where before they were negative. Rietveld refinements of hexagonal Dy_2TiO_5 have shown that 12.5 % of Dy atoms are typically found on the B-site [2]. The relatively small amount of Dy occupying B-site positions would be contributing very little to the overall average XAS signal and as such not having an appreciable effect on the fit quality, as such these contributions were excluded from the fit. Nearest neighbour oxygens of Ln consisted of six Ln(1)-O scatterers at a bond distance of 2.326 Å corresponding to the immediate Ln coordination polyhedra and two more distant Ln(2)-O scatterers found parallel to the *z*- axis at 2.955 Å, based on structural refinements by previous authors [3]. More distant contributions were represented by a single Ln-Ti path and two Ln-Ln paths. The hexagonal crystal structure and respective coordination polyhedra of Ln and Ti are shown in Figure C1b.

The local structural environment around Ho, Lu and Ti atoms of cubic Ho_2TiO_5 and Lu_2TiO_5 were investigated using a previously established methodology used in the EXAFS analysis of the Yb L_3- Y K- and Ti K-edges of XAS spectra collected on Yb_2TiO_5 and Y_2TiO_5 [reference needed]. Here, an appropriate CIF of an $Ln_2Ti_2O_7$ structure was edited to reflect the Ln_2TiO_5 stoichiometry (recast as $Ln_2(Ln_{0.66}Ti_{1.33})O_{6.67}$). The pyrochlore structure is typically characterised by an 8-fold coordinated lanthanide in a scalenohedra geometry and 6-fold coordinated Ti within a trigonal antiprism geometry (Figure C1c). The coordination number of the B-site Ti cations were allowed to refine as the results from the XANES analysis and previous studies indicate a 5-fold coordinated environment with XAS features reminiscent of a trigonal bipyramidal geometry.

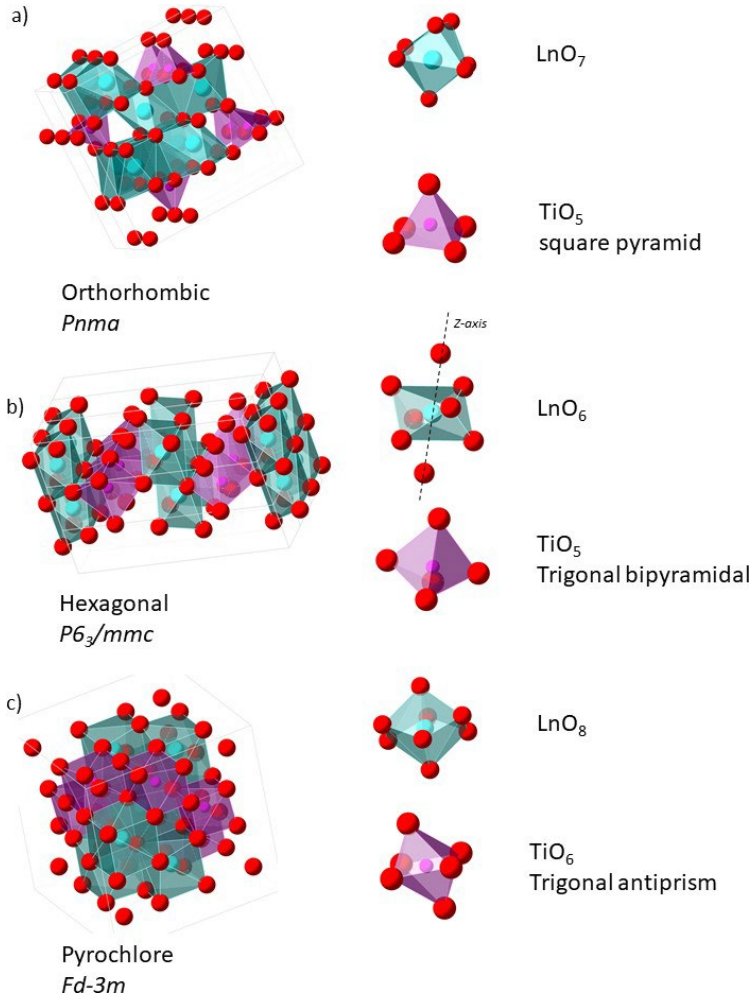

Figure C1: General crystal structure of a) orthorhombic *Pnma* Ln_2TiO_5, the respective coordination polyhedra of the lanthanide (LnO_7) and titanium (TiO_5) is also shown separately; b) hexagonal *P6₃/mmc* Ln_2TiO_5, the respective coordination polyhedra of the lanthanide (LnO_6) and titanium (TiO_5) is also shown separately. Also shown for the enlarged lanthanide polyhedra are the two additional oxygen atoms, about the *z-axis*, which are part of the nearest neighbour oxygen shell; c) cubic *Fd-3m* Ln_2TiO_5, the respective coordination polyhedra of the lanthanide (LnO_8) and titanium (TiO_6) is also shown separately.

D: Amplitude reduction factor (S_n^2) determination

For the purpose of extracting a suitable S_n^2 value for use in refining structural models of Ln_2TiO_5 EXAFS data, models were constructed for a suite of appropriate standards targeting relevant elemental edges. $Pr(OH)_3$ and $Nd(OH)_3$ were used for the Pr and Nd Ln L_3-edges, respectively.

The models were based on structural refinements from the following: $Pr(OH)_3$ and $Nd(OH)_3$ by *Khidirov and Om* [4]; $Sm_2Ti_2O_7$ at the Sm L_3-edge by *Knop et al.* [5]; Gd_2O_3 by *Zein et al.* [6]; Dy_2O_3 and Ho_2O_3 by *Maslen et al.* [7] and Lu_2O_3 by *Guzik et al.* [8].

Single scattering paths were added until a satisfactory fit that modelled the spectral features was achieved. Starting from Ln-O scattering paths the k^3 χ(k) waveform and the Fourier transform k^3 χ(k) spectral envelope as indicated by the R-factor values. Further confidence of the models can be seen in the sensible BVS figures calculated for each model, all within ~5 % of the formal valence of Ln (3 v.u.).

An EXAFS model of $Eu_2Ti_2O_7$ was constructed to extract a suitable S_0^2 value for use in models of the Ln_2TiO_5 EXAFS data at the Ti K-edge. The S_0^2 value can be taken with confidence given the reasonable R-factor and calculated BVS for Ti^{4+}. The Ti K-edge model was based upon structural refinements by *Chtoun et al.* [9].

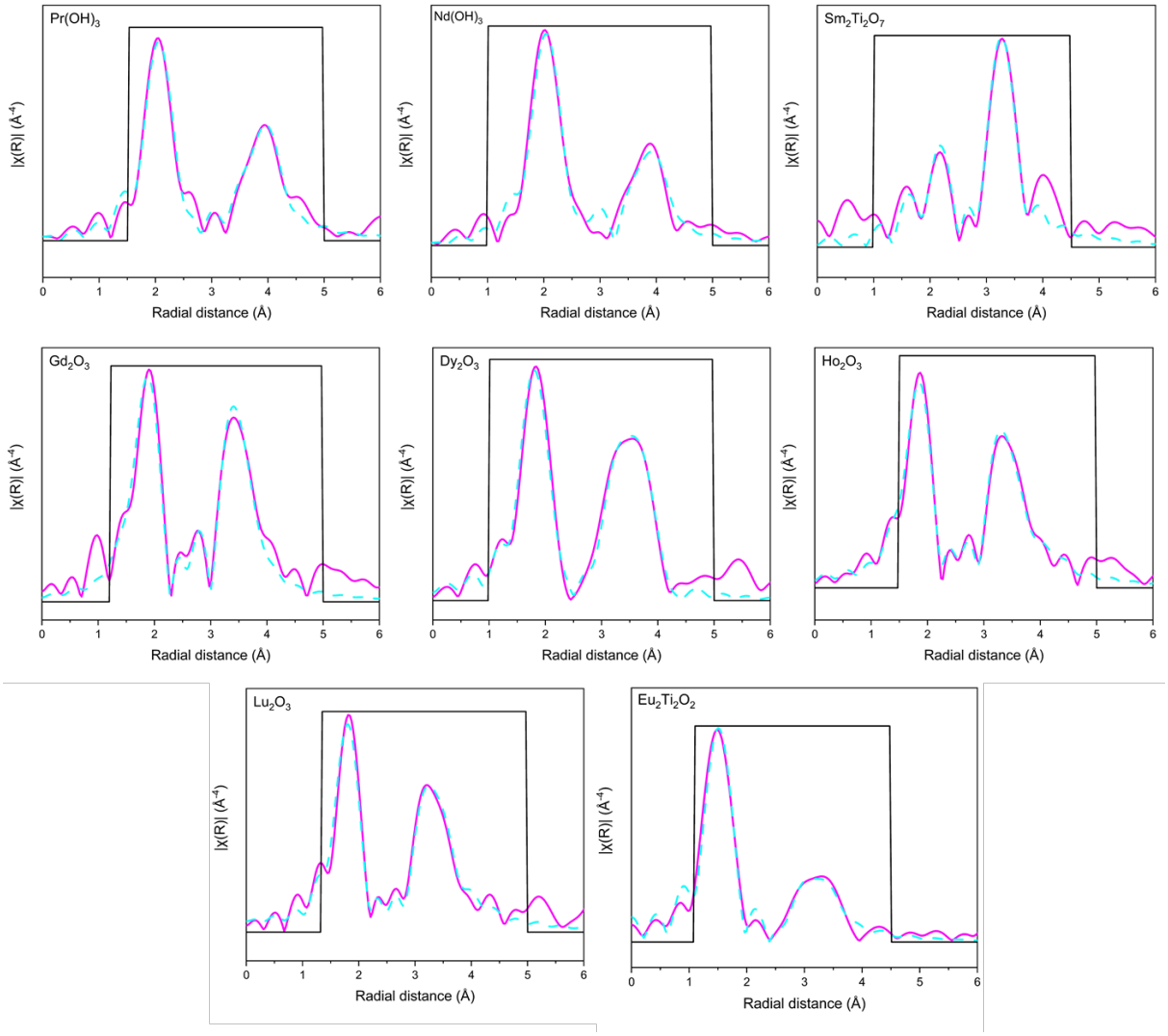

Figure D1: Fourier transform of various standards measured at Ln L_3-edge and Ti K-edge. From top to right, $Pr(OH)_3$ (Pr L_3-edge), $Nd(OH)_3$ (Nd L_3-edge), $Sm_2Ti_2O_7$ (Sm L_3-edge); from centre to right Gd_2O_3 (Gd L_3-edge), Dy_2O_3 (Dy L_3-edge), Ho_2O_3 (Ho L_3-edge); from bottom to right, Lu_2O_3 (Lu L_3-edge), $Eu_2Ti_2O_7$ (Ti K-edge). Solid pink lines represent the experimental data, blue dashed lines represent the theoretical fit and solid black line represents the fitting window

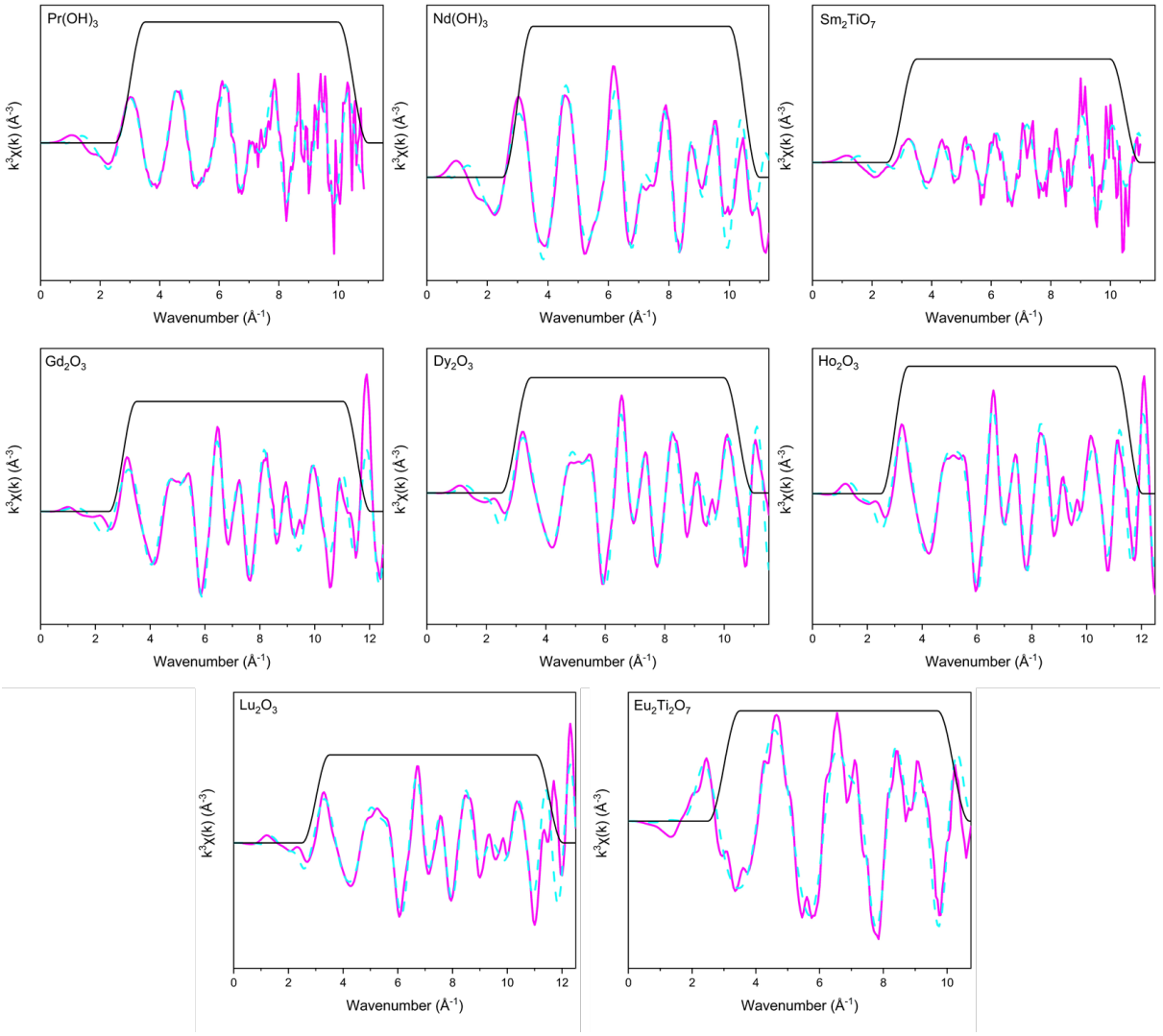

Figure D2: K^3 weighted waveform of various standards measured at Ln L_3-edge and Ti K-edge. From top to right, $Pr(OH)_3$ (Pr L_3-edge), $Nd(OH)_3$ (Nd L_3-edge), $Sm_2Ti_2O_7$ (Sm L_3-edge); from centre to right Gd_2O_3 (Gd L_3-edge), Dy_2O_3 (Dy L_3-edge), Ho_2O_3 (Ho L_3-edge); from bottom to right, Lu_2O_3 (Lu L_3-edge), $Eu_2Ti_2O_7$ (Ti K-edge). Solid pink lines represent the experimental data, blue dashed lines represent the theoretical fit and solid black line represents the fitting window.

Table D1: Refined structural parameters for Ln L_3edge standards (Ln = Pr, Nd, Sm, Gd, Dy, Ho, Lu). $Pr(OH)_3$ and $Nd(OH)_3$ were modelled using a *P6₃/m* structure, $Sm_2Ti_2O_7$ was modelled using a *Fd-3m* structure, Gd_2O_3, Dy_2O_3, Ho_2O_3 and Lu_2O_5 were modelled using a *Ia-3* structure. The average change in scattering path distance for a given absorber-scatterer pair is denoted as R, the Debye–Waller factor is denoted as σ^2, the degeneracy of the path denoted as N and Ln represents the corresponding metal cation. A dash denoted that there was no corresponding path included in a specific model.

Path		**$Pr(OH)_3$**	**$Nd(OH)_3$**	**$Sm_2Ti_2O_7$**	**Gd_2O_3**	**Dy_2O_3**	**Ho_2O_3**	**Lu_2O_3**
	S_o^2	0.7(7)	0.87(9)	0.7(26)	0.99(12)	1.06(10)	0.99(16)	0.85(13)
	E_o (eV)	2.7(9)	2.9(8)	5.0(2.5)	5.0(3)	0.8(7)	1.2(11)	4(12)
	R (Å)	2.53(1)	2.52(1)	2.24(3)	2.32(1)	2.28(1)	2.25(2)	2.22(1)
Ln-O(1)	*σ^2 (Å²)*	0.008(2)	0.009(2)	0.008(5)	0.007(2)	0.009(2)	0.008(2)	0.008(2)
	N	9	9	2	6	6	6	6
	R (Å)	-	-	2.54(11)	-	-	-	-
Ln-O(2)	*σ^2 (Å²)*	-	-	0.008(5)	-	-	-	-
	N	-	-	6	-	-	-	-
	R (Å)	3.81(2)	3.79(4)	3.62(6)	3.59(1)	3.56(1)	3.53(2)	3.46(2)
Ln-Ln(1)	*σ^2 (Å²)*	0.002(1)	0.003(2)	0.007(4)	0.006(1)	0.005(1)	0.006(2)	0.005(2)
	N	2	2	6	6	6	6	6
	R (Å)	4.20(7)	4.00(8)	-	4.05(2)	4.05(2)	3.98(3)	3.95(4)
Ln-Ln(2)	*σ^2 (Å²)*	0.018(11)	0.003(1)	-	0.008(3)	0.007(3)	0.009(4)	0.008(4)
	N	6	6	-	6	6	6	6
		-	-	3.62(2)	-	-	-	-
Ln-Ti		-	-	0.004(2)	-	-	-	-
		-	-	6	-	-	-	-
	R (Å)	3.67(2)	3.99(10)	-	-	4.15(3)	-	4.07(5)
Ln-O(2)	*σ^2 (Å²)*	0.007(2)	0.009(2)	-	-	0.017(7)	-	0.021(11)
	N	3	3	-	-	12	-	12
R-factor		0.013	0.029	0.39	0.028	0.028	0.032	0.018
BVS (v.u.)		2.75	2.98	3.04	3.08	3.08	3.18	3.06

Table D2: Refined structural parameters for Ti K-edge $Eu_2Ti_2O_7$ standard modelled using a *Fd*-3m The average change in scattering path distance for a given absorber-scatterer pair is denoted as R, the Debye–Waller factor is denoted as σ^2, the degeneracy of the path denoted as N and Ln represents the corresponding metal cation.

Path		$Eu_2Ti_2O_7$
	S_o^2	0.6(6)
	E_o (eV)	-2.0(16)
Ln-O(1)	*R (Å)*	1.96(1)
	σ^2 (Å^2)	0.003(1)
	N	6
Ln-Ti	*R (Å)*	3.53(2)
	σ^2 (Å^2)	0.010(6)
	N	6
Ln-Ln	*R (Å)*	3.64(2)
	σ^2 (Å^2)	0.003(2)
	N	6
Ln-O(2)	*R (Å)*	3.85(4)
	σ^2 (Å^2)	0.007(5)
	N	6
R-factor		0.03
BVS (v.u.)		3.97

E: References

[1] F. Farges, G. E. Brown, and J. J. Rehr, “Coordination chemistry of Ti(IV) in silicate glasses and melts: I. XAFS study of titanium coordination in oxide model compounds,” *Geochim. Cosmochim. Acta*, vol. 60, no. 16, pp. 3023–3038, Aug. 1996.

[2] R. D. Aughterson, N. J. Zaluzec, and G. R. Lumpkin, “Synthesis and ion-irradiation tolerance of the Dy_2TiO_5 polymorphs,” *Acta Mater.*, vol. 204, p. 116518, Feb. 2021.

[3] R. D. Aughterson *et al.*, “Crystal structures of orthorhombic, hexagonal, and cubic compounds of the $Sm_{(x)}Yb_{(2-x)}TiO_5$ series,” *J. Solid State Chem.*, vol. 213, pp. 182–192, May 2014.

[4] I. Khidirov and V. T. Om, “Localization of hydrogen atoms in rare earth metal trihydroxides R (OH)3,” *Phys. status solidi*, vol. 140, no. 2, pp. K59–K62, Dec. 1993.

[5] O. Knop, F. Brisse, and L. Castelliz, “Pyrochlores. V. Thermoanalytic, X-ray, neutron, infrared, and dielectric studies of A2Ti2O7 titanates,” *https://doi.org/10.1139/v69-155*, vol. 47, no. 6, pp. 971–990, Mar. 2011.

[6] Z. Heiba, H. Okuyucu, and Y. S. Hascicek, “X-ray structure determination of the rare earth oxides $(Er_{1-x}Gd_x)_2O_3$ applying the Rietveld method,” *urn:issn:0021-8898*, vol. 35, no. 5, pp. 577–580, Sep. 2002.

[7] E. N. Maslen, V. A. Streltsov, and N. Ishizawa, “A synchrotron X-ray study of the electron density in C-type rare earth oxides,” *urn:issn:0108-7681*, vol. 52, no. 3, pp. 414–422, Jun. 1996.

[8] M. Guzik *et al.*, “Structural investigations of Lu_2O_3 as single crystal and polycrystalline transparent ceramic,” *Cryst. Growth Des.*, vol. 14, no. 7, pp. 3327–3334, Jul. 2014.

[9] E. H. Chtoun, L. Hanebali, and P. Garnier, “Analyse par diffraction des rayons x, méthode de rietveld, de la structure des solutions solides $(1-x)A_2Ti_2O_7$ - xFe_2TiO_5 A= Eu, Y,” *Ann. Chim. Sci. des Matériaux*, vol. 26, no. 3, pp. 27–32, May 2001.

6. Draft paper: The effects of ion irradiation on the short-range order of the crystalline phases of Ln_2TiO_5 stuffed pyrochlores investigated by GAXAS

As has been demonstrated thus far, the local coordination of the crystalline phase associated with Ln_2TiO_5 stuffed pyrochlores are complex. The response of these crystal structures to radiation damage is equal as so. It is well known that cubic Ln_2TiO_5 demonstrate the highest radiation tolerance of Ln_2TiO_5 compounds, but there is little understanding of how the short-range order is affected. This chapter will probe the effects that radiation damage, simulated *via* heavy-ion implantation of 1 MeV Kr and 5MeV Au ions, has on the short-range order of orthorhombic, hexagonal and cubic phases through GAXAS measurements. The application of glancing angle XAS techniques (including the analyses of XANES and EXAFS regions of spectra) has only been reported infrequently, therefore there is scope to explore the comprehensive application of this technique to study the complex structural ordering that Ln_2TiO_5 ceramics are shown to exhibit. The use of both Kr and Au ions will provide the opportunity to study the efficacy of GAXAS characterisation of irradiated materials, as the ion penetration depth will vary across different radiation damage conditions. Further, the different ion irradiation conditions have different rates of ion stopping power (ENSP, see section 3.3.2 for discussion), hence, this section will also aid in the understanding of the limitations of GAXAS in identifying any subtle changes in the short-range order as a consequence of varied ENSP ratio, if they exist.

The work presented here is the form of a draft paper intended for submission to *Physical Review B*, and as such are written in the appropriate style for that journal. Supporting information for each paper follows the refences sections. References to draft papers from chapters 4 and 5 are given in the appropriate journal format to keep contintiuty with other references.

The author's contribution was the synthesis of samples and consolidation into bulk monoliths appropriate for study, X-ray diffraction, analysis of XANES and EXAFS data and writing of the manuscript. Heavy-ion irradiations were undertaken by the author and S. K. Sun, in collaboration with beamline operators at the Dalton Cumbria Facility (DCF). GAXAS data were acquired by the author in collaboration with M. C. Stennett, N. C. Hyatt and B. Ravel. Manuscript proofing and editing were assisted by R. J. Hand, L. T. Townsend, B. Ravel and M. C. Stennett. All authors contributed to the discussions and interpretations of data.

Insights into the effects of ion irradiation on the short-range order of Ln_2TiO_5 stuffed pyrochlores investigated by GAXAS

Daniel A. Austin[1], Luke T. Townsend[1], Martin C. Stennett[1], S. K. Sun[1], Bruce Ravel[2], N. C. Hyatt[1], Russell J. Hand[1]

[1] *Immobilisation Science Laboratory, Department of Materials Science and Engineering, University of Sheffield, Sheffield S1 3JD, United Kingdom*

[2] *National Institute of Standards and Technology, 100 Bureau Drive, Gaithersburg, MD 20899, USA*

Abstract

Ln_2TiO_5 stuffed pyrochlores are currently used as inclusions in control rod configurations and in oxide dispersion-strengthened steels for nuclear reactor operations. Furthermore, they have been suggested as a potential ceramic hosts of actinide wastes arising from nuclear activities. The performance of these materials in high intensity radiation environments is key to their success, therefore a thorough understanding of the effects of radiation damage to short-range ordering of these structures is needed. The effect of heavy ion-irradiation (5 MeV Au^{2+} and 1 MeV Kr^{+}) on orthorhombic, hexagonal and cubic Ln_2TiO_5 (Ln = Gd, Dy, Yb) stuffed pyrochlores has been investigated *via* glancing-angle X-ray absorption spectroscopy (GAXAS), collected at both the Ln L_3-edges and Ti K-edge. GAXAS accurately probed the effects of radiation damage on the short-range ordering of these structures, giving key insights into the mechanisms that govern the radiation response of these compounds. The medium-range order of each compound was significantly reduced due radiation damage however, the short-range order of each Ln_2TiO_5 stuffed pyrochlore varied across structures. Whilst the hexagonal Dy_2TiO_5 appeared to have lost all atomic order and was rendered effectively amorphous, the orthorhombic and cubic structures retained significant degrees of long-range order and the short-range ordering of both was equivalent to coordination polyhedra of that observed in more disordered crystalline structures. These results appear to indicate that cation anti-site defects, where different atoms exchange positions, (e.g., 6-fold coordination for both Gd and Ti sites) are the predominant defect mechanism for orthorhombic Gd_2TiO_5, where Ln_2-Ti sites become significantly mixed. The cubic Yb_2TiO_5 maintained the YbO_8 and TiO_5 polyhedra that characterise the pristine structure, however the coordination polyhedra are more distorted. This study serves to underscore the importance of short- and medium-range order analyses to develop comprehensive descriptions of the behaviour of crystalline materials under irradiation and that GAXAS techniques is an effective technique to study this.

1. Introduction

The immobilisation of actinide waste products in a ceramic matrix will require a material that can not only accommodate a wide range of radioisotopes and be chemically durable enough to tolerate disposal environments (for example, natural geological and man-made systems) but also have a demonstratable resistance to radiation induced damages [1]–[3]. A vital factor when considering a potential wasteform for immobilisation purposes is the response of both the short- and long-range order to radiation damage as both inform the understanding of durability and chemical behaviour during long-term storage. This work focuses on probing the radiation resistance and response of the short-range order of a series of A_2TiO_5 (A = trivalent lanthanide, Ln^{3+}) compounds by utilising X-ray absorption spectroscopy (XAS) techniques. Ln_2TiO_5 (Ln = La – Lu, Y) compounds are a derivative of the $Ln_2Ti_2O_7$ pyrochlore and often referred to as stuffed pyrochlores due to the additional lanthanides incorporated onto the Ti-site (i.e. $Ln_2(Ti_{1.33}Ln_{0.66})O_{6.67}$). Stuffed pyrochlores have recently been the subject of interest due to their reportedly favourable physical and chemical properties in addition to a high tolerance to radiation damage [4]–[8]. Furthermore, the stuffed pyrochlore series has already seen application within the broader nuclear industry, for example, Gd_2TiO_5 and Dy_2TiO_5 have been used as burnable poisons, due to the large thermal neutron absorption cross sections, σ, of Gd (σ = 257,000 for ^{157}Gd, which has natural abundance of 15.65%) and Dy (σ = 2780 barns for ^{164}Dy, which has natural abundance of 28.26%), as inclusions in UO_2 fuel pellets and control rods, respectively [9], [10].

A ceramic's response to radiation damage may be conditional on many properties, such as the specific chemistry, thermal history and crystal structure [11]. As the crystal structures of the Ln_2TiO_5 series are known to vary based upon the ionic radius of the Ln cation and their thermal history, their radiation responses are varied. The temperature stability diagram proposed by *Shepelev and Petrova* illustrated the possible crystal structures Ln_2TiO_5 can take [12]. For compounds containing relatively large lanthanides (Ln = La – Dy, Y), an orthorhombic *Pnma* symmetry can be observed, where the Ln occupies two 7-fold coordinated mono-capped octahedra and Ti is found to be in a 5-fold square based pyramid geometry [13]. Intermediate sized lanthanides (Gd – Ho, Y) are known to be polymorphic, and depending on reaction temperature and cooling regime, can possibly crystalise with an orthorhombic hexagonal or cubic symmetry [12]. The hexagonal *$P6_3/mmc$* structure consists of the lanthanide exclusively occupying the A-site in an octahedral coordination and a Ti-site, which can be partially occupied by the lanthanide, found in a 5-fold coordinated, trigonal bipyramidal geometry [6], [13]. Smaller lanthanides (Ln = Dy – Lu, Y) will crystallise in a cubic symmetry. Observations from X-ray diffraction (XRD) and neutron diffraction (ND) studies show that the cubic crystal structure consists of long-range defect-fluorite *Fm-3m* and short-range pyrochlore-like ordering [8], [14], [15]. The *Fd*-3*m* pyrochlore structure consists of 8-fold coordinated lanthanide and a 6-fold coordinated Ti site, the related *Fm*-3*m* defect-fluorite structure has complete cation disordering. The presence of short-range pyrochlore-like ordering becomes evident as the ionic radius of the lanthanide gets larger (from Lu to Dy) and weak reflections become evident in the diffraction patterns that are indexable to an $Ln_2Ti_2O_7$

pyrochlore *Fd-3m* unit cell [14]–[16]. Transmission electron microscopy (TEM) and electron diffraction (ED) techniques have been used to show that cubic Ln_2TiO_5 is comprised of pyrochlore nano-domains, where the domain size is dependent of the ionic radius of the lanthanide (3 nm in Ho_2TiO_5 and 2 nm in Yb_2TiO_5) [8], [14]. Analysis of the short-range order through X-ray absorption spectroscopy techniques shows that the Ti is located in a 5-fold coordinated environment, commensurate with that of other Ln_2TiO_5 crystal structures [17]. Results from the analysis of the X-ray absorption near edge structure (XANES) of Ti K-edge data indicates a Ti environment similar to that of hexagonal Ln_2TiO_5 stuffed pyrochlores. Qualitative inspection of both the Ln L_3-edge and Ti K-edge spectra shows similarities between cubic and hexagonal samples, however, modelling of the extended X-ray absorption fine structure (EXAFS) region concluded that it could satisfactorily be fit using a structure based upon the *Fd-3m* pyrochlore structure, albeit with Ti in a 5-fold coordination [17].

Fundamental ion-irradiation studies of Ln_2TiO_5 stuffed pyrochlores have demonstrated that, through *in-situ* ion-irradiation in combination with TEM, compounds that adopt a cubic symmetry have markedly improved response to radiation damage [6], [14], [18], [19]. One metric for indicating the radiation tolerance of a material is the critical temperature of amorphisation T_c, above which the sample would remain crystalline. There is a general trend of cubic stuffed pyrochlores having a lower T_c property compared to the other orthorhombic and hexagonal structures, which has been linked to the defect-fluorite structure's ability to incorporate more disorder. For instance, the T_c of orthorhombic Ln_2TiO_5 compounds varies between 712 K and 1143 K, whereas in studies of cubic Ln_2TiO_5 this property was found to be between 479 K and 738 K, in both cases there was a general trend towards improved radiation resistance as the lanthanide ionic radius decreased [7], [15], [18]. Furthermore, it has been noted that hexagonal Ln_2TiO_5 stuffed pyrochlores perform comparatively poorer than orthorhombic and cubic stuffed pyrochlores [19], as illustrated by comparing the T_c of cubic, hexagonal and orthorhombic Dy_2TiO_5 polymorphs [6]. The 1 MeV Kr ion-irradiation of orthorhombic and cubic polymorphs of Dy_2TiO_5 were shown to have T_c values of 761 K and 711 K, respectively, however the hexagonal polymorph had a T_c of 1130 K. The improved resistance to radiation damage of cubic stuffed pyrochlores has been attributed to their ability to accommodate a greater amount of disorder induced by defects from radiation damage. The radiation resistance of orthorhombic compounds has been proposed to be related to the anti-site defect formation, which becomes less energetically favourable as the ionic radius of the lanthanide decreases. This mechanism is contrary to the radiation resistance of defect-fluorite Ln_2TiO_5 where the cation disordered structure is relatively stable, the complex and highly ordered crystal structure of orthorhombic Ln_2TiO_5 makes the accommodation of cation anti-site defects less tenable.

Additional studies comparing the radiation tolerance of *Fm-3m* Ln_2TiO_5 and the parent *Fd-3m* $Ln_2Ti_2O_7$ pyrochlore have also shown that Ln_2TiO_5 stuffed pyrochlores have a comparatively improved tolerance. *Whittle et al.* found, that after the 1 MeV Kr irradiation of Y_2TiO_5 and Yb_2TiO_5, which adopt a defect-fluorite *Fm-3m* structure, the T_c values were 589 K and 457 K, respectively. For comparison,

related *Fd-3m* $Y_2Ti_2O_7$ and $Yb_2Ti_2O_7$ pyrochlores had T_c values of 665 K and 594 K, respectively [8], with Whittle *et al.* associating this to the inherent ability of *Fm-3m* defect-fluorite compounds to maintain greater levels of disorder more readily. The relationship between radiation tolerance of pyrochlore and defect-fluorite structures has been comprehensively studied in other, related compounds such as $La_2Hf_2O_7$ (pyrochlore) and $La_{1.6}Y_{0.4}Hf_2O_7$ (defect-fluorite), and the trend of increased radiation resistance of defect-fluorite structured compounds is consistent [20].

Whilst determination of radiation tolerance is important, it is equally as necessary to understand the mechanisms of the structural changes of materials after they have become amorphised or reached a highly damaged state. Radiation damage can cause significant changes in the local coordination of cations, induce phase transformations, and form a variety of defects, in addition to exhibiting other structural alterations [21]–[23]. These changes can have profound effects on the materials efficacy as a wasteform, potentially leading to a less stable crystal structure, a change in aqueous dissolution rates, or an alteration in the durability of the ceramic [24]. The short-range order of amorphous or disordered crystalline oxides can be studied through a variety of methods. Pair distribution function (PDF) analysis of neutron total scattering data has been previously used to demonstrate that, whilst the long-range order exhibits a significant loss in crystallinity, the local coordination of cations in orthorhombic Dy_2TiO_5 after 2.2 GeV Au irradiation at a fluence of 8 x 10^{12} ions cm^{-2} remains intact, with some distortions to the coordination polyhedra [25]. In the same study the related $Dy_2Ti_2O_7$ pyrochlore was proven to more radiation resistant over the long-range, however, the short-range order underwent an atomic rearrangement, best described as pyrochlore-to-weberite transitions (the weberite space group is *Ccmm*). Local-order transitions from pyrochlore-to-weberite have also been identified in other pyrochlore compounds irradiated under similar conditions *via* techniques such as Raman spectroscopy, neutron total scattering and extended X-ray absorption fine structure (EXAFS) analysis [26]–[29]. These experiments have exclusively made use of high energy ion irradiations (up to GeV), which aim to simulate the elastic collisions that are associated with fragments from fission events and predominately interact with electrons. Less penetrating, lower energy (keV – MeV) ion irradiations, such as those used in the investigations of the T_c of ceramic materials aim to simulate alpha-decay events of immobilised radioisotopes, this interaction is dominated by inelastic ballistics. However, these studies do serve to highlight the significance of using techniques sensitive to changes in local coordination [26]–[29].

Recently, there have been studies aiming to utilise XAS techniques to further investigate the effects of radiation damage [23], [30]–[34]. Difficulties of these types of measurements on bulk ceramic samples irradiated by ions with an energy in the range of keV to MeV, where inelastic nuclear collisions are dominant, can arise due to the penetration depth of indecent X-rays being significantly greater than that of damaged surface region (~1 µm) when collected in standard experimental geometries [35] (i.e., fluorescence detector 45° from the sample). Attempts to probe the damaged regions of nuclear glasses and ceramics have utilised more surface sensitive measurement techniques such as soft X-ray absorption spectroscopy (SXAS) and collection of total electron yield (TEY) regions [33], [34], however

methods such as TEY XAS were complicated due to X-ray penetration depth exceeding that of the damaged layer, resulting in sampling of both undamaged and damaged regions. Furthermore, there has recently been developments in utilising glancing angle X-ray absorption spectroscopy measurements (GAXAS) to investigate surface damaged regions of ceramics [23], [30]–[32]. Fixing the incident X-ray beam at a shallow angle allows for the collection of fluorescent X-rays originating from only the surface region, by slightly altering the incident angle different zones of the damaged surface can be analysed. This technique has been used successfully to demonstrate, by analysis of both the XANES and EXAFS regions, that there were reductions of the TiO_6 species to TiO_5 in both $Gd_2Ti_2O_7$ and $CaZrTi_2O_7$ (zirconolite) irradiated by 2 MeV Kr ions in addition [23], [31].

This study has used GAXAS measurements for the first time to study the ion-irradiation response of Ln_2TiO_5 (Ln = Gd, Dy, Yb), representative of the three crystal structures associated with stuffed pyrochlores, irradiated by different ion species and energies. The use of GAXAS provides significant insight into the nature of the radiation response of the short-range ordering of these structures by collecting GAXAS data at both the Ln L_3-edge and Ti K-edge and applying quantitative analysis to both the XANES and EXAFS regions. This study demonstrates the first instance of quantitative analyses of XANES, and EXAFS data collected in a GAXAS mode on irradiated ceramics. The comprehensive GAXAS study presented here provides a detailed account of changes to the short-range order of Ln_2TiO_5 stuffed pyrochlore post-irradiation, whilst also demonstrating the powerful applicability of GAXAS measurements within nuclear wasteform research.

2. Experimental

2.1 Solid-state synthesis

Ln_2TiO_5 stuffed pyrochlores were synthesised through a typical solid-state route. TiO_2 and lanthanide sesquioxide precursors, Gd_2O_3, Dy_2O and Yb_2O_3 were dried prior to being stoichiometrically batched according to target composition. Batched reagent mixtures were milled alongside SiAlON milling media at 500 RPM for 15 minutes, using isopropyl carrier fluid. Milled powder slurries were dried at 80 °C prior to being sieved (250 mesh) and consolidated in a stainless-steel die by uniaxially pressing under 4 tonnes of pressure. The resultant powder compacts were reacted between 1300 – 1550 °C for 48 hours, with a ramp rate of 5 °C/min. Subsequent heat treatments, with intermittent milling of the ceramic product, were carried out until a single-phase product had been achieved. The targeted hexagonal phase of Dy_2TiO_5 is an intermediate polymorph that can be achieved at temperatures between around 1300 – 1600 °C. Stabilisation of this phase required alternate cooling regime and as such the procedure laid out in previous studies was followed [6], [36].

Once single-phase products had been obtained the ceramic powders were reconsolidated into pellet compacts following the same procedure described previously in the above paragraph. Samples were initially sintered for 12 hours at 1300 °C, checked for porosity *via* scanning electron microscopy (SEM) and any changes in phase assemblage *via* X-ray diffraction (XRD). The sintering process was repeated

at 250 °C intervals above 1300 °C until porosity had reduced significantly, or no appreciable improvement was detected. The surfaces of sample monoliths were ground down, using subsequently finer SiC paper. All samples were then polished to a 1 µm finish with diamond pastes.

2.2 Solid-state characterisation

Characterisation of the phase assemblage *via* XRD was carried out using a Bruker D2 Phaser operating in a Bragg-Brentano geometry, with Cu Kα radiation and a Lynxeye solid state detector. Data were collected over a range of $0 \leq 2\theta \leq 70°$, with a step size of 0.02°, counting for 1.8 s step^{-1}. Glancing-angle X-ray diffraction (GAXRD) of bulk monoliths was conducted using a Siemens D5000 diffractometer, also operating with Cu Kα radiation, operating at 40 kV and 30 mA, with a graphite diffracted beam monochromator. A Hitachi TM3030 scanning electron microscope operating with a 15 kV accelerating voltage and a working distance of approximately 8 mm was used for observations of sample surfaces. Bulk density measurements were conducted using the Archimedes immersion method.

2.3 Ion-beam irradiations

Ion beam irradiations were carried out at the Dalton Cumbria Facility (DCF), University of Manchester, UK, using a 5 MV Pelletron. Ceramic monoliths were mounted onto a NIMONIC75 alloy block sand secured in place using carbon adhesive pads. Irradiations were conducted in focused raster mode using ion beams with 1 MeV Kr^{+} with fluence of 5 x 10^{15} ions cm^{-2} and 5 MeV Au^{+} with a fluence of 1.2 x 10^{15} ions cm^{-2}. The beam current was maintained at 0.5 µA to avoid heating. Displacement profiles were calculated using the Stopping Range In Matter (SRIM) software package [37]. The thickness of the radiation damaged region of samples was given particular consideration prior to ion beam irradiations. SRIM [37] simulations determined the damage depth and profile in Ln_2TiO_5 (Ln = Gd, Dy, Yb) ceramics irradiated by 1MeV Kr ions at a fluence of 5 x 10^{15} ions cm^{-2} and 5 MeV Au^{2+} ions at a fluence of 1.2 x 10^{15} ions cm^{-2}, the profiles and tabulated results from the SRIM simulations for all samples can found in the Supplementary Information, Section S1. The damage depth profiles show that a peak damage depth is reached between the regions of 150 – 300 nm and 400 – 700 nm across all sample stoichiometries and structures irradiated with either Kr or Au ions, respectively. The calculated dpa and ESNP ratios can be found in Table S1 of the Supplementary Material.

2.4 XAS measurements

Ln L_3-edge and Ti K-edge XAS measurements were performed on the 6-BM beamline at the National Synchrotron Light Source II (NSLS-II), Brookhaven National Laboratory (BNL), USA. Samples of pristine Ln_2TiO_5 were prepared for standard transmission and fluorescence modes by finely dispersing ground up powder into polyethylene glycol (PEG), such that they were one absorption length thick. Simultaneous transmission and fluorescence mode data were collected by mounting samples at a 45° angle to the incident X-ray beam and fluorescence detector. These types of measurements are referred to throughout as 'standard-geometry'. The beam size was collimated using slits to 6 mm x 1

mm. Ionisation chambers were utilised to measure the incident (I_0) and transmitted (I_t) X-ray energies, and a 4-element Si drift detector (SII Vortex ME4, Hitachi) was used to collect the fluorescence signal. Data were collected at room temperature at the Ti K-edge (4966 eV), Gd L_3-edge (7243 eV), Dy L_3-edge (7790 eV) and Yb L_3-edge (8944 eV). Ti, Fe and Co foils were used to calibrate the data, taking the first inflection as the absolute energy value [38].

GAXAS data were acquired on the same beamline by placing pristine or irradiated bulk monoliths on a motor-driven stage permitting translation in the x-, y-, z-axis and rotation about z- and x-axis. The sample was moved in the x and y directions to bisect the X-ray beam and was tilted about the z- and x-axis in relation to the plane of the incoming X-ray beam until flat (the maxima of the transmitted X-ray intensity). The incident angle of the X-ray beam was then set to a value corresponding to a chosen sample surface penetration depth. Glancing angles were set to maintain a path length of at least two absorption lengths within the peak of the damage profile produced by SRIM simulations (see section S1 of the Supplementary Information for angles used), the equation: $\sin \alpha = t / 3\ I_{att}$, where the targeted penetration depth (or thickness) is t, and I_{att} is the attenuation length calculated through the Hephaestus software [39], was used to determine the incident angle appropriate for a given t (e.g. 300 nm). This was sufficient to allow measurement of 95% of fluorescent X-rays, originating from the selected surface region. The angle of incidence exceeded the critical angle, α_c, for total external reflection of these materials, which would otherwise restrict the depth penetration <10 nm. The angles selected for purposes of the present experiment were such that, across the range of incident X-ray energy, the fluorescence signal would arise from the surface damaged layer. The fluorescence detector, again set 45° from the sample, was used to measure the X-ray signal. Analysis of the short-range order of irradiated samples was undertaken by measuring the XAS spectra at the Ln L_3-edge and Ti K-edges of Gd_2TiO_5, Dy_2TiO_5 and Yb_2TiO_5 in glancing angle mode, following a similar methodology initially described by *Reid et al.* [23]. Spectra were collected on bulk monoliths of irradiated and pristine samples, for comparison.

2.5 XAS analysis

Analysis of both the XANES and EXAFS regions were undertaken using the Demeter software package with FEFF6 [39]–[41]. Information regarding the local coordination environment of Ti cations was derived from fitting the pre-edge feature of Ti K-edge data following methods previously outlined in literature [17], [42], [43]. An arctangent function was fit to model the photoelectric edge step, a series of gaussians were used to fit the pre-edge components. The intensity weighted average of the energy positions of the first four gaussians was used to determine the pre-edge position and normalised intensity. Analysis of the EXAFS region of pristine and irradiated Ln_2TiO_5 GAXAS data followed the same methodology outlined by the authors previously, which were demonstrated to effectively model the EXAFS region of orthorhombic, hexagonal and cubic Ln_2TiO_5 [17], [36].

EXAFS models of pristine and irradiated models were assigned individual parameters to refine the bond distance, R, and Debye-Waller factors, σ^2. Global parameters for the shift in absolute energy, E_0,

and amplitude reduction factor, S_0^2, were assigned to each scattering path in the models. Degeneracies, N, were assigned based upon the crystallographic models [6], [13], [44]. Fitting ranges in R-space were selected to model the major contributions in the Fourier transform, up to 5 Å, and the fitting range used in k-space between 8.5 to 9.5 $Å^{-1}$. Bond valence sums (BVS) were calculated using methods previously established to determine the reliability of models [45].

3. Results and discussions

3.1 Pre-irradiation solid-state characterisation

The samples used in this study had been previously synthesised and characterised by both XRD, SEM coupled with energy dispersive X-ray analysis, and XAS. In short, the results show single phase products were produced and that the long- and short-range order of Gd_2TiO_5 and Dy_2TiO_5 were well described by an orthorhombic *Pnma* and hexagonal *$P6_3/mmc$* structure, respectively. Single phase Yb_2TiO_5 was also fabricated with an apparent long-range order indexable in a *Fm-3m* space group, however the short-range order was more complex. XAS studies of the local structure of Yb_2TiO_5 was well described by a structural model based on a *Fd-3m* pyrochlore structure, where Ti is found to be in a 5-fold coordination environment. A full discussion of the long-range and short-range order, as determined *via* XAS, can be found elsewhere [17], [36]. These compounds were selected to be representative of the three crystal structures associated with Ln_2TiO_5 stuffed pyrochlores, facilitating a direct comparison of the effect different crystal structures will have radiation response.

The microstructure of samples was examined after sintering using SEM. Due to the refractory nature of these materials, multiple sintering treatments were necessary to achieve a sufficiently dense product required for ion-irradiation and GAXAS studies. For reference, a representative example of the microstructures and densification of Ln_2TiO_5 (Ln = Gd, Dy, Yb) can be found in Figure 1 after initial and subsequent sintering treatment of Yb_2TiO_5, along with the polished product and its final state. The homogenous greyscale is indicative of a homogenous distribution of elements. Dark regions in the images are pores and the small pits seen in Figure 1d are areas of grain pull-out, which occurred during the grinding and polishing processes, but otherwise Figure 1d shows that densification has been achieved. XRD patterns in Figure 1e were taken from the polished surfaces of the bulk monoliths. It is clear from the XRD data that the surface regions of the samples are comprised of the intended crystal phases. Near theoretical density was achieved for all samples (between 91 – 96 %). Subsequent sintering treatments did not improve density by a significant margin. Bulk density measurements using the Archimedes method can be found in the Supplementary Information (Section S2, Table S2). Furthermore, it is evident that multiple sintering treatments, at high temperatures, are necessary to achieve dense, single-phase ceramics. Whilst this would not preclude Ln_2TiO_5 stuffed pyrochlores from being used to host radioactive wastes, the high energy input to reach and sustain these high temperatures, both during synthesis and sintering, should be considered in their application. Other synthesis methods may yield beneficial results such as hot isostatic pressing (HIP) or spark plasma

sintering (SPS), which have demonstrated previously to form highly dense ceramics at lower temperatures or more rapidly [46], [47].

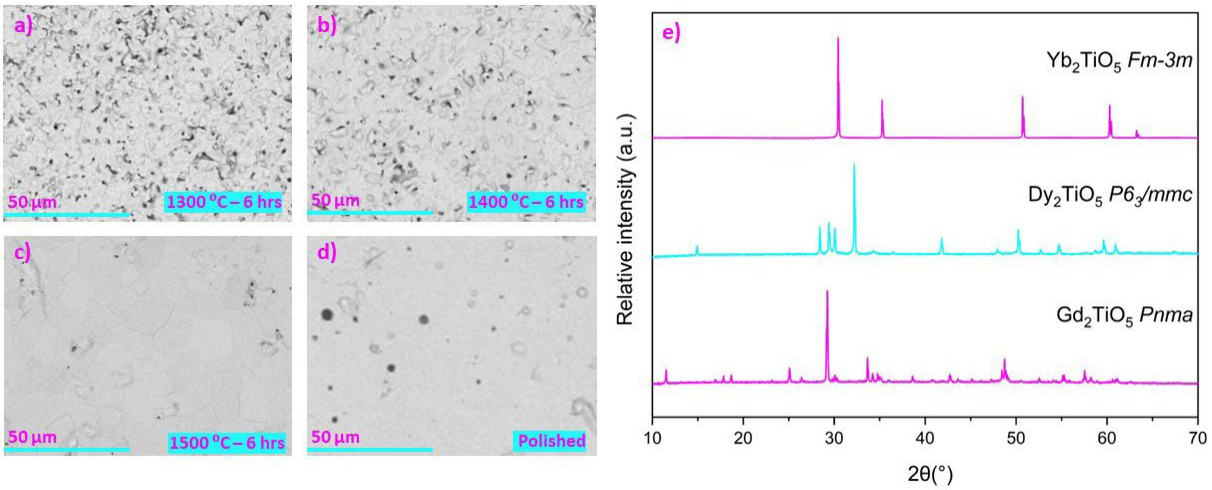

Figure 1: Back-scattered electron images of Yb_2TiO_5 after a) initial sintering at 1300 °C for 6 hours; b) additional sintering at 1400 °C for 6 hours; c) a final sintering at 1500 °C for 6 hours; and d) the polished surface of Yb_2TiO_5 after densification. Also shown, e) the crystal structures measured by XRD taken from the surface of polished Gd_2TiO_5 (*Pnma*), Dy_2TiO_5 (*P6₃/mmc*) and Yb_2TiO_5 (*Fm-3m*).

3.2 Post-irradiation solid-state characterisation

GAXRD was used to examine the changes in structure post-irradiation (Figure 2). GAXRD data of irradiated Yb_2TiO_5, which adopted a cubic *Fm-3m* structure, showed signs of amorphisation across all depths but a majority of the crystalline phase was retained as indicated by the presence of the main (111) peak visible across all depths for both ion irradiation conditions, equivalent to a maximum dose of 8.5 and 4.5 dpa from Kr or Au ion irradiations, respectively. There does appear to be some asymmetry in the peak profile of the (111) peak of Yb_2TiO_5 suggesting significant distortions of the crystal lattice such as an increase in lattice parameters. This asymmetry is not as pronounced in the less intense (200) peak. These results are in agreement with those of *Yang et al.* where the crystalline phase was found to remain intact in the related cubic Lu_2TiO_5 after irradiation under 2.7 MeV Ar ions over a range of fluences, up to a maximum of 8×10^{14} ions cm^{-2}, as also probed *via* GAXRD.

Similarly, orthorhombic Gd_2TiO_5 (Figure 2) also showed little evidence of amorphisation under both ion irradiation conditions, though there is slight diffuse scattering occurring in the regions between 25 – 35 2θ of data measured at an incident X-ray angle of 1°, corresponding to a depth of ~100 nm, for Gd_2TiO_5 irradiated under 5 MeV Au^{2+} ions. Diffuse scattering is an indication of the loss of long-range order but given the intensity of the remaining (210) peak it is clear that the majority of the crystal structure remained crystalline. Studies of related orthorhombic Dy_2TiO_5 by *Aughterson et al.* likewise found that the main (210) peak remained after irradiation by 12 MeV ions (fluences between 1×10^{13} – 2.5×10^{14} ions cm^{-2}) [7].

The hexagonal Dy_2TiO_5, performed more poorly given the significant diffuse scattering observed. GAXRD measurements at 1°, corresponding to a depth ~100 nm, are devoid of any crystalline peaks (Figure 2). Measurements at higher angles (which allow for deeper penetration depth) do retain crystal peaks associated with the most intense reflections (012) but remain significantly damaged. This is expected given that hexagonal Ln_2TiO_5 stuffed pyrochlores have been reported to be significantly more susceptible to radiation damage induced amorphisation in literature [6], [19], [48].

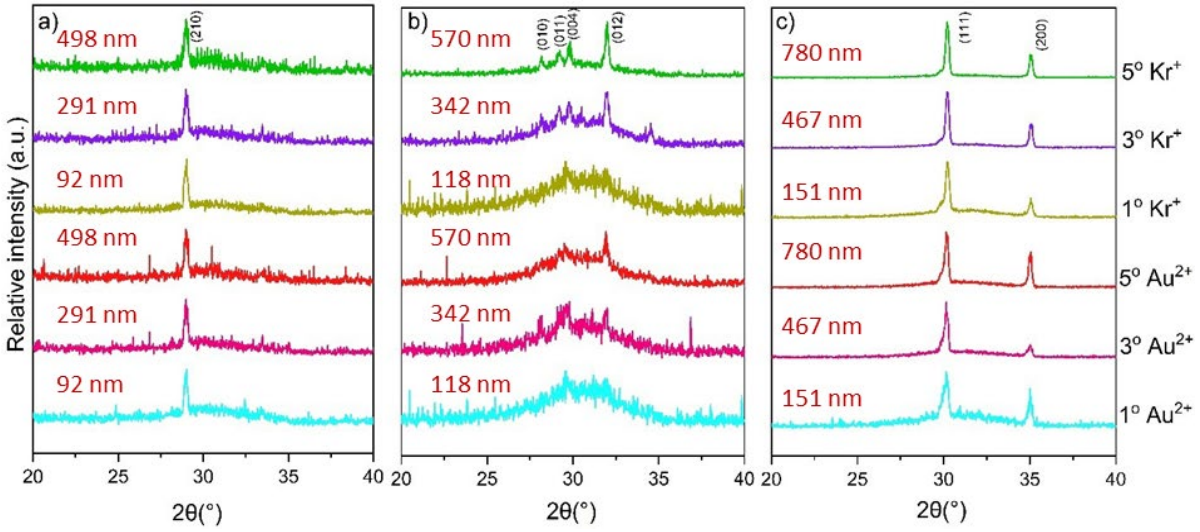

Figure 2: GAXRD data of a) Gd_2TiO_5, b) Dy_2TiO_5 and, c) Yb_2TiO_5 stuffed pyrochlores irradiated under 1 MeV Kr^+ ions with a fluence of 5 x 10^{15} and 5 MeV Au^{2+} with a fluence of 1.2 x 10^{15} ions cm^{-2}. The penetration depth of the incident X-rays (8040 eV) are shown in red. Major reflections of Gd_2TiO_5, Dy_2TiO_5 and Yb_2TiO_5 are indexed in the orthorhombic *Pnma*, hexagonal *P6₃/mmc* and cubic *Fm-3m* space groups, respectively [13], [14].

3.3 Short-range structure analysis

3.3.1 XANES analysis of Gd, Dy, Yb L_3-edges and Ti K-edges

Figure 3 shows a comparison of the normalised XANES spectra collected in GA mode at the Ln L_3-edges and Ti K- edges of the samples. Features A and C in Figure 3 highlight regions where a dampening in the oscillations (~30 and 20 eV after the white line, respectively) of the Ln L_3- and Ti K-edge spectra is apparent in radiation damaged samples. This is particularly pronounced in the Ln L_3-edge spectra for Gd_2TiO_5, but does occur to some degree across the entire series of crystal structures. The dampening in oscillations is likely an indication of an increase in disorder (i.e. changes in bond length) of the nearest neighbour and next-nearest neighbour bonds [49]. These changes are commonly observed where long- and medium-order has been lost but may also be indicators of a loss of short-range order or a phase transition into a less ordered structure [32], [50]. Radiation damage induced phase transitions have been observed in the related $Ln_2Ti_2O_7$ pyrochlore structure, for instance, where the

pyrochlore *Fd-3m* transitions into the less ordered fluorite *Fm-3m* structure [32], [51]. Changes in the short-range order, either to a disordered or amorphous phase, can be further examined by quantitative analysis of the Ti K-edge pre-edge feature, which can yield information regarding the local coordination environment and symmetry of Ti cations post-irradiation [42], [50].

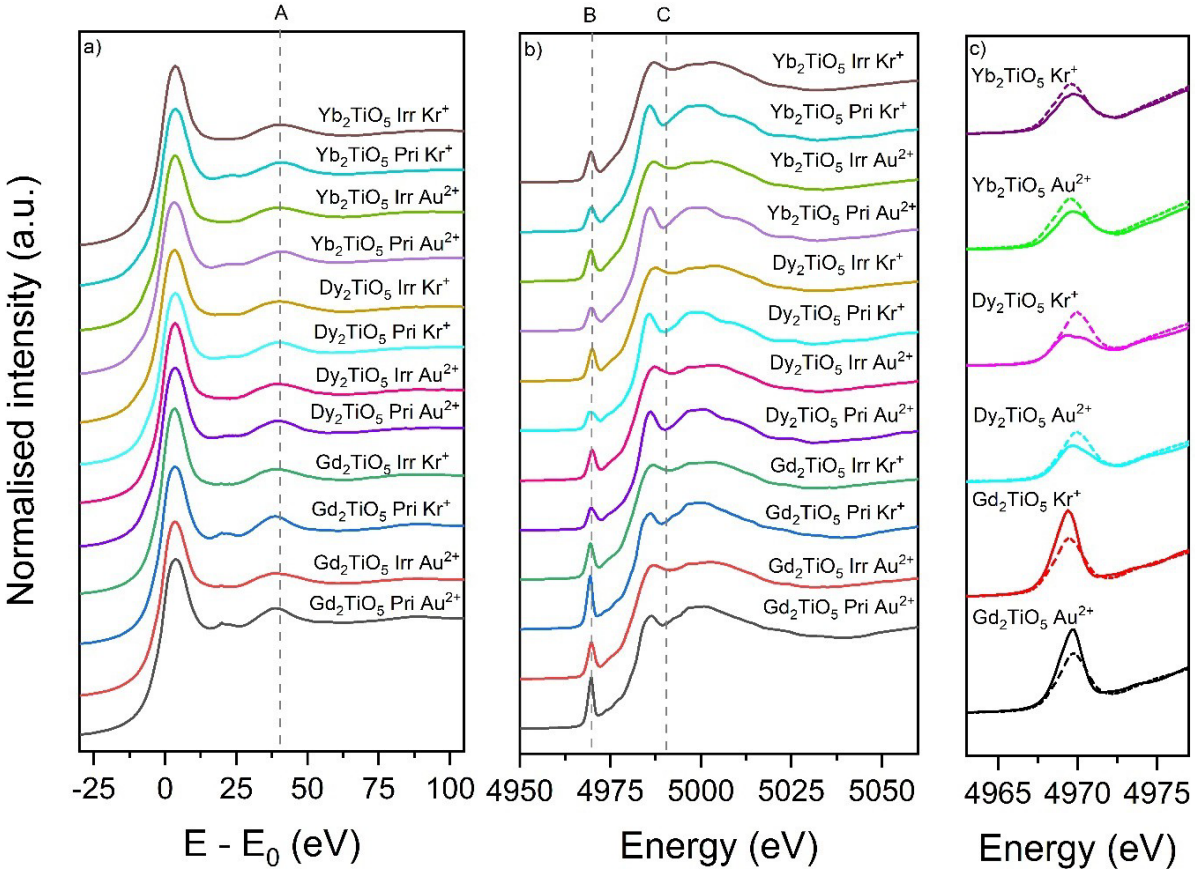

Figure 3: a) Normalised Ln L_3-edge XANES spectra of pristine (Pri) and irradiated (Irr) Ln_2TiO_5 (Ln = Gd, Dy, Yb) irradiated by 1 MeV Kr^+ and 5 MeV Au^{2+} ions, all spectra are shifted to their corresponding E_0 positions to aid comparisons; b) normalised Ti K-edge XANES spectra of Ln_2TiO_5 (Ln = Gd, Dy, Yb). Labels A, B and C, as well as dashed lines, are included to highlight key features and guide the eye; c) an enhanced view of the pre-edge feature, dashed lines are of spectra collected on irradiated samples and solid lines are of spectra collected on pristine samples.

The profile and position of the pre-edge feature (labelled B, in Figure 3a) are both a consequence of electron transitions from the *1s* energy level in the core Ti atoms to hybridised Ti *3d* / O *2p* molecular orbitals. Diagnostic information, regarding the coordination number and symmetry of the Ti cations, was obtained by deconvoluting the region between 4965 – 5040 eV into a step-like arctangent function and a set of Gaussians components using previously established methodologies [36], [42], [52]. The arctangent function was used to model the photoelectric edge step that represents the transition of ejected photoelectrons into the continuum and Gaussian components were used to model the pre-edge features (located ca. 20 eV before the crest on the absorption edge) [53].

Depending upon the degree of *d-p* orbital mixing, the height of the pre-edge feature will vary, relating to changes in centro-symmetry. The position of the pre-edge is further indicative of coordination number.

The results of the quantitative analysis of the pre-edge feature of the Ti K-edge XAS data are interpreted graphically in Figure 4. The pre-edge position and normalised height of spectra collected on pristine samples in both a standard geometry and glancing angle geometry are consistent with each other, for all chemistries. Interpretations of Figure 4 indicate that there have been changes regarding the coordination environment of Ti. The normalised height of the pre-edge features of all irradiated samples are remarkably consistent with each other, possibly indicating that after sufficient disordering there is little difference in Ti site-symmetry of Ln_2TiO_5 compounds. However, this observation is taken in isolation of the changes in pre-edge position, which can give further information with respects to the Ti-O coordination. Under both irradiation conditions, the pre-edge position of irradiated Gd_2TiO_5 had shifted to a region that has been related to either mixed 5- and 6-fold coordination, based on measurements of mechanical mixtures of compounds containing TiO_5 and TiO_6 polyhedra [23], [50]. This region could also be associated with a TiO_5 trigonal bipyramidal geometry, however, the slight broadening apparent in the pre-edge feature of Gd_2TiO_5 (Figure 3c) has been associated with mixed Ti coordination [43]. As both scenarios are plausible, based on these results, further investigation *via* EXAFS analysis will aid in the interpretation. The pre-edge position and profile of pristine cubic Yb_2TiO_5 has been closely related to a TiO_5 trigonal bipyramid previously [17]. An increase in the normalised pre-edge height and shift to lower energy can be observed for irradiated Yb_2TiO_5 samples (Figure 4). This appears to suggest a transition from a nominally 5-fold coordination in the pristine samples, towards a slightly lower coordination approaching 4-fold in the irradiated samples. The pre-edge position of hexagonal Dy_2TiO_5 remains consistent between the pristine and irradiated samples, however there is a noticeable increase in normalised height of irradiated Dy_2TiO_5 pre-edge features. As the degree of *d-p* orbital mixing is reflected in the intensity of the pre-edge feature, a change in normalised height can reflect a change in centrosymmetry of the Ti cations [50], [52]. The increased normalised height of Ti cations in Dy_2TiO_5 may well reflect a decrease in the centrosymmetry of the Ti coordination site, and as such an increase in disorder.

Whilst there are clear changes to the Ti coordination environment, it is difficult to say with confidence what the exact nature of the changes are. Further investigation of the Ti coordination environment, along with that of the Ln, through EXAFS analysis will be able to yield further information about the local structural properties (such as bond length, average coordination number, changes in short- and medium-range order etc.) of irradiated Ln_2TiO_5 stuffed pyrochlores.

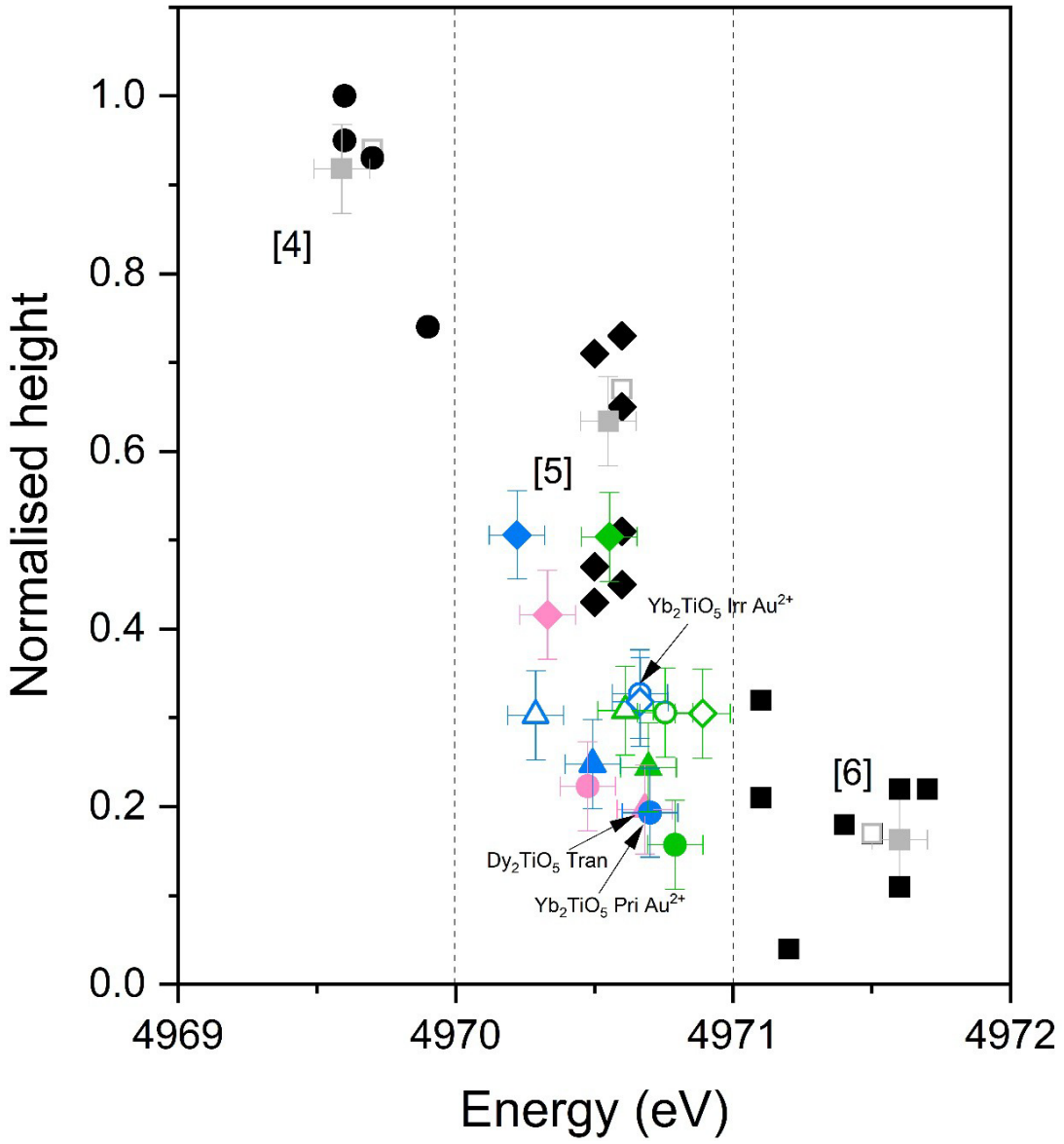

Figure 4: Ti coordination environment of irradiated and pristine Ln_2TiO_5 samples as specified by pre-edge energy position and normalised height of pre-edge feature in Ti K-edge XANES. Black solid squares show data for 6-fold coordination standards from previous studies; solid diamonds show data for 5-fold coordination standards and solid black circles show 4-fold coordination standards from previous studies [42]. Data points in solid grey circles represent standards. Going from right to left are: anatase (4971.6 eV), fresnoite (4970.5 eV) and $Ni_{2.6}Ti_{0.7}O_4$ (4969.6 eV), data points outlined in grey are the corresponding standards collected from previous studies. The diamond shapes represent Gd_2TiO_5, triangles represent Dy_2TiO_5 and circles Yb_2TiO_5. Solid pink colours refer to data collected in transmission mode, shapes with a solid or outlined green colour are pristine and corresponding 1MeV Kr^+ irradiated samples measured at the same depth (300 nm) and, shapes with a solid or outlined blue colour are pristine and corresponding 5 MeV Au^{2+} irradiated samples measured at the same depth (700 nm). Regions associated with 4-, 5- and 6-fold coordination polyhedra are labelled [4], [5] and [6], respectively.

3.3.2 EXAFS analysis of Gd, Dy, Yb L_3-edges and Ti K-edges

Quantitative analysis of the EXAFS region of spectra was undertaken to provide detailed models of the structural coordination around the central absorbing atom (Ln or Ti for each sample) of orthorhombic Gd_2TiO_5, hexagonal Dy_2TiO_5, and cubic Yb_2TiO_5. In order to extract information regarding the coordination number of the central absorbing atom, referred to as the degeneracy, N, of irradiated Ln_2TiO_5 stuffed pyrochlores the amplitude reduction factor, S_0^2, must remain fixed, as the N and S^2 parameters are directly correlated with one another. This was achieved by fitting models of pristine Ln_2TiO_5 samples, measured in glancing-angle geometries, as the S_0^2 parameter is transferable between chemically and structurally similar compounds. The pristine models were established based on previously established methodologies [17], [36], and were also fit alongside XAS data of pristine samples measured in a standard XAS geometry to ensure that the data and fitting results are consistent. A standard geometry refers to measurements of Ln L_3-edge spectra in transmission mode and/or measurements of the Ti K-edge in fluorescent mode, where the detector is 45° from the sample. Due to the limited data ranges of glancing-angle measurements, data were fit up to 9 $Å^{-1}$ in k-space, compared to 11 $Å^{-1}$ for samples measured in a standard geometry. In order to satisfactorily fit the Fourier transform k^3 χ(k) spectral envelope of pristine samples measured in a GA mode, certain paths/variables needed to be sensibly grouped together to minimise the amount of variables in the model, given the reduced independent points. The pristine Ln_2TiO_5 models, collected in both geometries, gave satisfactory fits with sensible R-factors. The refined bond distances, R, and calculated BVS values are broadly consistent between the two measurement modes in addition to previously published results [17], [36]. This gives confidence in applying the refined S_0^2 value in irradiated models.

The results of the EXAFS modelling for samples irradiated under 1 MeV Kr^+ and 5 MeV Au^{2+} were consistent with each other and little to no deviation in results were found. As such the results discussed below will be in the context of samples irradiated by 5 MeV Au^{2+} ions and the results of the 1 MeV Kr^+ ion irradiations can be found in the Supplementary Information (Section S3). The discussion that follows is applicable to both ion irradiation scenarios.

3.3.2.1 Gd_2TiO_5 EXAFS

EXAFS models of both the Gd L_3-edge and Ti K-edge afforded good fits, with R-factors between 1.9 % and 3.1 %, respectively. The refined parameters can be found in Table 1 and the theoretical fits to the experimental data in Figure 5. As can be seen in Figure 5, there is a significant loss of signal after irradiation of data measured at both elemental edges. This is typical of a loss of medium-range order (>2.5 Å in the Fourier transforms) due the disordering effects of heavy-ion irradiation. Refinements of the Ti-O coordination number (N) and bond distance (R) of nearest-neighbour oxygen atoms indicate slight increases from those of the pristine model, equating to a bond lengthening of 1.91 ± 0.01 to 1.95 ± 0.01 Å and average coordination number change from 5 to 5.5 ± 0.9. The refined N and R parameters of the Gd-O path, however, demonstrated a decrease in both properties. Specifically, a

2.37 ± 0.01 to 2.32 ± 0.02 Å bond length contraction and average coordination number decrease from 7 to 6.5 ± 0.9. Whilst the errors associated with the refined N values are considerably large, due to the limited data ranges in both R and k-spaces the data were fit over, the BVS for both Ti-O and Gd-O give confidence in the results as the BVS calculation is independent of the model and takes into consideration the bond lengths of coordinating anions (which is influenced by coordination number), where the error is considerably smaller. Fitting this same model with an N of 7 yielded unreasonably higher BVS (i.e., 3.51 v.u.). As the intensity of the EXAFS signal is not dependent on the bond distance of scattering pairs, any changes in distance are not a consequence of the distortions to the EXAFS signal intensity that are a product of the glancing-angle measurement geometry. This allows for bond distance, and hence calculated BVS, to be an effective means to evaluate changes in coordination independent of measurement geometry and corroborate any refined coordination numbers. Both BVS were calculated to be within 10% of the formal valence's of the absorber atoms (Ti = 4 valence units (v.u.) and Gd = 3.0 v.u.), indicating good agreement between the refined coordination numbers and bond lengths for irradiated models.

The increase in observed coordination number of Ti could be an indication of a mixed TiO_5 and TiO_6 species, a refined coordination number of 5.4 and Ti-O bond distance of 1.94 Å is consistent with a presence of around 40 % TiO_6 species, based upon published Ti-O bond distances of $Gd_2Ti_2O_7$ where Ti is found in a 6-fold coordination [31]. This finding is in agreement with the XANES analysis of the Ti K-edge of radiation damaged Gd_2TiO_5, where the pre-edge feature intensity and position were consistent with mixed TiO_5 / TiO_6 species. Given the decrease in Gd-O bond length from 2.37 to 2.33 Å, which corresponds to a decrease in coordination number (from 7 to 6.6), could suggest a certain atomic rearrangement occurs where both cation degeneracies are moving towards a common 6-fold coordination. Though analysis of short-range ordering of radiation damaged orthorhombic Ln_2TiO_5 under similar conditions is limited in literature, there is some suggestion that a defect-fluorite transition can occur. The defect-fluorite structure is characterised by having complete A- and B-site cation disordering with average 7-fold coordination. *Zhang et al.* reported that the selected area electron diffraction (SAED) of irradiated Gd_2TiO_5 showed diffraction maxima associated with the defect-fluorite *Fm-3m* symmetry [54]. However, *Aughterson et al.* indicated that the SAED were interpreted incorrectly due to a lack of a ring pattern (which would indicate misalignment of nano-domains one would expect) and that whilst the weaker diffraction maxima could be lost in the amorphous contributions, stronger ones still be evident [7]. Furthermore, the GAXRD results of radiation damaged Gd_2TiO_5 in this study show no indication of reflections that are associated with defect-fluorite symmetry but as XRD is more sensitive to long-range order compared to techniques such as SAED and XAS, it would not preclude a short-range order transition with resemblance to cubic ordering. Investigations of atomic ordering in related A_3BO_7 (where A = Ln and B = Os, Re, Ru, Re, Mo, Ir, Sb, Nb or Ta) compounds have also shown the coexistence of long-range orthorhombic symmetries with short-range cubic ordering [55], [56]. Therefore, a possible explanation for the radiation response of Gd_2TiO_5 could be the formation of a 'defect-fluorite-like' structure, where the A- and B-site cations become partially disordered, followed by a complete disordering after increased dosage. This

interpretation would explain the variation in observed GAXRD and SAED studies of Gd_2TiO_5. As both the pristine and irradiated samples were measured at room temperature the changes in the Debye-Waller factor (σ^2), which is nominally a measure of thermal and static disorder, of irradiated Gd_2TiO_5 is assumed to be due to changes in physical disorder rather than thermal effects. Therefore, the increase in σ^2 values from 0.005 to 0.017 $Å^2$ and 0.003 to 0.008 $Å^2$ for Gd-O and Ti-O paths, respectively, provides additional evidence of a more disordered nearest neighbour configuration. Increases in disorder parameters are also likely to be observed in defect-fluorite *Fm-3m* compounds as the orthorhombic *Pnma* structure is comparatively more ordered.

The results of the EXAFS and XANES analysis showing a possible common 6-fold coordination between Gd and Ti would also give further reasoning behind the apparent increased radiation resistance of Ln_2TiO_5 compounds that adopt orthorhombic symmetries. It has been previously reported that the radiation tolerance of Ln_2TiO_5 is dependent upon the size of the Ln ionic radius, with smaller Ln cations showing the most improved response (i.e., Gd – La) [7]. Though not fully understood, highly disordered structures, such as defect-fluorite, have been shown to have enhanced radiation tolerances due to comparatively higher defect mobilities, therefore a transition from orthorhombic to defect-fluorite-like structure (where there is A- and B-site cation mixing) could offer a route to understand this phenomenon [8], [19]. Computations of the anti-site defect formation energies of orthorhombic Ln_2TiO_5 have suggested that this defect mechanism plays a significant role in the radiation tolerance of these compounds. The orthorhombic Ln_2TiO_5 structure is characterised as having two distinct Ln-sites (Ln_1 and Ln_2) and given that the Ln_2-Ti anti-site defect formation is the most energetically favourable (compared to Ln_1-Ti), it is possible to extrapolate from the EXAFS results of the Gd L_3-edge and Ti K-edge that there may be a split or uneven distribution of Ln-Ti anti-site defects, with a preference for the Ln_2-Ti site. This would leave the Ln_1O polyhedra remain largely 7-fold coordinated.

Another interpretation of the EXAFS results is the possibility that the short-range orthorhombic structuring remains intact, albeit in a disordered state, as seen in the swift heavy-ion irradiation of orthorhombic Dy_2TiO_5 analysed through neutron PDF analysis [25]. This interpretation of the results could be plausible, particularly given that the error associated with the coordination numbers falls within the 5-fold and 7-fold coordination associated with the Ti- and Ln-sites of orthorhombic Ln_2TiO_5, though the changes in bond length of Gd-O and Ti-O have significantly smaller associated errors and as such are a more reliable indication changes to coordination. Whilst this observation is informative, a direct comparison is not entirely appropriate as the two irradiation methods utilise different stopping mechanics. Swift heavy-ion irradiation makes use of high energy ions (GeV range) where the damage mechanics are dominated by interactions between electrons, emulating the fragments from fission events, which interact primarily with the electrons within a material compared to the ion irradiations in this experiment where nuclear interactions are more present (to simulate the effects of alpha-recoil damage from decaying radioactive nuclei). Furthermore, the results of the Ti pre-edge fitting of irradiated Gd_2TiO_5 suggest change in coordination where Ti is found in a mixed 5- and 6-fold coordination. This agrees with the EXAFS results that show that the structure is transitioning towards a structure with slightly higher Ti coordination environments (5.5).

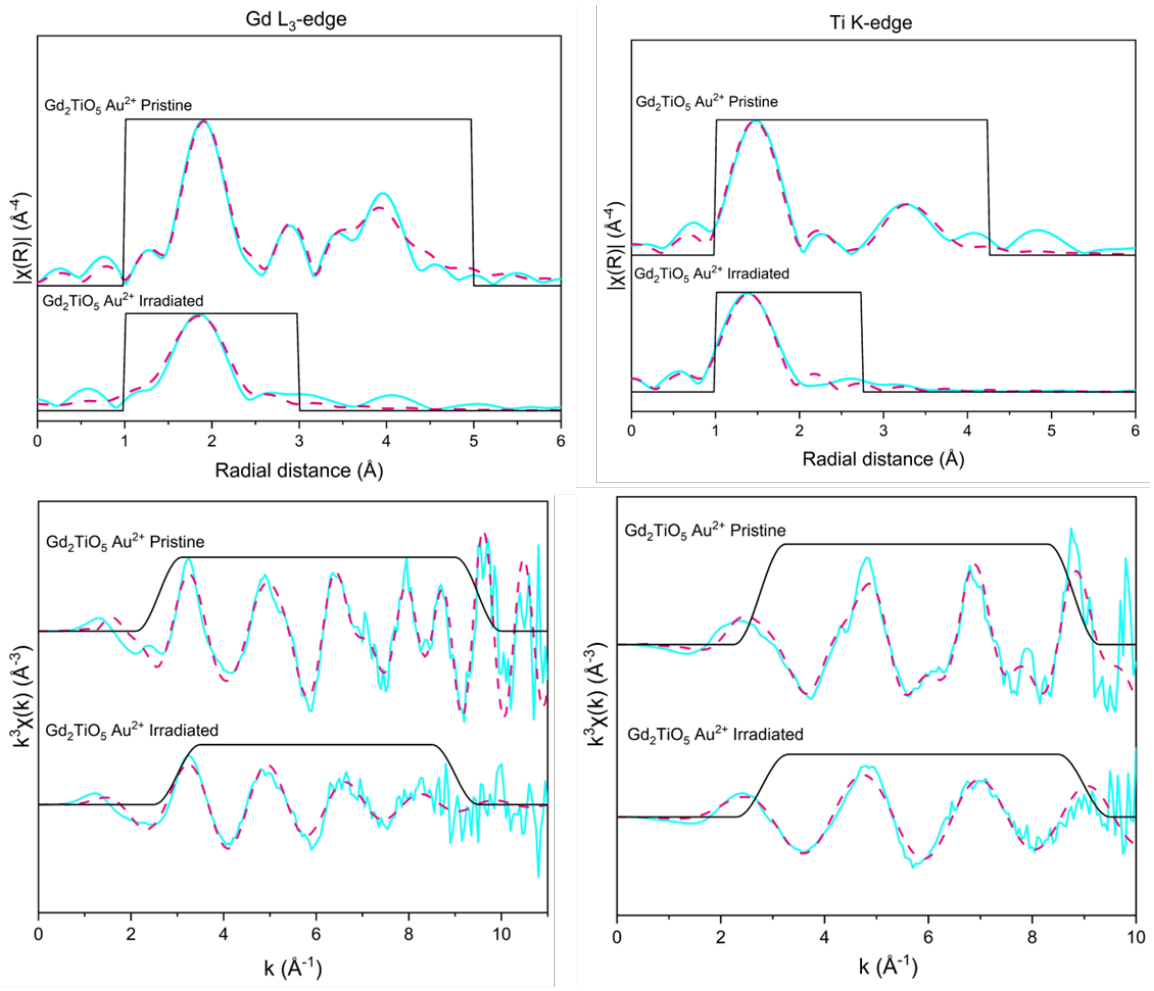

Figure 5: The top panels show fits to the Fourier transform of the waveform in R-space of pristine and irradiated Gd_2TiO_5 (5 MeV Au^{2+}) measured in GA mode at a depth of 700 nm. The fitting range in R was constrained to fit the first oxygen peak in the irradiated model. The k^3 weighted Gd L_3-edge and Ti K-edge waveforms are shown below. Data on the left-hand side were measured at the Gd L_3-edge, and on the right-hand side were measured at the Ti K-edge. Solid blue lines represent the experimental data, dashed pink lines represent the theoretical fit to the data and solid black lines indicate the fitting windows used.

Table 1: Refined structural parameters of pristine and irradiated Gd_2TiO_5 (5 MeV Au^{2+}) measured in GA mode at a depth of 700 nm. Also shown for comparison are models of pristine Gd_2TiO_5 measured in a standard geometry. The left-hand side shows the results of models of data from the Gd L_3-edge and the right-hand side shows the results of models of data from the Ti K-edge. The average change in the scattering path distance for a given absorber-scatterer pair is denoted as R, the Debye–Waller factor is denoted as σ^2, the number of scatters in the coordination shell is denoted as N, the amplitude reduction factor is given by the term S_0^2. A dash resents that there is no data associated with that field.

Gd L_3-edge					Ti K-edge				
Path		**Gd_2TiO_5 Tran**	**Gd_2TiO_5 Pri Au**	**Gd_2TiO_5 Irr Au**	**Path**		**Gd_2TiO_5 Tran**	**Gd_2TiO_5 Pri Au**	**Gd_2TiO_5 Irr Au**
	E_o (eV)	3.2(18)	3.6(5)	1.7(14)		*E_o (eV)*	-3.9(11)	-1.5(13)	-3.0(15)
	S_o^2	1.17	0.53(4)	0.53		*S_o^2*	0.54(9)	0.49(6)	0.49
	R (Å)	2.37(2)	2.37(1)	2.33(2)		*R (Å)*	1.91(1)	1.91(1)	1.94(1)
Gd-O(1)	*σ^2 (Å²)*	0.009(2)	0.005(2)	0.017(3)	**Ti-O**	*σ^2 (Å²)*	0.003(1)	0.003(2)	0.008(3)
	N	7	7	6.7(9)		*N*	5	5	5.4(9)
	R (Å)	3.81(3)	3.72(3)	-		*R (Å)*	3.60(6)	3.58(3)	-
Gd-Gd(1)	*σ^2 (Å²)*	0.009(4)	0.010(7)	-	**Ti-Ln(1)**	*σ^2 (Å²)*	0.008(6)	0.005(2)	-
	N	7	7	-		*N*	7	7	-
	R (Å)	4.11(8)	4.11(2)	-		*R (Å)*	3.50(5)	3.74(6)	-
Gd-Gd(2)	*σ^2 (Å²)*	0.009(3)	0.009(3)	-	**Ti-Ti**	*σ^2 (Å²)*	0.003(2)	0.011(9)	-
	N	9	9	-		*N*	2	2	-
	R (Å)	3.44(8)	3.40(1)	-	**R-factor**		0.025	0.029	0.031
Gd-Ti(1)	*σ^2 (Å²)*	0.005(4)	0.004(1)	-	**BVS (v.u.)**		3.83	3.92	3.80
	N	3	3	-					
	R (Å)	3.74(5)	3.75(1)	-					
Gd-Ti(2)	*σ^2 (Å²)*	0.004(3)	0.007(2)	-					
	N	4	4	-					
R-factor		0.022	0.010	0.019					
BVS (v.u.)		3.02	3.04	3.28					

The radiation damage response of the short-range structure of orthorhombic Gd_2TiO_5 is indicative of a transition towards a disordered defect-fluorite-like structure, where anti-site defects are the

predominate defect mechanism. This observation may be an explanation of the high radiation tolerance observed for orthorhombic Ln_2TiO_5 seen in other studies [6], [7], [19] as the system appears to undergo an order-disorder transition prior to an eventual collapse into an amorphous regime. This result is encouraging for the use of orthorhombic Ln_2TiO_5 stuffed pyrochlores as host materials for actinide wastes, as despite a loss of medium-range order at high levels of radiation the local structure retains an ordering commensurate with a disordered crystalline structure, instead of outright complete amorphisation. This means that long-term behaviour of this material in geological disposal environments can be predicted and adverse effects arising from amorphisation, such as macroscopic cracking, may not become an issue within its expected lifetime of use.

3.3.2.2 Dy_2TiO_5 EXAFS

Initial assessment of the EXAFS spectra acquired at the Dy L_3- and Ti K-edges of pristine and irradiated hexagonal Dy_2TiO_5 (Figure 6) show a clear difference in features. Whilst both the pristine and irradiated samples measured at both edges retain an initial peak (1 – 2 Å), which consists of contribution form the nearest neighbour oxygen anions, the spectral regions between 2 Å and 4 Å appear much diminished in intensity after irradiation. Similar to the Gd_2TiO_5 samples, this suggests a significant disordering of the medium-range order. Models of the irradiated Dy_2TiO_5 were fit with only a single Dy-O or Ti-O contribution and the coordination number N, Debye-Waller factor σ^2, bond distance R and E_0 were refined. The results are presented in Table 2. Good fits were obtained at both edges for irradiated samples with R-factors of approximately 3 % for both. The fitting range in R-space was extended due to Nyquist criterion, which resulted in a worse R-factor but visual inspection of Figure 6 shows the first peak is well modelled. Attempts to reasonably fit the more distant regions of waveforms were unsuccessful.

The refined Ti-O bond distance in the irradiated model was 1.86 ± 0.02 Å, a change of -0.06 Å from the pristine model. The refined Ti-O coordination of the irradiated samples was 4.3 ± 0.7, a change of 0.7 from the initial 5. The inherent precision associated with refined coordination numbers typically observed in EXAFS refinements does not preclude a 5-fold coordination of the irradiated model (at a coordination number of 4.3 ± 0.7). However, given the consistency in BVS results between the pristine and irradiated models (3.75 v.u. and 3.90 v.u., respectively) the changes in coordination number and bond length appear to be in good agreement with each other, giving clear evidence of a change in coordination. The change in coordination, bond length as well as increased σ^2 parameter (0.002 to 0.005 $Å^2$) all indicate that short-range order has been distorted. This agrees with observations of increased disorder from the pre-edge fitting Ti K-edge data. Similar observations can be made with respects to the Dy-O coordination. In this case, a decrease in both Dy-O bond distance (2.36 ± 0.02 to 2.29 ± 0.03 Å) and coordination number (7.0 ± 1.0) is observed once again. The BVS of the pristine and irradiated models were in good agreement, calculated to be 3.10 v.u. and 3.22 v.u., respectively.

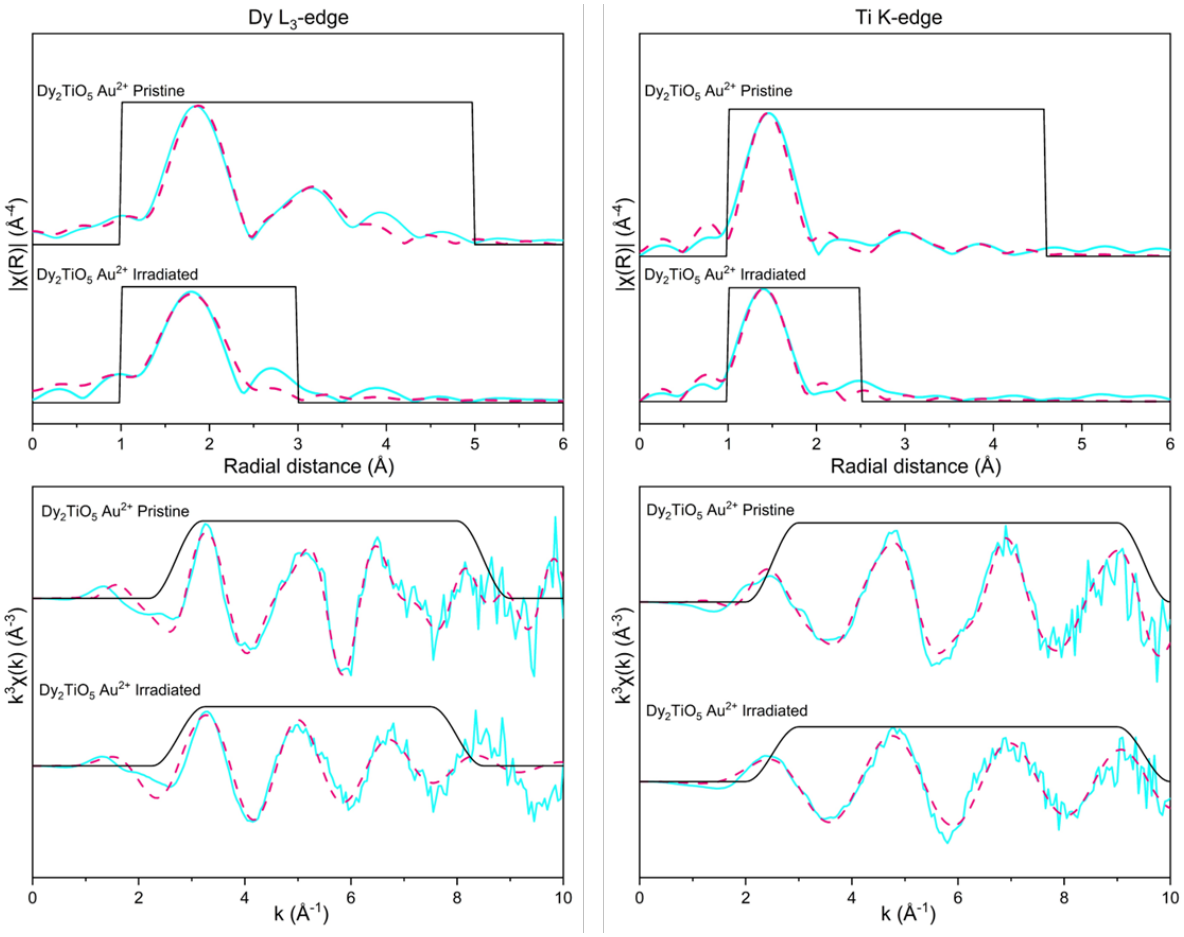

Figure 6: The top panels show fits of the Fourier transform of the waveform in R-space of pristine and irradiated Dy_2TiO_5 (5 MeV Au^{2+}) measured in GA mode at a depth of 700 nm. The k^3 weighted Dy L_3-edge and Ti K-edge waveforms are shown in the bottom panels. The fitting range in R was constrained to fit the first oxygen peak in the irradiated model. Data on the left-hand side of the image were measured at the Dy L_3-edge, and on the right-hand side they were measured at the Ti K-edge. Solid blue lines represent the experimental data, dashed pink lines represent the theoretical fit to the data and solid black lines indicate the fitting windows used.

Table 2: Refined structural parameters of pristine and irradiated Dy_2TiO_5 (5 MeV Au^{2+}) measured in GA mode at a depth of 700 nm. Also shown for comparison are models of pristine Dy_2TiO_5 measured in a standard geometry. The left-hand side shows the results of models of data from the Dy L_3-edge and the right-hand side shows the results of models of data from the Ti K-edge. The average change in the scattering path distance for a given absorber-scatterer pair is denoted as R, the Debye–Waller factor is denoted as σ^2, the number of scatters in the coordination shell is denoted as N, the amplitude reduction factor is given by the term S_0^2. A dash resents that there is no data associated with that field.

Dy L_3-egde					Ti K-edge				
Path		**Dy_2TiO_5 Tran**	**Dy_2TiO_5 Pri Au**	**Dy_2TiO_5 Irr Au**	**Path**		**Dy_2TiO_5 Fluo**	**Dy_2TiO_5 Pri Au**	**Dy_2TiO_5 Irr Au**
	E_o (eV)	5.6(11)	3.2(13)	3.1(5)		*E_o (eV)*	-3.9(11)	-2.0(11)	-4.0(18)
	S_o^2	1.06	0.56(9)	0.53		*S_o^2*	0.54(9)	0.48(5)	0.48
	R (Å)	2.32(1)	2.36(2)	2.29(3)		*R (Å)*	1.91(1)	1.92(1)	1.86(2)
Dy-O(1)	*σ^2 (Å²)*	0.009(1)	0.013(3)	0.018(5)	**Ti-O**	*σ^2 (Å²)*	0.003(1)	0.002(1)	0.005(2)
	N	6	8	7.0(10)		*N*	5	5	4.3(7)
	R (Å)	2.56(4)	-	-		*R (Å)*	3.60(6)	3.66(21)	
Dy-O(2)	*σ^2 (Å²)*	0.011(5)	-	-	**Ti-Dy(1)**	*σ^2 (Å²)*	0.008(6)	0.015(10)	
	N	2	-	-		*N*	6	6	
	R (Å)	3.46(3)	3.46(6)	-		*R (Å)*	3.50(5)	3.46(6)	
Dy-Dy(1)	*σ^2 (Å²)*	0.013(3)	0.008(7)	-	**Ti-Dy(2)**	*σ^2 (Å²)*	0.003(2)	0.008(7)	
	N	6	6	-		*N*	2	2	
	R (Å)	3.70(3)	3.66(13)	-		*R (Å)*	3.32(8)	3.44(8)	
Dy-Dy(2)	*σ^2 (Å²)*	0.013(3)	0.015(6)	-	**Ti-Ti**	*σ^2 (Å²)*	0.004(2)	0.015(6)	
	N	2	2	-		*N*	4	4	
	R (Å)	3.46(3)	3.44(8)	-	**R-factor**		0.025	0.024	0.035
Dy-Ti	*σ^2 (Å²)*	0.020(3)	0.020(15)	-	**BVS (v.u.)**		3.83	3.75	3.90
	N	4	4	-					
R-factor		0.015	0.021	0.022					
BVS (v.u.)		2.97	3.10	3.22					

Taken completely, the EXAFS results for both Dy L_3- and Ti K-edges indicate a significantly disorder material, this observation is consistent with the GAXRD results in addition to reports in literature regarding the poor radiation tolerance of hexagonal Ln_2TiO_5 polymorphs compared to cubic and orthorhombic stuffed pyrochlores [6], [48]. Given the polymorphic nature of Dy_2TiO_5, attempts to synthesise Dy_2TiO_5 in alternate crystal structures should be made if intended for use within

environments where the compound would be exposed to high intensity radiation fields, such as an inclusion as a burnable poison in nuclear reactor control rods. A high temperature cubic polymorph of Dy_2TiO_5 has been reported to be achieved *via* the use of arc-melting and rapid quenching or the addition of an MoO_3 flux, which produced a near single-phase cubic Dy_2TiO_5 in addition to cubic $Dy_2Ti_2O_7$ [57], [58]. Where a relatively simple synthesis route is desired, the orthorhombic *Pnma* Dy_2TiO_5 polymorph, where standard solid-state synthesis methods can yield single-phase orthorhombic ceramic products, would be an ideal candidate for general application within the nuclear industry given the higher degree of radiation tolerance (as seen in the related orthorhombic Gd_2TiO_5 stuffed pyrochlore as well as literature [6], [7]).

3.3.2.3 Yb_2TiO_5 EXAFS

The models of pristine and irradiated Yb_2TiO_5 were based on structures previously established through EXAFS analysis, where the local-ordering can be described as pyrochlore-like with *Fd-3m* symmetry but with a reduced Ti coordination (5 to 6) [17]. Single scattering paths included in the fits were each generally assigned individual parameters to refine the bond distances, R, and Debye-Waller factor, σ^2 (the Yb-O(1) and Yb-O(2) shared a common σ^2 in pristine models). Global parameters, E_0 and S_n^2, were assigned to each path. The refined S_n^2 parameters of the pristine models of Yb_2TiO measured in a glancing-angle geometry (0.57 and 0.50 for EXAFS models of the Yb L_3-edge and Ti K-edge, respectively) were used as a fixed variable to model the EXAFS of the irradiated sample to allow for the coordination, N, of the absorber atom to be refined and to fit more distant contributions to the Fourier transform.

Attempts to fit the first O peak of Ti K-edge EXAFS spectra yielded good fits based upon the R-factors (2.5 %), however the Yb L_3-edge fit had a slightly higher R-factor than might be expected (4.1%). The results of these fits are found in Table 3 and Figure 7. The refined Yb-O coordination number post irradiation, based upon these models, was 7.0 ± 1.1 with bond distance of 2.29 ± 0.06 Å. Both these properties decreased from the ideal pristine structure where Yb-O is 8-fold coordinated with an average bond distance of 2.37 Å. The BVS determined for both the pristine and irradiated models were within 6.5 % and 7.5 % of the formal valence of Yb (3 v.u.), respectively. Based upon the calculated BVS, the Yb-O bond distances refined in the model are satisfactory, however the error associated with the irradiated Yb-O bond distance (± 0.06 Å) is considerably large and would possibly allow for a higher coordination number. The Ti-O bond distance and coordination numbers showed very little change, remaining consistent with both models of the Ti K-edge measured in standard and glancing-angle geometry (1.91 ± 0.0 Å and 5.29 ± 0.10, respectively). A 5-fold Ti coordination is also consistent with the results of the pre-edge fitting. The refined bond distance is consistent with a 5-fold coordination and, taken within error, the refined coordination is in agreement with the bond length. A 7-fold and 5-fold Ln and Ti coordination is similar to what is observed for orthorhombic Ln_2TiO_5 compounds, however this structure is more highly ordered than the cubic structure associated with Yb_2TiO_5, as such a disorder-order transition is suggested. However, this is unlikely due to the disordering effect

ion-irradiation has on a crystal lattice, the expected transition would be the inverse (i.e., order-disorder). Based on this discrepancy further examination of the model was needed. Inspection of the theoretical fits to the experimental data of irradiated Yb_2TiO_5 (Figure 7) appear to show the fit does not quite match the intensity of the first O peak of the Yb L_3-edge data. The amplitude of the model fit to the Fourier transform of the experimental data is dependent upon the Debye-Waller factor, σ^2, amplitude reduction factor, S_0^2, and degeneracy, N, used in the model. As the S^2 parameter used in the irradiated model was obtained from fitting the pristine model, its use in this model is valid. Therefore, the intensity mismatch between theoretical fit and the experimental data is likely due to either an inaccurate representation of the oxygen degeneracy or an over estimation of the σ^2 value. An excessively large σ^2 can be produced when there is significant disorder in the coordination shell the scattering path is representing which cannot be accounted for solely by a path length variation parameter such as σ^2.

Based on these observations, further consideration was given to the Yb-O path configuration. In pristine models two Yb-O scattering paths, one short with a degeneracy of 2 and one long with a degeneracy of 6, are needed to satisfactory fit the first O peak. Attempts to fit this shell in pristine models with one path with a total degeneracy of 8 returns high BVS values (3.8 v.u.) and bond lengths of 2.24 Å. An 8-fold coordination would be expected to have longer Yb-O bond distances of around 2.35 Å, in order for the calculated BVS to satisfy a 3 v.u. The requirement of *Fd-3m* structured compounds to have 2 Ln-O paths has been related to the significant distortion of the coordination environment of Ln cations [59]. Due to the limited data range, models where two paths were included and the N of each was refined produced a model with very large physical errors with the overall fit was of poor quality. A model of the irradiated Yb_2TiO_5 Yb L_3-edge data was subsequently produced that fixed the N of both Yb-O paths to 2 and 6, respectively. This gave a good fit with a lower R-factor (1.6 %) and sensible BVS (2.93 v.u.). The higher σ^2 values produced in for this model, compared to the pristine, further indicate an increase in the static disorder of the Yb-O coordination environment as a consequence of irradiation. This also managed to account for the deficit in intensity of the apparent in the theoretical fit to the first Yb-O peak (Figure 7). The tabulated results of this model can be found in Table 3. Moreover, this would reconcile with the large associated bond length error (± 0.06 Å) of the Yb-O bond in the simple model where only one oxygen contribution was fit as the average bond length of the two-oxygen contribution model (2.32 Å) falls within this margin. Based upon the results of this model, and the deficiencies of the one oxygen path model, it would appear that the immediate Yb-O coordination retains the 8-fold coordination of the pristine structure, albeit with significant distortions.

The medium-range (2 – 4 Å) order present in the Fourier transforms of the irradiated Yb_2TiO_5 for both the Yb L_3- and Ti -Kedge appear to have a much-reduced signal intensity but retain the general features seen in the pristine models. As the signal intensity is directly related to the degeneracy of the paths that contribute to this region (nominally cation-cation scattering paths), single scattering paths were included to attempt to fit this region and their degeneracies were sequentially reduced from those of

the pristine model. Fitting paths that had the same degeneracies as the pristine model gave comparatively higher R-factors, higher correlations between variables and χ^2 values. The medium-range order of the irradiated sample at the Yb L_3-edge region was well fit with Yb-Ti and Yb-Yb paths that had degeneracies of 3 and 6, respectively, compared to 8 and 4 in the pristine model. Likewise, the Ti-Ti and Ti-Yb paths fit to the Ti K-edge spectra of the irradiated sample had similarly reduced degeneracies of 3 and 6, respectively, reduced from 4 and 8 in the pristine model. The results of these models are found in the Supplementary Information, Section S3.

A lack of appreciable change in the coordination environment (i.e., 8- and 5-fold coordinated Yb-O and Ti-O environments remain) is consistent with the lack of significant diffuse scattering (indicative of amorphisation) and retention of crystalline phase observed in the GAXRD pattern of irradiated Yb_2TiO_5. Furthermore, previous studies have observed that some fluorite-like compounds remain crystalline after irradiation, such as $Y_2Sn_{1.6}Ti_{0.4}O_7$ and $Y_2Sn_2O_7$, due to the chemical and static disorder inherent to these compounds [60], similar to the retention of YbO_8 and TiO_5 polyhedra seen here. *In-situ* ion-irradiation experiments coupled with TEM measurements of Yb_2TiO_5 do, however, show that the compound amorphised under 1 MeV Kr^{2+} irradiation [8] and had a critical temperature of 456 K., The results of this study suggest that within the precision of EXAFS determined Yb-O and Ti-O bond distances and coordination refinements, radiation damaged polyhedra are consistent with 8- and 5-fold coordinations, respectively, observed in the short-range order of pristine Yb_2TiO_5.

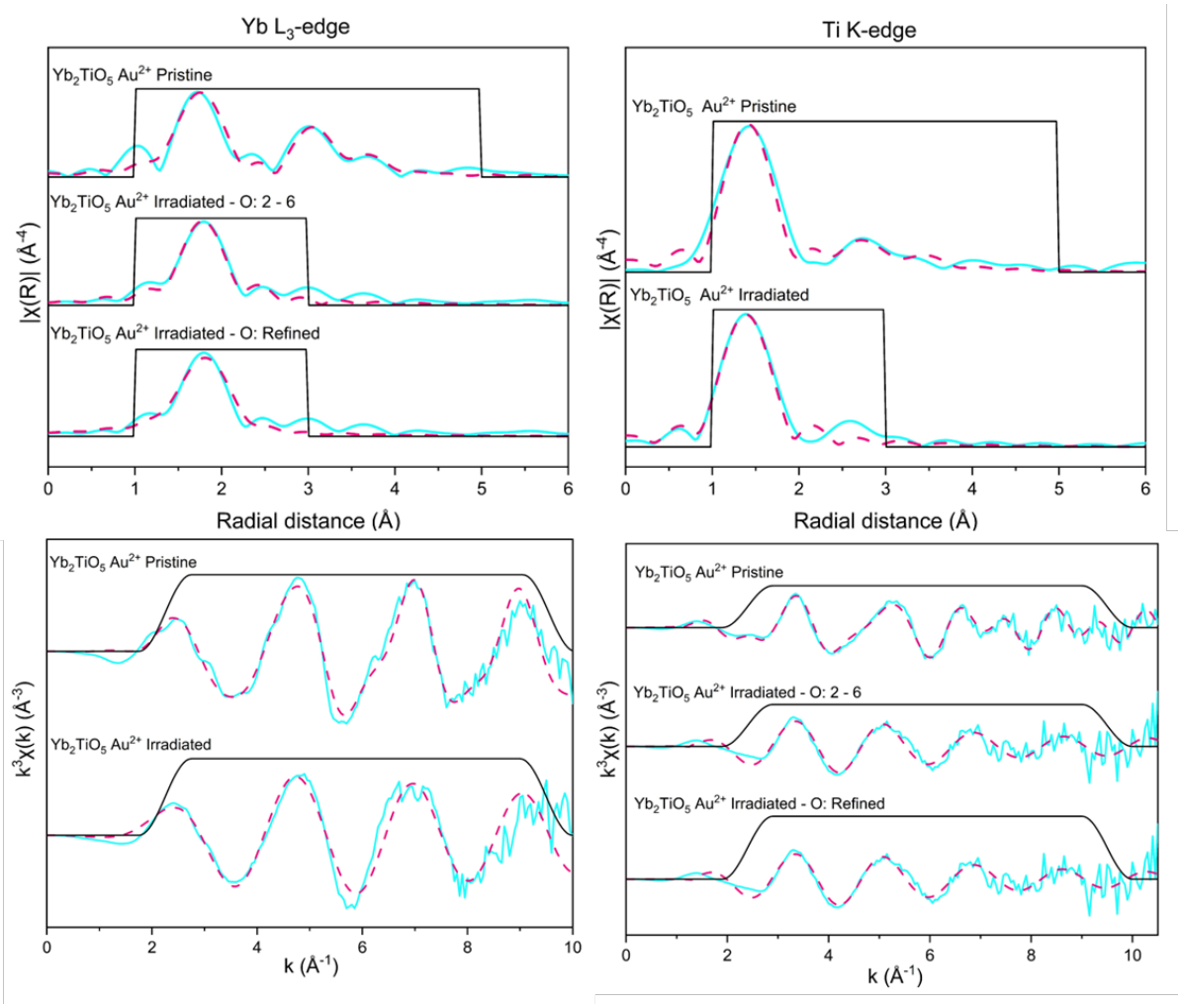

Figure 7: The top panels show fits to the Fourier transform of the waveforms in R-space of pristine and irradiated Yb_2TiO_5 (5 MeV Au^{2+}) measured in GA mode at a depth of 700 nm. The top panels show the theoretical fits of models to the experimental Yb L_3-edge and Ti K-edge data. The k^3 weighted Yb L_3-edge and Ti K-edge waveforms are shown below. Models of the Yb L_3-edge include fits to the pristine data and two fits to model the first oxygen shell of the irradiated data. One model had a single Yb-O path where the path degeneracy was allowed to be refined and is indicated by the label 'O: Refined'. The other model has two Yb-O paths (2 short, 6 long) with a total degeneracy of 8 and indicated by the label 'O: 2 -6'. Solid blue lines represent the experimental data, dashed pink lines represent the theoretical fit to the data and solid black lines indicate the fitting windows used.

Table 3: Refined structural parameters of pristine and irradiated Yb_2TiO_5 (5 MeV Au^{2+}) measured in GA mode at a depth of 700 nm. Also shown for comparison are models of pristine Yb_2TiO_5 measured in a standard geometry. The left-hand side shows the results of models of data from the Yb L_3-edge and the right-hand side shows the results of models of data from the Ti K-edge. The average change in the scattering path distance for a given absorber-scatterer pair is denoted as R, the Debye–Waller factor is denoted as σ^2, the number of scatters in the coordination shell is denoted as N, the amplitude reduction factor is given by the term S_0^2. A dash resents that there is no data associated with that field.

Yb L_3-edge						Ti K-edge				
Path		**Yb_2TiO_5 Tran**	**Yb_2TiO_5 Pri**	**Yb_2TiO_5 Irr Au^{2+} O: refine**	**Yb_2TiO_5 Irr Au^{2+} O: 2 -6**	**Path**		**Yb_2TiO_5 Fluo**	**Yb_2TiO_5 Pri**	**Yb_2TiO_5 Irr Au^{2+}**
	E_0 (eV)	5.4(7)	4.0(21)	4.3(14)	6.2(20)		E_0 (eV)	-1.7(14)	-3.0(13)	-3.4(18)
	S_0^2	0.86(12)	0.57(18)	0.57	0.57		S_0^2	0.63(4)	0.50(6)	0.50
	R (Å)	2.24(4)	2.24(3)	2.28(6)	2.22(2)		R (Å)	1.91(1)	1.92(1)	1.91(2)
Yb-O(1)	σ^2 (Å^2)	0.010(2)	0.008(4)	0.018(4)	0.003(3)	**Ti-O**	σ^2 (Å^2)	0.003(2)	0.002(1)	0.005(3)
	N	2	2	7.0(12)	2		N	5	5	5.3(10)
	R (Å)	2.45(1)	2.42(3)	-	2.36(2)		R (Å)	3.38(2)	3.42(4)	-
Yb-O(2)	σ^2 (Å^2)	0.010(2)	0.008(4)	-	0.025(3)	**Ti-Yb**	σ^2 (Å^2)	0.011(2)	0.012(8)	-
	N	6	6	-	6		N	8	8	-
	R (Å)	3.45(6)	3.48(2)	-	-		R (Å)	3.58(2)	3.61(7)	-
Yb-Ti	σ^2 (Å^2)	0.022(6)	0.023(12)	-	-	**Ti-Ti**	σ^2 (Å^2)	0.022(12)	0.012(8)	-
	N	4	4	-	-		N	4	4	-
	R (Å)	3.55(2)	3.52(2)	-	-	**R-factor**		0.020	0.032	0.029
Yb-Yb	σ^2 (Å^2)	0.003(2)	0.012(3)	-	-	**BVS (v.u.)**		4.01	3.78	4.12
	N	8	8	-	-					
	R (Å)	3.99(5)	3.96(9)	-	-					
Yb-O(3)	σ^2 (Å^2)	0.019(14)	0.028(13)	-	-					
	N	12	12	-	-					
R-factor		0.005	0.027	0.039	0.016					
BVS (v.u.)		3.18	3.20	2.78	2.93					

Given the retention of YbO_8 and TiO_5 polyhedra, characteristic of the *Fd-3m* pyrochlore-like structure identified as being representative of the short-range ordering of pristine Yb_2TiO_5 [17], results of XAS analysis suggest that the amorphisation pathway for these materials begins with a loss of long- and medium-range order. This is seen in the reduction to the intensity of the region associated with this scale of ordering of the Fourier transforms of the irradiated data (Figure 7) and that the nearest

neighbour coordination remains unaffected. This shows that cubic Ln_2TiO_5 compounds are remarkably efficient at resisting radiation induced structural changes that could be detrimental to their performance as a ceramic wasteform for actinide wastes, and as such are an ideal candidate for actinide waste immobilisation.

The high anti-site defect energy of cubic Ln_2TiO_5 stuffed pyrochlores (highest those with the smallest lanthanides such as Yb or Lu) may cause the structure to eventually collapse into an amorphous state through the accumulation of cation interstitial and vacancy pairs. Studies at higher ion irradiation fluences could introduce further damage to the crystalline structure of Yb_2TiO_5 may yield further results regarding the local-scale structural transitions. It may be expected, then, that behaviours similar to the related $Ln_2Zr_2O_7$ compounds, that adopt a long-range pyrochlore *Fd-3m* structure undergo a transition into a more disordered *Fm-3m* defect-fluorite structure before becoming amorphous, could be identified at higher fluences. Furthermore, as the effect of the lanthanide cation size has been well reported to affect the ability of cubic Ln_2TiO_5 (Ln = Dy – Lu, Y) stuffed pyrochlores to resist radiation damage, it would be interesting to see if the local structure of cubic Ln_2TiO_5 compounds that have larger lanthanide ionic radii, such as Ho_2TiO_5. are more adversely affected by irradiation as has been suggested in other related compounds such as $Ln_2Ti_2O_7$ [20].

Both orthorhombic and cubic Ln_2TiO_5 compounds demonstrated similar radiation behaviour, where anti-site defects are likely to highly influence their tolerance. Though cubic Ln_2TiO_5 nominally have been reported to have lower T_c values than orthorhombic counterparts, they both excel in their ability to resist radiation damage. As such, the applicability of both would be suitable for different roles. Due to the varying ionic radii of likely actinide waste products immobilised in ceramic matrices, different structures of Ln_2TiO_5 will be more easily formed (based upon the structure stability of Ln_2TiO_5 [12]), which will have to be a key consideration during wasteform design. Furthermore, it has been shown previously [19], [48] that the addition of larger or smaller lanthanides can influence the Ln_2TiO_5 structure obtained during synthesis. This may allow for designer ceramics where either orthorhombic or cubic structures could be synthesised with a minority lanthanide occupancy of those not typically associated with the strtcutre (e.g., cubic $Sm_{0.6}Yb_{1.4}TiO_5$, where typically Sm_2TiO_5 is only stable as an orthorhombic structure).

4. Conclusions

The radiation resistance of different structure types of Ln_2TiO_5 (Ln = Gd, Dy, Yb) have been successfully investigated for the first time *via* combined glancing-angle XANES and EXAFS techniques. When used in concert EXAFS and XANES analyses, a detailed picture of the short-range order of the radiation damage behaviour of orthorhombic Gd_2TiO_5, hexagonal Dy_2TiO_5 and cubic Yb_2TiO_5 stuffed pyrochlores can be assembled. GAXAS has been used to show that the short-range order of orthorhombic Gd_2TiO_5 likely transitions towards a more disordered structure that bear similarities to a defect-fluorite-like *Fm-3m* coordination upon irradiation. Cation anti-site defects are induced by heavy-ion beam irradiations and drive this transition in the hexagonal Dy_2TiO_5 system, Dy-O and Ti-O polyhedra of

hexagonal Dy_2TiO_5 undergoes significant reduction in coordination and a complete loss of medium range order is observed, consistent with previous findings. In the cubic Yb_2TiO_5 system, irradiation appears to result in pyrochlore-like coordination polyhedra that are retained from the pristine samples, albeit with some increased static disorder and the medium-range order. The two different ion irradiation experiments conducted in this study, 5 MeV Au^{2+} with a fluence of 1.2 x 10^{15} ions cm^{-2} and 1 MeV Kr^{+} with a fluence of 5 x 10^{15} ions cm^{-2}, aimed to produce varied penetration depths however, the results presented here have shown no appreciable difference between the two in terms of GAXAS analysis. This could either indicate that both irradiation schemes produce very similar results or that there is a limit in the precision of the GAXAS technique to detect the very fine differences in structure. Further experimental investigation utilising other techniques, such as neutron PDF analysis or TEY XAS would be required to explore these possible limitations. The results from this study will inform future decisions and understanding regarding the applicability of these materials for roles within the nuclear sector, including as actinide hosting wasteforms and as burnable poisons in control rods. Furthermore, the methodology and approach used in this work provide a valuable foundation for future experiments aiming to utilise GAXAS for the characterisation of radiation damaged materials.

Acknowledgments

DAA is grateful to the Engineering and Physical Sciences Research Council (EPSRC) for funding. This research utilised the HADES/MIDAS facility at The University of Sheffield established with financial support from EPSRC and BEIS, under grant EP/T011424/1 and was supported by grant EP/S01019X/1. This research used 6-BM of the National Synchrotron Light Source II, a U.S. Department of Energy (DOE) Office of Science User Facility operated for the DOE Office of Science by Brookhaven National Laboratory under Contract No. DE-SC0012704. We are also grateful to the staff and scientists at DCF who allowed us to make use of their beamlines.

5. References

[1] R. C. Ewing, W. J. Webert, and F. W. Clinard, “Radiation Effects in Nuclear Waste Forms for High-Level Radioactive Waste,” *Prog. Nucl. Energy*, vol. 29, no. 2, pp. 63–121, 1995.

[2] R. C. Ewing, “Ceramic matrices for plutonium disposition,” *Prog. Nucl. Energy*, vol. 49, no. 8, pp. 635–643, Nov. 2007.

[3] K. P. Hart *et al.*, “Aqueous Durability of Titanate Ceramics Designed to Immobilise Excess Plutonium,” *MRS Online Proc. Libr. 2000 6081*, vol. 608, no. 1, pp. 353–358, Feb. 2011.

[4] X. Liu *et al.*, “Insights into the radiation behavior of Ln_2TiO_5 (Ln = La - Y) from defect energetics,” *Comput. Mater. Sci.*, vol. 139, pp. 295–300, 2017.

[5] H. Niu, H. Gou, R. C. Ewing, and J. Lian, “First principles investigation of structural, electronic, elastic and thermal properties of rare-earth-doped titanate Ln_2TiO_5,” *AIP Adv.*, vol. 2, no. 3, p. 032114, Sep. 2012.

[6] R. D. Aughterson, N. J. Zaluzec, and G. R. Lumpkin, “Synthesis and ion-irradiation tolerance of the Dy_2TiO_5 polymorphs,” *Acta Mater.*, vol. 204, p. 116518, Feb. 2021.

[7] R. D. Aughterson *et al.*, “Ion-irradiation resistance of the orthorhombic Ln_2TiO_5 (Ln = La, Pr, Nd, Sm, Eu, Gd, Tb and Dy) series,” *J. Nucl. Mater.*, vol. 467, pp. 683–691, 2015.

[8] K. R. Whittle, M. G. Blackford, R. D. Aughterson, G. R. Lumpkin, and N. J. Zaluzec, “Ion irradiation of novel yttrium/ytterbium-based pyrochlores: The effect of disorder,” *Acta Mater.*, vol. 59, no. 20, pp. 7530–7537, Dec. 2011.

[9] V. D. Risovany, A. V. Zakharov, E. M. Muraleva, V. M. Kosenkov, and R. N. Latypov, “Dysprosium hafnate as absorbing material for control rods,” *J. Nucl. Mater.*, vol. 355, no. 1–3, pp. 163–170, Sep. 2006.

[10] H. S. Kim, C. Y. Joung, B. H. Lee, S. H. Kim, and D. S. Sohn, “Characteristics of $Gd_xM_yO_z$ (M=Ti, Zr or Al) as a burnable absorber,” *J. Nucl. Mater.*, vol. 372, no. 2–3, pp. 340–349, Jan. 2008.

[11] L. Wang and T. Liang, “Ceramics for high level radioactive waste solidification,” *J. Adv. Ceram.*, vol. 1, no. 3, pp. 194–203, 2012.

[12] Y. F. Shepelev and M. A. Petrova, “Crystal structures of Ln_2TiO_5 (Ln = Gd, Dy) polymorphs,”

Inorg. Mater., vol. 44, no. 12, pp. 1354–1361, Dec. 2008.

[13] R. D. Aughterson, G. R. Lumpkin, G. J. Thorogood, Z. Zhang, B. Gault, and J. M. Cairney, "Crystal chemistry of the orthorhombic Ln_2TiO_5 compounds with Ln=La, Pr, Nd, Sm, Gd, Tb and Dy," *J. Solid State Chem.*, vol. 227, pp. 60–67, Jul. 2015.

[14] R. D. Aughterson *et al.*, "Crystal structures of orthorhombic, hexagonal, and cubic compounds of the $Sm_{(x)}Yb_{(2-x)}TiO_5$ series," *J. Solid State Chem.*, vol. 213, pp. 182–192, May 2014.

[15] G. C. Lau, T. M. McQueen, Q. Huang, H. W. Zandbergen, and R. J. Cava, "Long- and short-range order in stuffed titanate pyrochlores," *J. Solid State Chem.*, vol. 181, no. 1, pp. 45–50, Jan. 2008.

[16] J. Shamblin *et al.*, "Structural and magnetic short-range order in fluorite Yb_2TiO_5," *Phys. Rev. B*, vol. 96, no. 17, p. 174418, Nov. 2017.

[17] D. A. Austin, L. T. Townsend, M. C. Stennett, B. Ravel, and R. J. Hand, "Probing the local coordination of Ln_2TiO_5 (Ln = Yb, Y) through multi-element X-ray absorption techniques [Unpublished manuscript]," *Dep. Mater. Sci. Eng. Univ. Sheff.*, 2022.

[18] R. D. Aughterson *et al.*, "The ion-irradiation tolerance of the pyrochlore to fluorite $Ho_{(x)}Yb_{(2-x)}TiO_5$ and Er_2TiO_5 compounds: A TEM comparative study using both in-situ and bulk ex-situ irradiation approaches," *J. Nucl. Mater.*, vol. 507, pp. 316–326, Aug. 2018.

[19] R. D. Aughterson *et al.*, "The influence of crystal structure on ion-irradiation tolerance in the $Sm_{(x)}Yb_{(2-x)}TiO_5$ series," *J. Nucl. Mater.*, vol. 471, pp. 17–24, Apr. 2016.

[20] G. R. Lumpkin *et al.*, "Nature of the chemical bond and prediction of radiation tolerance in pyrochlore and defect fluorite compounds," *J. Solid State Chem.*, vol. 180, no. 4, pp. 1512–1518, Apr. 2007.

[21] W. J. Weber *et al.*, "Radiation effects in crystalline ceramics for the immobilization of high-level nuclear waste and plutonium," *J. Mater. Res. 1998 136*, vol. 13, no. 6, pp. 1434–1484, Jan. 2011.

[22] S. U. Campisano, S. Coffa, V. Raineri, F. Priolo, and E. Rimini, "Mechanisms of amorphization in ion implanted crystalline silicon," *Nucl. Instruments Methods Phys. Res. Sect. B Beam Interact. with Mater. Atoms*, vol. 80–81, pp. 514–518, Jun. 1993.

[23] D. P. P. Reid *et al.*, "The structure of ion beam amorphised zirconolite studied by grazing angle X-ray absorption spectroscopy," *Nucl. Instruments Methods Phys. Res. Sect. B Beam Interact. with Mater. Atoms*, vol. 268, no. 11–12, pp. 1847–1852, Jun. 2010.

[24] D. Simeone, J. M. Costantini, L. Luneville, L. Desgranges, P. Trocellier, and P. Garcia, "Characterization of radiation damage in ceramics: Old challenge new issues?," *J. Mater. Res.*, vol. 30, no. 9, pp. 1495–1515, Jan. 2015.

[25] R. Sherrod, E. C. O'Quinn, I. M. Gussev, C. Overstreet, J. Neuefeind, and M. K. Lang, "Comparison of short-range order in irradiated dysprosium titanates," *npj Mater. Degrad. 2021 51*, vol. 5, no. 1, pp. 1–7, Apr. 2021.

[26] J. Shamblin *et al.*, "Probing disorder in isometric pyrochlore and related complex oxides," *Nat. Mater. 2016 155*, vol. 15, no. 5, pp. 507–511, Feb. 2016.

[27] J. Shamblin *et al.*, "Similar local order in disordered fluorite and aperiodic pyrochlore structures," *Acta Mater.*, vol. 144, pp. 60–67, Feb. 2018.

[28] G. Sattonnay *et al.*, "Key role of the short-range order on the response of the titanate pyrochlore $Y_2Ti_2O_7$ to irradiation," *Phys. Rev. B*, vol. 94, no. 22, p. 224109, Dec. 2016.

[29] C. L. Tracy *et al.*, "Role of composition, bond covalency, and short-range order in the disordering of stannate pyrochlores by swift heavy ion irradiation," *Phys. Rev. B*, vol. 94, no. 6, p. 064102, Aug. 2016.

[30] M. Stennett *et al.*, "Heavy ion implantation combined with grazing incidence X-ray absorption spectroscopy (GIXAS): A new methodology for the characterisation of radiation damage in nuclear ceramics," *MRS Proc.*, vol. 1193, p. 67, Jan. 2011.

[31] M. C. Stennett, N. Peng, E. R. Maddrell, B. Ravel, and N. C. Hyatt, "Probing radiation damage in ceramic wasteforms using X-ray absorption spectroscopy," *Diam. '10 Conf. Proceedings; Decommissioning, Immobil. Manag. Nucl. Waste Dispos.*, 2010.

[32] E. R. Aluri, J. R. Hayes, J. D. S. Walker, and A. P. Grosvenor, "Investigation of the structural stability of ion-implanted $Gd_2Ti_{2-x}Sn_xO_7$ pyrochlore-type oxides by glancing angle X-ray absorption spectroscopy," *J. Phys. Chem. C*, vol. 118, no. 15, pp. 7910–7922, Apr. 2014.

[33] A. S. Gandy, M. C. Stennett, C. Brigden, and N. C. Hyatt, “Ion Beam Irradiation Induced Structural Modifications in Iron Phosphate Glasses: A Model System for Understanding Radiation Damage in Nuclear Waste Glasses,” *MRS Online Proc. Libr.*, vol. 1757, no. January, pp. 65–70, 2015.

[34] C. L. Dube, · M C Stennett, · A Ananthanarayanan, · C David, · J G Shah, and · N C Hyatt, “Radiation stability study on cerium loaded iron phosphate glasses by ion irradiation method,” vol. 323, pp. 1381–1386, 2020.

[35] S. Pizzini *et al.*, “Instrumentation for glancing angle x-ray absorption spectroscopy on the Synchrotron Radiation Source,” *Rev. Sci. Instrum.*, vol. 60, no. 7, p. 2525, Aug. 1998.

[36] D. A. Austin, L. T. Townsend, B. Ravel, M. C. Stennett, and R. J. Hand, “Characterisation of the local structure of Ln_2TiO_5 (Ln = La, Pr, Nd, Sm, Eu, Gd, Tb, Dy, Ho, Er, Tm, Yb, Lu) compounds through multi element XANES and EXAFS analyses [Unpublished manuscript],” *Dep. Mater. Sci. Eng. Univ. Sheff.*, 2022.

[37] J. F. Ziegler, M. D. Ziegler, J. P. Biersack, J. F. Ziegler, M. D. Ziegler, and J. P. Biersack, “SRIM - The stopping and range of ions in matter (2010),” *NIMPB*, vol. 268, no. 11–12, pp. 1818–1823, Jun. 2010.

[38] J. A. Bearden and A. F. Burr, “Reevaluation of X-ray atomic energy levels,” *Rev. Mod. Phys.*, vol. 39, no. 1, pp. 125–142, Jan. 1967.

[39] B. Ravel and M. Newville, “ATHENA, ARTEMIS, HEPHAESTUS: Data analysis for X-ray absorption spectroscopy using IFEFFIT,” in *Journal of Synchrotron Radiation*, 2005, vol. 12, no. 4, pp. 537–541.

[40] B. Ravel and M. Newville, “ATHENA and ARTEMIS: Interactive graphical data analysis using IFEFFIT,” *Phys. Scr. T*, vol. T115, no. T115, pp. 1007–1010, 2005.

[41] M. Newville, “IFEFFIT: Interactive XAFS analysis and FEFF fitting,” *J. Synchrotron Radiat.*, vol. 8, no. 2, pp. 322–324, Mar. 2001.

[42] F. Farges, G. E. Brown, and J. J. Rehr, “Coordination chemistry of Ti(IV) in silicate glasses and melts: I. XAFS study of titanium coordination in oxide model compounds,” *Geochim. Cosmochim. Acta*, vol. 60, no. 16, pp. 3023–3038, Aug. 1996.

[43] F. Farges, “Coordination of Ti^{4+} in silicate glasses: A high-resolution XANES spectroscopy study at the Ti Kedge,” *Am. Mineral.*, vol. 82, pp. 36–43, 1997.

[44] A. V. Shlyakhtina *et al.*, “Effect of the Ca-doping on the electrical conductivity of oxide ion conductor $Yb_2Ti_2O_7$,” *Solid State Ionics*, vol. 179, no. 21–26, pp. 1004–1008, Sep. 2008.

[45] I. D. Brown and D. Altermatt, “Bond-valence parameters obtained from a systematic analysis of the Inorganic Crystal Structure Database,” *Acta Crystallogr. Sect. B*, vol. 41, no. 4, pp. 244–247, Aug. 1985.

[46] L. R. Blackburn *et al.*, “Synthesis and characterisation of $Ca_{1-x}Ce_xZrTi_{2-2x}Cr_{2x}O_7$: Analogue zirconolite wasteform for the immobilisation of stockpiled UK plutonium,” *J. Eur. Ceram. Soc.*, vol. 40, no. 15, pp. 5909–5919, Dec. 2020.

[47] L. R. Blackburn *et al.*, “Influence of accessory phases and surrogate type on accelerated leaching of zirconolite wasteforms,” *npj Mater. Degrad. 2021 51*, vol. 5, no. 1, pp. 1–11, May 2021.

[48] R. D. Aughterson, G. R. Lumpkin, K. L. Smith, Z. Zhang, N. Sharma, and J. M. Cairney, “The crystal structures and corresponding ion-irradiation response for the $Tb_{(x)}Yb_{(2-x)}TiO_5$ series,” *Ceram. Int.*, vol. 44, no. 1, pp. 511–519, Jan. 2018.

[49] P. Zasimov, L. Amidani, M. Retegan, O. Walter, R. Caciuffo, and K. O. Kvashnina, “HERFD-XANES and RIXS Study on the Electronic Structure of Trivalent Lanthanides across a Series of Isostructural Compounds,” *Inorg. Chem.*, vol. 61, no. 4, pp. 1817–1830, Jan. 2022.

[50] F. Farges, “Fivefold-coordinated Ti^{4+} in metamict zirconolite and titanite: A new occurrence shown by Ti K-edge XANES spectroscopy,” *Am. Mineral.*, vol. 82, no. 1–2, pp. 44–50, Feb. 1997.

[51] J. Lian *et al.*, “Radiation-induced amorphization of rare-earth titanate pyrochlores,” *Phys. Rev. B*, vol. 68, no. 13, p. 134107, Oct. 2003.

[52] F. Farges and G. E. Brown, “Ti-edge XANES studies of Ti coordination and disorder in oxide compounds: Comparison between theory and experiment,” *Phys. Rev. B - Condens. Matter Mater. Phys.*, vol. 56, no. 4, pp. 1809–1819, Jul. 1997.

[53] A. G. Waychunas, “Synchrotron radiation xANES spectroscopy of Ti in minerals: Effects of Ti bonding distances, Ti valence, and site geometry on absorption edge structure,” 1987.

[54] J. Zhang, F. Zhang, M. Lang, F. Lu, J. Lian, and R. C. Ewing, “Ion-irradiation-induced structural transitions in orthorhombic Ln_2TiO_5,” *Acta Mater.*, vol. 61, no. 11, pp. 4191–4199, Jun. 2013.

[55] J. Shamblin *et al.*, “Probing disorder in isometric pyrochlore and related complex oxides,” *Nat. Mater.*, vol. 15, no. 5, pp. 507–511, May 2016.

[56] G. King, C. M. Thompson, J. E. Greedan, and A. Llobet, “Local structure of the vacancy disordered fluorite Yb_3TaO_7 from neutron total scattering,” *J. Mater. Chem. A*, vol. 1, no. 35, pp. 10487–10494, Sep. 2013.

[57] G. C. C. Lau, B. D. D. Muegge, T. M. M. McQueen, E. L. L. Duncan, and R. J. J. Cava, “Stuffed rare earth pyrochlore solid solutions,” *J. Solid State Chem.*, vol. 179, no. 10, pp. 3126–3135, Oct. 2006.

[58] A. Sinha and B. P. Sharma, “Development of Dysprosium Titanate Based Ceramics,” *J. Am. Ceram. Soc.*, vol. 88, no. 4, pp. 1064–1066, Apr. 2005.

[59] S. Finkeldei *et al.*, “Insights into the fabrication and structure of plutonium pyrochlores,” *J. Mater. Chem. A*, vol. 8, no. 5, pp. 2387–2403, Feb. 2020.

[60] G. R. Lumpkin *et al.*, “Ion irradiation of ternary pyrochlore oxides,” *Chem. Mater.*, vol. 21, no. 13, pp. 2746–2754, Jul. 2009.

Supporting information

S1: SRIM simulations of the damage depth profiles of Ln_2TiO_5 (Ln = Gd, Dy, Yb)

Damage depth profiles of orthorhombic Gd_2TiO_5, hexagonal Dy_2TiO_5 and cubic Yb_2TiO_5 were calculated to aid in the design of GAXAS measurements by setting the angle of incidence of the X-ray beam to probe the regions of peak damage depths. The electronic to nuclear stopping power (ENSP) ratios of the samples were also calculated using SRIM for the different irradiation conditions [1]. The ENSP ratios (Table 1) indicate that the there is an increase in electronic stopping rates from Kr to Au ion irradiations, suggesting that inelastic scattering (electronic stopping) interactions between the ions and crystal structure are occurring more frequently under 5 MeV Au^{2+} ion irradiation than elastic interactions (nuclear stopping). This is behaviour is known and expected given the increase in kinetic energy of Au ions compared to that of Kr ions [2], [3].

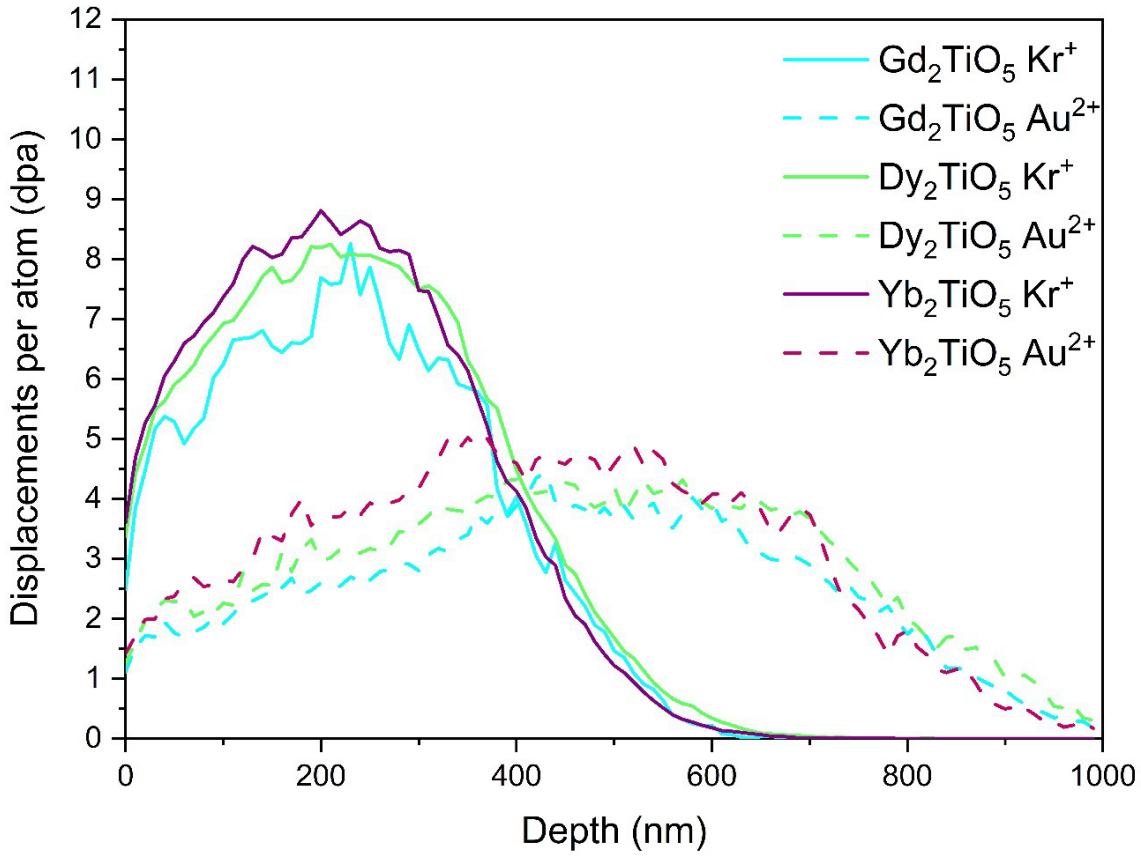

Figure S1: Damage-depth profiles of Ln_2TiO_5 (Ln = Gd, Dy, Yb) stuffed pyrochlores (in displacements per atom). Profiles consisting of solid lines were calculated using 1 MeV Kr^+ ions with a fluence of 5 x 10^{15} ions cm^{-2}, profiles consisting dashed lines were calculated using 5 MeV Au^{2+} ions with a fluence of 1.2 x 10^{15} ions cm^{-2}. Sample stoichiometry are denoted by colour: Gd_2TiO_5 – blue, Dy_2TiO_5 – green and Yb_2TiO_5 – purple.

Table S1: Damage per atom (dpa) at given depths of interest and electronic to nuclear stopping powers (ENSP) for Ln_2TiO_5 samples irradiated under different ion beam conditions. Also shown is the required incident X-ray beam angle to measure near the Gd, Dy and Yb L_3-edges (7243 eV, 7790 eV and 8944 eV, respectively) and Ti K-edge (4966 eV).

Ln_2TiO_5	1 MeV Kr^+ 5 x 10^{15} ions cm^{-2}					5 MeV Au^{2+} 1.2 x 10^{15} ions cm^{-2}				
	depth (nm)	dpa	ENSP	Incident angle (degrees)		depth (nm)	dpa	ENSP	Incident angle (degrees)	
				Ln	Ti				Ln	Ti
Gd_2TiO_5	300	6.5	0.72	1.042	0.971	700	3	0.96	2.431	2.267
Dy_2TiO_5	300	7.4	0.63	0.424	1.102	700	3.6	0.91	0.990	2.572
Yb_2TiO_5	300	7.5	0.65	0.392	1.508	700	3.7	0.93	0.654	2.614

S2: EXAFS of 1 MeV Kr^+ ion irradiations at a fluence of 5 x 10^{15} ions cm^{-2}

Table S2: Refined structural parameters of pristine and irradiated Gd_2TiO_5 (1 MeV Kr^+) measured in GA mode at a depth of 300 nm. Also shown for comparison are models of pristine Gd_2TiO_5 measured in a standard geometry. The left-hand side shows the results of models of data from the Gd L_3-edge and the right-hand side shows the results of models of data from the Ti K-edge. The average change in the scattering path distance for a given absorber-scatterer pair is denoted as R, the Debye–Waller factor is denoted as σ^2, the number of scatters in the coordination shell is denoted as N, the amplitude reduction factor is given by the term S_0^2. A dash resents that there is no data associated with that field.

Gd L_3-edge					Ti K-edge				
Path		**Gd_2TiO_5 Tran**	**Gd_2TiO_5 Pri Kr^+**	**Gd_2TiO_5 Irr Kr^+**	**Path**		**Gd_2TiO_5 Fluo**	**Gd_2TiO_5 Pri Kr^+**	**Gd_2TiO_5 Irr Kr^+**
	E_0 (eV)	3.2(18)	3.5(17)	1.3(3)		*E_0 (eV)*	-3.9(11)	-1.2(9)	5.4(23)
	S_0^2	1.17	0.55(10)	0.55		*S_0^2*	0.54(9)	0.45(6)	0.45
	R (Å)	2.37(2)	2.36(2)	2.33(1)		*R (Å)*	1.91(1)	1.90(1)	1.95(3)
Gd-O(1)	*σ^2 ($Å^2$)*	0.009(2)	0.008(3)	0.016(3)	**Ti-O**	*σ^2 ($Å^2$)*	0.003(1)	0.002(1)	0.006(4)
	N	7	7	6.7(8)		*N*	5	5	5.5(14)
	R (Å)	3.81(3)	3.77(10)	-		*R (Å)*	3.60(6)	3.55(6)	-
Gd-Gd(1)	*σ^2 ($Å^2$)*	0.009(4)	0.014(7)	-	**Ti-Ln(1)**	*σ^2 ($Å^2$)*	0.008(6)	0.007(5)	-
	N	7	7	-		*N*	7	7	-
	R (Å)	4.11(8)	4.07(3)	-		*R (Å)*	3.50(5)	3.73(4)	-
Gd-Gd(2)	*σ^2 ($Å^2$)*	0.009(3)	0.007(3)	-	**Ti-Ti**	*σ^2 ($Å^2$)*	0.003(2)	0.006(4)	-
	N	9	9	-		*N*	2	2	-
Gd-Ti(1)	*R (Å)*	3.44(8)	3.41(12)	-	**R-factor**		0.025	0.019	0.032

	σ^2 (Å^2)	0.005(4)	0.008(6)	-	**BVS (v.u.)**	3.83	3.78	3.82
	N	3	3	-				
	R (Å)	3.74(5)	3.67(4)	-				
Gd-Ti(2)	σ^2 (Å^2)	0.004(3)	0.008(6)	-				
	N	4	5	-				
R-factor		0.022	0.021	0.006				
BVS (v.u.)		3.02	3.18	3.30				

Table S3: Refined structural parameters of pristine and irradiated Dy_2TiO_5 (1 MeV Kr^+) measured in GA mode at a depth of 300 nm. Also shown for comparison are models of pristine Dy_2TiO_5 measured in a standard geometry. The left-hand side shows the results of models of data from the Dy L_3-edge and the right-hand side shows the results of models of data from the Ti K-edge. The average change in the scattering path distance for a given absorber-scatterer pair is denoted as R, the Debye–Waller factor is denoted as σ^2, the number of scatters in the coordination shell is denoted as N, the amplitude reduction factor is given by the term S_0^2. A dash resents that there is no data associated with that field.

Dy L_3-egde					Ti K-edge				
Path		**Dy_2TiO_5 Tran**	**Dy_2TiO_5 Pri Kr^+**	**Dy_2TiO_5 Irr Kr^+**	**Path**		**Dy_2TiO_5 Fluo**	**Dy_2TiO_5 Pri Kr^+**	**Dy_2TiO_5 Irr Kr^+**
	E_o (eV)	5.6(11)	1.8(14)	3.8(10)		*E_o (eV)*	-3.9(11)	-2.0(11)	-4.0(18)
	S_o^2	1.06	0.67(12)	0.67		*S_o^2*	0.54(9)	0.48(5)	0.48
	R (Å)	2.32(1)	2.41(1)	2.28		*R (Å)*	1.91(1)	1.92(1)	1.89(2)
Dy-O(1)	*σ^2 (Å²)*	0.009(1)	0.015(4)	0.011(7)	**Ti-O**	*σ^2 (Å²)*	0.003(1)	0.002(1)	0.004(3)
	N	6	8	6.8(12)		*N*	5	5	4.4(7)
	R (Å)	2.56(4)	-	-		*R (Å)*	3.60(6)	3.66(21)	-
Dy-O(2)	*σ^2 (Å²)*	0.011(5)	-	-	**Ti-Dy(1)**	*σ^2 (Å²)*	0.008(6)	0.015(10)	-
	N	2	-	-		*N*	6	6	-
	R (Å)	3.46(3)	3.60(5)	-		*R (Å)*	3.50(5)	3.46(6)	-
Dy-Dy(1)	*σ^2 (Å²)*	0.013(3)	0.016(7)	-	**Ti-Dy(2)**	*σ^2 (Å²)*	0.003(2)	0.008(7)	-
	N	6	8	-		*N*	2	2	-
	R (Å)	3.70(3)	-	-		*R (Å)*	3.32(8)	3.44(8)	-
Dy-Dy(2)	*σ^2 (Å²)*	0.013(3)	-	-	**Ti-Ti**	*σ^2 (Å²)*	0.004(2)	0.015(6)	-
	N	2	-	-		*N*	4	4	-
	R (Å)	3.46(3)	3.44(4)	-	**R-factor**		0.025	0.024	0.035
Dy-Ti	*σ^2 (Å²)*	0.020(3)	0.025(18)	-	**BVS (v.u.)**		3.83	3.75	3.77
	N	4	4	-					
R-factor		0.015	0.021	0.030					
BVS (v.u.)		2.97	3.11	3.29					

Table S4: Refined structural parameters of pristine and irradiated Yb_2TiO_5 (1 MeV Kr^+) measured in GA mode at a depth of 300 nm. Also shown for comparison are models of pristine Yb_2TiO_5 measured in a standard geometry. The left-hand side shows the results of models of data from the Yb L_3-edge and the right-hand side shows the results of models of data from the Ti K-edge. The average change in the scattering path distance for a given absorber-scatterer pair is denoted as R, the Debye–Waller factor is denoted as σ^2, the number of scatters in the coordination shell is denoted as N, the amplitude reduction factor is given by the term S_0^2. A dash resents that there is no data associated with that field.

Yb L_3-edge						Ti K-edge				
Path		**Yb_2TiO_5 Tran**	**Yb_2TiO_5 Pri**	**Yb_2TiO_5 Irr Kr^+ O: Refine**	**Yb_2TiO_5 Irr Kr^+ O:2-6**	**Path**		**Yb_2TiO_5 Fluo**	**Yb_2TiO_5 Pri**	**Yb_2TiO_5 Irr Kr^+**
	E_o (eV)	4.2(10)	4.0(20)	4.5(17)	6.0(27)		*E_o (eV)*	-4.3(13)	-4.1(21)	-3.2(11)
	S_o^2	0.69(10)	0.49(13)	0.49	0.49		*S_o^2*	0.51(7)	0.51(6)	0.51
	R (Å)	2.24(6)	2.23(1)	2.26(3)	2.22(4)		*R (Å)*	1.91(1)	1.91(1)	1.90(2)
Yb-O(1)	*σ^2 (Å^2)*	0.010(2)	0.009(3)	0.015(5)	0.003(3)	**Ti-O**	*σ^2 (Å^2)*	0.002(1)	0.002(1)	0.004(3)
	N	2	2	7.0(11)	2		*N*	5	5	5.3(9)
	R (Å)	2.43(2)	2.45(2)	-	2.35(8)		*R (Å)*	3.38(3)	3.42(4)	-
Yb-O(2)	*σ^2 (Å^2)*	0.010(2)	0.009(3)	-	0.024(8)	**Ti-Yb**	*σ^2 (Å^2)*	0.012(4)	0.013(7)	-
	N	6	6	-	6		*N*	8	8	-
	R (Å)	3.42(4)	3.49(2)	-	-		*R (Å)*	3.50(3)	3.62(7)	-
Yb-Ti	*σ^2 (Å^2)*	0.015(4)	0.009(3)	-	-	**Ti-Ti**	*σ^2 (Å^2)*	0.021(9)	0.013(7)	-
	N	4	4	-	-		*N*	4	4	-
	R (Å)	3.54(4)	3.55(4)	-	-	**R-factor**		0.024	0.029	0.029
Yb-Yb	*σ^2 (Å^2)*	0.015(4)	0.016(9)	-	-	**BVS (v.u.)**		3.88	3.87	4.18
	N	8	8	-	-					
	R (Å)	4.01(7)	3.95(3)	-	-					
Yb-O(3)	*σ^2 (Å^2)*	0.018(12)	0.022(15)	-	-					
	N	12	12	-	-					
R-factor		0.012	0.012	0.040	0.024					
BVS (v.u.)		3.31	3.29	3.04	3.02					

Table S5: Refined structural parameters of irradiated Yb_2TiO_5 (5 MeV Au^{2+} and 1 MeV Kr^{+}) measured in GA mode at a depth of 700 and 300 nm, respectively. Fitting range was extended to 4 Å in R-space to fit contributions to Fourier transform from next-nearest neighbour scatterers. The average change in the scattering path distance for a given absorber-scatterer pair is denoted as R, the Debye–Waller factor is denoted as σ^2, the number of scatters in the coordination shell is denoted as N, the amplitude reduction factor is given by the term S_0^2. A dash resents that there is no data associated with that field.

Path		**Yb_2TiO_5 Irr $Au2^{+}$: Extended fit**	**Yb_2TiO_5 Irr Kr^{+}: Extended fit**
	E_o (eV)	5.6(3)	5.9(4)
	S_o^2	0.57	0.49
	R (Å)	2.23(6)	2.22(1)
Yb-O(1)	*σ^2 (Å²)*	0.020(5)	0.003(2)
	N	2	2
	R (Å)	2.33(2)	2.34(2)
Yb-O(2)	*σ^2 (Å²)*	0.015(2)	0.014(6)
	N	6	6
	R (Å)	3.34(5)	3.34(3)
Yb-Ti	*σ^2 (Å²)*	0.025(11)	0.020(9)
	N	3	2
	R (Å)	3.72(4)	3.77(7)
Yb-Yb	*σ^2 (Å²)*	0.025(4)	0.025(12)
	N	6	4
R-factor		0.031	0.028
BVS (v.u.)		3.06	3.04

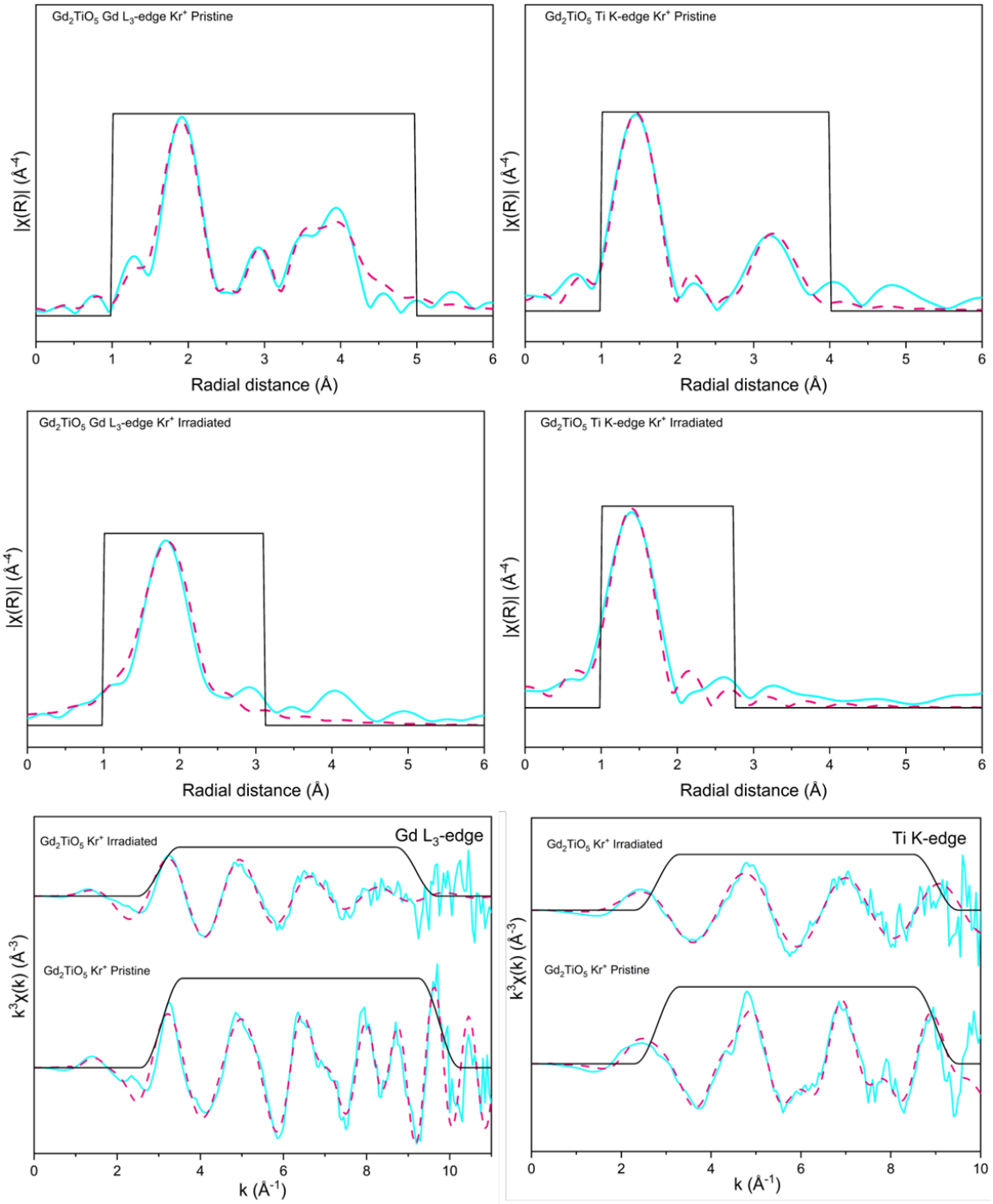

Figure S2: Fourier transform of the waveform in R-space of pristine and irradiated Gd_2TiO_5 (1 MeV Kr^+) measured in GA mode at a depth of 300 nm. The k^3 weighted Gd L_3-edge and Ti K-edge waveforms are shown alongside. Data at the top of the image were measured at the Gd L_3-edge, at the bottom they were measured at the Ti K-edge. Solid blue lines represent the experimental data, dashed pink lines represent the theoretical fit to the data and solid black lines indicate the fitting windows used.

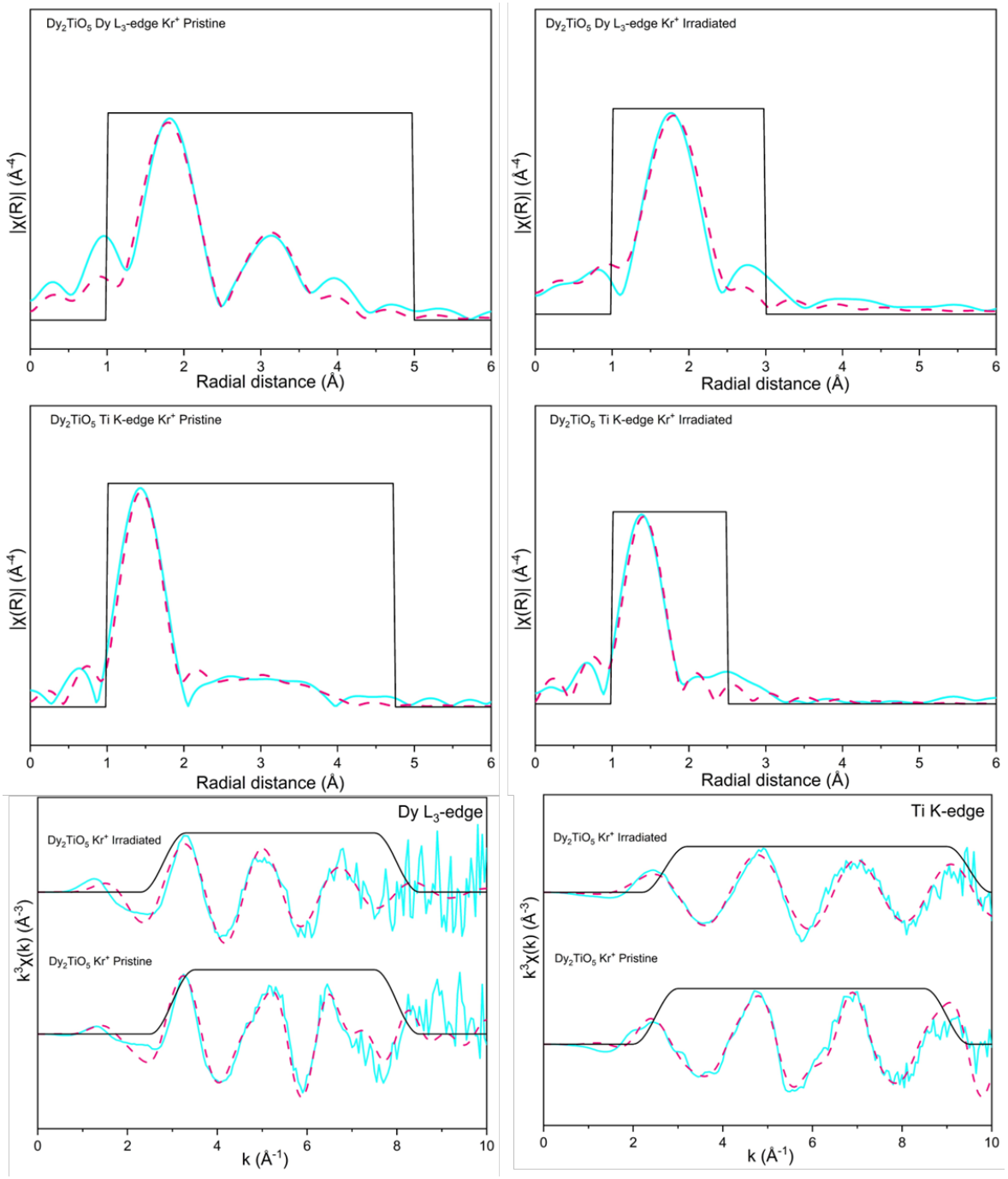

Figure S3: Fourier transform of the waveform in R-space of pristine and irradiated Dy_2TiO_5 (1 MeV Kr^+) measured in GA mode at a depth of 300 nm. The k^3 weighted Dy L_3-edge and Ti K-edge waveforms are shown alongside. Data at the top of the image were measured at the Dy L_3-edge, at the bottom they were measured at the Ti K-edge. Solid blue lines represent the experimental data, dashed pink lines represent the theoretical fit to the data and solid black lines indicate the fitting windows used.

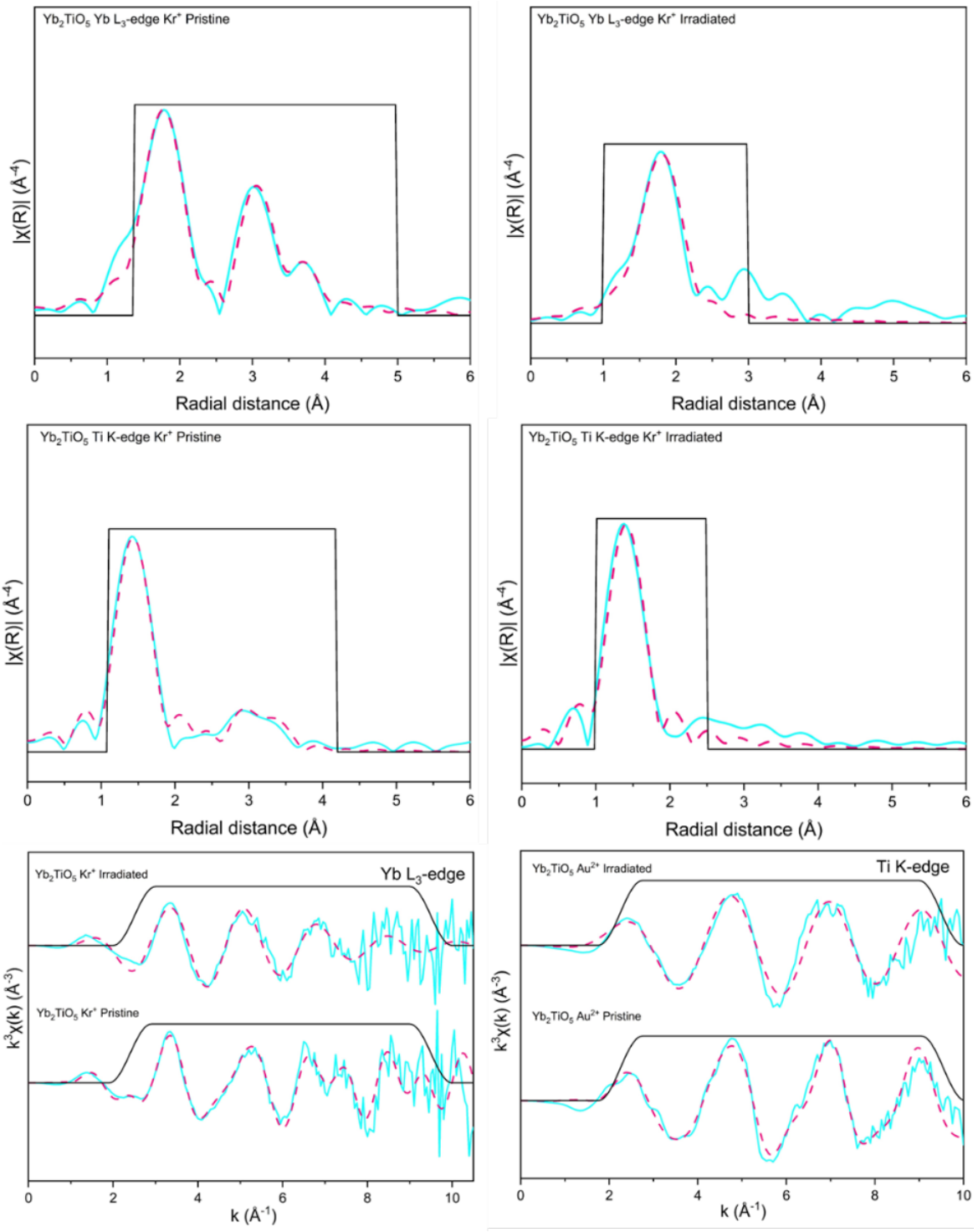

Figure S4: Fourier transform of the waveform in R-space of pristine and irradiated Yb_2TiO_5 (1 MeV Kr^+) measured in GA mode at a depth of 300 nm. The k^3 weighted Yb L_3-edge and Ti K-edge waveforms are shown alongside. Data at the top of the image were measured at the Yb L_3-edge, at the bottom they were measured at the Ti K-edge. Solid blue lines represent the experimental data, dashed pink lines represent the theoretical fit to the data and solid black lines indicate the fitting windows used.

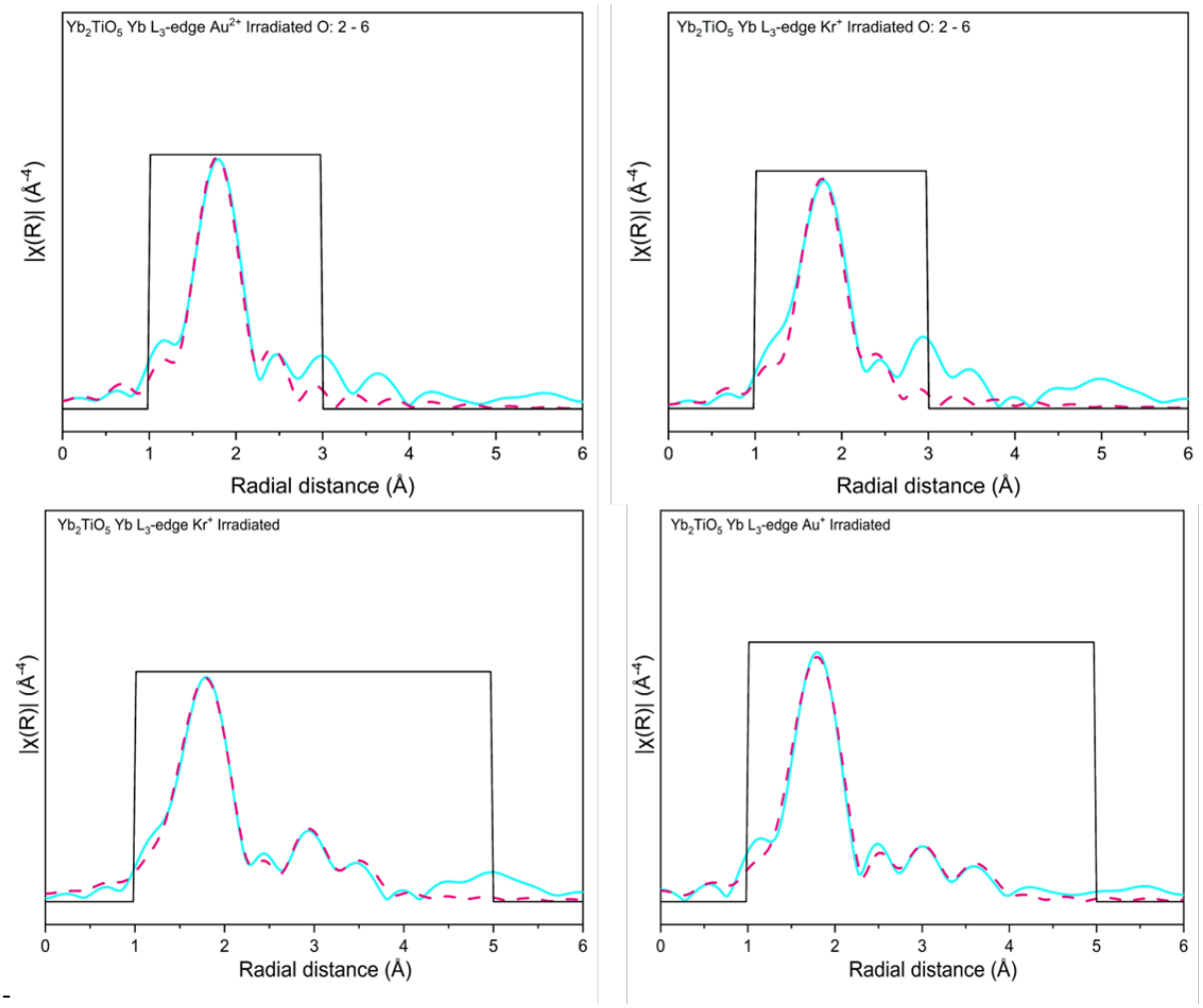

Figure S5: Fourier transform of the waveform in R-space of pristine and irradiated Yb_2TiO_5 (5 MeV Au^{2+} and 1 MeV Kr^{+}) measured in GA mode at a depth of 700 and 300 nm, respectively. Data at the top of the image were measured at the Gd L_3-edge and used two induvial O paths, with degeneracies of 2 and 6, to fit the first peak of the Fourier transform. The bottom graphs were measured at the Yb L_3-edge and fit over a data range up to 4 Å in R-space. Solid blue lines represent the experimental data, dashed pink lines represent the theoretical fit to the data and solid black lines indicate the fitting windows used.

References

[1] J. F. Ziegler, M. D. Ziegler, J. P. Biersack, J. F. Ziegler, M. D. Ziegler, and J. P. Biersack, “SRIM - The stopping and range of ions in matter (2010),” *NIMPB*, vol. 268, no. 11–12, pp. 1818–1823, Jun. 2010.

[2] R. D. Aughterson *et al.*, “The influence of crystal structure on ion-irradiation tolerance in the Sm(x)Yb(2-x)TiO5 series,” *J. Nucl. Mater.*, vol. 471, pp. 17–24, Apr. 2016.

[3] R. Sherrod, E. C. O’Quinn, I. M. Gussev, C. Overstreet, J. Neuefeind, and M. K. Lang, “Comparison of short-range order in irradiated dysprosium titanates,” *npj Mater. Degrad. 2021 51*, vol. 5, no. 1, pp. 1–7, Apr. 2021.

7. Published paper: A preliminary investigation of the molten salt mediated synthesis of Gd_2TiO_5 stuffed pyrochlore

This section explores the feasibility of using a molten salt synthesis (MSS) route to produce single-phase Ln_2TiO_5 (Ln = Gd, Dy, Yb). MSS has been demonstrated to produce single-phase ceramics at significantly reduced reaction temperatures and durations compared to typical solid-state synthesis routes (SSS), which are much more energy intensive. Not only would this be desirable from an energy-cost point-of-view but could also lead to applications of direct use of Cl contaminated waste streams that are produced as a product of pyrochemical reprocessing activities, without the need to remove the Cl before immobilisation.

The following paper was published in MRS Advances and compares the MSS and SSS routes of Gd_2TiO_5. A discussion of the MSS and SSS of Dy_2TiO_5 and Yb_2TiO_5 follows the paper and is designed to give an insight into the reasoning behind not taking these samples for further study through SEM.

The author's contribution was the synthesis of MSS and SSS samples, the collection and analysis of X-ray diffraction data. SEM microscopy was collected by M. Cole under the direction of the author. Manuscript proofing and editing were assisted by N. C. Hyatt and M. C. Stennett.

MRS Advances (2021) 6:149–153
https://doi.org/10.1557/s43580-021-00057-6

ORIGINAL PAPER

A preliminary investigation of the molten salt mediated synthesis of Gd_2TiO_5 'stuffed' pyrochlore

D. A. Austin[1] · M. Cole[1] · M. C. Stennett[1] · C. L. Corkhill[1] · N. C. Hyatt[1]

Received: 22 January 2021 / Accepted: 7 April 2021 / Published online: 19 April 2021

Abstract

Refractory 'stuffed' pyrochlores such as Gd_2TiO_5 are of interest for nuclear applications, including as matrices for actinide disposition and as neutron absorbers in control rods. Here, we report the results of a preliminary comparative investigation of the synthesis of Gd_2TiO_5 by molten salt and conventional solid-state synthesis. We show that synthesis of Gd_2TiO_5 proceeds from the pyrochlore phase $Gd_2Ti_2O_7$ which is first formed as a kinetic product. Molten salt synthesis afforded single phase Gd_2TiO_5 at 1300 °C in 2 h, via a template growth mechanism, and is effective for the synthesis of these refractory materials. This work demonstrates molten salt mediated synthesis of 'stuffed' pyrochlore for the first time.

Introduction

The fabrication of single phase ceramics is typically achieved through the use of Solid State Synthesis (SSS) methods, wherein a reaction between metal oxides precursors occurs. To enhance the solid-state diffusion necessary to produce single phase products, a combination of repeated milling and reactions at high temperatures for long durations is often necessary [1]. High temperature processing may yield large grain sizes which are an undesirable characteristic for high strength ceramic materials, and lead to non-stoichiometric products, due to the loss of volatile constituents. Issues such as these, along with the time and energy consumption of SSS methods, have motivated the development of alternative synthesis methods such as the co-precipitation, sol–gel or Molten Salt Synthesis (MSS) methods, which proceed at comparatively lower temperature.

The MSS method of synthesis exploits a salt, or a eutectic mixture of salts, which will melt at low temperature to create a liquid medium to assist in the diffusion of reactants [2–4]. MSS has been applied to the synthesis of lanthanide titanate pyrochlores at lower reaction temperatures and in shorter time scales, compared to conventional SSS. In MSS the rapid, low temperature formation of single phase products is typically achieved through either solution-precipitation or solution-diffusion mechanisms [1, 3]. The relative dissolution rate of the reactants determines which process is dominant. Solution-precipitation is achieved when the dissolution rates of the reactants are comparable, allowing both reactants to dissolve into the molten salt creating a high degree of supersaturation, prior to precipitation of the product phase [1, 5, 6]. Solution-diffusion, also referred to as template growth, involves a mechanism wherein the dissolution rate of one the reactants is significantly higher than that of the other. As the more soluble reactant dissolves into the salt medium it diffuses onto the surface of the less soluble reactant and reacts to form the target product [1]. This mechanism can also be used to control particle morphology and size.

In this preliminary study, we investigate the efficacy of MSS of Gd_2TiO_5 'stuffed' pyrochlore, to assess the potential advantages over conventional SSS. Gd_2TiO_5 is one member of the Ln_2TiO_5 (Ln = La… Lu) system, which are often termed as 'stuffed pyrochlores' due to the additional lanthanide incorporated onto the B-site of the parent pyrochlore structure (the composition may be expressed as $Ln_2(Ti_{2-x}Ln_x)O_{7-x/2}$ ($x = 0.67$)) [7]. Typically, the B site occupancy is within the range $0 \leqslant x \leqslant 0.67$ [8]. This family of titanate ceramics have been proposed as potential waste forms for actinide wastes because of their high tolerance to radiation damage, physical properties and chemical flexibility [9]. Ln_2TiO_5 'stuffed' pyrochlores exhibit different structures dependant on the size of the lanthanide, temperature and pressure used during synthesis as well as cooling

✉ D. A. Austin
daaustin1@sheffield.ac.uk

[1] NucleUS Immobilisation Science Laboratory, Department of Materials Science and Engineering, The University of Sheffield, Sheffield S1 3JD, UK

regime. Gd_2TiO_5 crystallises in an orthorhombic structure (*Pnma*), comprising a framework of intersecting columns of edge sharing LnO_7 polyhedra, with Ti cations occupying interstices within the tunnels forming TiO_5 square pyramids [10]. The range of "stuffing" reported in $Gd_2(Ti_{2-x}Gd_x)O_{7-x/2}$ is $0 \leqslant x \leqslant 0.67$ [11]; this work targets the composition with $x = 0.67$.

Experimental procedure

Gd_2O_3 and TiO_2 were used as the reagents for MSS and SSS of Gd_2TiO_5. The materials were dried at 800 °C and 180 °C, respectively, overnight. Stoichiometric amounts of the reagents were batched to 10 g. One batch for SSS was planetary ball milled (Pulverisette 6, Fritsch) at 500 rpm, for 15 min, using isopropanol as the carrier fluid (Sialon pot and media). The resulting powder slurry was dried at 80 °C overnight and passed through a 250 µm sieve. 0.5 g samples were then uniaxially pressed as 13 mm pellets (3 tonnes applied for 1 min). Green pellets were reacted at 700–1500 °C, in 100 °C intervals, for 24 h. The heating and cooling rates were 5 °C/min.

For MSS, the molten salt flux of NaCl:KCl was added at an equimolar eutectic ratio (1:1 mol NaCl:KCl; dried at 110 °C), with a 7:1 mol ratio of molten salt to ceramic precursor, as previously shown to be effective [12]. The salt and precursor mixture were milled together using the same planetary mill as for the SSS feedstock, but at a lower rotational frequency and duration; 250 rpm for 5 min, to minimise size reduction of the reagents. Cyclohexane was used as the carrier fluid. Green pellets were produced as described above and reacted at 700–1500 °C, in 100 °C intervals, for 2 h. The heating and cooling rates were 5 °C/min. The product was washed with ultrapure water to remove the molten salt medium and the powder collected via vacuum filtration.

X-ray powder diffraction analysis of reagents and products utilised a Bruker D2 Phaser instrument, operating with Cu Kα radiation and a Lynxeye solid-state detector (40 mA and 45 kV; step size of 0.02°, counting 1.8 s per step). Diffraction data were analysed for phase identification with the ICDD PDF-4 + database and ICSD sources. The PDF numbers for each phase ar as follows: Gd_2O_3 (01-074-3085), TiO_2 (01-076-0317), $Gd_2Ti_2O_7$ (01-072-9773) and Gd_2TiO_5 (21-0342) and the lattice parameters were refined through the use of the DIFFRQAC.SUITE TOPAS software [13]. Samples studied through a Scanning Electron Microscope (SEM) were prepared by mixing powder material with acetone in a 7 ml vial. The vials were placed in an ultrasonic bath for 10 min to break up any agglomerates. Samples were withdrawn from the suspension using a disposable Pasteur pipette and dropped onto a carbon sticky pad on an aluminium stub. The solvent was allowed to evaporate prior to being carbon coated. SEM micrographs were obtained with an FEI Inspect F50 operating in secondary electron (SE) mode. The accelerating voltage and spot size ranged were 20 kV and 5.0, respectively. A working distance of approximately 10 mm was used throughout.

Results and discussion

Figure 1 shows the XRD patterns of the products from MSS after reaction for 2 h at the target temperature. There was no evidence of reflections associated with either NaCl or KCl, indicating that the salt eutectic has been successfully removed. As assessed from the relative intensity of reflections, Gd_2TiO_5 and $Gd_2Ti_2O_7$ (pyrochlore) were formed at

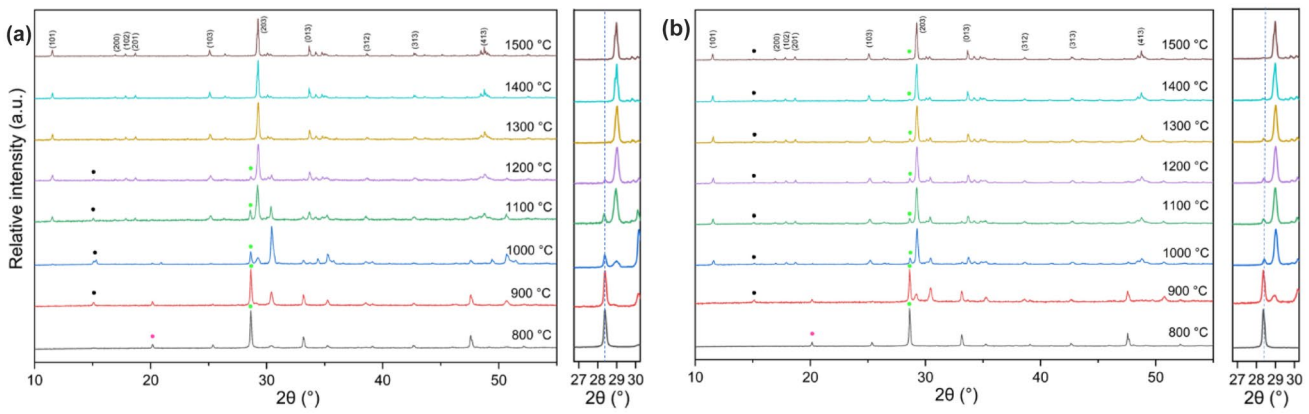

Fig. 1 XRD patterns of products from **a** MSS for 2 h and **b** SSS for 24 h, at stated temperatures. Labels correspond to reflections associated with a specific phase: Primary diagnostic reflections of reagents and accessory phases are denoted by: Solid green circles—Gd_2O_3 (222), Solid pink circles—TiO_2 (Rutile) (110), Solid black circles—$Gd_2Ti_2O_7$ (111), Miller indices indicate the major reflections of Gd_2TiO_5 (Orthorhombic). The inserts highlight the Gd_2O_3 (222) reflections

800–900 °C, with significant residual Gd_2O_3. At 1100 °C, Gd_2TiO_5 was predominant, with $Gd_2Ti_2O_7$ and Gd_2O_3 reflections diminished in relative intensity. At 1300 °C, all reflections were indexed to Gd_2TiO_5 and the product was apparently single phase. The XRD patterns for materials produced by SSS, Fig. 1, demonstrated a similar phase assemblage as a function of temperature, after reaction at the target temperatures for 24 h. Formation of Gd_2TiO_5 was first observed at 900 °C after SSS (with $Gd_2Ti_2O_7$ and residual Gd_2O_3) and was the major phase at 1000 °C. However, trace $Gd_2Ti_2O_7$ and Gd_2O_3 remain present even in specimens heated to 1500 °C, as demonstrated, for example, by the apparent (222) reflection of Gd_2O_3 ($2\theta = 29°$), which is highlighted in Fig. 1, and (111) reflection of $Gd_2Ti_2O_7$ ($2\theta = 15°$). Evidently, additional heat treatments would be needed to generate a single phase product by SSS, at 1300 °C or higher. In contrast, single phase Gd_2TiO_5 can be obtained by MSS at 1300 °C for only 2 h. The refined lattice parameters for Gd_2TiO_5, for both synthesis routes, are in good agreement with literature, Table 1. Additionally, the QPA values confirm the presence of excess $Gd_2Ti_2O_7$ and Gd_2O_3 in Gd_2TiO_5 (SSS) synthesised at 1500 °C and the absence of either phases in Gd_2TiO_5 (MSS).

SEM micrographs of Gd_2O_3 and TiO_2 reagents, Gd_2TiO_5 (MSS) and Gd_2TiO_5 (SSS) are shown in Fig. 2. Inspection of these SEM images show that the TiO_2 and Gd_2TiO_5 prepared through MSS had an average size of ~ 1 µm, and, moreover, a similar faceted morphology. In contrast, the Gd_2O_3 and Gd_2TiO_5 (SSS) particles were larger, typically 3–4 µm and 2–3 µm, respectively, comprising a more angular morphology. The striking similarity of the particulate morphology and dimensions of the Gd_2TiO_5 product and TiO_2 reagent, strongly implies a "template growth" mechanism of molten salt mediated synthesis, consistent with that previously reported for closely related $Ln_2Ti_2O_7$ pyrochlores [4, 10] The larger size of the Gd_2TiO_5 particles produced by SSS reflect

Table 1 Showing the refined lattice parameters and QPA values of primary and accessory phases for Gd_2TiO_5 synthesised at 1500 °C through either SSS or MSS routes

Gd_2TiO_5	a (Å)	b (Å)	c (Å)	V (Å^3)	Gd_2TiO_5		$Gd_2Ti_2O_7$		Gd_2O_3	
					wt%	±	wt%	±	wt%	±
SSS	10.4811 (2)	3.7575 (5)	11.3216 (2)	446.01 (14)	94.47	0.44	3.27	0.33	2.26	0.24
MSS	10.4816 (3)	3.7574 (9)	11.3245 (3)	445.87 (19)	100	–	–	–	–	–
Gd_2TiO_5 [14]	10.46	3.75	11.31	446.00	–	–	–	–	–	–

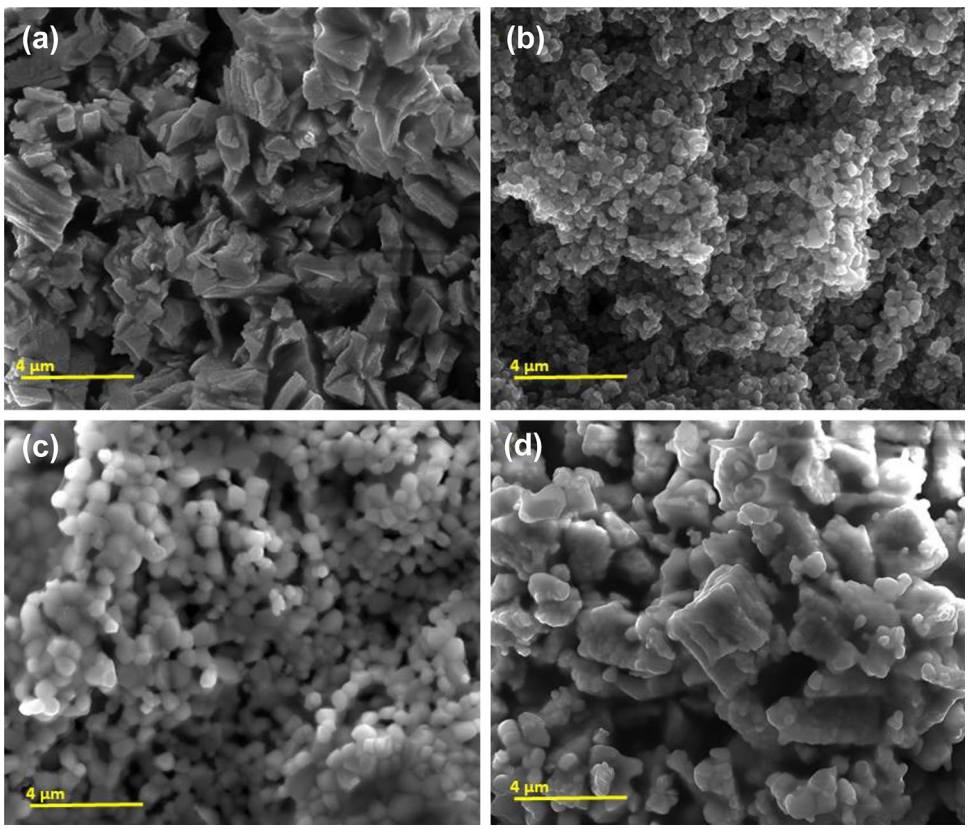

Fig. 2 SEM Micrographs of reagent materials and resultant products collected in secondary electron mode. **a** Gd_2O_3, **b** TiO_2, **c** Gd_2TiO_5 (MSS: 1300 °C 2 h) and **d** Gd_2TiO_5 (SSS: 1500 °C 24 h)

the process of solid-state diffusion and growth at comparatively higher temperature. Size reduction was minimised during the milling stage of preparing the MSS samples so as to rule out that the reduction in the size of the larger Gd_2O_3 reagents produced the observed size of the Gd_2TiO_5 particles prepared by MSS. The very low solubility of TiO_2 in alkali chloride salts has been established in several previous studies of the synthesis of ternary titanate materials, leading to a common "template growth" mechanism that has been exploited to produce titanate materials as nanopowders and with rod-like morphologies, directed by the TiO_2 template [15–18]. In the present study, the solubility of TiO_2 is also expected to control the synthesis mechanism by "template growth" resulting in a product with morphological and dimensional characteristics of the TiO_2 reagent.

Comparing the MSS and SSS routes, the pyrochlore phase is the first to be formed below 900 °C, giving way to the 'stuffed' pyrochlore Gd_2TiO_5 at 1000 °C as the major phase, with single phase Gd_2TiO_5 achieved at 1300 °C by MSS. The pyrochlore phase is apparently a kinetic product in the synthesis of 'stuffed' pyrochlores by MSS and SSS below 1300 °C; subsequent reaction with Gd_2O_3 yields the desired 'stuffed' pyrochlore. As far as we are aware, this is the first such mechanistic understanding developed with regard to the synthesis of 'stuffed' pyrochlores. It is evident that molten salt mediated diffusion is effective in achieving the synthesis of single phase Gd_2TiO_5 at much lower temperature and time, 1300 °C for 2 h, compared to SSS which did not afford a single phase product even at 1500 °C for 24 h.

Conclusion

This preliminary investigation has determined that the $Gd_2Ti_2O_7$ pyrochlore phase forms as the kinetic product in the synthesis of Gd_2TiO_5 'stuffed' pyrochlore. The MSS method effectively yields single phase Gd_2TiO_5 at 1300 °C for 2 h, via a template growth mechanism, in which TiO_2 acts as the initial nucleating substrate. In contrast, SSS failed to yield single phase Gd_2TiO_5 after reaction at 1500 °C for 24 h. Given the highly refractory nature of the Ln_2TiO_5 pyrochlores, and their potential application in nuclear environments, MSS is therefore clearly worthy of further investigation as a route to the synthesis of this family of ceramic materials.

Acknowledgments DAA is grateful to the Engineering and Physical Sciences Research Council (EPSRC) for funding. This research utilised the HADES/MIDAS facility at The University of Sheffield established with financial support from EPSRC and BEIS, under grant EP/T011424/1 and was supported by grant EP/S01019X/1 [19].

References

1. D. Segal, Chemical synthesis of ceramic materials. J. Mater. Chem. **7**(8), 1297–1305 (1997)
2. A.R. Mason, F.Y. Tocino, M.C. Stennett, N.C. Hyatt, Molten salt synthesis of Ce doped zirconolite for the immobilisation of pyroprocessing wastes and separated plutonium. Ceram. Int. **46**(18), 29080–29089 (2020)
3. S. Zhang, Low temperature synthesis of complex refractory oxide powders from molten salts. J. Pak. Mater. Soc **1**, 49 (2007)
4. M.R. Gilbert, Molten salt synthesis of titanate pyrochlore wasteforms. Ceram. Int. **42**(4), 5263–5270 (2016)
5. Z. Li, W.E. Lee, S. Zhang, Low-temperature synthesis of $CaZrO_3$ powder from molten salts. J. Am. Ceram. Soc. **90**(2), 364–368 (2007)
6. C. Liu, X. Liu, Z. Hou, Q. Jia, B. Cheng, S. Zhang, Low-temperature molten salt synthesis and the characterisation of submicron-sized Al8B4C7 powder. Materials **13**(1), 70 (2020)
7. S. Park et al., Swift-heavy ion irradiation response and annealing behavior of A2TiO5(A = Nd, Gd, and Yb). J. Solid State Chem. **258**, 108–116 (2018)
8. G.C. Lau, B.D. Muegge, T.M. McQueen, E.L. Duncan, R.J. Cava, stuffed rare earth pyrochlore solid solutions. J. Solid State Chem. **179**(10), 3126–3135 (2006)
9. X. Liu et al., Insights into the radiation behavior of Ln2TiO5(Ln = La-Y) from defect energetics. Comput. Mater. Sci. **139**, 295–300 (2017)
10. M.A. Petrova, R.G. Grebenshchikov, Specific features of the phase formation in the titanate systems Ln_2TiO_5-Ln'_2TiO_5 (Ln = La, Gd, Tb, Er; Ln′ = Tb, Lu). Glass. Phys. Chem. **34**, 603 (2008)
11. J.L. Waring, S.J. Schneider, Phase equilibrium relationships in the system Gd_2O_3-TiO_2. J. Res. Natl. Bur. Stand. A **69A**(3), 255 (1965)
12. M.L. Hand, M.C. Stennett, N.C. Hyatt, Rapid low temperature synthesis of a titanate pyrochlore by molten salt mediated reaction. J. Eur. Ceram. Soc. **32**(12), 3211–3219 (2012)
13. A.A. Coelho, TOPAS and TOPAS-Academic: an optimization program integrating computer algebra and crystallographic objects written in C++: An. J. Appl. Crystallogr. **51**(1), 210–218 (2018)
14. R.D. Aughterson, G.R. Lumpkin, G.J. Thorogood, Z. Zhang, B. Gault, J.M. Cairney, Crystal chemistry of the orthorhombic Ln 2 TiO 5 compounds with Ln =La, Pr, Nd, Sm, Gd, Tb and Dy. J. Solid State Chem. **227**, 60–67 (2015)
15. Q. Ji, P. Xue, H. Wu, Z. Pei, X. Zhu, Structural characterizations and dielectric properties of sphere- and rod-like $PbTiO_3$ powders synthesized via molten salt synthesis. Nanoscale Res. Lett. **14**(1), 1–12 (2019)
16. J. Yang, Y. Hou, C. Wang, M. Zhu, H. Yan, Relaxorbehavior of $(K_{0.5}Bi_{0.5})TiO_3$ ceramics derived from molten salt synthesized single-crystalline nanowires. Appl. Phys. Lett. **91**(2), 023118 (2007)

17. Z. Cai, X. Xing, R. Yu, X. Sun, G. Liu, Morphology-controlled synthesis of lead titanate powders. Inorg. Chem. **46**(18), 7423–7427 (2007)
18. T. Kimura, Molten salt synthesis of ceramic powders, in *Advances in Ceramics - Synthesis and Characterization, Processing and Specific Applications* (InTech, 2011)
19. N.C. Hyatt, C.L. Corkhill, M.C. Stennett, R.J. Hand, L.J. Gardner, C.L. Thorpe, The HADES facility for high activity decommissioning engineering & science: part of the UK National Nuclear User Facility, in *IOP Conference Series: Materials Science and Engineering*, vol. 818(1) (2020)

MSS and SSS of Dy_2TiO_5 and Yb_2TiO_5 stuffed pyrochlores

The section that follows is a preliminary trial of the feasibility of an MSS route for the synthesis of cubic Yb_2TiO_5 and either orthorhombic or hexagonal Dy_2TiO_5. An MSS route that produced single-phase ceramics would be desirable for the same reasoning gave in the manuscript above. Furthermore, an MSS route would also provide a method of directly using the actinide waste and chlorine salt eutectic (e.g., $PuCl_3$) generated as a product of pyrochemical reprocessing. Pyrochemical reprocessing is an alternative method of reprocessing nuclear fuel to recover Pu metal, avoiding the intermediate step of conversion to PuO_2, as is the case with typical plutonium uranium reduction extraction (PUREX) reprocessing [1]. In this method an electrorefining process separates Pu from other impurities present in SNF in a molten salt, or salt eutectic. Additional separations can be carried out to reduce the content of the radionuclide, ^{241}Am, that has been produced as a result of radioactive decay of Pu, yielding both Pu and Am salts (i.e. $PuCl_3$, $AmCl_2$ or $AmCl_3$) [2]. The synthesis of these compounds followed the route given in the manuscript above. This section is aimed at discussing why studies of these samples were not taken further and ultimately resulted in the publication of the results of the MSS of Gd_2TiO_5, which was successful.

The MSS and SSS fabrication routes of Yb_2TiO_5 can be found in Figure 3. The formation of Yb_2TiO_5 begins at 900 ^oC and 1100 ^oC, respectively, for the samples synthesised using a MSS or SSS route. Both synthesis methods are accompanied by accessory phases of Yb_2O_3 and $Yb_2Ti_2O_7$ but the absence of NaCl or KCl peaks indicates that the salt eutectic has been removed. The SSS route appears to have produced a phase assemblage of near complete Yb_2TiO_5 at 1400 ^oC, indexed in the *Fm-3m* space group. By 1500 ^oC the characteristic peaks are highly resolved, and no evidence of any other phase remains. Conversely, the MSS route did not yield as encouraging results. Reflections associated with $Yb_2Ti_2O_7$ were still observable at 1500 ^oC, the inset of Figure 1b clearly shows the progressive reduction in peak intensity of Yb_2O_3 and $Yb_2Ti_2O_7$ reflections as they react with one another to produce Yb_2TiO_5. The $Yb_2Ti_2O_7$ reflection in the inset, highlighted by a blue dashed line and labelled with a diamond symbol, can be seen to cause a slight asymmetry in the Yb_2TiO_5 reflection (spades, green) which occurs at a very similar 2θ position (~ 30.5 ^{o}). Following the initial study, a Yb_2TiO_5 MSS sample was reacted for 24 hours at 1500 ^oC and the resultant phase assemblage does indicate a very near single phase product, however the slight Yb_2TiO_5 peak asymmetry, as well as the peak 15 ^{o}, indicate that a small amount of $Yb_2Ti_2O_7$ remains, though the relative peak intensity is reduced compared to the sample reacted for 2 hours.

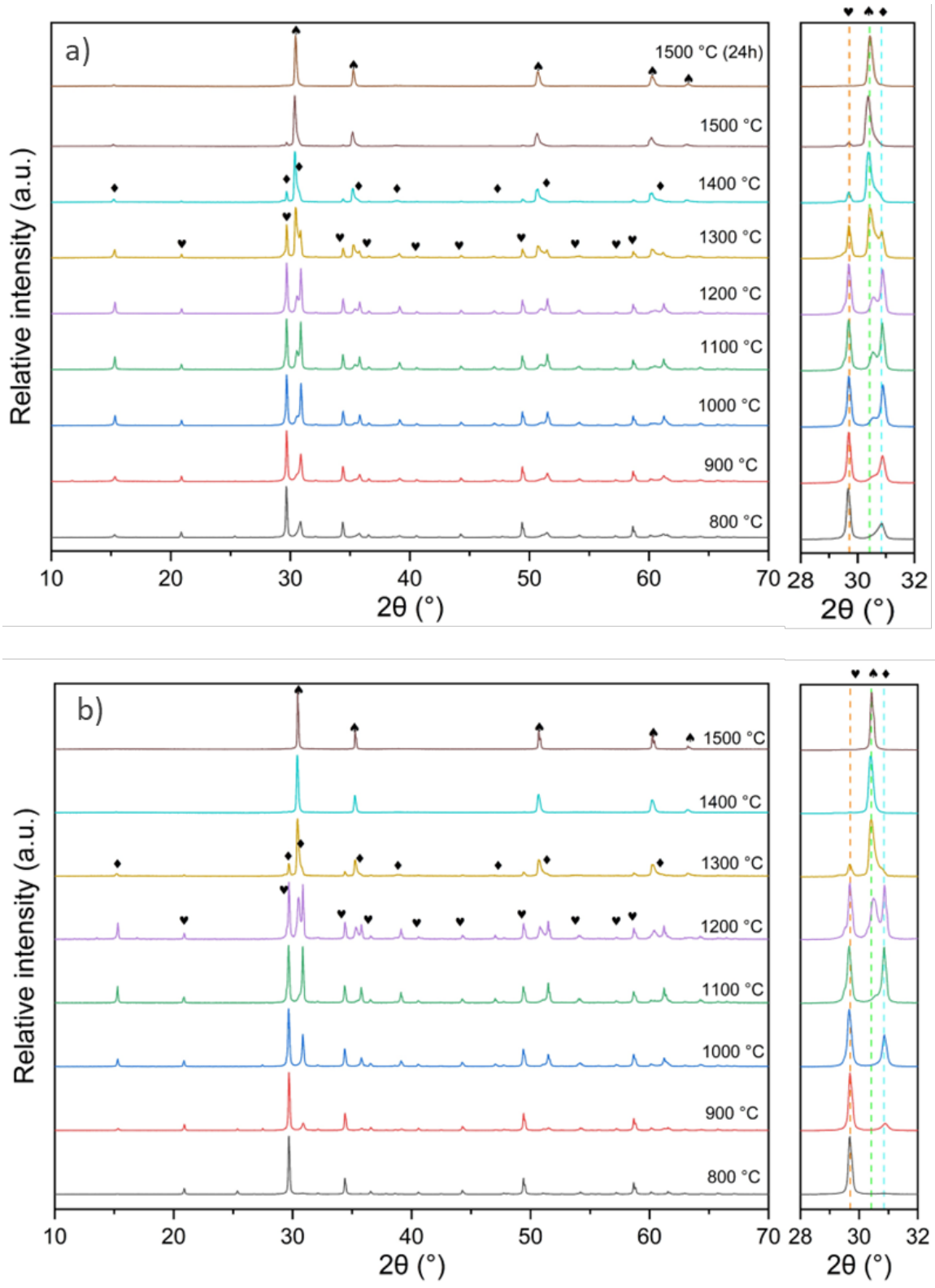

Figure 3: XRD patterns of products from a) MSS for 2 h at the stated temperatures and at 1500 °C for 24 h and b) SSS for 24 h, at stated the temperatures. Spades indicate reflections of Yb_2TiO_5 (*Fm-2m*), diamonds indicate reflections of $Yb_2Ti_2O_7$ (*Fd-3m*), and hearts indicate reflections for Yb_2O_3 (*Ia-3*).

Primary diagnostic reflections are highlighted in the inset and are further indicated by colours dashed lines (coloured orange for Yb_2O_3, green for Yb_2TiO_5 and blue for $Yb_2Ti_2O_7$)

The MSS of Dy_2TiO_5 also failed to produce a single-phase product. As shown by *Shepelev and Petrova*, Dy_2TiO_5 can undergo polymorphic transitions depending on the synthesis temperature, between 1350 – 1650 ^oC a hexagonal structure can be obtained, above this temperature a cubic structure and below an orthorhombic [3]. Due to the narrow stability range of the hexagonal polymorph, it is difficult to form hexagonal Dy_2TiO_5 through typical SSS routes, it has been demonstrated that rapid cooling regimes are needed to obtain this phase [4]. Both SSS and MSS routes produced a mixed phase assemblage of orthorhombic and hexagonal Dy_2TiO_5, the hexagonal phase is significantly more unstable than the orthorhombic phase, therefore as the reaction temperature reduces part of the hexagonal phase relaxes back into an orthorhombic symmetry. Both synthesis routes formed a mixture orthorhombic Dy_2TiO_5 at 1200 ^oC and hexagonal Dy_2TiO_5 at 1400 ^oC (Figure 4) at the highest reaction temperature trialled (1500 ^oC). The SSS route did result in complete reaction of Dy_2O_3 and $Dy_2Ti_2O_7$, as indicated by the absence of reflections associated with those phases, by 1400 ^oC; compared to the MSS which saw complete reaction of these precursors at 1500 ^oC, longer reaction durations or alternate salt eutectics could possibly aid the reaction process of the MSS of Dy_2TiO_5 and result in complete reaction of precursor materials at lower temperatures.

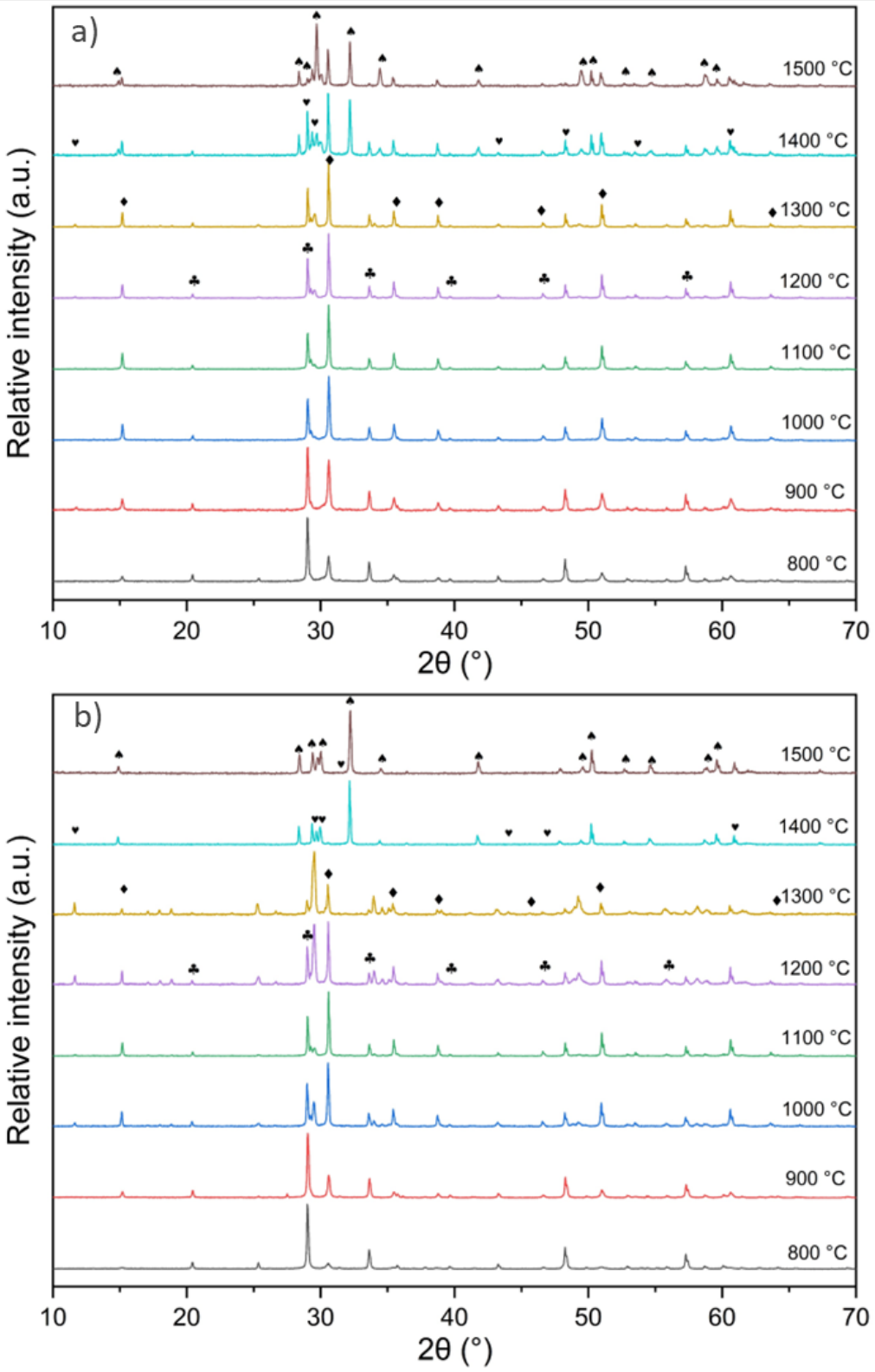

Figure 4: XRD patterns of products from a) MSS for 2 h and b) SSS for 24 h, at stated the temperatures. Spades indicate reflections of Dy_2TiO_5 (*P6₃-mmc*), hearts indicate reflections of Dy_2TiO_5 (*Pnma*), diamonds indicate reflections of $Dy_2Ti_2O_7$ (*Fd-3m*) and clubs indicate reflections for Dy_2O_3 (*Ia-3*).

The purpose of this study was to investigate the feasibility of a MSS route for both Dy_2TiO_5 and Yb_2TiO_5, and as has been shown, the MSS route failed to produce single-phase products of either. Whilst Yb_2TiO_5 did produce a near single-phase product after reaction at 1500 ^oC for 24 hours, the SSS route produced a completely single-phase product. This nullifies the benefit the MSS route typically provides, i.e. a reduced rection temperature and/or shorter reaction duration. A NaCl:KCl eutectic was chosen for this study to be consistent with the composition used to model wastes arising from pyrochemical reprocessing activities mixed oxide fuels at the Research Institute for Atomic Reactors in Russia, pyrochemical reprocessing of metallic fuel produced at Argonne National Laboratory from the Experimental Reactor Breeder II and pyrochemical reprocessing of thorium fuels at the Joint Research Centre-Institute for Trans Uranium Elements (JRC-ITU) [5]–[7]. Additionally, MSS of Dy_2TiO_5 utilising faster cooling rates could also potentially lead to a higher proportion of the hexagonal polymorph being produced. Due to limited time constraints, Gd_2TiO_5 samples were taken forward for further study as they demonstrated positive results due to the formation of single phase Gd_2TiO_5 over comparatively much shorter time scales through an MSS compared to a SSS route.

References

[1] T. Nishimura, T. Koyama, M. Iizuka, and H. Tanaka, “Development of an environmentally benign reprocessing technology—pyrometallurgical reprocessing technology,” *Prog. Nucl. Energy*, vol. 32, no. 3–4, pp. 381–387, Jan. 1998.

[2] M. R. Gilbert, “Molten salt synthesis of titanate pyrochlore waste-forms,” *Ceram. Int.*, vol. 42, no. 4, pp. 5263–5270, Mar. 2016.

[3] Y. F. Shepelev and M. A. Petrova, “Crystal structures of Ln_2TiO_5 (Ln = Gd, Dy) polymorphs,” *Inorg. Mater.*, vol. 44, no. 12, pp. 1354–1361, Dec. 2008.

[4] R. D. Aughterson, N. J. Zaluzec, and G. R. Lumpkin, “Synthesis and ion-irradiation tolerance of the Dy2TiO5 polymorphs,” *Acta Mater.*, vol. 204, p. 116518, Feb. 2021.

[5] O. N. E. Agency, “Management of the UK’s Plutonium Stocks: A Consultation Response on the Proposed Justification Process for the Reuse of Plutonium,” 2013.

[6] N. R. Council, “Electrometallurgical Techniques for DOE Spent Fuel Treatment: Final Report,” National Academies Press, Apr. 2000.

[7] O. N. E. Agency, “Pyrochemical Separations in Nuclear Applications, A Status Report,” 2004. [Online]. Available: http://www.oecd.org/.

8.1 Conclusions and recommendations for future work

For a material to be considered as a potential actinide waste host, it must exhibit a series of appropriate characteristics and properties. One such property is a demonstratable resistance to radiation damage since radionuclides such as ^{241}Am and ^{239}Pu, present in waste material, undergo α-decay which can have detrimental effects on the performance of the wasteform over its expected lifetime (10^5 – 10^6 years). A predictable and well understood response to radiation damage is paramount to the successful and appropriate implementation of a wasteform.

Whilst there is an emerging focus of research on the development of Ln_2TiO_5 stuffed pyrochlores as potential ceramic wasteforms, there is a distinct lack of understanding or consensus of the short-range structural ordering of these materials, with respect to both the irradiated and unirradiated stuffed pyrochlores. This thesis utilised various XAS techniques to probe the local structure of the various structure types of these materials for the first time, in addition to collecting XAS data in a glancing-angle geometry to probe the irradiated, surface damaged region of ceramic stuffed pyrochlore monoliths. Additionally, a comparative study of solid-state and molten salt synthesis routes was conducted to determine if any of these structures could exploit the processing benefits of a MSS method to achieve single-phase products at lower temperatures and/or reaction durations. Following the summaries of these studies, a discussion of potential future work is given to aid the development of Ln_2TiO_5 stuffed pyrochlores as nuclear wasteform materials.

The studies detailed in chapters 4 and 5 have developed a substantial understanding of the local structural properties of stuffed pyrochlores through extensive characterisation by XRD and XAS. Furthermore, these chapters form the necessary groundwork for future studies employing XAS techniques to probe the effects of radiation damage on the local coordination and structures of ceramic wasteforms.

In chapter 6, the effect of radiation damage upon the short-range order of the three crystal structures associated with Ln_2TiO_5 stuffed pyrochlore were studied. These samples were orthorhombic *Pnma* Gd_2TiO_5, hexagonal *P6₃/mmc* Dy_2TiO_5 and cubic *Fm-3m* Yb_2TiO_5 (with a short-range *Fd-3m* structure). These samples were subject to 5 MeV Au^{2+} and 1 MeV Kr^+ heavy ion beam irradiations to simulate the effects of α-recoil damage, and were characterised using GAXRD, SEM and GAXAS techniques. The profile and depth of the ion beam irradiation was modelled using the SRIM software, showing that the peak of the damage profile was around 500 nm for samples irradiated under 5 MeV Au^{2+} ions and 300 nm for those irradiated under 1 MeV Kr^+ ions, informing the setup of the GAXAS experiment. XAS spectra measured at the Gd L_3- (7243 eV), Dy L_3- (7790 eV), Yb L_3- (8944 eV) and Ti K-edges (4966 eV) were collected on the damaged surface region of ceramic samples and compared to pristine analogues to enable more robust analyses.

8.1 Synthesis of Ln_2TiO_5 stuffed pyrochlores

A broad range of Ln_2TiO_5 (Ln = La, Pr, Nd, Sm, Eu, Gd, Tb, Dy, Ho, Er, Tm, Yb, Lu) stuffed pyrochlores were synthesised and their structures studied using XAS techniques (including XANES and EXAFS analyses), XRD, and SEM/EDX. The crystal structure of Ln_2TiO_5 compounds was largely dictated by the ionic radius of the lanthanide used or by thermal history. The long-range order of samples was described, *via* XRD, as orthorhombic *Pnma* for Ln_2TiO_5 (Ln = La – Tb), hexagonal *P6₃/mmc* for Dy_2TiO_5 and cubic *Fm-3m* for Ln_2TiO_5 (Ln = Ho – Lu). Despite hexagonal polymorphs being theoretically possible for Gd_2TiO_5 and Tb_2TiO_5, only Dy_2TiO_5 could be successfully stabilised with a hexagonal structure. This was due to the very narrow stability range of the hexagonal polymorphic transition for the former two compositions.

To probe the effect of different thermal histories on both the long- and short-range structures of these materials, stuffed pyrochlores of Y_2TiO_5 and Yb_2TiO_5 were synthesised under different cooling regimes. Ln_2TiO_5 (Ln = Ho – Lu, Y) have been shown to adopt cubic structures with long-range defect-fluorite *Fm-3m* symmetries, depending on reaction temperatures. XRD showed that a slow cooling rate of these compounds promoted the appearance of small, weak reflections in both samples but were absent in those that were rapidly cooled. These reflections, which could be indexed on a pyrochlore *Fd-3m* unit cell, had been previously linked to an arrangement of nanodomains that have a pyrochlore- type structure.

To further enhance the synthesis process of Ln_2TiO_5 stuffed pyrochlores, preliminary trials of the molten salt mediated synthesis (MSS) of Ln_2TiO_5 compounds was undertaken. A detailed study of comparing solid-state synthesis (SSS) and MSS proved to be an effective route for only orthorhombic Gd_2TiO_5. Compared to typical SSS methods, the molten salt reaction facilitated the formation of a single-phase, orthorhombic Gd_2TiO_5 at 1300 °C after 2 hours (an entirely single-phase product could not be produced of the same sample using solid-state synthesis methods after reaction at 1500 °C for 24 hours). This was driven by a template growth mechanism, where TiO_2 acted as nucleating substrate. Similar trials of Dy_2TiO_5 and Yb_2TiO_5 yielded multiphase composites. Further work to develop other orthorhombic Ln_2TiO_5 compounds should be undertaken to ascertain whether molten salt synthesis methods are effective for the entire series. This result could also open the doorway to the development of orthorhombic Ln_2TiO_5 ceramic wasteforms that directly incorporate Cl contaminated actinide waste streams arising from pyroprocessing processes.

8.2 Orthorhombic Ln_2TiO_5 structural details and their response to radiation as exemplified by Gd_2TiO_5

XAS measurements were collected on orthorhombic Ln_2TiO_5 (Ln = La – Tb) stuffed pyrochlores at the Ln L_3-edge (5483 eV – 7514 eV) and Ti K-edge (4966 eV) for all samples to probe the short-range order of each structure. Qualitative and quantitative interpretations of the XANES region of Ti K-edge spectra

showed that the Ti-O coordination of Ln_2TiO_5 (Ln = La – Tb) stuffed pyrochlores contain 5-fold coordinated Ti in a square pyramidal motif, consistent with the Ti coordination of ascribed to long-range order determined by XRD. EXAFS analysis was undertaken on representative samples Pr_2TiO_5, Nd_2TiO_5, Sm_2TiO_5 and Gd_2TiO_5 to model changes in the short-range order of compounds that were also characterised as having long-range orthorhombic ordering. No distinction could be found between the local coordination of the two Ln-sites. Interestingly, multiple paths were required to satisfactorily fit the O shell in the 8-fold coordinated systems, such as cubic Lu_2TiO_5, indicating that there are greater levels of distortion to the local coordination of cubic compounds than observed in the 7-fold coordinated species characteristic of orthorhombic *Pnma* structured Ln_2TiO_5. It was further seen that an increase in ionic radii (e.g., 1.13 Å and 1.05 Å for Pr and Gd, respectively) was accompanied by an increase in bond lengths, as would be expected. The establishment of a model to describe the short-range order of orthorhombic Ln_2TiO_5 allowed for determination of radiation effects.

Results of the GAXAS investigation of radiation damaged surface of Gd_2TiO_5 showed the local structure of orthorhombic Gd_2TiO_5 undergoes a transition towards a more disordered structure following irradiation, with anti-site defects driving this change. Consequently, the resulting structure was shown by electron diffraction to be similar to the *Fm-3m* defect-fluorite structure, where there is complete cation disordering. Furthermore, evidence from both the XANES and EXAFS analysis show the Gd-O and Ti-O coordination numbers are moving towards an average of 6, suggesting the predominant formation of Ln_2-Ti, followed by Ln_1-Ti, anti-site defects. However, it should be noted that there is some uncertainty surrounding the exact Ln site that is favoured due to the limitations of XAS.

8.3 Hexagonal Ln_2TiO_5 structural details and their response to radiation as exemplified by Dy_2TiO_5

XRD and SEM/EDX confirmed the successful synthesis of hexagonal *P6₃/mmc* Dy_2TiO_5. As this structure is infrequently reported in literature, the use of XAS characterisation measured at the Dy L_3- (7790 eV) and Ti K-edges (4966 eV) allowed for a unique insight into the short-range structure of this compound.

Pre-edge features of Ti K-edge spectra of Dy_2TiO_5 were comparatively less intense, consistent with a coordination geometry of a higher degree of centrosymmetry, such as TiO_5 trigonal bipyramid motif than pre-edge features of orthorhombic Ln_2TiO_5 stuffed pyrochlores (which has squared based pyramidal TiO coordination). The short-range order of hexagonal Dy_2TiO_5 was well represented by models of the same structural types observed through XRD (i.e., hexagonal *P6₃/mmc*), indicating little deviation between measurement ranges and no super structure modulation. EXAFS showed the Ln-O and Ti-O coordination was 8-fold and 5-fold coordinated, respectively. Attempts to quantify the amount of Dy cations occupying Ti-sites proved unsuccessful. As XAS is a measurement of the average local structure of the absorbing atom, the minor Ti-site occupancy of Dy atoms was not significant enough to alter the XAS signal.

GAXAS measurements of radiation damaged hexagonal Dy_2TiO_5 showed that a significant loss in both medium- and short-range order occurred post-irradiation. Consequently, a disturbance to local structure of Dy_2TiO_5 the coordination polyhedra of Dy and Ti cations was found, where the Dy-O coordination reduced from 8 to 7 and for Ti-O from 5 to 4.3, contractions in cation to oxygen bond lengths were also observed. The radiation behaviour of hexagonal Dy_2TiO_5 was comparatively poor when considered alongside other Ln_2TiO_5 structures as it was found to readily amorphise under identical irradiation conditions. Therefore, it is justifiable to suggest that Ln_2TiO_5 ceramics that adopt hexagonal *$P6_3/mmc$* structures would not make ideal candidates for actinide waste immobilisation.

8.3 Cubic Ln_2TiO_5 structural details and their response to radiation as exemplified by Yb_2TiO_5

XAS data collected at the Yb L_3- (8944 eV), Y K- (17038 eV), and Ti K-edges (4966 eV) revealed a structure that corresponded to a pyrochlore-like structure. However, some differences were present with the Ti coordination reducing from the characteristic TiO_6 polyhedra, seen in *Fd-3m* $Ln_2Ti_2O_7$ pyrochlores, to a TiO_5 coordination. Additionally, Ti K-edge pre-edge features in both Y_2TiO_5 and Yb_2TiO_5 had peak profiles and positions in line with centrosymmetric geometries, such as trigonal bipyramidal motif. Furthermore, there was evidence in the EXAFS analysis of Yb L_3-, Y K- and Ti K-edges that the cooling regime had a direct impact on the bond distances of cation-anion and cation-cation pairs, where slow cooled (1 °C/min) samples had larger bond distances. This agrees with the presence of weak reflections in the XRD patterns of slow cooled samples, as their prevalence had been previously shown to depend upon the size of nanodomains, where the larger domains gave rise to more readily observable reflections. The results of this study were further corroborated in chapter 5, where cubic Ln_2TiO_5 (Ho – Lu) were synthesised and subsequently analysed by XRD, XANES and EXAFS analyses. The long-range structure of cubic Ln_2TiO_5 in chapter 5 was confirmed by XRD to adopt a defect-fluorite *Fm-3m* structure, with evidence of weak reflections indicative pyrochlore-like short-range order ordering. The models produced from the EXAFS analysis of the Ln L_3-edges (8071 – 9244 eV) and Ti K-edge (4966 eV) indicated the local structural environment of cubic Ln_2TiO_5 compounds was consistent with that previously observed for Yb_2TiO_5 synthesised under varied cooling regimes. Here, Ti was again found to be in 5-fold coordination and Ln cations in 8-fold coordination.

GAXAS measurements were collected to probe the effects of 5 MeV Au^{2+} and 1 MeV Kr^{+} heavy-ion irradiation on the short-range order of cubic Ln_2TiO_5. The heavy ion irradiation of cubic Yb_2TiO_5 caused a significant reduction in medium range order. EXAFS analysis showed a reduction in intensity of features in the irradiated Yb_2TiO_5 Fourier transform (between 2 – 4 Å). This change from the pristine EXAFS data was a consequence of a change in the average degeneracies of the paths (Yb-Ti and Yb-Yb) which contribute to this region of the spectrum. These lower path degeneracies indicated that whilst some Yb-Yb / Yb-Ti paths remain intact, significant disorder was present in the short-range structure, which was further reinforced by the need for two Yb-O paths to accurately model the first O shell. Furthermore, whilst the YbO_8 polyhedra remained intact, the Yb-O paths in the irradiated

model had higher Debye-Waller factors, σ^2, values compared to the pristine model as a consequence of the increased disorder of the Yb-O coordination polyhedra. The TiO_5 coordination found in the pristine Yb_2TiO_5 also remained intact following irradiation.

Overall, the result of the GAXAS analysis show that the amorphisation pathway for these materials begins with a loss of long- and medium-range order. The proposed mechanism is thought to rely on the high anti-site defect energy of cubic Ln_2TiO_5 stuffed pyrochlores (highest were those with the smallest lanthanides such as Yb_2TiO_5 or Lu_2TiO_5) which may cause the structure to eventually collapse into an amorphous state through the accumulation of cation interstitial and vacancy pairs.

8.4 Comparison of radiation behaviour of Ln_2TiO_5 structures

The work presented in this thesis constitutes the first experimental study that confirms the mechanisms for enhanced radiation resistance of orthorhombic Ln_2TiO_5. By underpinning such mechanisms, the design of Ln_2TiO_5 compounds can be optimised to enhance their performance and reliability when utilised in reactor operations (control rods configurations etc.) or as ceramic wasteforms. Furthermore, is has also been demonstrated that cubic Yb_2TiO_5 is efficient at resisting potentially detrimental radiation induced structural changes and as such are an ideal ceramic wasteform candidate for actinide waste immobilisation. The mechanisms for radiation tolerance of both orthorhombic and cubic systems, then, are quite similar and are highly influenced by the anti-site defect mobility of the structures. However, the extent of defect accumulation in the cubic system does appear to be lesser than that of the orthorhombic system, highlighting that more extensive or prolonged damage to the cubic structure would be required before it collapses. Nonetheless, both structure types would be an efficient choice of ceramic wasteform. This is a particularly positive result as the structure stability is likely to be influenced by the ionic radius of actinide species immobilized in the matrix (or waste loading % thereof).

Whilst this work offers important insights into the radiation response of the local structures of Ln_2TiO_5 stuffed pyrochlores, it also constitutes a significant development in the application of GAXAS to study irradiated nuclear materials. Previously, the study of radiation damaged materials by XAS had been limited to samples that incorporated short-lived, highly radioactive elements directly (i.e., ^{244}Cm-doped $Gd_2Ti_2O_7$) or naturally metamict mineral analogues. The methods used here demonstrate how GAXAS can be utilised for the rapid, safe, and accurate determination of radiation behaviour in nuclear materials when used in conjunction with heavy-ion beam irradiations.

8.5 Further work

The work in this thesis has thoroughly investigated stuffed pyrochlores, from initial synthesis methods to comprehensive structural characterisation. However, there are areas of further work that should be addressed to further develop and underpin the knowledge base of these compounds. Firstly, synthesis of the stuffed pyrochlores whilst effective, is not optimised. Therefore, alternative routes should be explored.

During this work, dense, single-phase ceramic products could only be achieved after iterative sintering treatments. This process is time and energy intensive and poses the risk of losing radioactive material to volatilisation. Other densification and synthesis methods, such as hot isostatic pressing (HIP) and spark-plasma sintering (SPS), have proven to be successful for the fabrication of dense zirconolite and pyrochlore ceramics. Both synthesis methods offer advantages over conventional cold press and sinter approaches; HIP significantly reduces the bulk volume through the application of both heat and isostatic pressure to consolidate ceramic products; and SPS offers a very high throughput and duplicability due to rapid heating rates (up to 1000 $^{o}C\ min^{-1}$). The synthesis Ln_2TiO_5 stuffed pyrochlores through these methods would not only provide an effective means of achieving highly dense ceramics but could exploit the numerous advantages that they offer.

Additional consideration should be given to further developing and understanding the radiation tolerance of these materials. Following on from the conclusions on chapter 6, whereby a Ln_2-Ti anti-site defects were observed to be a primary mechanism behind the radiation response of orthorhombic Ln_2TiO_5, further work to elucidate the mechanism behind this relationship is needed. A future study employing GAXAS on an orthorhombic Ln_2TiO_5 stuffed pyrochlore series would enable a deeper understanding of the dependency of radiation response on the ionic radius of lanthanide cations.

Studies by other authors showed that the variation in trend of Ln_2-Ti anti-site defect formation energy in orthorhombic Ln_2TiO_5 stuffed pyrochlores appears to accurately follow the trend of the critical temperatures for amorphisation (T_c). The T_c improved with decreasing lanthanide size from Nd_2TiO_5 to Y_2TiO_5 but deteriorated from La_2TiO_5 to Nd_2TiO_5. This close relationship suggests a link between radiation resistance of anti-site defect formation and was evident in the GAXAS results of irradiated Gd_2TiO_5 (chapter 6). A comparison of the radiation behaviour of suite of orthorhombic Ln_2TiO_5 stuffed pyrochlores (e.g., La_2TiO_5, Nd_2TiO_5 and Y_2TiO_5 characterised by GAXAS methods used in this thesis) would further elucidate this behaviour and give more credence behind the theory that anti-site defect formation is the primary mechanism responsible for radiation tolerance improvements. This work would also further enable better tailoring of wasteform compositions by limiting waste loading of specific actinides to achieve an ideal lanthanide/actinide ion radius ratio (or including additional lanthanides of different sizes to achieve this effect) based upon radiation tolerance dependency of this quality.

Further attention should also be given to compositional variations of Ln_2TiO_5 such as $Ln_2Ti_{1-x}Zr_xO_5$, $Ln_2Ti_{1-x}Hf_xO_5$ and $Ln_2Ti_{1-x}Fe_xO_5$ to determine whether the samples can be formed in a single-phase with the inclusion of different transition metals. Studies of related pyrochlore structures, where Ti is substituted for either Zr or Hf, have produced materials with alternate radiation behaviours and tolerances that can be superior to the titanite variants. The substitution of Ti^{3+} for Fe^{4+} is a particularly interesting avenue of research as the $Ln_2Ti_{1-x}Fe_xO_5$ system would require a charge balance by some form of defect mechanism, such as an increase in oxygen vacancies. An increase in oxygen vacancy defects would consequently increase the ionic conductivity and potentially affect the radiation tolerance of the ceramic wasteform. Therefore, further investigation of varied structural formations of these compounds and, subsequently, the radiation behaviour should be explored.

The emergence of Ln_2TiO_5 ceramics as a prospective candidate to host actinide wastes is thoroughly supported by this work. However, to fully realise the potential for use as a wasteform, further work is needed. Whilst numerous studies have shown that orthorhombic and cubic structured Ln_2TiO_5 stuffed pyrochlores have a high tolerance to radiation damage, there are no studies which test the durability of such materials in conditions relevant to their storage and disposal (i.e., the dissolution behaviour in the presence of groundwater solutions) or assess the practicability of material recovery for reprocessing/non-proliferation assurance (i.e., accelerated dissolution in acidic media). Therefore, a future study of merit would be durability studies of Ln_2TiO_5 to assess the likelihood of radioactive isotope release in solution over a range of pHs, temperatures and time scales.